Characterisation of CMOS APS Technologies for Space Applications

Thesis

Characterisation of CMOS APS Technologies for Space Applications

Thesis submitted for the degree of

Doctor of Philosophy

at The Open University

by

Benjamin James Dryer

e2v Centre for Electronic Imaging

Discipline of Planetary and Space Sciences

Department of Physical Science

2nd January 2013

Characterisation of CMOS APS Technologies for Space Applications

Benjamin James Dryer

Abstract

In recent years, the performance of scientific CMOS active pixel sensors has been improved to the point that it is now approaching that of the current silicon sensor of choice, CCDs. For some applications, CMOS APSs is believed to present significant advantages over CCDs, such as improved radiation hardness. In this work, the effect of radiation damage on a 'baseline' commercial APS, e2v technologies' Jade APS, is characterised in response to gamma, proton and heavy ion irradiation. Specific performance problems encountered during this radiation characterisation, such as dark current non-uniformity under gamma irradiation, random telegraph signals under proton irradiation, and single event effects under heavy ion irradiation are described and analyzed. The X-ray spectroscopic imaging performance of the device is measured and compared to the Ocean Colour Imager APS test array showing progress towards a high frame rate spectroscopic X-ray imager for space science. The implications of these results for using similar devices in space applications are considered. Furthermore, possible novel techniques for measuring inter-pixel responsivity non-uniformity, heavy ion detection and spectroscopy, and measuring the dynamics of radiation-induced trap formation are discussed.

Declaration

I hereby declare that no part of this thesis has been previously submitted to this or any other university as part of the requirement for a higher degree. The work described herein was conducted solely by the undersigned except for those colleagues and other workers acknowledged in the text.

Ben Dryer, December 2012

Dedication

To my mother, father, and Em.

Acknowledgements

Thank you to my supervisors Andrew Holland, Neil Murray and Thomas Greig for much needed direction, motivation, and technical support.

Thank you to David Burt, Paul Jerram, Mark Robbins and James Endicott for their vast knowledge, probing questions, and guidance.

Thank you to the whole of the CEI, James Tutt, David Hall, Ross Burgon, Konstantin Stefanov, Jason Gow, Anthony Evagora, Richard Harriss, Phillipa Smith, Matthew Soman, Andrew Clarke, Edgar Allenwood, Calum MacCormick, Simeon Barber, Salah Karout, and George Seabroke; insightful conversations, much needed stress relief, and lasting friendships.

Thank you to members of JAXA, especially Sakao-Sensei, Narukage-san, Joten-san, Toshiaki-san, Kazuhiro-san and Takuji-san for their guidance, hospitality and friendship during my stay.

Thank you to all my colleagues past and present at the Open University, of which there are too many to name. I would however like to especially thank Jemma Davidson, Ben Rozitis, Paul Davey, Andrew Carter, Jen Ferreira, Minh Tran, Jon Mason, Naomi Murdoch, Andy Morris, Tim Tomkinson, and Kathryn McDermot for keeping spirits high.

Thank you to Nadia Pantidi for her support and friendship, and never failing to put a smile on my face. Without her I would not be who I am today.

I would like to again thank my parents and sister for their unwavering support and love. I cannot imagine getting this far without them.

Table of Contents:

List of Acronyms

3T	3 Transistor
4T	4 Transistor
5T	5 Transistor
ADC	Analog-to-Digital Convertor
ADU	Analog-to-Digital Unit
APS	Active Pixel Sensor
BI	Back Illuminated
CCD	Charge Coupled Device
CDS	Correlated Double Sampling
CEI	Centre for Electronic Imaging
CMOS	Complementary Metal-Oxide-Semiconductor
CTE	Charge Transfer Efficiency
CYCLONE	CYClotron of LOuvain-la-NEuve
DC	Direct Current
DN	Digital Number
DSNU	Dark Current Non-Uniformity
ECR	Electron Cyclotron Resonance
EJSM	Europa-Jupiter System Mission
ESA	European Space Agency
EUVS	EUV/FUV high-throughput Spectroscopic telescope
FET	Field Effect Transistor
FI	Front Illuminated
FIB	Focussed Ion Beam
FPGA	Field Programmable Gate Array
FPN	Fixed Pattern Noise
FWHM	Full-Width at Half Maximum
GCR	Galactic Cosmic Rays
GOES	Geostationary Operational Environmental Satellite
HIF	Heavy Ion Facility
HRC	High Resolution Camera
ILT	Inter-Line Transfer
IR	Infra-Red
ISAS	Institute of Space and Astronautical Science
JAXA	Japan Aerospace Exploration Agency
JEO	Jupiter-Europa Orbitor
JGO	Jupiter-Ganymede Orbitor
JPL	Jet Propulsion Laboratory
KVI	Kernfysisch Versneller Instituut
LEO	Low Earth Orbit
LET	Linear Energy Transfer
MOS	Metal-Oxide-Semiconductor
MOSFET	Metal-Oxide-Semiconductor Field Effect Transistor

MTF	Modulation Transfer Function
NASA	National Aeronautics and Space Administration
NIEL	Non-Ionising Energy Loss
NOAA	National Oceanic and Atmospheric Administration
OCI	Ocean Colour Imager
PD	PhotoDiode
PIPS	Passivated Implanted Planar Silicon
PKA	Primary Knock-on Atom
PPD	Pinned PhotoDiode
PRNU	Photo-Response Non-Uniformity
PTC	Photon Transfer Curve
QE	Quantum Efficiency
RAL	Rutherford Appleton Laboratories
RC	Resistance/Capacitance Circuit
RTS	Random Telegraph Signal
SAA	South Atlantic Anomaly
SEE	Single Event Effect
SEFI	Single Event Functional Interrupt
SEGR	Single Event Gate Rupture
SEM	Scanning Electron Microscope
SEU	Single Event Upset
SF	Source Follower
SI	International System of units
SIDC	Solar Influences Data Analysis Centre
SNR	Signal-to-Noise Ratio
SPENVIS	SPace ENVironment Information System
STFC	Science and Technology Facilities Council
STI	Shallow Trench Isolation
SUVIT	Solar Ultra-violet Visible and IR Telescope
TDI	Time Delay and Integration
TID	Total Ionising Dose
TRL	Technology Readiness Level
UKSA	United Kingdom Space Agency
USB	Universal Serial Bus
UV	Ultra-Violet
WFS	Wave-Front Sensor
XIT	X-ray Imaging (Spectroscopic) Telescope

Chapter 1: Introduction

1.1 Context

e2v technologies plc. is a world leading manufacturer of scientific imaging devices. Their core products are based on the Charge Coupled Device (CCD), a silicon imaging technology that has been available since the 1970s. However, the Complementary Metal Oxide Semiconductor Active Pixel Sensor (CMOS APS or APS) is a relatively recent development that has progressed to a stage that it can offer a viable alternative to CCD technology, and since then has become the imaging technology of choice for low-cost, low-power and mid-performance applications such as industrial inspection and consumer electronics.

Currently, APSs are used in relatively few space imaging instruments, especially in Europe, with CCDs being the imaging sensor of choice; able to provide high sensitivity, low dark current, and low read noise in a large format sensor based on Metal Oxide Semiconductor (MOS) technology that has proven to be reliable over the past 50 years. APSs have been flown, however, they are normally used to provide navigational support in the form of star trackers rather than scientific payloads.

Recently, state of the art APS technology has progressed to a point where their imaging capabilities are beginning to match CCDs, and furthermore APSs offer some significant advantages over CCDs for specific high-end space applications, due to their inherent higher tolerance to radiation damage, capability for faster readout rates, and capability for pixel addressing.

Owing to these advantages, there is growing interest in using APSs for scientific instruments, specifically those likely to encounter a particularly harsh radiation environment, or where fast readout is important such as in photon counting applications.

e2v technologies' acquisition of Atmel Grenoble in 2006 provided e2v with expertise in APS design, with APS products marketed for use in terrestrial applications such as machine vision and medical imaging. Understanding how these sensors react to radiation damage should allow improvements to the design to be made, and will provide a path to allow production of APSs that can offer an alternative to CCDs for applications in space science.

1.2 Aims

This work is funded as a Co-operative Award in Science and Engineering studentship between STFC and e2v technologies plc. The work is jointly funded and supervised by The Open University and e2v technologies plc. as part of the e2v centre for electronic imaging, a research group specialising in research into silicon imaging technologies for use in space science.

The main aim of this work is to characterise the effects of different species of radiation damage on a baseline APS technology. It is understood that this work would provide measurements of RTS effects, allowing for a significant contribution to understanding a poorly understood phenomenon in sensor science.

APSs, as a comparatively young technology, have far less flight heritage than CCDs, and as such there is less confidence in targeting a APS as a space sensor. A secondary aim of this body of work is to improve the Technology Readiness Level (TRL) of APS technology. This will lead to possibilities for APS to be baselined on board upcoming imaging instruments.

1.3 Thesis Organisation

This thesis is organised into nine chapters, with Chapter 1 being this introductory chapter.

Chapter 2 provides a historical overview of the development of the CCD, and the APS. A description of the operating principles of the basic building blocks of CCDs and APSs is

provided. A brief comparison of CCD and APS architecture and how this affects imager performance follows.

Chapter 3 begins by detailing how the building blocks described in Chapter 2 are assembled to create a APS imager, from the simple capabilities of a 1T (with a single transistor) pixel, to more complicated structures such as 5T pixels. It then goes on to describe techniques used in the commercial manufacture of the device that are relevant to later parts of the thesis. The chapter ends by describing the devices related to and used in this work.

Chapter 4 describes the different radiation environments encountered by space missions that imaging sensors will be subjected to. The chapter then goes on to describe the interactions of different radiation sources with semiconductor imagers, including any differing effects due to different architecture. An outline of APS use for space science, current missions that require a large study of radiation damage effects, and future instruments for which APS provides a viable option is then presented.

Chapter 5 describes the characterisation of semiconductor imagers. It begins by defining and detailing the characteristics that are important to sensor function, such as Dark Signal, Noise, QE, Responsivity and Linearity. The Photon Transfer Curve (PTC); an important characterisation technique, is detailed and presented with sample photon transfer curves measured from experimental devices. Chapter 5 then describes work analysing the X-ray characteristics of the several devices, including charge collection efficiency, analysis of split events, and a novel responsivity characterisation technique.

Chapter 6 presents measurements of the effects of gamma radiation on specific APSs sensors (Jade APS), characterising the change in performance due to irradiation. ‘Central Brightening’, an effect that seems to affect only a small number of device types and so has not been robustly explained in the literature, is characterised, and investigations into possible causes of the effect are reported.

Chapter 7 describes the effects of proton radiation on APSs. Specifically this work focuses on the characterisation of Random Telegraph Signal (RTS) 'noise' generated by proton interactions. These RTS effects are characterised well in the literature, but a consensus to the cause has not been reached. The chapter will discuss the suggested mechanisms responsible for the effect and where these measurements sit with respect to these mechanisms.

Chapter 8 describes damage due to heavy ion impacts, producing Single Event Effects (SEEs) which can drastically affect device behaviour. The transient and permanent effects of the damage are also reported and discussed.

Chapter 9 summarises the findings of this work and describes implications for the future use of APS in space science. Outstanding issues of this work are presented and highlighted as avenues for further work to be carried out.

1.4 Publications arising from this study

Dryer, B.J., Holland, A., Murray, N.J., Jerram, P., Robbins, M. & Burt, D., "Gamma Radiation Damage Study of 0.18 µm Process CMOS Image Sensors", SPIE Vol. 7742, (2010).

Dryer, B.J., Holland, A., "X-ray detection in EV76C454 CMOS devices", Technical Note (2011)

Harriss, R.D., Holland, A.D., Barber, S.J., Karout, S., Burgon, R., Dryer, B.J., *et al.*, "Compact CMOS camera demonstrator (C3D) for Ukube-1", SPIE Vol. 8146, (2011)

Dryer, B.J., Holland, A., "OCI X-ray Analysis", Technical Note (2012)

Dryer, B.J., Holland, A.D., Jerram, P., and Sakao, T., "X-ray performance of e2v's 0.18 µm CMOS APS test arrays for solar observation", SPIE Vol. 8453, (2012).

Chapter 2: The use of Solid State Imagers in Space

Semiconductor imagers have revolutionised image sensor technology by supplying high quality, low cost, real-time, well integrated, customisable solutions for almost every application. The most prevalent of these are silicon based imagers, namely the Charge Coupled Device (CCD) and the Complementary Metal-Oxide-Semiconductor Active Pixel Sensor (CMOS APS or APS). High-end science applications are now dominated by CCDs, and commercial and industrial applications are dominated by APSs, almost fully replacing older technologies such as photographic film and photomultiplier tubes.

When considering using an image sensor for space science, the criteria for selecting a sensor are based around image quality. CCDs are generally able to offer better image quality performance, however the gap between APS and CCD performance has been narrowing due to significant development effort in recent years. To separate the two, it is important to consider the features that an application requires, and to compare the benefits and drawbacks of each technology. One of the advantages in the case of APSs is a potential decreased degradation in performance after irradiation when compared to CCDs making the APS the technology of choice for imaging missions visiting high radiation environments such as the solar orbit or the Jupiter system. Characterising the reaction of APSs to radiation is therefore important for the future development of the technology.

This chapter introduces the history of the development of semiconductor imagers, and gives an overview of their operating principles, performance and advantages.

2.1 Semiconductor Imager History

This section outlines the major events in the development of CCD, APS, and Hybrid imaging technology. For a more detailed overview, see Janesick, 2001 (CCDs), Fossum, 1997 (APSs), and Rogalski, 2002 (Hybrids).

2.1.1 Charge Coupled Devices

The CCD was first conceived in 1969 when Boyle and Smith of Bell Telephone Laboratories were tasked with developing a semiconductor analogue of magnetic bubble memory, a type of computer memory that was quickly made obsolete by hard disk technology. Borne from this was the idea of using regions ('bubbles') of high electric field within the semiconductor to hold charge. The idea was developed in an afternoon and within a few weeks the first device was fabricated, consisting of nine electrodes, and charge storage and transfer under these electrodes was successfully demonstrated (Boyle & Smith, 1970).

It quickly became clear that the CCD had applications beyond information storage, and that with sufficient development they could compete with both the main astronomical imaging technology of the time, photographic film; as well as the main electronic video camera technology, the tube detector. It was also realised that CCDs would be ideal for space applications that were in planning at the time, such as the precursor to the Hubble Space Telescope.

The first CCD imagers became commercially available in 1974, and the technology rapidly developed due to several competing companies' involvement, and the increasing demand for the technology to progress in several diverse applications. Today, the technology is mature, and major development in scientific applications is geared towards sensing in low light levels such as the Electron Multiplying CCD (Madan, 1983), extending the usable wavelength range (Lesser, 1994), and development of high performance large format arrays for high resolution imaging (*e.g.* the Gaia focal plane array consisting of 106 CCDs totalling 974 Mpixels (Short, 2004)). Boyle and Smith received the Nobel Prize in Physics for their invention in 2009.

2.1.2 Active Pixel Sensors

The development of the APS has had to overcome more hurdles than the CCD. While the elementary design of the APS was first suggested and defined before CCDs had been considered in the late 1960s (Weckler, 1967, Dyck & Weckler, 1968), fabricated devices were found to have high Fixed Pattern Noise (FPN) due to the difficulty in fabricating identical pixels, and due to the densely packed pixel structure and large semiconductor fabrication feature size at the time, small pixels could not be made, and the electronics technology needed to address a large array of pixels was not available. When CCDs were introduced, they offered a much simpler, smaller pixel, simpler readout schemes, and relative freedom from FPN. Over the next 20 years, MOS sensors were investigated only periodically, with little continued research, and were generally compared unfavourably to CCDs.

During this time however, the development of exponentially smaller MOS feature sizes continued as described by Gordon Moore (Moore, 1965) driven by the demand for computing power created by the introduction of the personal computer. Towards the end of the 1980s, it was becoming clear that CCDs could not provide the best solution for every imaging application, especially in fields such as particle physics, where CCD performance quickly deteriorates due to radiation damage. In the early 1990s, it was recognised that APS could now be reliably fabricated, and could provide solutions to these specific imaging problems. NASA's Jet Propulsion Laboratory (JPL) was instrumental in the development of the technology, and was responsible for the fabrication of the first 'modern' APS (Mendis *et al.*, 1993).

Over the past 20 years, developments in APS design have overcome FPN problems due to better fabrication techniques and the development of noise cancellation circuitry. Due to Moore's Law, pixel size is now limited by external optics design rather than minimum CMOS feature size (pixel size has shrunk to about 2-3 μm at the smallest, while minimum CMOS

feature size is 22 nm and shrinking, although most devices are fabricated using significantly larger processes *e.g.* 180 nm). The widespread use of CMOS fabrication ensures that CMOS sensors cost less to mass manufacture and in general consume less power than CCDs, leading to widespread use in consumer electronics. In recent years, as the performance of APSs has increased closer to CCD levels, the APS has even begun attracting attention for use in high-end space applications (see Chapter 4), a realm almost entirely dominated by CCDs for close to 40 years, owing to its inherent radiation hardness (due to reduced reliance on charge transfer), low power consumption and fast readout speeds.

2.1.3 Hybrid Imager

It is important to recognise a third, specialised imaging technology called hybrid arrays which couple exotic semiconductors such as InGaAs and HgCdTe to a Si-CMOS device providing readout circuitry. These sensors became popular in the mid-1980s for infrared astronomy (Rogalski, 2012). Hybrid devices separate the CMOS readout circuitry from the sensing substrate, allowing customisation of each to extend the ability of the device to operate outside of the wavelengths that CCDs and APSs are limited to due to the silicon bandgap. Hybrid sensors do not form part of this thesis. Further information can be found in Rogalski (2002) and Rogalski (2012).

2.2 Charge Coupled Device and Active Pixel Sensor Method of Operation

The major differences between the APS and the CCD design lie not in the collection of signal charge, but in the method of reading out this charge after it has been collected. Here a summary of the readout method of each is provided. Details of the structures responsible for charge collection and readout are provided in Chapter 3.

2.2.1 Charge Coupled Device

A CCD is formed of an array of MOS capacitors (See Chapter 3) vertically divided by undoped ‘channel-stops’ to define pixel columns, and using a series of electrodes

horizontally to define pixel rows. A common device type called 'three-phase' has three horizontal electrodes per pixel. Figure 2.1 shows a cross-section through a three-phase pixel.

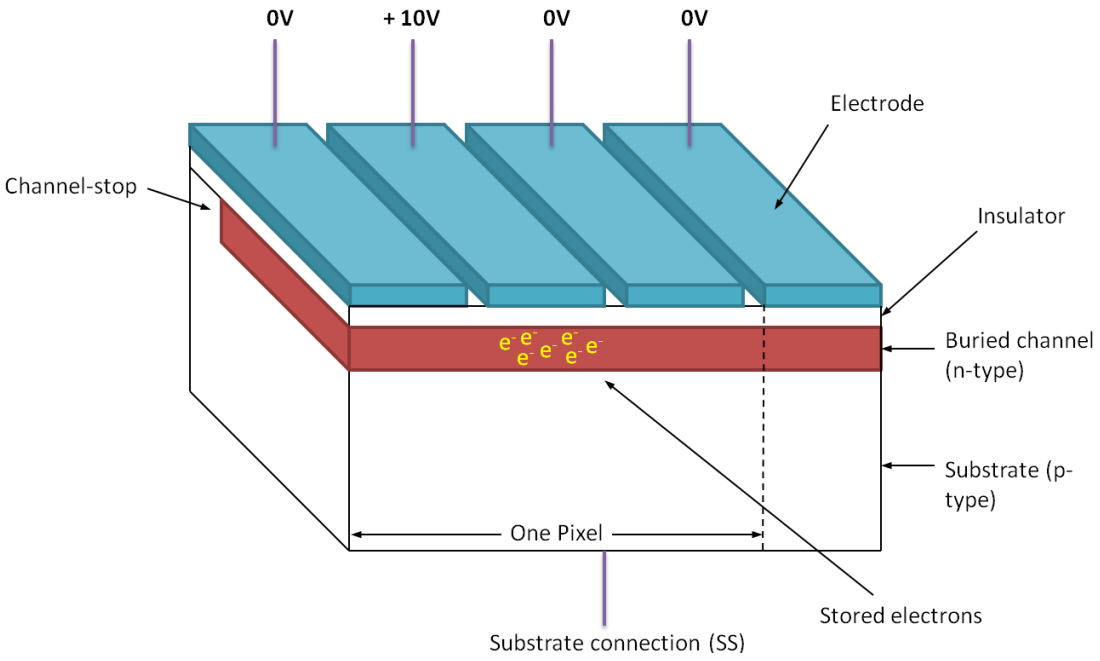

Figure 2.1. Cross-section of a three-phase CCD pixel.

During image integration, one or more of these electrodes is held at a higher voltage (than the other electrodes), and charge generated close to this area will be captured underneath the electrode in an area defined by the depletion layer as outlined in Chapter 3.

All CCDs move charge packets by increasing the voltage on a neighbouring electrode such that the charge packet spreads beneath ('couples' between) both electrodes, and then the initially active electrode has its voltage decreased to the baseline voltage. This causes the charge packet to move along the 'doped' column in the clocked direction as shown in Figure 2.2.

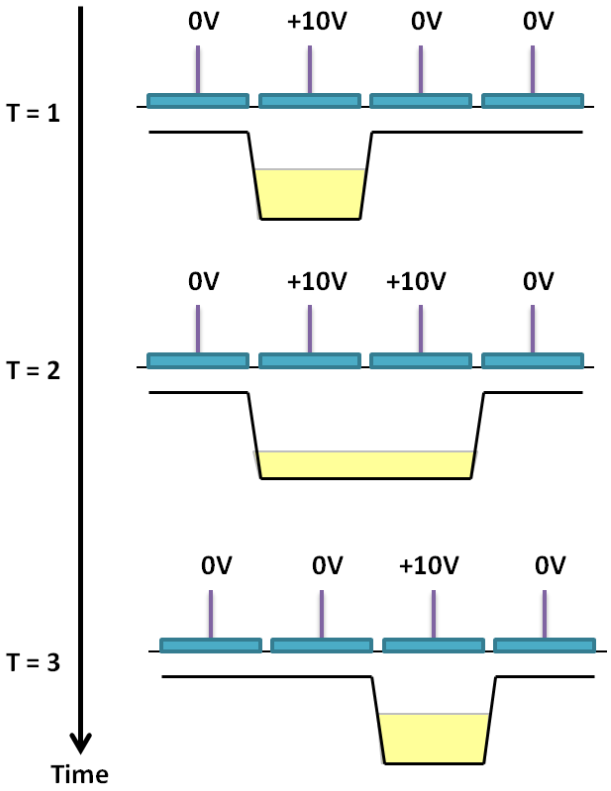

Figure 2.2. Diagram showing method of charge clocking, yellow regions denote electron packet.

Each time the image is clocked across the device by an entire pixel, the row at the bottom of the image must then be readout, and this is performed in a specialised region called the readout register, where the electrodes run perpendicular to the image transfer and the clock speed is much higher. Charge is clocked, pixel-by-pixel, to the sense node, a small capacitance that modulates the current through a MOSFET, and so can be measured as a potential difference across a resistor. Figure 2.3 shows a microscope image of a CCD electrode structure close to and including a section of the readout register.

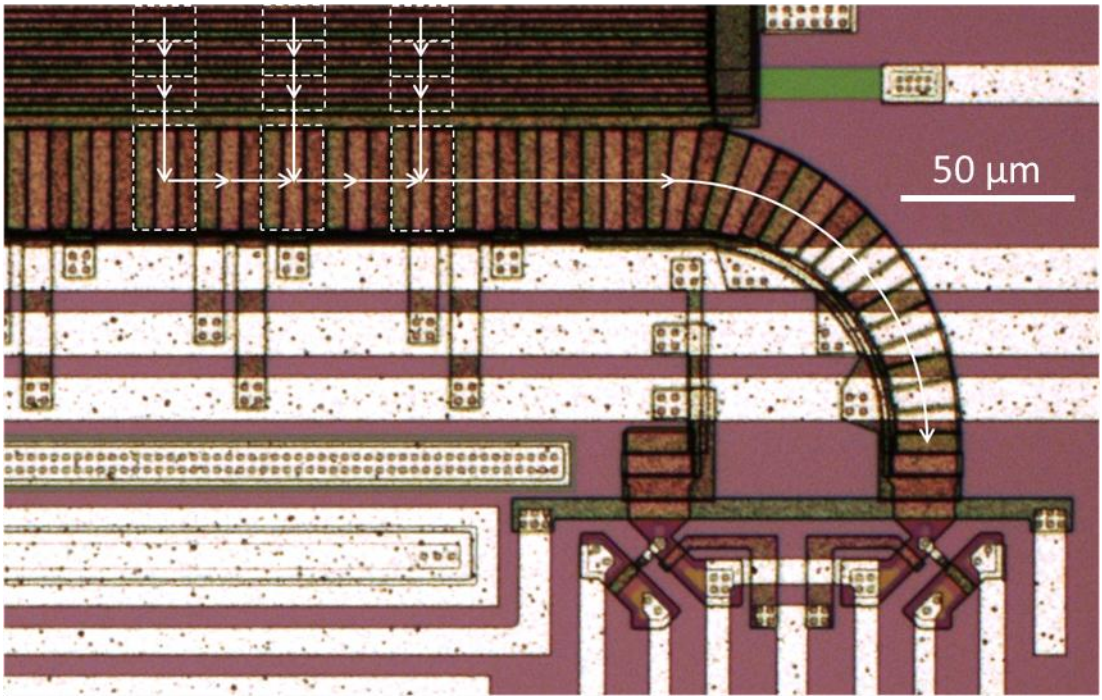

Figure 2.3. Microscope image of an e2v technologies (4-phase parallel, 3-phase serial) CCD annotated with charge packet clocking directions.

The simplest CCD layout is the full-frame device which does not store the image before reading it out. This is contrasted with the frame transfer and Inter-Line Transfer (ILT) devices, which both have shielded regions on-device to enable the next image to be integrated while readout is occurring, negating the need for a mechanical shutter.

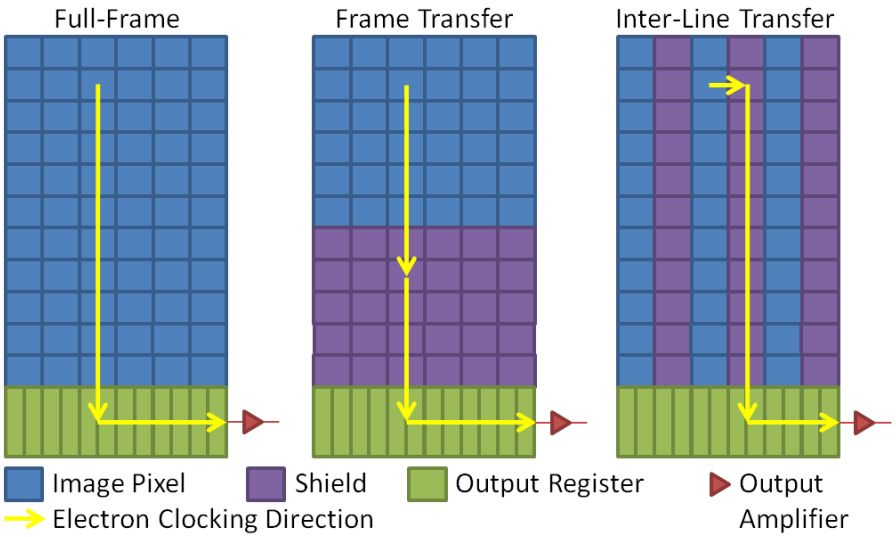

Figure 2.4. Schematic showing layout and readout path of three common CCD designs.

A key property of CCDs is the Charge Transfer Efficiency (CTE), a measure of the efficiency of the charge transfer process during clocking. While this is generally only stated as a figure

of merit for the CCD, APSs must also transfer charge from the photodiode to the sense node, and so having a very low CTE can also affect the performance of an APS. However, CTE in modern devices is generally very high (>99.9999%), so loss in the single transfer in an APS has a negligible effect. In CCDs where a charge packet may be transferred thousands of times, depending on the resolution of the device, even a small amount of charge lost in each transfer can be problematic, as charge is 'deferred' and is seen as charge in neighbouring pixels.

The degradation of CTE due to device irradiation is the main source of the inherent radiation hardness of APSs compared to CCDs, as even a small reduction in CTE can have large effects on CCD performance. The characteristic trails created by poor CTE as X-ray events are clocked through an increasing number of pixels can be seen in Figure 2.5. Here signal from the charge packets is momentarily trapped in the array during transfer and then some time later released into the subsequent pixels in the column.

Figure 2.5. Image of X-ray events in a proton-irradiated CCD47 showing severe CTE degradation arising from radiation damage. The readout direction is towards the top of the image.

One can see deferred charge tails growing longer at the bottom of the image, due to the increased number of pixels that charge travels through compared to the upper region which is closer to the readout register. Measurements of this device indicated a CTE of only 99.9% after irradiation. The same effect is also present in the readout register, similarly 'smearing' charge in the horizontal direction.

The CCD readout mechanism offers some advantages for certain applications, for example an imager onboard a moving satellite can clock the charge at the same rate that objects transit over the imager (called Time Delay and Integration (TDI) mode), allowing longer effective integration times to collect more signal from faint objects.

2.2.2 Active Pixel Sensor

The APS, in comparison to the CCD, is a highly integrated and considerably more complex system. Each pixel has a photodiode and dedicated readout circuitry. The collected charge on the photodiode is amplified through each source-follower. The addressing electronics then samples the signal from each pixel by a single output (see Figure 2.6 for an overview of a simplified common layout).

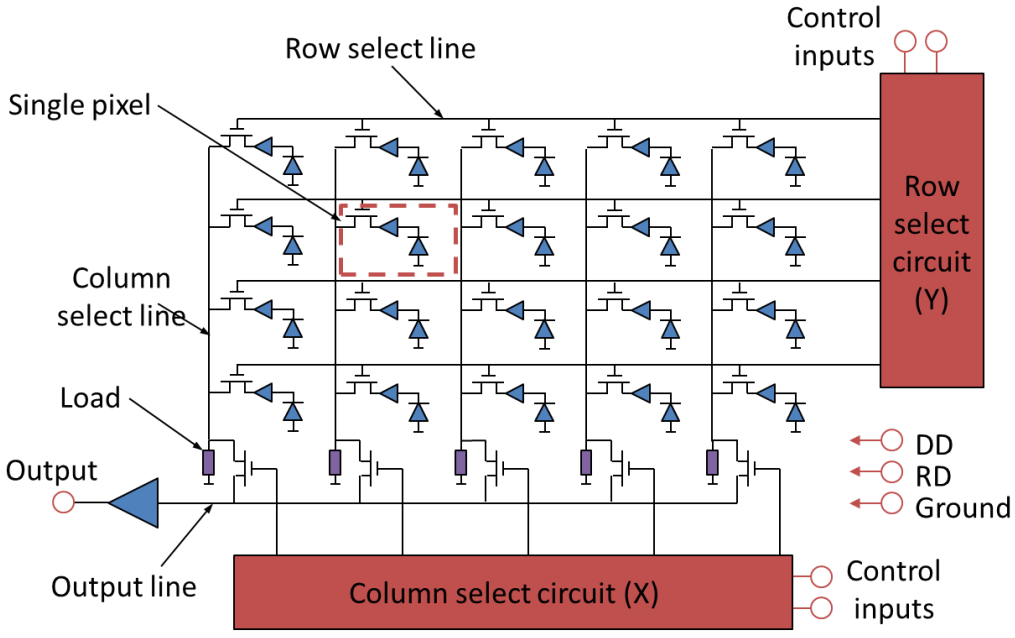

Figure 2.6. Schematic of typical APS layout, showing a 5×4 pixel array.

Each pixel acts as an autonomous light sensor, and readout is achieved by rastering across the image using the row and column select clocks. This allows any pixel or section of pixels to be read out independently without reading any signal from other pixels, providing increased readout speed of an identified area of interest, a feature that is difficult to implement in CCDs. In addition to this, because of the independent nature of pixels, any damage occurring somewhere in the image area will affect only the damaged pixels.

2.3 Charge Coupled Device vs. Active Pixel Sensor State of the Art

Due to different photodiode designs and processing pipelines, CCDs and APSs have inherent strengths and weaknesses when compared to one another. These can be mitigated with careful design, and much of the development in the field concentrates on raising APS performance to the standard of the more mature CCD on a certain figure of merit.

Table 2-1 shows basic figures of merit for scientific CCD and APSs. For more detail on the definition and measurement of some of these figures of merit see Chapter 5.

Feature	CCD	APS
Quantum Efficiency (Back Illuminated)	90%	<90%
Fill Factor	100%	<80%
Amplifier Mismatch	None	Moderate
System Noise	<1 e^- rms	>3 e^- rms
Drive System Complexity	High	Low
Sensor Complexity	Low	High
Responsivity	1-5 $\mu V \cdot e^{-1}$	5-50 $\mu V \cdot e^{-1}$
Dynamic Range	High	Moderate
Linearity	High (<1%)	Medium (<5%)
Uniformity	Good	Low-Moderate
Frame Rate	30 fps	1000+ fps
Voltage Requirement	30 V	5 V
Power Requirement/cm^2	100 mW	10+ mW
Development Cost	Moderate	High
Radiation Hardness	Moderate	High

Table 2-1. Comparison of figures of merit for current scientific APS and CCDs.

2.4 Use of Semiconductor Imagers in Space

To date, relatively few APS imagers have been used in space despite the advantage of their improved radiation hardness. Instead, CCDs are often selected as scientific imagers due to their higher performance and more proven heritage. With the performance gap between APS and CCD closing, the APS offers a real performance advantage due to low power requirements and high radiation hardness. This affords a few niche space instrumentation applications where the APS can become the imager of choice:

- Harsh radiation environments such as Solar or Jupiter system missions.
- Missions with low power requirements such as cubesat missions or planetary rovers.
- High framerate applications such as solar photon counting.

This thesis concentrates on the characterisation of radiation damage effects in the e2v technologies 'Jade' APS and similar imaging devices, with a view to possible use of devices of similar design in space. In addition, complex effects of radiation damage on semiconductor imager components such as Random Telegraph Signal (RTS) noise (Chapter 6) and central brightening (Chapter 7) are analysed in depth. The suitability of APSs in select high framerate and low power applications are also mentioned.

Chapter 3: Active Pixel Sensor Technology

This chapter presents an overview of the theory, design and operation of general semiconductor imaging devices, the MOS Field Effect Transistor (MOSFET), and finally the APS in its most common configurations. The chapter ends with the specifications of several APSs used in the work contained within this thesis.

3.1 Semiconductor Imager Theory

In this section a very brief overview of the most pertinent theory behind the operation of CCDs and APSs is given. A more detailed description of the theory is given by Sze (1981).

3.1.1 MOS Capacitor

The Metal Oxide Semiconductor (MOS) capacitor is the simplest 'building block' of a semiconductor imager and plays an important role in accumulating photon-generated charge in CCDs. It also forms a key component of the MOS Field Effect Transistor (MOSFET), of which there are several in each APS pixel. It consists of a conductive electrode (commonly called a 'gate' and fabricated from polysilicon) and doped bulk silicon, separated by a thin layer of dielectric material (normally a native SiO_2 layer).

The doping of the silicon is dependent on the desired majority charge carrier. A p-MOS capacitor uses n-type silicon, which is doped with a group V element, typically phosphorous, which acts as a 'donor'. The donor provides an abundance of valence electrons, which increase the conductivity of the silicon. Conversely, an n-MOS capacitor uses p-type silicon doped with a group III element, *e.g.* boron, which acts as an 'acceptor'. This acceptor will create holes as the majority charge carrier.

Using the example of the n-MOS capacitor, by applying a potential difference between the gate and silicon substrate, the structure can be operated in three regimes: accumulation, depletion and inversion. Depletion is the regime of interest for normal operation of

semiconductor imagers. Applying a positive voltage between the gate and the underlying doped silicon will drive the surface into depletion. In depletion (in the case of n-MOS, when a small positive voltage is applied), the abundant majority carrier, holes, are repelled from the Si-SiO_2 interface as the potential from the gate propagates into the bulk silicon. The potential at a given depth in the silicon, and therefore the total depth of depletion, can be calculated by solving Poisson's equation:

$$\frac{d^2V}{dx^2} = \frac{\rho}{\varepsilon} \tag{3.1}$$

Where V (V) is the electric potential at a depth x (m) for a given permittivity of the substrate ε (F·m^{-1}), and charge density ρ (C·m^{-3}). For the case of an n-MOS capacitor in depletion, it can be assumed that the mobile carriers have been swept out of the region and that there are no fixed donors, the present charge is then solely defined by the fixed acceptors so $\rho = qN_A$ where q (= 1.602 × 10^{-19} C) is the electronic charge and N_A (m^{-3}) is the number density of acceptors. It can also be assumed that at the depletion depth x_d the boundary conditions $V = 0$ and $dV/dx = 0$ apply and therefore integrating equation 3.1 to find V at a depth x yields:

$$V = \frac{qN_A}{2\varepsilon}(x - x_d)^2 \tag{3.2}$$

Plotting Equation 3.2 provides the potential profile shown in Figure 3.1.

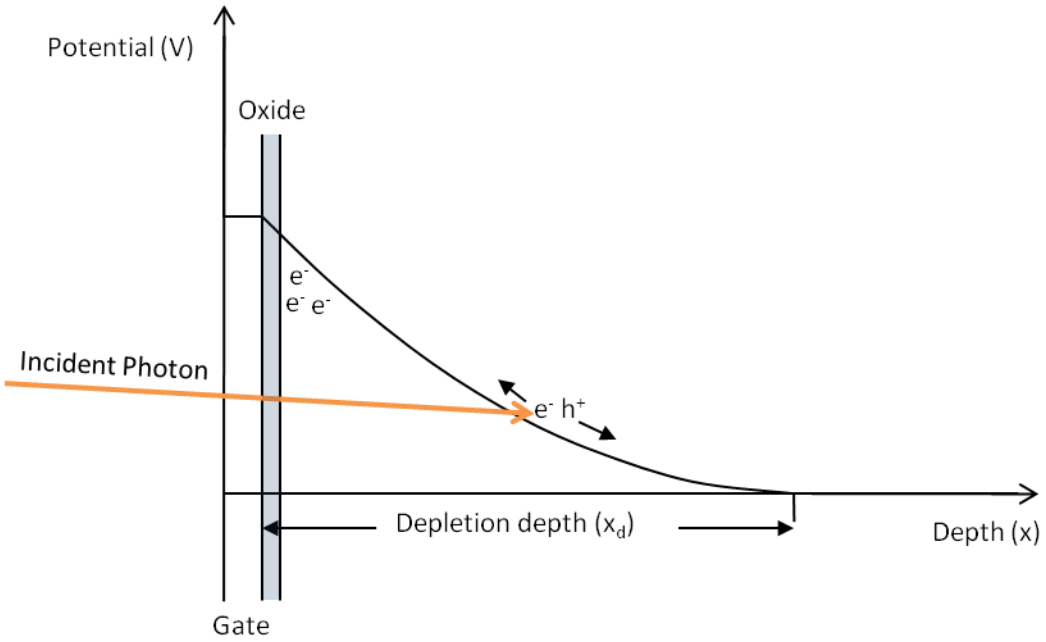

Figure 3.1. Graph showing potential drop through bulk silicon, illustrated with the direction of photo-generated charge movement.

Any electron-hole pair created within the depleted region will be separated and the electron will be attracted to the Si-SiO_2 interface under the electrode, as it is the area of highest potential. This flow of photo-generated charge towards the surface gives rise to the term 'photodiode'. Charge generated by the photoelectric effect (Einstein, 1905) within the depletion region is accumulated at the surface to later be measured as signal. A p-MOS capacitor can be used in the same manner but will require negative bias and use less mobile holes as the photo-generated carrier.

The simple MOS capacitor generates a large quantity of dark current (thermally generated charge). At the interface the Si and SiO_2 do not bond perfectly, leaving 'dangling bonds' (Helms & Poindexter, 1994). These dangling bonds provide an energy level or 'surface state' that allows electrons with thermal energy lower than the silicon band gap to excite to the conduction band, increasing the amount of spurious charge collected alongside photo-generated charge. These dangling bonds are generally referred to as 'traps', as they are capable of trapping electrons from both the conduction and valence bands, releasing them

some time later. This is generally not a problem for MOSFETs, described later, but is a significant problem for imaging devices as it contributes noise to the image.

3.1.2 p-n Junction

The p-n junction allows for the creation of a 'buried channel' MOS capacitor and photodiode which holds photo-generated charge away from the Si-SiO_2 interface, reducing the effects of surface states.

The p-n junction consists of a region of p-type silicon in close contact with a region of n-type silicon. When the regions are brought into contact, a large electron density gradient exists, and electrons will diffuse from the n-type region to the electron sparse p-type region. As these carriers diffuse over the junction, they leave behind fixed ions, which form a depletion layer at the interface. In this case no external bias is needed to generate the depletion layer, unlike the MOS capacitor.

If a photon interacts within the depletion layer creating an electron-hole pair, the electron and hole will be accelerated out of the depletion layer by the electric field in opposite directions, causing a current to flow. The size of the depletion region can be altered by subjecting the junction to a potential difference. In forward biased mode, where the p-type region is held at a more positive voltage than the n-type region, the depletion width is reduced. In reverse biased mode, where the n-type region is held at a more positive voltage, the depletion layer grows.

3.1.3 Buried Channel Photodiode

Now consider the case of a reverse biased p-n junction, but with a gate electrode separated by an oxide on top of the n-type region. By reverse biasing the junction, the depletion layer at the p-n junction grows, and at some point within the n-type region the potential is greater than the gate bias. Due to this 'negative bias', the surface will be depleted of electrons to some depth. As the two depletion regions meet, there is a point where the

potential is at a local maximum, and this is what is referred to as the buried channel. In the buried channel, the photo-generated charge is accumulated away from the surface, and therefore away from the surface states.

If the depletion regions are fully depleted of mobile carriers, in the n-type region doped to a depth x_n the charge density $\rho = qN_A$ and in the p-type region until $x = x_p$ (where x_p (m) is the depletion depth in the p-type region), $\rho = -qN_D$ (where N_D (m^{-3}) is the number density of donors), giving us simultaneous Poisson equations:

$$\frac{d^2V}{dx^2} = \frac{-qN_D}{\varepsilon}, \qquad 0 < x < x_n \tag{3.3}$$

$$\frac{d^2V}{dx^2} = \frac{qN_A}{\varepsilon}, \qquad x_n < x < x_n + x_p \tag{3.4}$$

Assuming continuous and equal functions at the boundaries, the solution for the n-type region is:

$$V = V_{max} - \frac{qN_D}{2\varepsilon}(x - x_{max})^2, \qquad 0 < x < x_n \tag{3.5}$$

and for the p-type region:

$$V = \frac{qN_A}{2\varepsilon}(x - x_n - x_p)^2, \qquad x_n < x < x_n + x_p \tag{3.6}$$

Using equations 3.5 and 3.6 it is possible to plot the buried channel potential, shown in Figure 3.2. This indicates a potential well held away (or 'buried') from the trap-filled surface of the device, and thus, in the case of CCDs, prevents the 'smearing' of charge packets as they are clocked under the trap-filled surface. However unless the surface is 'pinned', as described below, surface dark current can still be generated into the buried channel.

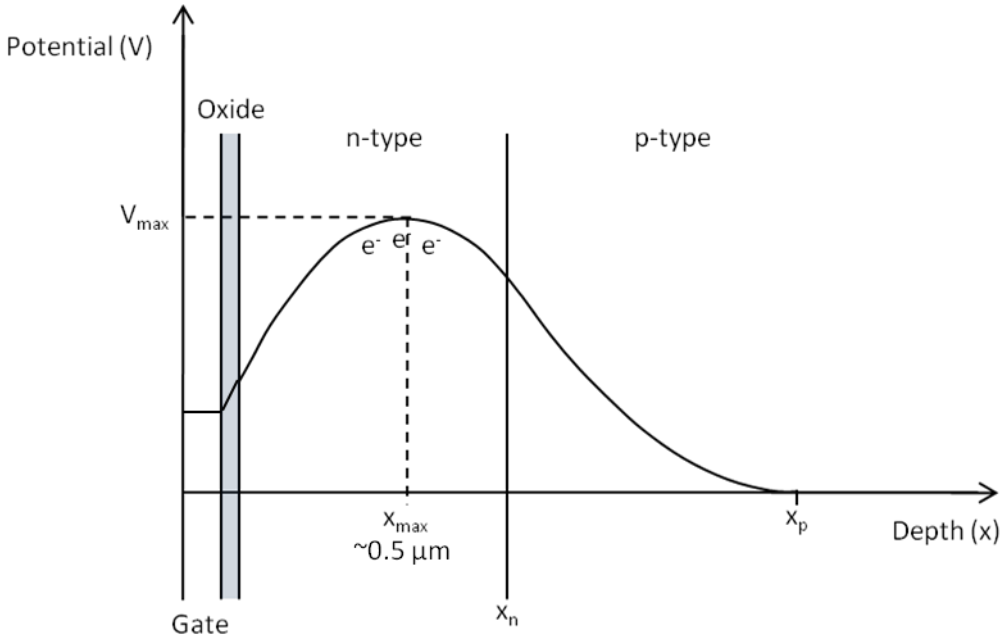

Figure 3.2. Graph showing potential profile through a buried channel.

3.1.4 Pinned Photodiode

To decouple the photodiode from the effects of the noisy surface, it must be made pinned. This can be accomplished in several ways, for example adding a thin region of p-type silicon at the surface or applying a lower potential to the surface of the device. This has the effect of driving the potential at Si-SiO_2 interface below 0 V, attracting holes to the surface of the silicon. This layer of holes quenches the generation of carriers by the interface through recombination, preventing them from entering the photodiode. This results in a device with a much lower dark current and therefore shot noise, as the surface is one of the major contributors of noise to the device.

3.1.5 MOSFET

The MOS Field Effect Transistor (MOSFET) is one of the most important structures, not only for imaging devices, but for the entire field of integrated circuits as it constitutes an elementary part of microprocessors and memory technology. In CCDs the MOSFET provides the main component of read-out circuitry, and in APSs each pixel has a number of MOSFETs

for read-out and other more complex functions. Figure 3.3 shows the basic structure of an n-channel MOSFET.

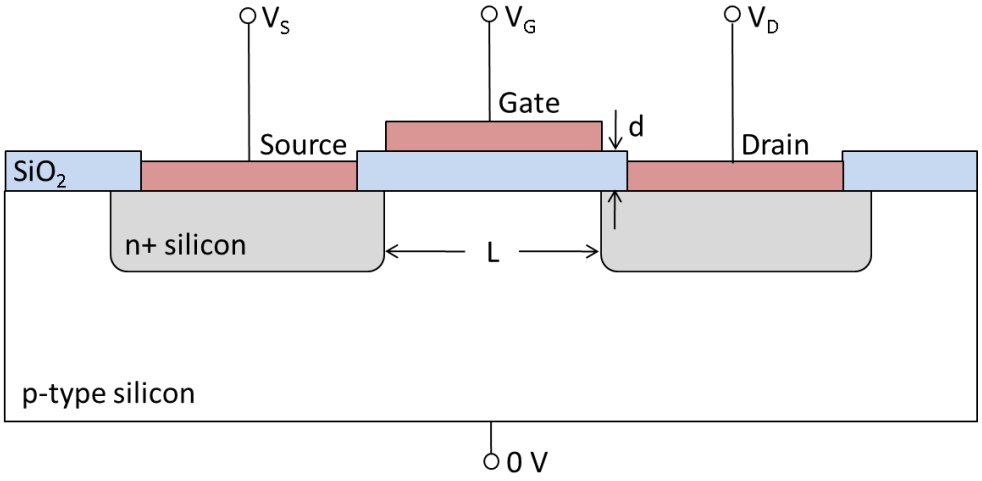

Figure 3.3. Diagram of basic structure of an n-channel MOSFET

The n-channel MOSFET can be visualised as an n-p-n junction, with two depletion regions formed around each p-n interface. It should be noted that the V_G gate is fabricated as a MOS structure, whereas V_S and V_D are ohmic contacts. As a voltage is applied at the gate (V_G becomes greater than some threshold voltage, V_T), the surface of the silicon between the n+ regions becomes inverted, forming a channel connecting the two regions where, if a small voltage is applied to the drain, current (proportional to V_G) can flow. For $V_G > V_T$ and small V_{DS} (potential between drain and source), the MOSFET operates in a linear regime, and the current flowing is described by:

$$I_{DS} = \mu C_0 \frac{W}{L}\left(V_{GS}V_{DS} - \frac{1}{2}V_{DS}^2\right), \qquad V_G > V_T, V_D < V_{GS} - V_T \tag{3.7}$$

Where W (m) and L (m) are the channel width and length respectively, μ ($m^2 \cdot V^{-1} \cdot s^{-1}$) is the carrier mobility, and C_0 ($F \cdot m^{-2}$) is the effective gate capacitance. V_{GS} (V) is the electric potential between the gate and source electrodes and V_{DS} (V) is the electric potential between the drain and source electrodes.

As V_D is increased, a point is reached called 'pinch-off' where I_{DS} no longer depends on V_D. This voltage is the saturation voltage $V_{DSAT} = V_{GS} - V_T$, and the current flowing in the channel above this point is described by:

$$I_{DS} = \frac{1}{2}\mu C_0 \frac{W}{L}(V_{GS} - V_T)^2, \qquad V_G > V_T, V_D > V_{DSAT} \tag{3.8}$$

$$= \frac{1}{2}\beta(V_{GS} - V_T)^2 \ \ where \ \ \beta = \mu C_0 \frac{W}{L} \tag{3.9}$$

Again taking the linear regime, but this time decreasing the gate potential such that $V_G < V_T$, the sub-threshold condition is derived. Since there is no inverted channel, the current in this mode should be zero, but instead a small leakage current flows as a result of some of the electrons having sufficient energy to overcome the potential barrier between the source and channel (*i.e.* effectively $V_{GS} - V_S$) and are then able to reach the drain by diffusion (Gosney, 1972). The sub-threshold regime of operation is described by Equation 3.10:

$$I_{DS} \approx I_{D0} e^{\frac{V_{GS} - V_T}{k\frac{T}{q}}}, \qquad V_G < V_T, V_D < V_{DSAT} \tag{3.10}$$

Where T (K) is the temperature, k (= 1.38×10^{-23} $m^2 \cdot kg \cdot s^{-2} \cdot K^{-1}$) is the Boltzmann constant and I_{D0} is the current at $V_{GS} = V_T$. This mode is of particular interest in switching applications, where the MOSFET is switched between 'on' and 'off' states by applying voltages above and below the threshold voltage. Figure 3.4. shows the current-voltage characteristics of an idealised MOSFET.

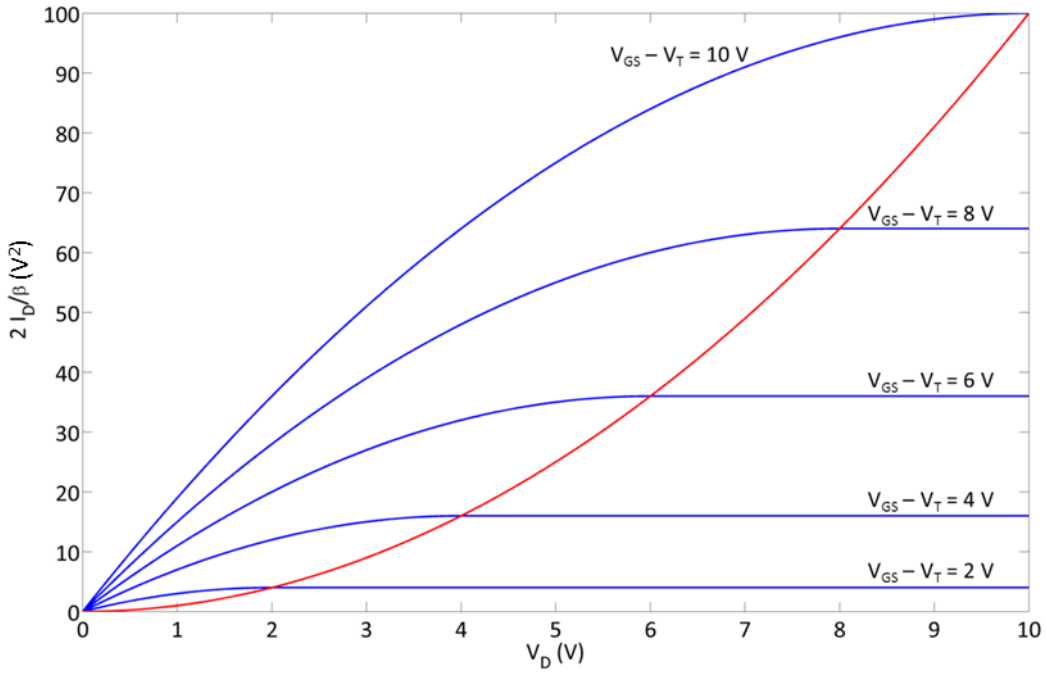

Figure 3.4. Idealised MOSFET drain characteristics for differing V_{GS}-V_T (blue), plotted with V_{DSAT} (red), beyond which value I is constant

3.1.6 Source Follower

The source follower circuit is used in both APS and CCD designs to convert the integrated charge to a measurable output voltage. In the case of CCDs there is a single source follower circuit at the end of the readout register, whereas APSs have a source follower circuit in each pixel. The circuit consists of two MOSFETs, the 'follower' and the 'load' transistors, connected in series between the supply voltage and ground (see Figure 3.5).

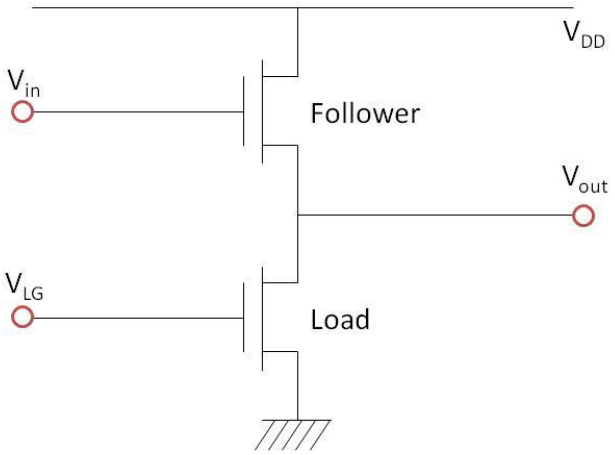

Figure 3.5. Schematic of a source follower circuit

The load transistor is operated in saturation and supplies a constant current, I_{DS}, over the transistor pair, which can be fixed by setting V_{LG}. For a given V_{DD} the follower transistor's gate to source voltage $V_{GS} = V_{in} - V_{out}$ changes to keep the current flowing across it (I_{DS}) constant. Assuming the follower transistor is also biased above threshold, rearranging equation 3.8 gives the output voltage V_{out} as:

$$V_{out} = V_{in} - V_T - \sqrt{\frac{2I_{DS}L}{\mu C_0 W}} \tag{3.11}$$

This shows that the output voltage is equal to the input voltage plus some fixed DC offset dependent on the threshold voltage of the follower transistor. As the APS has a source follower circuit for each pixel, it is the difference in threshold voltage of the follower transistor between pixels that contributes a large fraction of the fixed pattern noise, due to difficulty in fabricating uniform CMOS features especially prevalent in the early history of development of APS. CCDs use the same follower transistor to read out every pixel, so variation between transistors merely alters the performance between devices.

3.2 Pixel Designs

The device-wide architecture of APSs is shown in Figure 2.6. This section outlines common pixel designs used in these devices, from the basic 3-transistor (3T) pixel to other, more complex pixel structures, which afford more complex features.

3.2.1 3T

The 3T pixel (shown in Figure 3.6) is both the most basic active pixel design and is similar to basic CCD readout circuitry (with the photodiode in Figure 3.6 replaced by the final element of the readout register, and excluding column and row-select transistors).

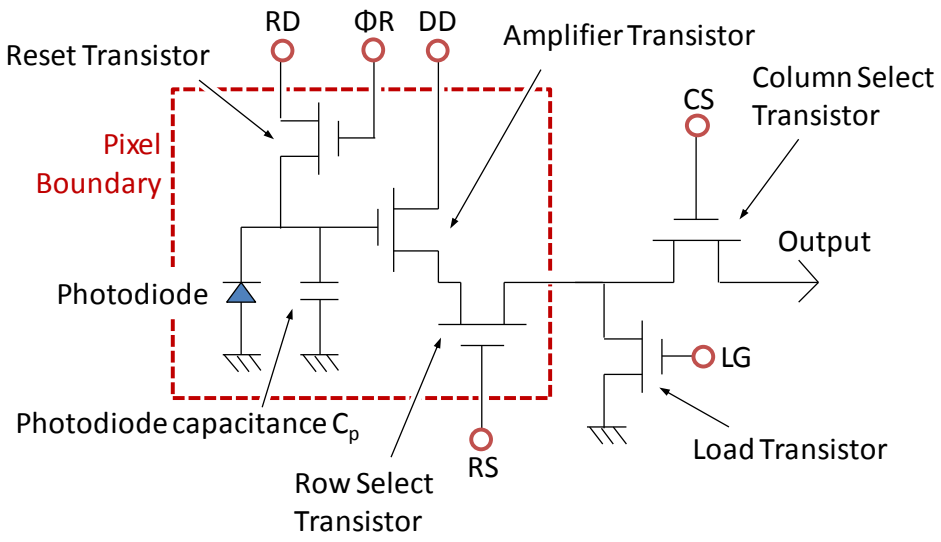

Figure 3.6. Schematic of typical 3T pixel design, including a reset transistor.

The 3T pixel is a source follower with the amplifier transistor acting as the follower. Also shown in Figure 3.6 are the column select and column load transistors which are common to an entire row of pixels (these external transistors are denoted by the node 'CL' in Figure 3.7 and Figure 3.9). This allows for a single load transistor (from the source-follower circuit) to be shared by an entire row of pixels. The row select transistor is only biased when the pixel is to be read out, determined by external clocks.

Charge accumulates on the capacitance connected to the gate of the amplifier transistor (also known as the 'sense node'). At the time of read-out, the column and row select transistors are biased (*i.e.* switched 'on') and the voltage at the source follower output is essentially connected through the device to be sampled by the output terminal and therefore provides a signal value. The reset gate voltage ΦR is then increased and the charge accumulated on the photodiode will discharge, allowing the pixel to re-accumulate from a base level after read-out.

It is important to mention the linearity of the pixel. The variation of the voltage on the photodiode over time is given by:

$$V_p = V_{RD} - \frac{I_0 A t q_e}{C_p} \tag{3.12}$$

Where V_p (V) is the potential of the photodiode, $I_0 A$ (photons.cm^{-2}.s^{-1}) is the photocurrent, t (s) is the integration time, and C_p (F) is the capacitance of the photodiode. As charge accumulates on the photodiode, the voltage difference V_{RD} across the amplifier transistor will decrease linearly with it; however this accumulation of charge also alters the node capacitance, resulting in a non-linear response. In the case of the APS this non-linearity can be severe, due to the small photodiode capacitances (which determines responsivity and maximum signal capacity) used in order to improve response.

The 3T pixel is entirely composed of elements that conform to standard CMOS processes, and as such can be fabricated cheaply and in bulk. A major issue with the design is that it cannot mitigate reset level noise, a major (and often the limiting) noise source caused by fluctuations in the level of the reset voltage. This means that each time the pixel is reset, the reference level is different, and so there can be a measured difference between identical amounts of accumulation. Another issue is that during reset the photodiode capacitance may not have sufficient time to discharge fully, resulting in deferred charge between reset periods in high pixel-rate applications, commonly referred to as ‘lag’. Pixel responsivity non-linearity is also an issue, but can largely be pre-characterised.

3.2.2 4T

Other pixel designs have been introduced to tackle the drawbacks of the 3T pixel. It is important to recognise that while image quality may increase by fabricating a more complex pixel structure, it comes at a cost of fitting more transistors into the pixel, and thus

lowering the fill-factor (the proportion of photosensitive regions of the pixel to non-photosensitive regions), so less incident light is converted to signal charge.

The modern 4T pixel introduces a transfer gate between the photodiode and the sense node as seen in Figure 3.7. The photodiode can be made pinned by means of a surface p+ diffusion (Lee *et al.*, 1997) to suppress dark current as discussed above. This introduces some difficulty in coupling the charge between the pinned photodiode and the sense node, and is usually best accomplished by using a charge-coupling structure such as in a CCD, rather than a true MOSFET fabricated with CMOS processes.

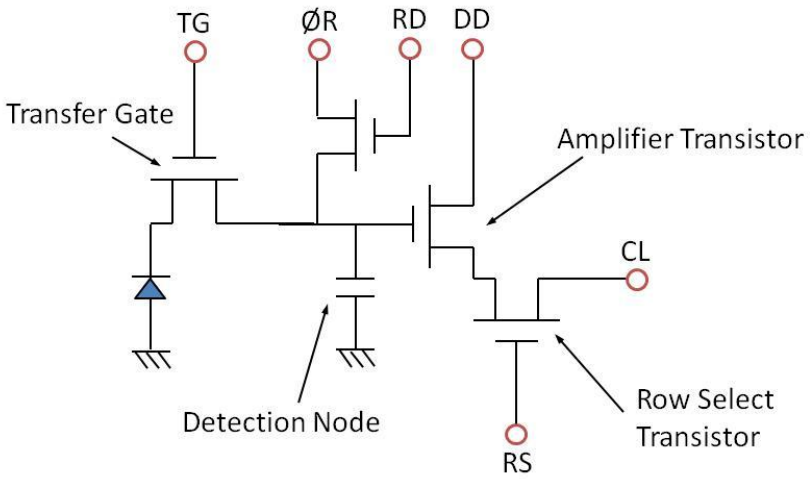

Figure 3.7. Schematic of a typical 4T pixel design; including a transfer gate to couple the generated charge to the sense circuit

While the buried channel photodiode reduces surface dark current, the introduction of the transfer gate allows Correlated Double Sampling (CDS), a technique used in all scientific CCDs. During reset, both the detection node and photodiode are set to the same level, and so the detection node can be sampled during integration. This value can then be subtracted from the measured signal to determine accurately the integrated signal, eliminating reset noise.

The design also eliminates deferred charge in fast pixel-rate applications, as the photodiode discharges very quickly to the detection node, leaving no charge behind. The pixel still suffers from non-linearity due to the low sense node capacitance. However, the 4T pixel

with buried channel photodiode was a significant breakthrough, and increased APS performance to levels required for scientific imaging.

3.2.3 5T

Another disadvantage of both the 3T and 4T pixels described above is that the external pixel clocking circuitry must raster across the image pixel-by-pixel. For high frame rate applications where the image is changing rapidly, the image becomes distorted as seen in Figure 3.8. Each pixel is integrating different moments in time, offset by the read time, and so if the imaged object changes on the timescale of the time taken to read out an entire image, the image can become distorted. However it is also possible to exploit this effect to measure the velocity of the imaged object (Ait-Aider *et al.*, 2006).

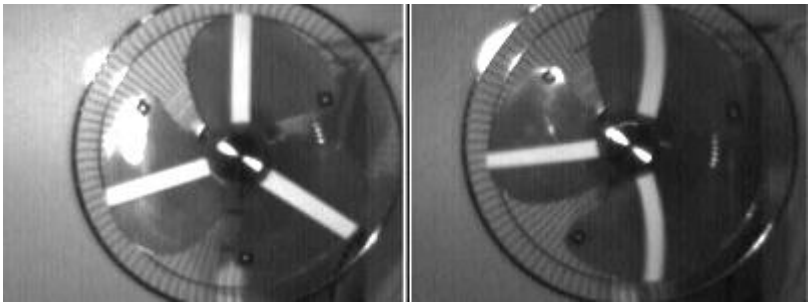

Figure 3.8. Image taken of still (left) and quickly rotating (right) desk fan. Note distortion of the fan blades when in motion. (after Ait-Aider et al., 2006)

The 5T pixel removes this problem by introducing a fifth transistor as a global reset (see Figure 3.9). This allows all pixels to be reset simultaneously. The advantage of this is that the transfer gate can be clocked simultaneously on all pixels at the end of the integration, then the image can be read out via rastering with no further integration, resulting in an undistorted image. It is generally favoured to add the fifth transistor to a 4T pixel rather than a 3T because the reset transistor can then be fabricated in the same way as the transfer gate in the 4T example, allowing very fast transfer from the photodiode.

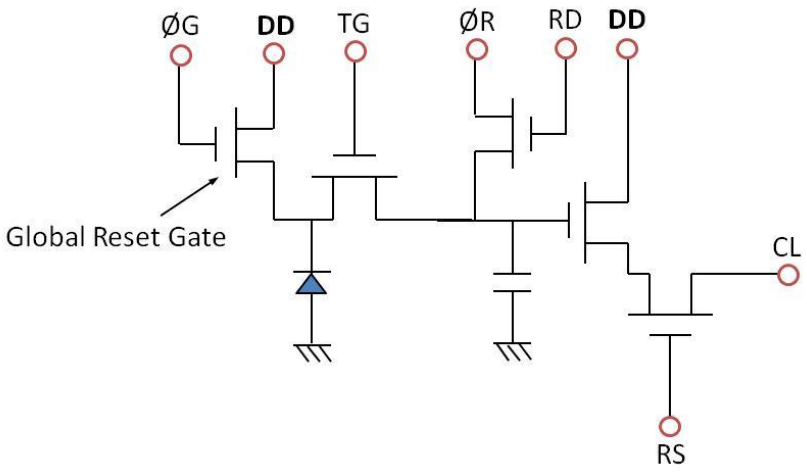

Figure 3.9. Schematic of a typical 5T pixel design. Note common DD connections in bold.

3.3 Active Pixel Sensors Relating to this Work

3.3.1 Previously Studied Devices

This work is in part a continuation of work carried out by Tom Greig (2008). The devices tested consisted of 10×10 3T test pixel arrays designed to study the effects of varying the doping of the reset transistor, photodiode size and pixel shape. Also tested were two larger 144×144 3T pixel arrays. The larger arrays consisted of 20 µm square pixels fabricated with a 0.5 µm CMOS process.

3.3.2 Jade

The e2v technologies Jade APS (Figure 3.10) is the device with which the majority of this work was performed. It is designed for use in industrial imaging applications, and as such does not incorporate any specialised radiation hard design, making it an ideal device to test the baseline performance of APS technology under irradiation.

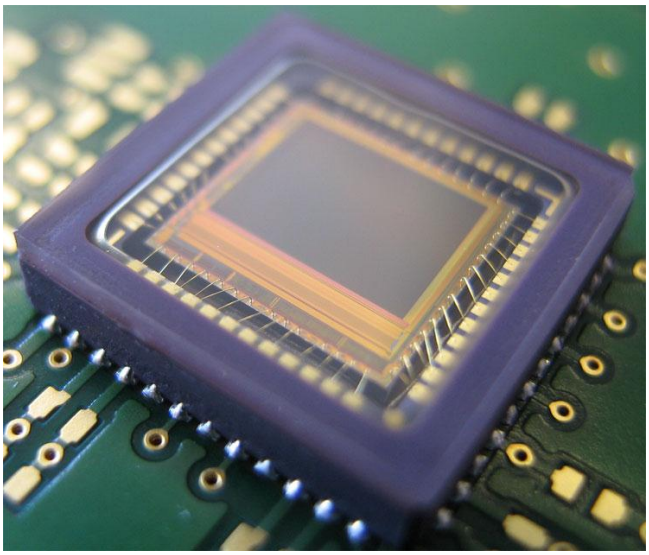

Figure 3.10. Close-up photograph of the e2v technologies Jade APS.

The device consists of a 876 × 652 array of 5.8 × 5.8 µm 5T pixels fabricated using 0.18 µm CMOS processing techniques in a 10 × 10 mm package. Of the 872 × 652 pixels, only an area of 838 × 640 are active (dummy pixels are included in sensor design to eliminate edge effects), totalling approximately 0.5 Mpixels. Applied above the imaging array is a sheet of microlenses (discussed in Chapter 4). On-device ADCs are 8-bit, and the device is designed to operate at frame rates up to 60 fps (full format). The device is available in black and white or colour versions. In the colour imager a Bayer filter (Bayer, 1976) is applied to limit pixel sensitivity to specific wavelength bands. Figure 3.11. is a block diagram of the device, showing the main on-device components. In addition to this, various filters such as clamp and sample (to allow auto-exposure), subsampling of the image area, and other signal processing techniques are applied to the signal after output, if specified.

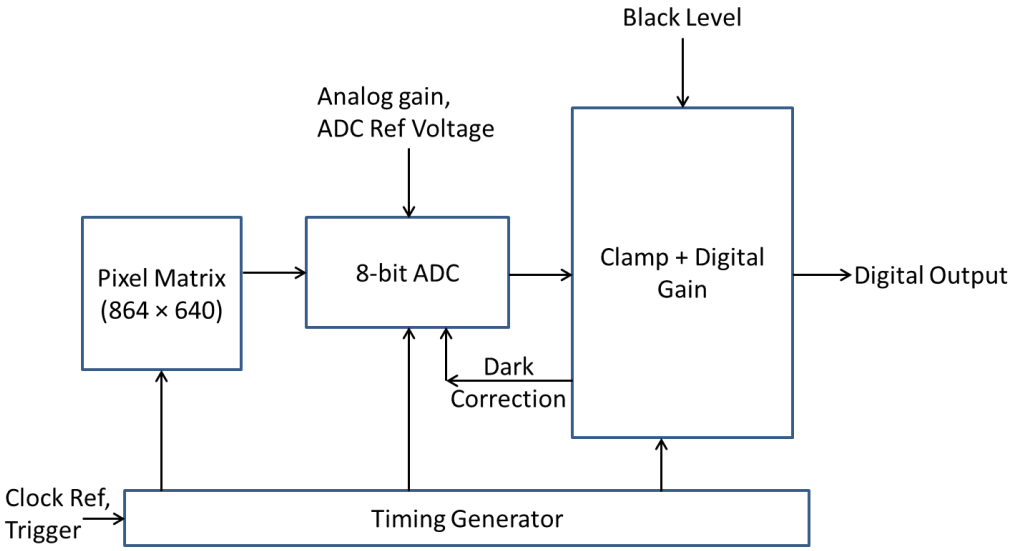

Figure 3.11. Block diagram of the Jade APS showing main imaging components.

The device is provided mounted on a USB demonstrator readout board (see Figure 3.12). While this provides ease of use it limits the monitoring of internal behaviour. The device is provided with software to drive the board, and this software allows many onboard (post-processing) and internal functions to be implemented. During experiments, the post-processing techniques were deactivated, to accurately gauge the performance of the device.

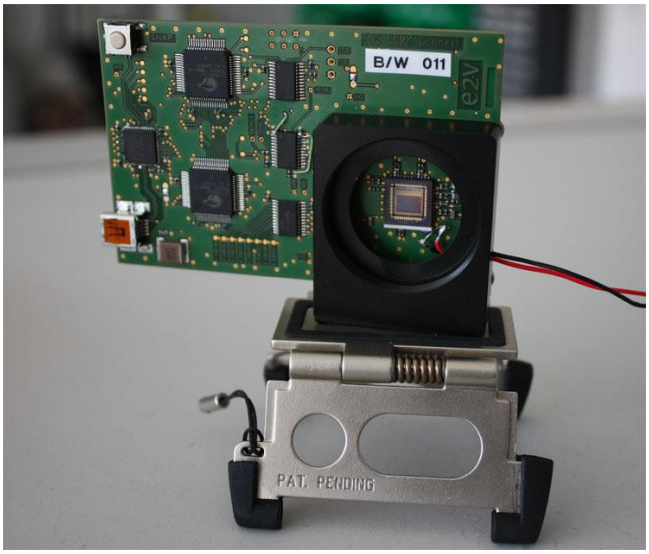

Figure 3.12. Photograph of the e2v technologies Jade APS with demonstrator readout board, stand, and with a PT1000 platinum resistance thermometer for temperature monitoring as part of this work.

3.3.3 Sapphire

The e2v technologies Sapphire APS is the larger counterpart of the Jade APS. The pixel design is largely unchanged, with the pixels being smaller at 5.3 µm square. The useful imaging array size is increased to 1280×1024, totalling 1.3 Mpixels. The ADCs allow 10-bit sampling resolution compared to the Jade's 8-bit. The Sapphire has considerably more complicated clocking architecture, with additional functionality such as reading out up to four regions of interest.

The Sapphire is the selected image sensor for the C3D instrument to be flown on UKube-1, the pilot cubesat mission commissioned by the UK Space Agency (see Chapter 4 for further details).

3.3.4 Ocean Colour Imager

The Ocean Colour Imager (OCI) CIS106 test array is a 2000 × 1504 pixel CMOS imager designed by e2v technologies for Earth observation applications. The currently available devices are designed as test beds for producing a range of future commercial imaging devices. There are a number of different device variants, with each device having 240 differing 7 µm square pixel designs on the die, each with potentially differing performance. A photograph of an OCI test-device is shown in Figure 3.13.

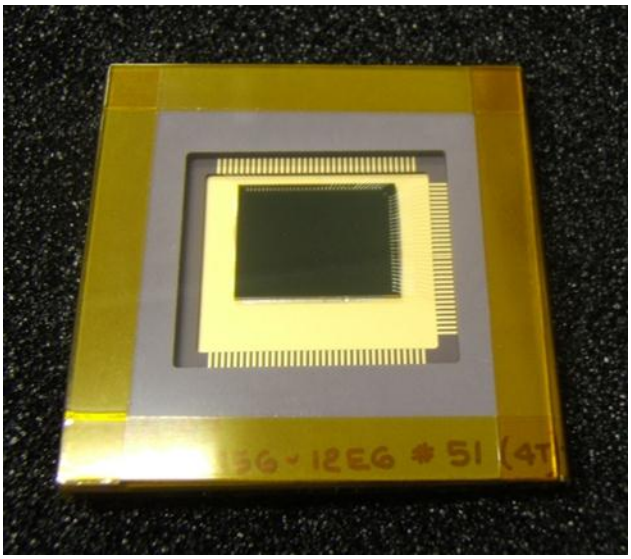

Figure 3.13. Photograph of an OCI test-device and package.

There are three differing device parameters, each available in two variants:

- Device thickness
    - 7 µm, 30 Ω.cm substrate, 1-2 µm depletion depth
    - 11 µm, 1-2 kΩ.cm substrate, 9 µm depletion depth
- Illumination face
    - Back Illuminated (BI)
    - Front Illuminated (FI)
- Pixel Design
    - 3T – Basic CMOS pixel
    - 4T – Low noise CMOS pixel

The large number of different on-pixel designs and different device parameters makes the OCI test arrays very useful for investigating the effects of small changes to pixel or device design on the device performance. Further information on the on-device design differences is given in Chapter 5.

Chapter 4: Radiation Damage in Semiconductor Devices

Radiation damage in semiconductor imagers can alter the fundamental performance of the device, introduce various effects that alter the image in complex ways, and in extreme cases can even damage the device to such an extent that it is no longer operational.

Gaining an understanding of how different types of device react to different types of radiation can inform future design decisions to mitigate damage in future technologies and allows for hardware measures and software correction for the effects of damage on the image.

This chapter outlines the interactions of different types of radiation species with semiconductor imaging structures and their effects on device performance, and gives an overview of the differing space radiation environments where devices may experience damage, concentrating on interplanetary space, Earth orbit and the Jovian system.

4.1 Radiation Effects in Silicon Imagers

Provided in this section is an outline of the damage induced in silicon devices due to radiation of all kinds, from high energy photons to heavy ions. Figure 4.1. shows the path of an incident damaging particle, and the common sources of damage: ionisation and atomic displacement.

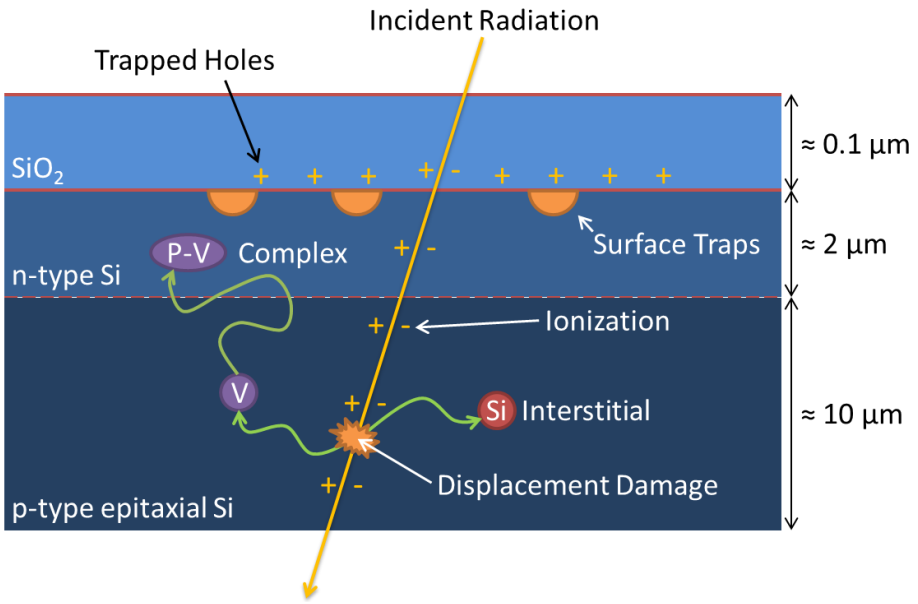

Figure 4.1. Diagram showing incident radiation's path through a silicon sensor, and the main interactions within the structure (not to scale).

4.1.1 Particle Interaction Mechanisms

The mechanisms through which particles interact with the device structure vary with the particle species and the dominant mechanism for each particle can vary with the particle energy. This section discusses the interactions of three categories of particle: photons, charged particles, and uncharged particles.

4.1.1.1 Photons

Photons interact with matter in a number of ways, the most dominant being the photoelectric effect (also exploited as the main detection mechanism in imaging devices), Compton scattering, and pair production (more details of these mechanisms can be found in Knoll (1979)). These mechanisms do not damage the device directly, but involve exciting electrons from their bound state around a nucleus, which then cause damage throughout the lattice as described below. Figure 4.2. shows the interaction mechanism cross sections of photons of energy between 1 keV (X-rays) and 1 GeV (high energy gamma rays) in silicon. Figure 4.3. shows how the energy dependence of the dominant interaction mechanism varies with the material. Once the photon has interacted, the unbound electron interacts in the same way that an electron hitting the device would, discussed below. The electron

released through the photoelectric effect is generally of low energy, and so causes only minor localised damage, but the electrons created in Compton scattering and pair production are of higher energies and can cause damage far from the interaction site. The interaction cross sections are low for photons of these energies, and so the damage is proportionately less than irradiating with equivalent electrons.

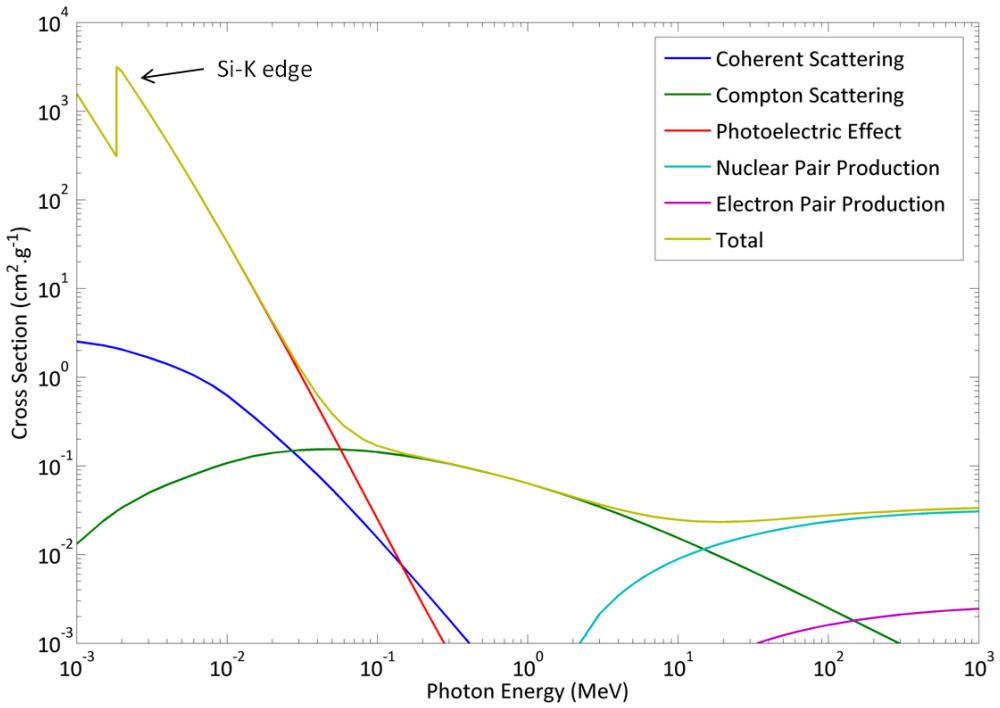

Figure 4.2. Graph showing measured cross-section for photon interactions in silicon, showing the cross section of photon interactions for each energy. (Hubbell et al., 1980)

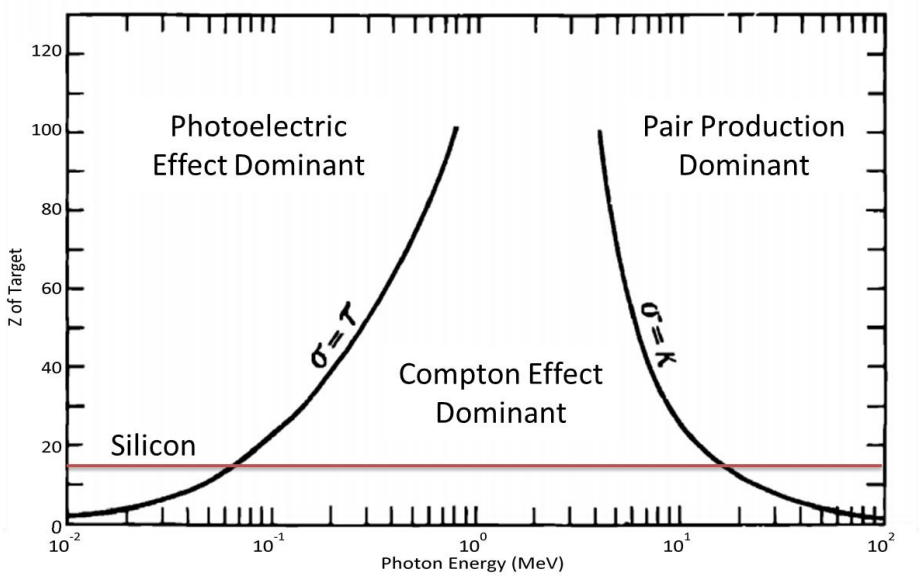

Figure 4.3. Graph illustrating the dominant photon interaction phenomena for photons of energies between 0.01 MeV and 100 MeV for materials of varying Z (after Evans, 1955).

4.1.2 Charged Particles

Charged particles interact with the silicon lattice in two ways:

- Elastically through Rutherford scattering (Rutherford, 1911). If the incident particle is of high enough energy (>210 keV for electrons interacting in silicon (Corbett, 1966)) the atom will be released from the lattice causing displacement damage (see below).
- Inelastically, with energy transferred as described for high energy protons and heavy ions by the Bethe formula (Bethe, 1930), causing excitation and ionisation of the electrons in the lattice. This causes further ionisation and displacement damage by the released electrons. Ionisation is the primary method of energy deposition for charged radiation.

While protons and heavy ions take a fairly straight path through the lattice, electrons, due to their low mass experience larger accelerations when interacting, leading to the emission of bremsstrahlung radiation. The emission of bremsstrahlung radiation and the indistinguishability of electrons is the reason that they cannot be described by the Bethe formula. Mott (1930) modified the Bethe formula for electrons.

The Linear Energy Transfer (LET) is a measurement of the energy loss of the particle to material local to the particle's trajectory *i.e.* it ignores secondary electrons that lose a large proportion of their energy far from the particle track as bremsstrahlung. From the LET, it is possible to calculate the number of ionisation events that occur due to a particle of specific energy, and therefore what kinds of effects (especially useful for Single Event Effects (see below)) are likely to occur.

4.1.3 Uncharged Particles

Neutrons, by virtue of having no charge, interact only through elastic collisions. However neutrons can cause significant ionisation damage through the effects of recoil atoms. Neutrons cause significant displacement damage as no energy is lost to ionisation.

4.1.4 Radiation Damage Quantification

There are many confounding factors presenting potential confusion regarding units used to measure dose:

- There are several types of damaging radiation which interact through different mechanisms.
- Each type of radiation deposits energy differently in different materials.
- There are several fields which have historically handled measurement of dose rate differently, *e.g.* biological dose rates focus on levels of biological damage rather than rate of energy deposition.

Historically, dose has been measured in roentgens (R), which is defined as the amount of radiation required to create ions with total charge 2.58×10^{-4} $C \cdot kg^{-1}$. This is due to the measurement of dose early in the field's history with a gas ionisation chamber.

The SI unit of dose is the gray (Gy), which corresponds to the deposition of 1 $J \cdot kg^{-1}$ of material; however a related unit, the rad, equivalent to 0.01 Gy is still predominantly used

in the field. It is important to note that the deposition of energy in a material is related not only to the particle depositing the energy, but also to the material. It is therefore important to specify the material that the dose was measured in. As an example a dosimeter may measure the dose received in water as rad(H_2O), but the dose in silicon (rad(Si)) will be significantly lower.

4.1.5 Ionising Damage

Ionising damage is caused by two mechanisms, the creation of electron-hole pairs in the device leading to long-term hole trapping and the creation of Si-SiO_2 surface states. All forms of radiation can cause ionisation damage to some extent. More details on the subject are given in Oldham & McLean (2003). A brief summary is given below.

4.1.5.1 Long Term Hole Trapping

Long term hole trapping is caused by the creation of electron-hole pairs within the device. Energetic charged particles cause this directly by ionising atoms as they pass through the device, and neutral particles cause it indirectly through the photoelectric effect ($E_{bandgap} < E_{photon} < 100\ keV$), Compton scattering ($100\ keV < E_{photon} < 1\ MeV$) and pair production ($E_{photon} > 1\ MeV$).

The total density of electron-hole pairs created per rad of incident radiation ρ_{eh} is given by:

$$\rho_{eh} = 6.24 \times 10^{13} \frac{\rho}{E_{ion}} \tag{4.1}$$

Where ρ (g·cm^{-3}) is the material density, 6.24 × 10^{13} (eV·g^{-1}) is the energy deposited per rad, and E_{ion} (eV) is the mean energy required to create an electron-hole pair. In silicon and SiO_2 the mean ionisation energy is 3.65 eV (Emery & Rabson, 1965) and 18 ± 3 eV (Ausman & McLean, 1975) respectively. Using these measurements and Equation 4.1, the density of created electron-hole pairs is 4 × 10^{13} cm^{-3}·rad^{-1} in silicon and 9.1 × 10^{12} cm^{-3}·rad^{-1} in SiO_2. For a typical 100 nm thick CCD gate oxide with area 10 µm^2 the number of generated

electron-hole pairs N_{eh} ≈ 100 rad^{-1} with typical radiation levels being over 1 krad. After the event this initial number of generated electron-hole pairs is reduced dramatically as the electron-hole pairs will recombine on timescales shorter than that required to separate them in an electric field. The fraction of pairs that recombine depends on the strength of the local electric field and the line density of generated electron-hole pairs. The line density is correlated to the Linear Energy Transfer (LET) of the ionising particle, which varies with the particle species and particle energy. The fractional yield (inverse of recombination probability) of a variety of particles in SiO_2 against local electric field is given in Figure 4.4.

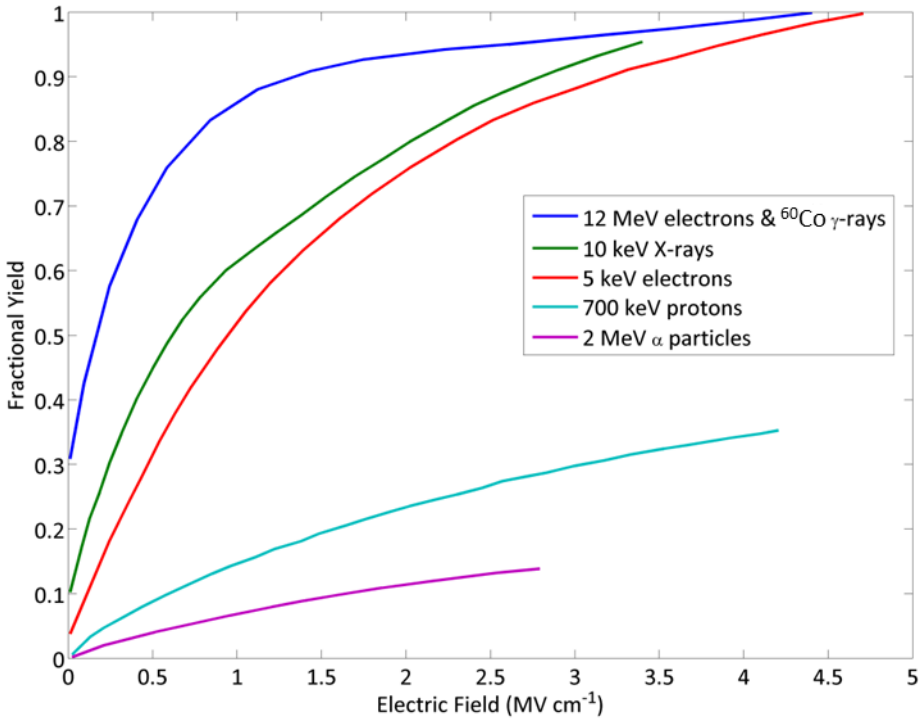

Figure 4.4. Graph showing variation of fractional yield of electron-hole pairs in SiO_2 with applied electric field and particle species and energy after Oldham & McGarrity (1983).

The effects of electron-hole pairs generated within the depleted and bulk silicon are minimal. The electrons are quickly collected as signal charge as described in Chapter 3 and the holes are swept out by the substrate potential. There is little if any permanent damage, and the only effect is additional image noise if the device is integrating during the irradiation.

Electron-hole pairs generated within the SiO_2 layer can be damaging. Once separated the electrons are accelerated to the gate where they escape. The less mobile holes are repelled from the gate towards the Si-SiO_2 interface. The holes travel through the crystal lattice by tunnelling between trapping sites in a random walk in the direction of the electric field. It is interesting to note that the time taken for a given hole to move to the interface has a very wide distribution from the order of μs to the order of hours (Boesch *et al.*, 1975).

When the holes reach the Si-SiO_2 interface they become stable. Due to amorphous nature of the oxide layer, the interface does not have a crystalline SiO_2 lattice. Instead there are sites where two silicon atoms are bonded together, each bonded to three oxygen atoms. This configuration produces a weak Si-Si bond. When a hole arrives in such a site, the Si-Si bond breaks forming a stable configuration called the oxygen vacancy (Feigl *et al.*, 1974).

These holes, now stable in the oxide, alter the operating conditions of the device. The holes act as stable charge and alter the characteristic operation of a MOSFET or MOS capacitor through ‘flat-band voltage shift’. The change in operation of a MOSFET with increasing ionising dose is shown in Figure 4.5.

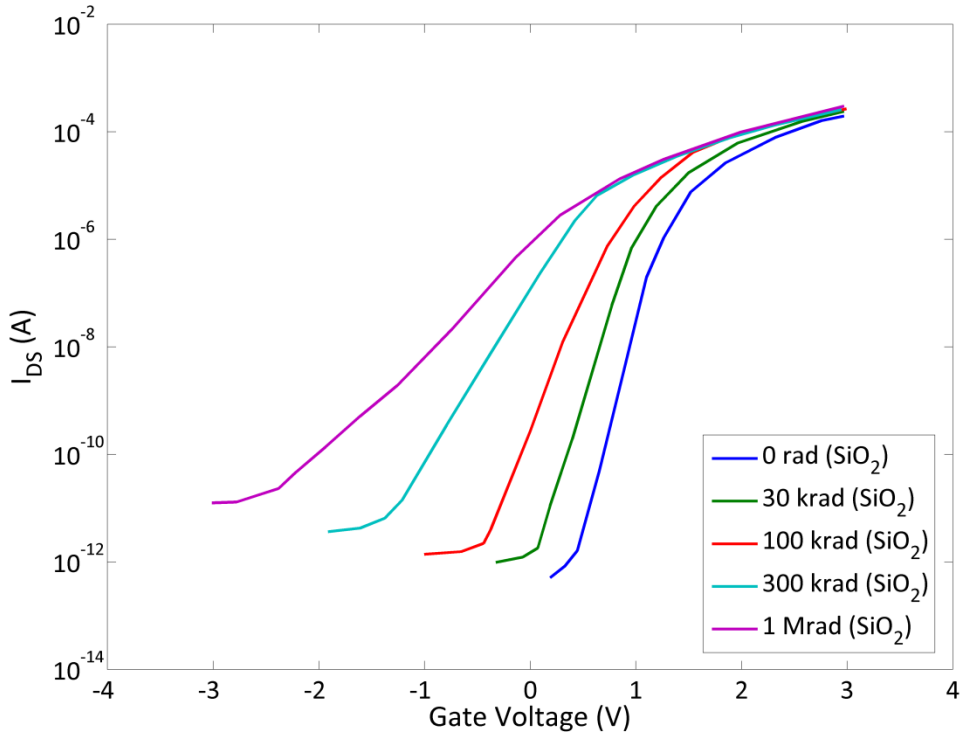

Figure 4.5. Change in the characteristic sub-threshold I-V curve of an n-channel transistor with increasing ionising dose after Winokur et al. (1984).

Due to the change in the operation of components of the device, the voltage needed to be supplied to the gate in order to, for example, pulse a reset transistor or pin a photodiode is changed. This can cause complex behaviours in a device, and if enough charge builds up can prevent a pixel or entire device from functioning completely (Winokur, 1987).

4.1.5.2 Radiation Induced Surface States

Radiation induced surface states are caused by an anti-annealing effect. At the Si-SiO_2 interface there are 'dangling' bonds due to lattice mismatch. These bonds are active traps that lie between the valence and conduction band of silicon. The traps provide a more probable pathway for electrons to be thermally excited (as opposed to photo-generated) to the conduction band and adding to the signal charge as 'dark current'. As discussed in Chapter 3 there are device structures designed to mitigate this effect.

A manufacturing technique commonly used to reduce this dark current source is a hydrogen anneal or passivation where the device is placed in a high temperature (≈ 400 ^{o}C)

hydrogen environment. The now monatomic hydrogen diffuses into the device structure and bonds with the 'dangling' bonds, annealing the traps (Janesick, 2001).

In the presence of a hole (created as detailed in the previous section), the Si-H bonds are broken, liberating a proton. The proton then moves through the lattice until it interacts with a second Si-H bond, and diatomic hydrogen is formed, which can diffuse out of the device (McLean, 1980). The 'dangling' bond is returned to its original state and can once again act as an interface state, increasing the dark current.

4.1.6 Displacement Damage

Displacement damage is caused by interactions not in the oxide, but in the bulk and depleted silicon. The effects of the interaction depend on a number of factors, including the interaction location, particle type, particle energy, device history after interaction and impurity levels in the device. An important quantification of the amount of damage caused by a specific particle is the particle's Non-Ionising Energy Loss (NIEL).

4.1.6.1 Non-Ionising Energy Loss

The NIEL is a quantification of the energy of a particle in silicon lost not due to ionising LET, but due to elastic and inelastic collisions with the material lattice. The success of NIEL analysis relies on the fact that particles with a given NIEL will, to a first approximation, cause the same amount of displacement damage independent of the particle species. The variation in measured NIEL in silicon over a number of different particles and energies is shown in Figure 4.6.

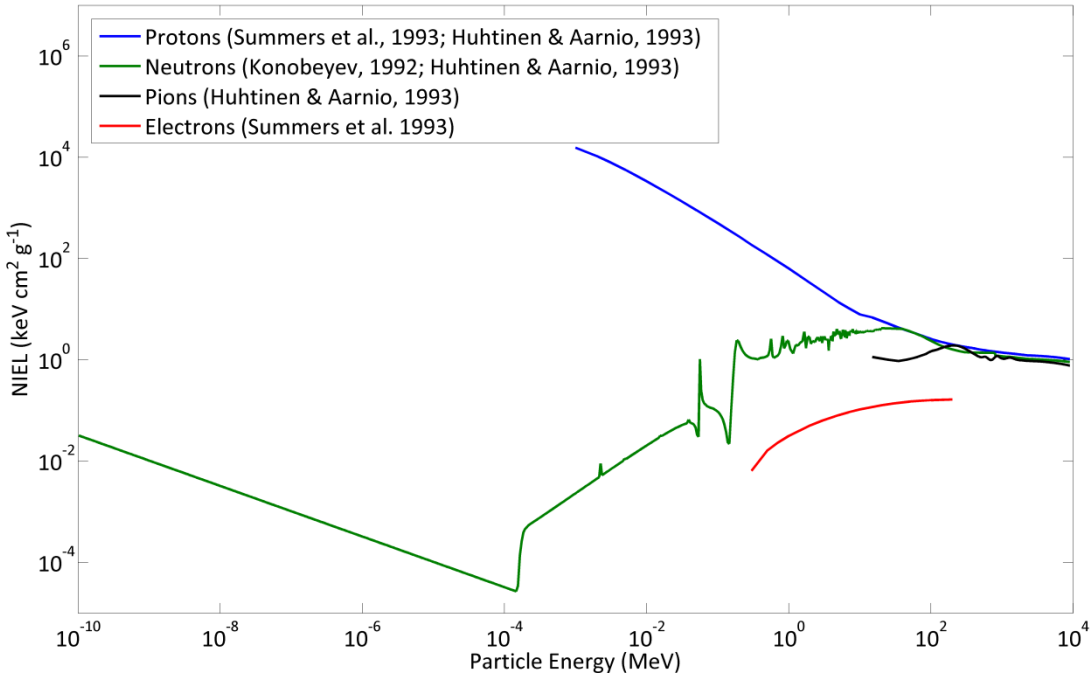

Figure 4.6. Graph showing variation of Non-Ionising Energy Loss in silicon for a number of different particle species from 10^{-10} to 10^{4} eV using results tabulated by Vasilescu & Lindstroem (2000).

NIEL allows normalisation of doses to a reference particle for ease of comparison between different doses, for example it is common to scale proton doses to an equivalent dose of 10 MeV protons using the NIEL function. It should be noted that NIEL is a useful tool, but not a complete description of interactions, and as such is not entirely accurate, especially at extremes of energy with specific particles, or within specific devices (Dale *et al.*, 1988). Continuing work refines models of NIEL calculations to better fit with measurements (see, for instance Inguimbert *et al.*, 2010).

4.1.6.2 Physical Effects

As an energetic particle passes through the bulk silicon, it may interact with and impart an amount of its energy to a silicon atom through inelastic or elastic collision. The minimum energy required to release a silicon atom from the lattice is estimated to be 20 eV (Seitz, 1949). The release leaves behind a gap in the lattice called a ‘vacancy’, and the released silicon atom (referred to as the Primary Knock-on Atom or PKA) occupies space between

the normal silicon lattice, and is referred to as an 'interstitial'. The vacancy-interstitial pair is called a Frenkel defect (Kittel, 1996).

The interstitial itself will quickly lose energy through ionisation and possibly the creation of further Frenkel defects. After losing this energy, the interstitials are generally static within the lattice. Vacancies are highly mobile even at low temperature, and will diffuse throughout the lattice until they either recombine with an interstitial, or form stable defect complexes with other vacancies, dopant atoms or impurities in the lattice. Of particular importance in phosphorous doped n-type silicon, and therefore most silicon imaging devices are the vacancy-phosphorous 'Si-E centre' (Watkins & Corbett, 1964), vacancy-oxygen 'Si-A centre' (Bemski *et al.*, 1958; Watkins & Corbett, 1961), and divacancy defect (Watkins & Corbett, 1965). These defects have different placements within the bandgap of silicon, as shown in Table 4-1.

Defect Name	Bond Type	Bandgap Energy
Si-A centre	Oxygen-Vacancy	E_C - 0.17 eV
Si-E centre	Phosphorous-Vacancy	E_C - 0.44 eV
Divacancy V_2^+	Vacancy-Vacancy	E_V + 0.2 eV
Divacancy V_2^-	Vacancy-Vacancy	E_C - 0.4 eV
Divacancy $V_2^=$	Vacancy-Vacancy	E_C - 0.2 eV

Table 4-1. Measurements of energy levels for common displacement-induced defects in n-type silicon, (Grove, 1967).

While it is possible for an electron to be thermally (as opposed to photonically) excited from the valence to the conduction band, it is significantly more likely in the presence of a defect centre or 'trap'. The relative probability P_{ex} of an electron being excited across an energy gap E_g is:

$$P_{ex} \propto e^{\frac{-E_g}{2kT}} \tag{4.1}$$

Using equation 4.1 and the values given for the bandgap placement of the Si-E centre given in Table 4-1, it is approximately 5000 times more likely for an electron to make the transition from valence to conduction band thermally in the presence of a Si-E centre and

thus an increase in amount of dark current (from the area in which the trap was created) of order 5000 is expected.

It is important to note that only traps within a depletion region will contribute to generated dark current. Outside of a depletion region it is more likely, as the region of the trap is abundant with carriers, for any trapped majority carrier to quickly recombine with a minority carrier and vice versa (Figure 4.7. a)). Only in a depletion region will the carriers be accelerated away from each other, the minority carrier being extracted through the substrate, and the majority carrier being collected as signal charge (Figure 4.7. b)). Charge trapping (illustrated in Figure 4.7. c)) causes charge in the vicinity of the trap to be captured into it, and then re-released some time later. This can cause, in high frame-rate applications in APS, signal charge to be deferred from one frame to a later frame, as the charge trapping and release has an associated time constant. A much more serious effect of charge trapping is degradation of the CTE, which severely effects the image quality of affected CCDs by causing charge to smear in the charge clocking direction (as shown in Figure 2.4). Decreased CTE is a fairly benign process in APS as charge transfer is only through a few microns of silicon, but in CCDs a charge packet can encounter several centimetres of silicon, and therefore many more traps. This ‘hardness’ to charge trapping is one of the drivers for developing scientific quality APS for extreme radiation environments.

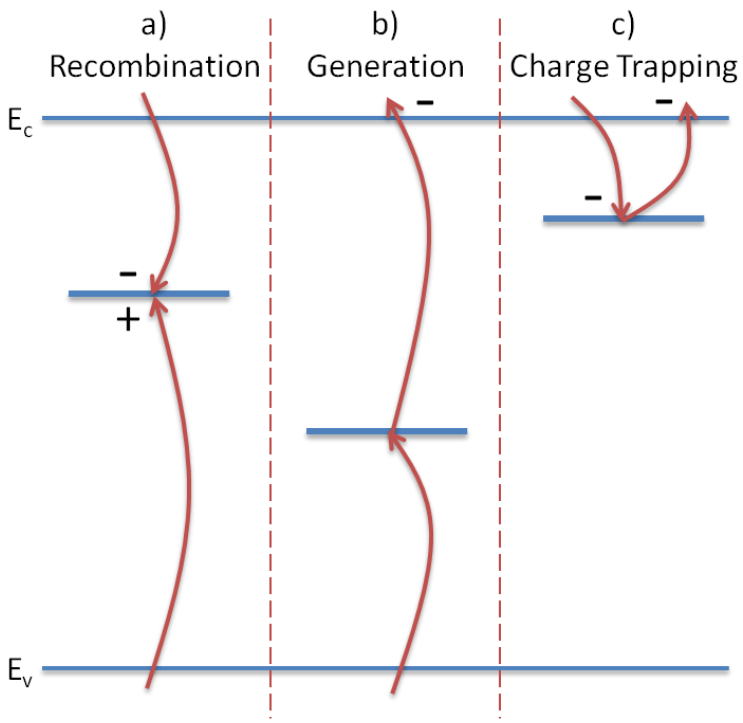

Figure 4.7. Diagram showing possibilities for carrier interaction with a trap: a) recombination, b) generation, or c) trapping.

The most harmful of these aforementioned physical effects in APS is generation, as it adds a large amount of spurious dark signal to the signal being measured. Furthermore, generation for a trap in a depletion region is further enhanced beyond what is expected by the Poole-Frenkel effect and phonon-assisted tunnelling, illustrated in Figure 4.8.

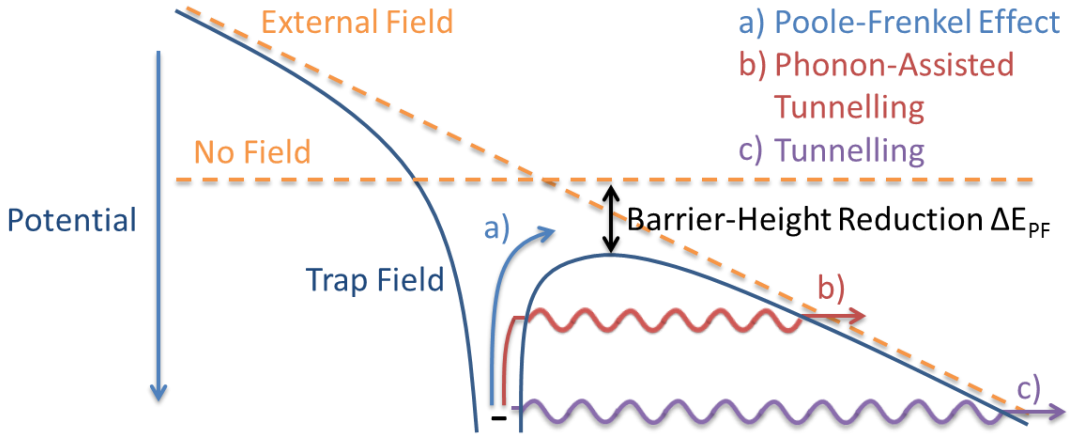

Figure 4.8. Illustration showing mechanisms of enhanced emissions from a trap via the Poole-Frenkel effect and phonon-assisted tunnelling.

The Poole-Frenkel effect results in the lowering of a potential barrier an electron must overcome to be liberated from a trap by virtue of an external field (*i.e.* the conditions in a

depletion region) bending the field lines of the trap (Frenkel, 1938). Quantum tunnelling and phonon-assisted tunnelling further enhance the emission from a trap (Martin *et al.*, 1981).

4.1.7 Single Event Effects

Single Event Effects (SEEs) or Single Event Phenomena (SEPs) are differentiated from ionisation and displacement damage as, rather than being an accumulative effect, they are caused by a single particle hitting a sensitive region of the device and depositing enough energy to damage that element. Therefore SEEs are triggered by particles above a threshold LET, below which no SEEs will occur, as they do not deposit enough energy within the sensitive regions. There may be several LET thresholds for a device caused by the different components on the device. As the LET is increased, the number and type of SEEs will change as each threshold is passed. Once the threshold LET of the most resilient component has been reached, an increase in LET will not produce any further increase in the number of SEEs. Measurement of the LET threshold is an important part of space assurance testing of components, as SEEs cause a variety of effects ranging from inaccurate measurements through bit-flips to catastrophic failure through latch-up or gate rupture. The most common types of SEE are described in the following sub-sections.

4.1.7.1 Single Event Upsets

Single Event Upsets (SEUs) are the least damaging SEE. These occur when a particle generates enough charge within a logic element to switch its value, more commonly referred to as a ‘bit-flip’. These bit-flips can have a variety of effects depending on the role of the digital information stored in the affected memory cell (*i.e.* an upset in a clamp reference value could change the dark level of the device, or an upset in addressing electronics could cause the device to cease functioning). The effect can be large or small depending on whether the cell holds a more or less significant bit.

4.1.7.2 Single Event Latch-up

Latch-up is a potentially destructive event caused by a large deposition of charge in a region such as that shown in Figure 4.9.

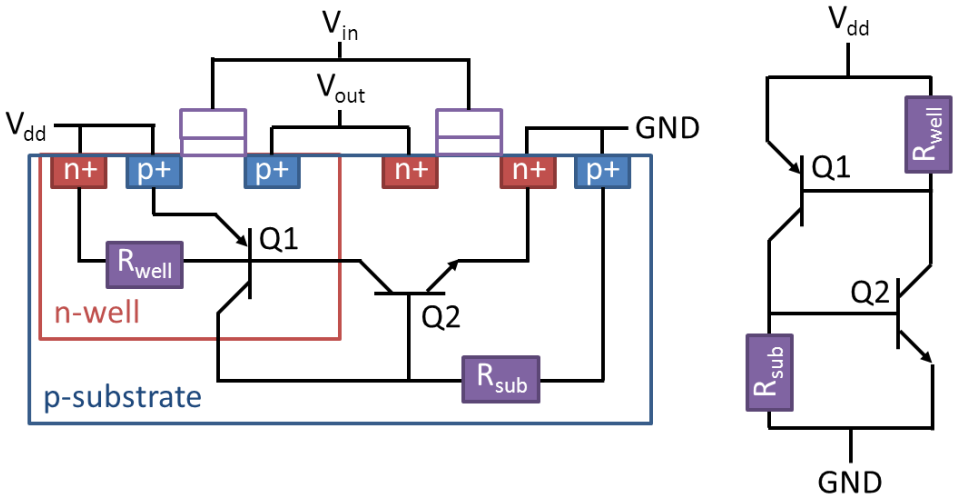

Figure 4.9. Structural (left) and corresponding electrical schematic (right) of a pixel region that is susceptible to latch-up after Soliman & Nichols (1983).

Referring to Figure 4.9., the structure shown forms a feedback loop that can be initiated from a large amount of deposited charge, causing latch-up. If a particle deposits a large density of charge into, for example, R_{sub}, then the parasitic bipolar transistor Q2 will switch 'on' and if the switch is large enough then the current flowing through R_{well} will be enough to switch 'on' Q1. The resulting situation is that both sides of the circuit are continuously open and current is flowing, and this is the effect termed 'Latch-up'. The current flowing through the circuit can cause excess heating leading to mechanical failure of metal tracks or silicon regions due to thermal runaway (Sexton, 2003).

4.1.7.3 Single Event Gate Rupture

Single Event Gate Rupture (SEGR) is caused by an ion of sufficient LET creating a charge patch through a device oxide such that conduction is achieved either between a gate and the surface or between two gates. This can cause rapid heating leading to failure of the affected component. Two characteristics increase the incidence of SEGRs:

- Thin gate dielectrics.
- Very high gate electric fields.

Some sensitive technologies such as Field Programmable Gate Arrays (FPGAs) are susceptible to SEGR and so must be shielded from particles above a SEGR threshold LET or designed with radiation hard design principles. APSs are generally not susceptible due to the low gate voltages, but as process feature sizes become smaller and novel device types requiring high electric fields (such as Electron-Multiplying CCDs) are fabricated, SEGR could become a risk with future technologies (Sexton *et al.* 1997).

4.1.8 Radiation Damage to Non-MOS Regions

It is important to note that regions of a device other than the silicon and oxide structure can also degrade due to radiation damage, especially materials such as polymers. The thin layer of microlenses (the use of which is discussed in Chapter 5) and plastic on top of the APS imaging area can become brittle and change colour in response to radiation. While this does not lead to catastrophic failure of the device like radiation damage to the MOS structure can, it still alters the response of the device, as it will absorb light in certain wavelength regions. This coloration of transparent materials is caused by two mechanisms:

- Crystalline materials such as glass and silica have their lattices disrupted in a similar manner to displacement damage above. This forms a trap (termed 'F-centre') at a lower energy level than that of the general structure, so electrons can absorb lower energy photons to be excited into the trap. This can result in absorption of photons in visible wavelengths, thus altering the transparency of the material (Mott & Gurney, 1940).
- Polymeric materials can have their long chemical chains broken by high energy radiation, and the left over fragments can re-bond or react with surrounding materials to form a variety of chemicals, some of which will have different optical

and mechanical properties to the bulk polymer (Reichmanis & O'Donnell, 1989). In the case of organic polymers, highly permeating gasses such as hydrogen can also be released from the polymer, where they may react further (van de Voorde, 1973).

The mechanical degradation is of little relevance to this thesis, as the films are generally under little stress and are not mechanically relevant, however the optical alterations are generally seen as a 'browning' of the film which alters the spectroscopic response and quantum efficiency of a device. For these reasons, microlenses are generally not applied to APSs for space applications. Some limited measurements of the change of colour of the microlens and plastic film over the device due to irradiation are presented in Chapter 6.

4.1.9 Annealing

Irradiated devices showing signs of damage can worsen, partially recover or fully recover over time after an irradiation. All three possibilities are termed 'annealing'. This is due to, in the case of the damage improving, traps having mobility due to having thermal energy, which if high enough can cause the trap to be liberated (or 'relaxed'), fully repairing the damage. The effects of displacement damage can worsen over time, as the time taken for a vacancy to migrate to an active region of the device and form an interface state can be of the order of minutes or hours, depending on irradiation temperature, so the device can degrade for some time after irradiation.

The rate of annealing is complex and highly dependent on time after the damage occurred, temperature, and local chemistry (*i.e.* device fabrication). High temperature anneals can repair damage quickly and almost fully, due to imparting more thermal energy to the lattice. Conversely, annealing at cryogenic temperatures can take a very long time to anneal only a small amount of the damage. Figure 4.10. shows the effect of temperature on

annealing a variety of defect complex species. Note that real data of annealing complexes is significantly less clear-cut than this schematic suggests.

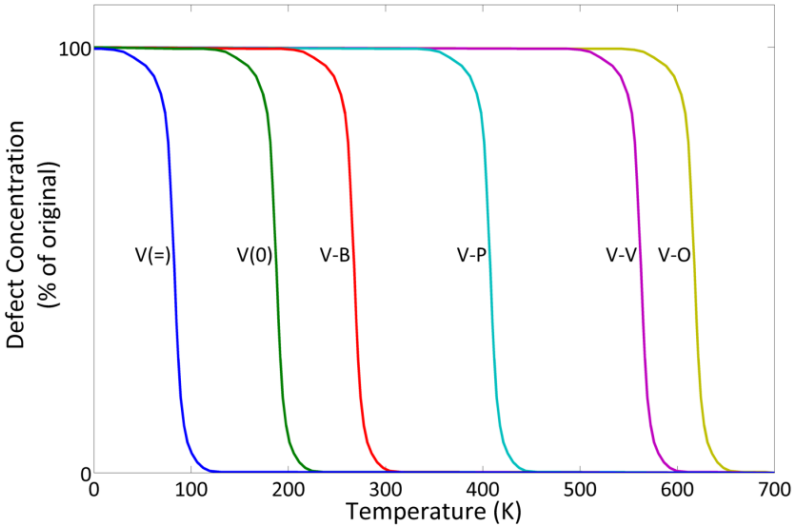

Figure 4.10. Schematic of temperature dependence of defect concentration during anneal for a selection of relevant defect types after Watkins (2000).

4.2 The Space Radiation Environment

There are two families of radiation in space, 'transiting' radiation, which 'transits' the region of space in question uniformly, and 'trapped' radiation, which is present around bodies with sufficient magnetic field to capture and 'trap' charged radiation around them.

4.2.1 Transiting Environment

The transiting environment is composed of particles generally termed as 'cosmic rays' originating from two sources: 'galactic' cosmic rays from outside the Solar System, and the solar wind, a flux of particles originating from the Sun. The overall flux of cosmic rays arriving at Earth is shown in Figure 4.11. These particles are generally composed of hydrogen ions (≈90%) and helium ions (≈9%), the other 1% being composed of heavier ions and electrons. The high-flux, low-energy particles (1-20 × 10^9 eV.nucleon^{-1}) are of most concern regarding instruments in the space environment (Dyer, 1998).

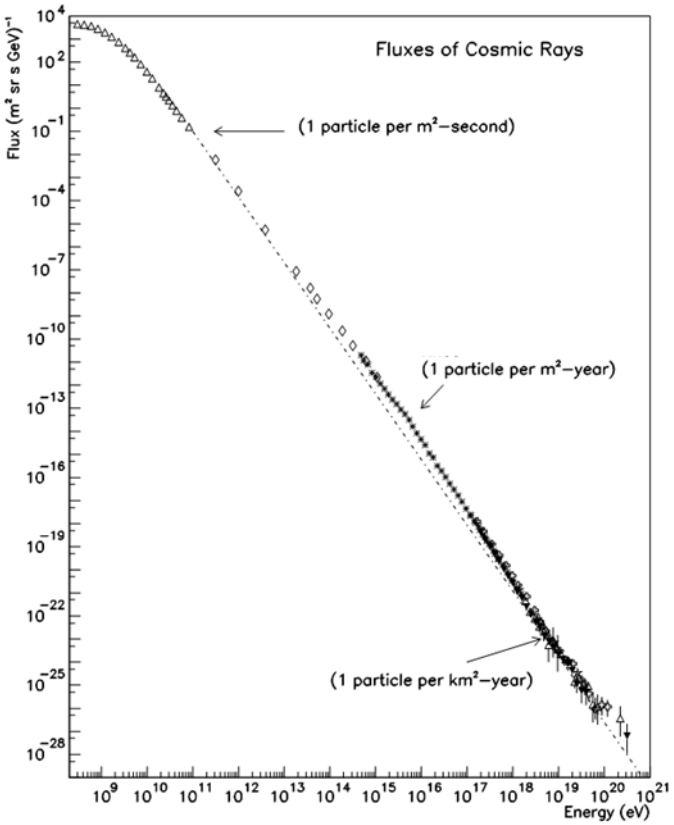

Figure 4.11. Graph showing cosmic ray energy composition (after Swordy, 2001).

4.2.1.1 Galactic Cosmic Rays

Galactic Cosmic Rays (GCRs) are predominantly charged particles generated from a number of sources inside our galaxy. The generation mechanism of these particles is still under debate, but the current theory suggests that supernova remnants hold the particles within their magnetic fields, accelerating them through the remnant's expansion until the particle is energetic enough to escape (Koyama *et al.*, 1995). However, this mechanism does not explain cosmic rays with very high energy $>10^{14}$ eV, a famous example being the 'Oh-My-God' particle (Taubes, 1993), which are hypothesised to likely be extragalactic, and have been accelerated by black holes at the centre of active galactic nuclei (Pierre Auger Collaboration, 2008). The flux of galactic cosmic rays is modulated by the presence of the solar wind (Barth *et al.*, 2003), and average GCR energy and flux is decreased in periods of high solar activity, due to the extended solar magnetosphere. GCRs are able to penetrate

the Earth's magnetosphere and cause damage to spacecraft in Low Earth Orbit (LEO), and are especially hazardous to those in high latitude or high altitude Earth orbits.

4.2.1.2 Solar Wind

The solar wind consists of a constant stream of low energy particles up to a few keV ejected from the Sun's upper atmosphere, which vary in fluence over the Sun's eleven-year cycle, predicted by counting the number of sunspots (Schwabe, 1843). The solar wind is enhanced and in some cases dominated by solar flares and solar storms, which expel numbers of protons peaking at up to (in the case of the largest flare recorded with modern instruments of magnitude 'X45' (Thomson *et al.*, 2005)) 7000 times greater than the background flux, returning to background level over just a few hours. The energy of these particles can reach a few GeV, presenting a significant threat to scientific instruments. The solar flare frequency is unpredictable, but is proportional to the solar activity. Storms can be predicted by monitoring the soft X-ray flux, which often precedes the particle flux by a few hours, however recently measured highly energetic flares have measured X-ray precursors arriving only 15 minutes before the main particle flux (Reames, 1999), presenting significant risks for astronauts working in the space environment. The soft X-rays themselves can confer significant dose to Sun-staring instruments. Figure 4.12. shows interplanetary proton flux (using data from the Geostationary Operational Environmental Satellite (GOES), operated between the National Oceanic and Atmospheric Administration (NOAA) and NASA), plotted over the monthly number of sunspots (produced by the Solar Influences Data analysis Centre (SIDC)).

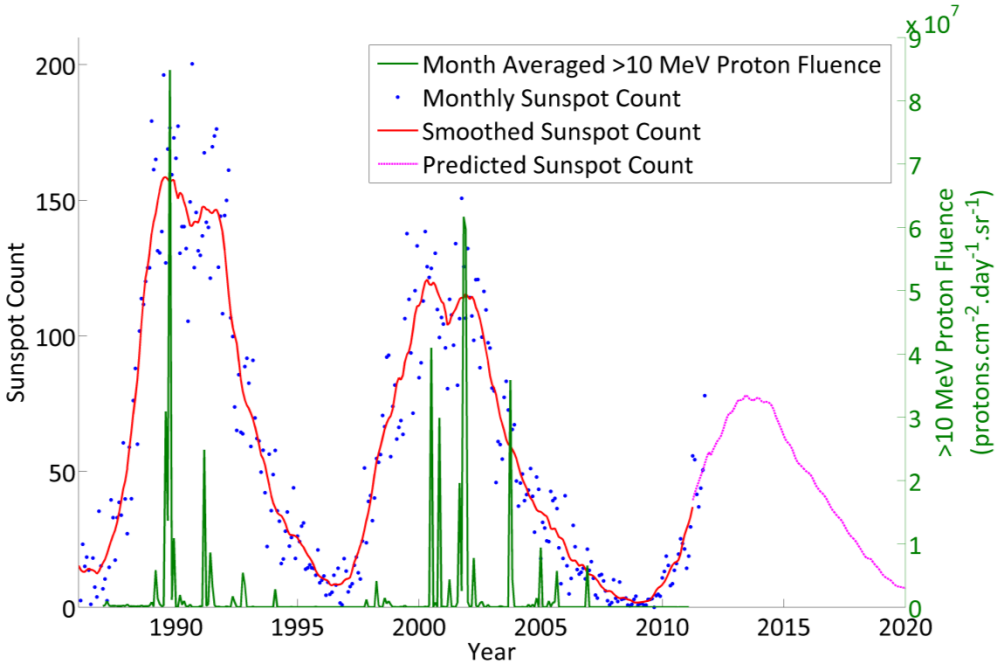

Figure 4.12. Graph showing proton fluence detected by GOES, and daily sunspot count between 1985 and 2012, and the predicted sunspot count to 2020.

Figure 4.12. shows the correlation between the 11-year solar cycle and the frequency of solar proton events. Also shown are the NOAA predictions for the next solar cycle, showing the next peak in solar activity in 2014. These solar storms are rarely energetic enough to penetrate the Earth's magnetosphere, but dominate the damage seen in instruments outside of the magnetosphere, or orbiting in weak areas of the magnetosphere, far from the equator. Solar activity can, however, modulate the population and extent of trapped environments.

4.2.2 Trapped Environments

Planetary bodies with a significant magnetic field will often have a trapped particle population associated with the field. The gas giants all have significant magnetospheres associated with them, along with the Earth, Mercury and Ganymede. These radiation belts are populated by particles from the solar wind, GCRs, and in the case of Earth, atmospheric nuclear weapon testing, but each planetary trapped environment has its own energy characteristics. Within the Earth's radiation belts, charged particles are trapped spiralling along magnetic field lines and oscillating from (magnetic) pole to pole. The number and

energy of particles depends on the size and strength of the magnetic field. Detail is provided below on the Earth's radiation belts, as it is of most relevance to space missions. Also presented is a brief overview of the Jovian trapped radiation environment, as it is the most hazardous trapped environment in the solar system, and of direct relevance to planned missions such as JUICE (see Section 4.3.3), which must consider radiation hard technologies such as APSs to be able to survive any considerable mission length. Planetary bodies with little or no magnetosphere such as Venus and Mars suffer from a transient radiation environment at the body's surface.

4.2.2.1 Earth Radiation Environment

Earth's magnetosphere prevents the surface of the planet being irradiated by harmful space radiation, allowing life as we know it to exist. However, the particles trapped within it form belts that present a harmful environment for communications and scientific satellites and manned space missions transiting through them. The belts are split into two populations with different sources, the inner belt extending from around 1.2 to 2.7 Earth radii (at the magnetic equator), and the outer belt at 3 to 6 Earth radii. Figure 4.13. shows simulated Van Allen belts created by plasma thruster in 1966.

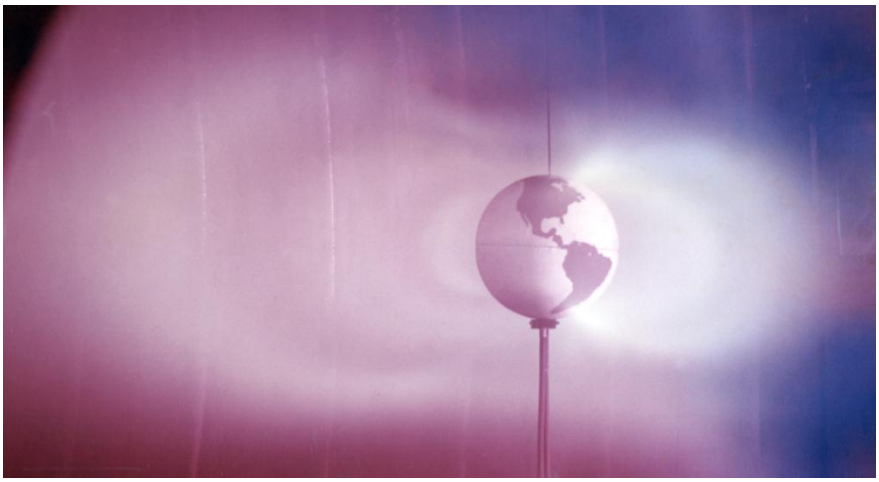

Figure 4.13. Photo of simulated Van Allen Belts generated by plasma thruster in tank #5 at the Electric Propulsion Laboratory at the Lewis Research Center, Cleveland Ohio, now John H. Glenn Research Center at Lewis Field (Credit NASA-HQ-GRIN).

The populations of both belts are dynamic and require constant renewal from their generation mechanisms (discussed below) in order to remain present. Both belts are referred to as the 'Van Allen belts' in honour of James Van Allen, instrument lead on a cosmic ray experiment using a Geiger counter on board Explorer 1 and Explorer 3, leading to the belts' discovery (Van Allen & Frank, 1959). In addition there are two 'anomalous' regions which allow these belts to extend beneath 500 km, close enough to affect craft in LEO: the 'South Atlantic Anomaly' (SAA) and the 'Auroral Horns'.

Inner Van Allen Belt

The inner radiation belt consists of protons and electrons, with a small population of heavier ions; the electrons are present out to around 2.4 Earth radii, and the protons are present out further to around 3.8 Earth Radii (Stassinopoulos, 1988). The particles in the inner belt are created from cosmic ray events in the upper atmosphere exciting neutrons out of the atmosphere and into the belts, which then decay into a proton, electron and antineutrino; on average the free neutron will travel far beyond the belts before this decay happens (the mean lifetime being 881.5 s (Nakamura *et al.* (2010)), but if the decay happens within the inner belt region, the particles can become trapped there. The electrons have energy of up to 5 MeV (Vette, 1991), while the protons have energy up to several hundred MeV, thus having enough energy to be of concern to instrument scientists. The highest energy particles are confined to thin belts close to the Earth, while lower energy particles are able to travel into weaker regions of magnetic field and still remain trapped. Lower energy protons can extend to 7 Earth radii at lower fluxes, but are of less concern due to their lower potential to cause damage.

Outer Van Allen Belt

The outer radiation belt consists solely of electrons and extends from 2.8 Earth radii to 12 Earth radii, as shown in Figure 4.14.

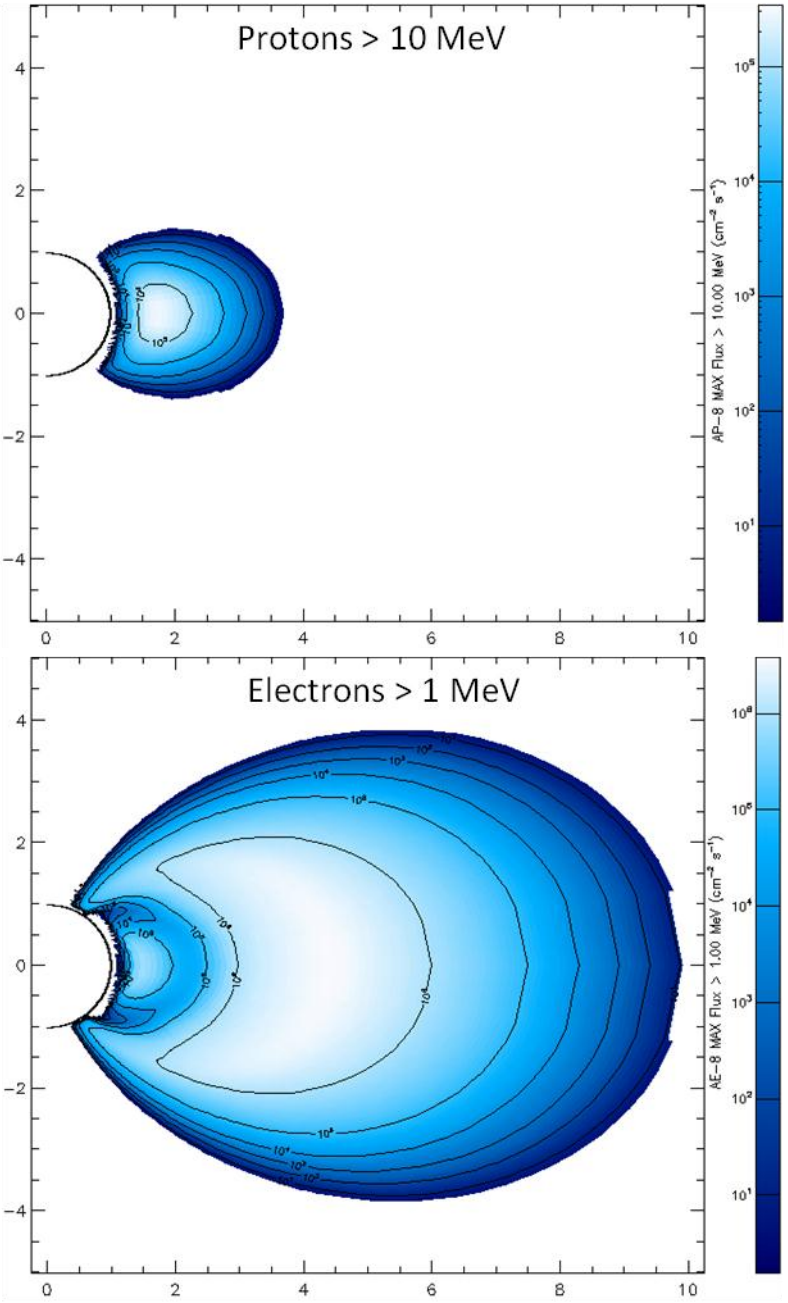

Figure 4.14. Diagram showing position of proton flux >10 MeV (top) and position of electron flux >1 MeV (bottom). X and Y axes measures in Earth radii from centre of the earth (at 0,0).

Outer belt electrons are more energetic than those in the inner belt, and have energies up to 7 MeV (Vette, 1991). The outer belt electrons are captured from the solar wind. The Earth's magnetosphere is distorted by the solar wind, as shown in Figure 4.15.

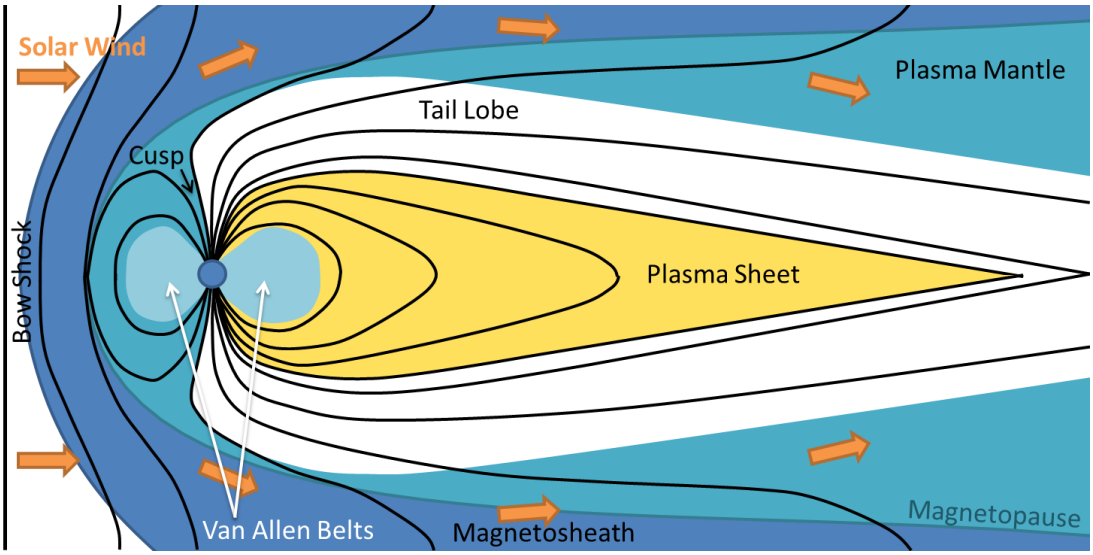

Figure 4.15. The Earth's magnetosphere, distorted by the solar wind, after Reiff (1999)

During heightened solar activity, either due to solar storms or during a peak in the eleven-year cycle, the magnetosphere is distorted further than usual due to increased charged particle flux, and it is mostly during this condition that electrons are captured by the Earth's magnetic field on the night side of the magnetosphere. The region between the two electron populations is called the 'slot', and the number of electrons and protons there can increase by several orders of magnitude during magnetic storms (Stassinopoulos & LaBel, 2004)

Anomalous Regions, the SAA and Auroral Horns

There are regions and conditions that cause the radiation belts to extend into LEO, which is where the vast majority of satellites are orbiting. During severe solar storms, the solar wind can distort the Earth's magnetosphere due to the incident charged particles warping the (relatively weak) magnetic field to such an extent that the radiation belts are pushed much closer to Earth, exposing craft in LEO to higher radiation doses than expected (Horne *et al.*, 2005).

The SAA is a region of enhanced penetration of the inner radiation belt causing it to dip far enough to cause several orders of magnitude more high energy protons, electrons, and ions to be present at LEO altitudes, presenting a radiation damage problem to the large

populations of LEO spacecraft. The cause of the anomaly is complex, but it is approximately due to the Earth's magnetic axis being 11° offset from the rotational axis, and the centre of the magnetic dipole being offset by approximately 500 km from the centre of the Earth. This causes a region of magnetic field at the SAA which is weaker than elsewhere on the surface of the Earth, and so charged particles can penetrate closer to the surface (Pinto *et al.*, 1992). Figure 4.16. shows the geographic region affected by the SAA, as well as the electronic auroral horns, modelled using the European Space Agency (ESA) SPace ENVironment Information System (SPENVIS) to show the flux of protons > 10 MeV and electrons > 1 MeV at a height of 600 km during solar maximum.

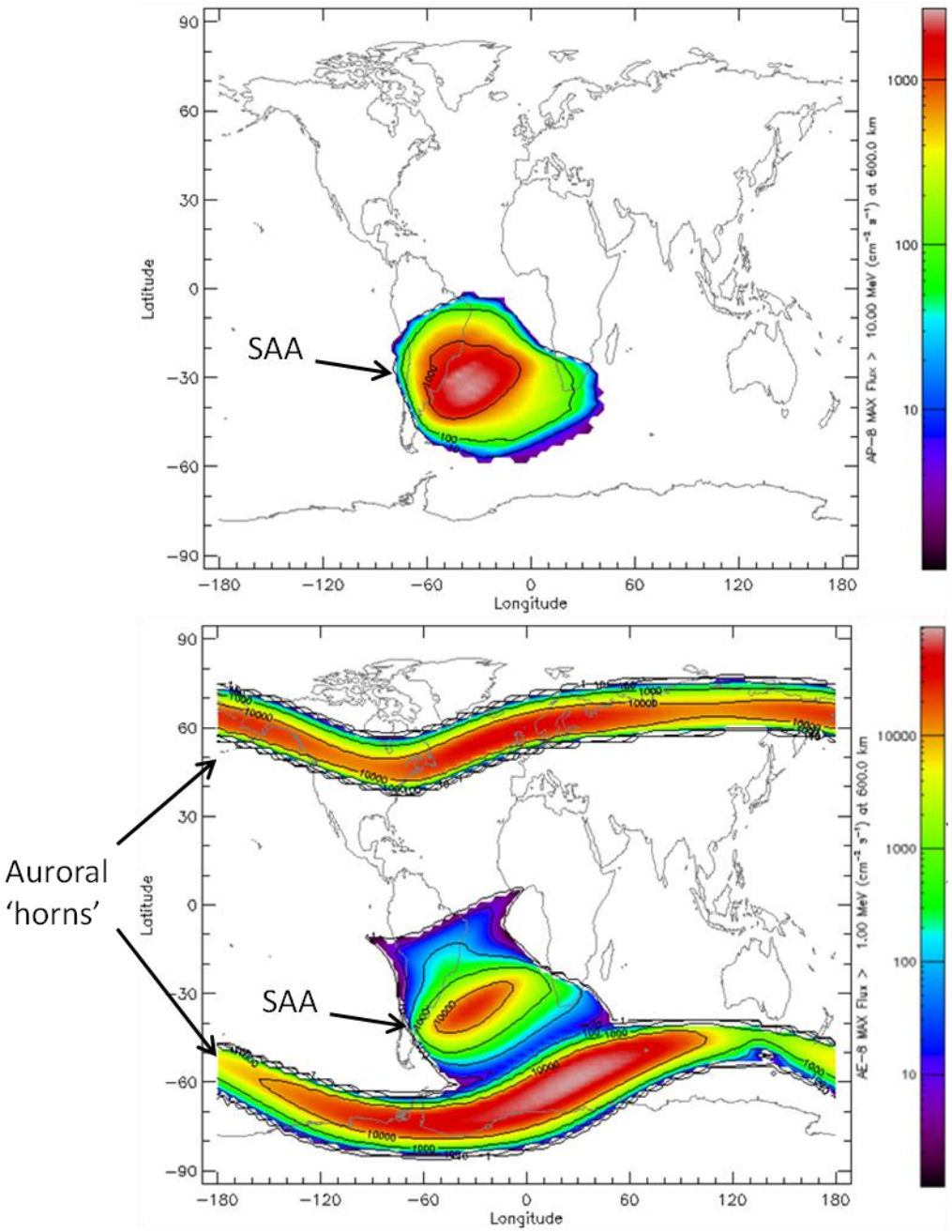

Figure 4.16. Map showing flux of high energy protons (top) and electrons (bottom) at 600 km altitude.

The SAA drifts and changes shape over time. The drift is of order 0.28°W and 0.08°N per year (Badhwar, 1997), which agrees with measurements of the difference between the speed of rotation the Earth and its liquid core (Zhang *et al.*, 2005). The magnetic field in the SAA is changing up to -100 nT.year^{-1} in some regions, and if current trends continue is modelled to cover half of the southern hemisphere by 2100 (Heirtzler, 2002). The charged particle population and extent of the SAA can also be enhanced by severe solar weather.

The auroral horns are regions of electron penetration close to the surface of the Earth. These regions can be seen in the electron map in Figure 4.16. and are caused by the same magnetic dipole offset that causes the SAA, as well as the large number of particles in the outer electron belt being able to extend closer to the surface at the poles, close to the polar cusp that allows the solar wind to travel to the upper atmosphere at the poles, causing the aurorae borealis and australis. The extension of the outer electron belt close to the Earth's surface at the poles can be seen in Figure 4.14.

Nuclear explosions at altitude have been shown to create artificial radiation belts that can increase the dose to spacecraft significantly. In the case of Starfish Prime, a 1.5 Mton detonation in 1962, a belt of high energy electrons was created that caused the failure of a third of all satellites in LEO at the time (Brown *et al.*, 1963; Lorenz & Harland, 2005). The belts were still present several years later (Hess, 1968).

4.2.2.2 Jovian Radiation Environment

Jupiter's magnetic dynamo is orders of magnitude stronger than the Earth's (a dipole moment of 1.55×10^{20} T·m^3 (Russell *et al.*, 1997) compared to the Earth's current moment of 7.75×10^{15} T·m^3 (IAGA, 2010)), meaning that it is able to trap much more energetic particles, and many more of them, within its belts. The compression of the magnetic field due to the solar wind is much less than seen at Earth (Figure 4.15), due to the much stronger field, the lower density of the solar wind at Jupiter's orbit, and the centrifugal force imparted on the trapped radiation belts by Jupiter's fast rotation (once every 0.41 Earth days (Abalakin *et al.*, 2002)). The magnetic field is, however, similar in its orientation to the Earth's; it is tilted 10° to the rotational axis, and has features similar to the SAA (Figure 4.16), which are suggested to be a contributing factor to the creation and stability of the 'Great Red Spot' (Luchkov, 1981), a storm in Jupiter's atmosphere the size of the Earth (Figure 4.17).

Figure 4.17. Photograph of Jupiter's great red spot taken by Cassini in 2000. (Credit NASA/JPL/University of Arizona)

The major source of particles in Jupiter's radiation environment between 5.2 and 10 Jovian radii is the volcanic moon Io, from which material is ionised into the magnetosphere at a rate of around 1000 $kg \cdot s^{-1}$ (Shemansky, 1988). The material retained in the magnetic field mostly consists of electrons and ions of sulphur and oxygen. The magnetosphere also captures protons and electrons from the solar wind. The electron environment reaches energies over 100 MeV at significant fluxes, originally detected from Earth by virtue of their radio frequency synchrotron emission (Sloanaker, 1959). The proton population is smaller, but is also present in energies over 100 MeV and can contribute significant damage (Divine & Garrett, 1983). Ions are also of energies up to tens of MeV, causing significant SEEs, resulting in possible instrument failure. In the case of the Pioneer 10 flyby, several images were lost due to false commands generated by SEEs (Fimmel *et al.*, 1980).

With regard to missions to the Jovian moons, Europa has no magnetosphere of its own, and is well within the inner radiation belt, offering very little shielding from the radiation environment (Paranicas *et al.*, 2007). Ganymede, the other body of major interest, has a small magnetosphere (Williams *et al.*, 1998) and is further from Jupiter, so offers some degree of shielding, for example the flux of high energy electrons is decreased by two orders of magnitude (Jun *et al.*, 2005). However any mission to Jupiter or its moons must be very careful to account for the radiation environment, and it is missions involving long-term studies in environments similar to that of the Jupiter magnetosphere that offer

opportunities for radiation hard instruments such as APS to be flown. Data from Galileo has shown that during 5 years of orbits around Jupiter, the instruments have experienced a dose of around 600 krad behind 2.2 $g.cm^{-3}$ of shielding (Fieseler, 2002). The radiation environment also offers significant hazards to manned missions to the Jupiter system (De Angelis *et al.*, 2003). More details of Jupiter's radiation environment can be found in Bagenal *et al.* (2007).

4.2.3 Shielding and Secondary Radiation

Most spacecraft offer some degree of radiation shielding by virtue of the mechanical structure of the craft. However, a goal of spacecraft design is to minimise mass, which can impact the available shielding. It is therefore important to design a shielding system carefully such that minimum mass is used to maximum effectiveness. No shielding system can hope to eliminate the irradiation of radiation sensitive components entirely, so the design goal is centred around reducing dose to acceptable levels (NASA, 1970). Figure 4.18. shows the ranges of different particles of different energies in aluminium, highlighting that different particle environments require different shielding design to properly mitigate the dose.

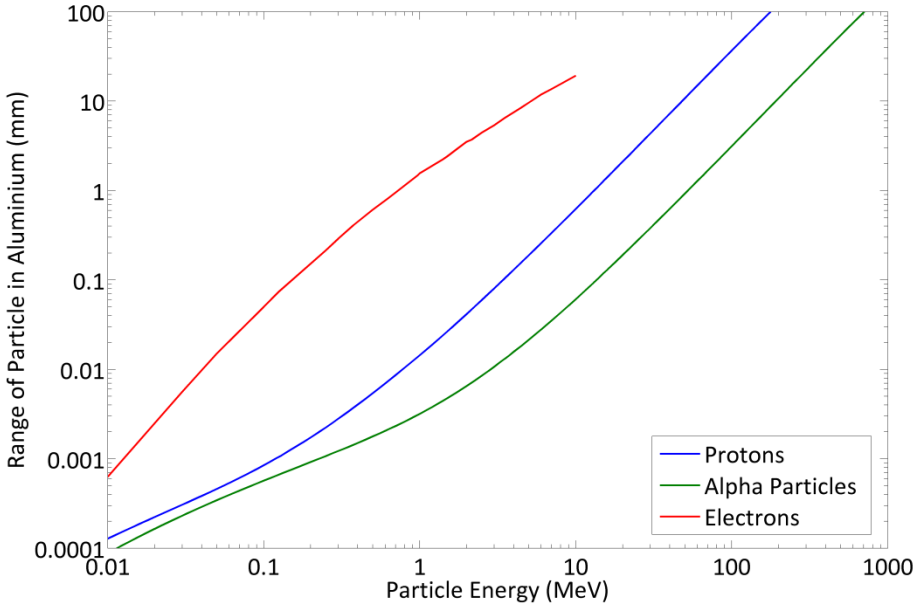

Figure 4.18. Ranges of protons, electrons and alpha particles in aluminium (data from SRIM-2011 (Biersack & Ziegler, 2008), and electron data from Linnenbom (1962)).

Calculating the effect of shielding is, nowadays, almost always achieved through using computer models. SPENVIS includes a shielding model SHIELDOSE-2 (Seltzer, 1994) that allows calculation of ionising and non-ionising dose when shielding with simple geometries. When used with SPENVIS orbital dose models, the total dose behind shielding for an entire space mission can be modelled.

Shielding can also produce its own radiation environment through 'secondary' bremsstrahlung radiation and particles that are released from the shielding by high energy particles, which sometimes are more harmful than the high energy particles that create them. These secondaries can present a significant portion of the total dose, normally around 10%. It has been shown that using an equal mass of lower Z material as shielding, *e.g.* RXF1 – a structural form of polyethylene, can reduce the number of secondaries (Bell *et al.*, 2011).

4.3 Missions

Space missions are the direct applications for the technologies and the work performed in this thesis. It is important to understand the overarching science goals and therefore the detector requirements for these missions, and the current limitations of the technologies and challenges offered by the very harsh working environments of space.

Presented here is an overview of radiation damage challenges and mitigation strategies in current CCD based instruments, and a view to future challenges and opportunities on space missions where APS may offer a more suitable choice of imager, especially instruments that the author has had opportunity to be involved with as a result of the work presented in this thesis.

4.3.1 Gaia

Gaia is an ESA mission due to be launched in 2013 and will carry a one billion pixel CCD array. The satellite will journey to L2 where it will survey the brightest billion stars in the Milky Way, resulting in the most accurate survey of the positions and velocities of objects in our galaxy. The CCDs will operate in Time Delay and Integration (TDI) mode, meaning that as the satellite rotates, the CCDs clock charge at the same rate that stars transit across the array, leading to a longer integration time for each star. A major concern for the mission is the impact of radiation damage leading to charge trapping effects such as degraded CTE. This degradation of CTE will lead to a smearing of the charge as the star moves across the device, leading to a less accurate measurement of the star's parameters.

The major effort in mitigating these effects is concerned with simulating, measuring and modelling the expected radiation damage prior to launch, so that the models can be applied to the data received from the satellite to recover information lost to CTE.

4.3.2 UKube-1 – C3D

UKube-1 is a mission commissioned by the UK Space Agency (UKSA) as a space demonstrator of UK technology. The craft is a Cubesat, composed of three 'cube' modules, designed to be fully autonomous and a cheap alternative to a full-blown space mission, providing frequent opportunities to scientists to both bid for and develop instruments to perform space science. Besides performing science, this prototype mission will offer opportunities for outreach to the public and schools to engage students about the UK contribution to the space industry and related sciences.

There are four payloads on-board the UKube-1 mission being provided by groups from around the UK:

- Janus (EADS Astrium); an experiment to test the feasibility of using the space radiation environment to generate random numbers (for possible use in satellite communications encryption).
- Funcube (UKSEDS); A payload consisting of a number of experiments designed by students to increase schools' and universities' access to space, as well as providing several outreach opportunities.
- TOPCAT (University of Bath, Chronos Technology, RAL, MSSL); a science payload designed to measure the Earth's upper ionosphere and plasma environment using GPS signals.

It is the fourth instrument, the Compact CMOS Camera Demonstrator (C3D) that is of interest as a continuation of the work contained in this thesis. Further details of the C3D design and development are available in Harriss *et al.* (2011).

4.3.2.1 Science Goals

C3D is an imaging demonstrator being developed by the centre for electronic imaging at the Open University in collaboration with e2v technologies. The instrument goals are threefold:

- Advancing the Technology Readiness Level (TRL) of APS imagers by flying several in space.
- Characterise the APSs response to radiation in the space environment.
- Providing opportunities for public relations for the UKSA and outreach to schools by capturing pictures of the Earth.

The radiation characterisation of the sensors directly relates to the work described in this thesis, as the sensors selected for flight are of the same family as the Jade APS. This provides a rare opportunity to compare lab-characterised radiation effects to those seen in the space environment.

4.3.3 JUICE - HRC

The JUpiter ICy moons Explorer (JUICE) is a joint ESA and NASA mission in the planning and initial study phase. The mission will travel to the Jovian system, performing fly-bys of Europa, Ganymede, and Callisto, finally resting in orbit around Ganymede. One of the planned instruments is the High Resolution Camera (HRC) which is the instrument of interest regarding this work.

4.3.3.1 Science Goals

JUICE has two overarching science objectives:

- Characterisation of the atmospheric and surface processes that occur in the Jupiter system
- Determination of the habitability of Jupiter and its moons

For the JUICE mission, 11 scientific instruments have been selected to reach these science goals, covering a wide range of physical measurements from radar to UV spectrometers to magnetic sensors. The HRC is designed to provide highly detailed multispectral images of the surface of Ganymede and Europa, and less detailed images of Io, Callisto and Jupiter during fly-bys.

4.3.3.2 HRC Detector Specifications

Parameter	Value
SNR	≥ 100
Pixel Count	> 1024 × 1024
Pixel Size	≤ 10 µm
Spectral Range	500 – 800 nm
QE	> 40% at 533 nm
Full Well Capacity	50 ke^-
Read-out Noise	< 50 e^- r.m.s.

Table 4-2. Detector imaging requirements for the proposed HRC instrument.

The detector requirements (outlined in Table 4-2) for the HRC are easily achievable with today's level of technology in both the APS and CCD. However, for the case of the JEO, the imager must be capable of withstanding up to 1 Mrad(Si) of TID and 1.3×10^8 $MeV.g^{-1}$ of assorted charged particles and ions and retain the same imaging capability. CCD performance at such a high dose has proven very difficult to achieve, so the mission provides an opportunity to study APS effectiveness in such harsh radiation environments and raise the TRL of APS technology for use in space.

The HRC instrument working group has therefore proposed an APS for study as the detector baseline, with a radiation-hardened CCD to be studied alongside as a second option.

4.3.4 Solar-C – XIT

Solar-C is a JAXA mission currently in the proposal phase. Two missions with differing science goals and instrumentation are proposed, referred to as 'Plan-A' and 'Plan-B'. The

details of these proposals are outlined in the Solar-C Interim Report (ISAS/JAXA SOLAR-C Working Group, 2011). The instrument of interest within the context of this thesis is the X-ray Imaging (Spectroscopic) Telescope (XIT) featured in Plan-B.

4.3.4.1 Science Goals

The proposed Plan-B mission is designed to investigate solar processes and dynamics. The main areas of interest for investigation are:

- Elementary structures of the magnetic atmosphere responsible for heating and dynamics.
- Energy transport and dissipation through small-scale magnetic structures.
- The role of the reconnection region in magnetic energy dissipation.
- How small-scale processes initiate large-scale phenomena that regulate space weather.

To achieve this, the Plan-B working group has proposed three instruments to be flown, the Solar Ultra-violet Visible and IR Telescope (SUVIT), the EUV/FUV High-Throughput Spectroscopic Telescope (EUVS), and the X-ray Imaging (Spectroscopic) Telescope (XIT).

The XIT aims to provide photon-counting imaging spectroscopy of soft X-rays between 1 keV and 5 keV, revealing the temperature structure of the solar corona and the structure and dynamics of plasmas in the magnetic reconnection region.

4.3.4.2 XIT Detector Specifications

The instrument is designed to be operated as a grazing incidence telescope, which focuses X-rays by reflecting them at a very small incident angle to increase signal throughput (reflecting X-rays at large incidence angles incurs loss of signal by transmission through the mirror).

The desired characteristics in a detector for the instrument are:

- Fast readout (≈ 1000 fps) with low readout noise (< 5 e^- r.m.s.) to be able to effectively provide X-ray photon counting at the high solar flux.
- Good soft X-ray spectroscopic capability to be able to resolve the energy of the X-ray events to characterise them sufficiently.

While CCDs currently offer superior X-ray spectroscopy capability, a high frame rate and radiation hard design can more easily be achieved with a bespoke APS. The XIT working group, who are in contact with e2v technologies regarding the design of such a sensor, have proposed a sensor similar to e2v's Wave Front Sensor (WFS), and are interested in studying the X-ray performance of e2v's current APS products. The characterisation of the Jade APS and the OCI test chip in regard to X-ray performance with a specific view to the requirements of an instrument such as XIT have formed a part of this work, and the results are presented in Chapter 5.

Chapter 5: Baseline Sensor Characterisation

A device, once fabricated, can differ from its nominal specifications by virtue of variations and complications in manufacturing and so it is important to be able to characterise a device once it has been made. Characterisation of devices also provides metrics through which different devices can be compared and considered for a certain application. It may also be of interest to characterise a device for uses not intended at manufacture, *e.g.* for X-ray spectroscopy, and so further tests should be performed to determine the device's suitability for any given application. It is not uncommon for these sensitive devices to vary within a batch and between batches due to small environmental or procedural differences during manufacture, and so each device may have quirks that should be characterised.

This chapter outlines the major metrics and techniques used to characterise a sensor, and results are presented for the characterisation of the Jade and OCI APSs. Specific focus is given to the spectroscopic X-ray performance of the devices within the context of the Solar-C photon counting spectrometer mentioned in the previous chapter.

5.1 Imager Characterisation Metrics

5.1.1 Noise and Dark Signal

The noise and dark signal present in an imaging device enforce fundamental limitations on the accuracy of the imaging, which is especially important for scientific applications. Ideally each optical photon falling on the device will be collected as a single electron, no charge will be added to this signal as it is read out, and this charge will be measured with no uncertainty. In reality the design of the sensor will allow generation of charge from non-photonic sources, and this charge will be measured with a level of uncertainty. The sources of these limitations are detailed below. A lot of the design and manufacturing effort in the realm of scientific sensors is focused on reducing noise and dark current levels within the

device to provide accurate imaging, allowing more detailed measurements to be performed.

5.1.1.1 Dark Signal

Dark signal occurs via the thermal (as opposed to photoelectric) excitation of electrons into the conduction band, causing a parasitic 'dark current'. Dark current shot noise is one of the fundamental noise sources in semiconductor imagers, the level of dark current being one of the most fundamental limitations on device performance. The reduction of dark current is essential for maximising signal-to-noise.

The three major sources of photodiode dark current are:

- Si-SiO_2 interface.
- Depleted silicon within the potential well.
- Non-depleted bulk silicon.

The majority of dark current sources are introduced in the silicon during pre-processing, device fabrication and design, and device post-processing. Once a device is fabricated, the dark current density ($A \cdot m^{-2}$) can be reduced by lowering the operating temperature, as shown by the general dark current equation:

$$I_{dark} = 2.5 \times 10^{15} A_{pix} D_{FM} T^{1.5} e^{-E_g/2kT} \quad (5.1)$$

Where I_{dark} ($e^- \cdot pixel^{-1} \cdot s^{-1}$) is the average dark current generation, A_{pix} (cm^2) is the pixel area, and D_{FM} ($nA \cdot cm^{-2}$) is the 'dark current figure of merit' at 300K, a measure of the baseline level of dark current in the device. It is interesting to note that reducing the temperature to liquid nitrogen temperatures (77 K) causes the device to enter the carrier freeze-out regime (as opposed to extrinsic and intrinsic regimes), which prevents the activation of impurity atoms, leading to a decrease in the carrier concentration.

Surface Dark Current

The surface of the device is the major source of dark current, and much development has resulted in several techniques to reduce it. The dark current is a result of the surface being an interface between silicon and the native oxide, SiO_2. The size of the Si and SiO_2 lattices are mismatched, leaving unbonded or 'dangling' bonds at the interface. Figure 5.1. shows the origin of these surface states.

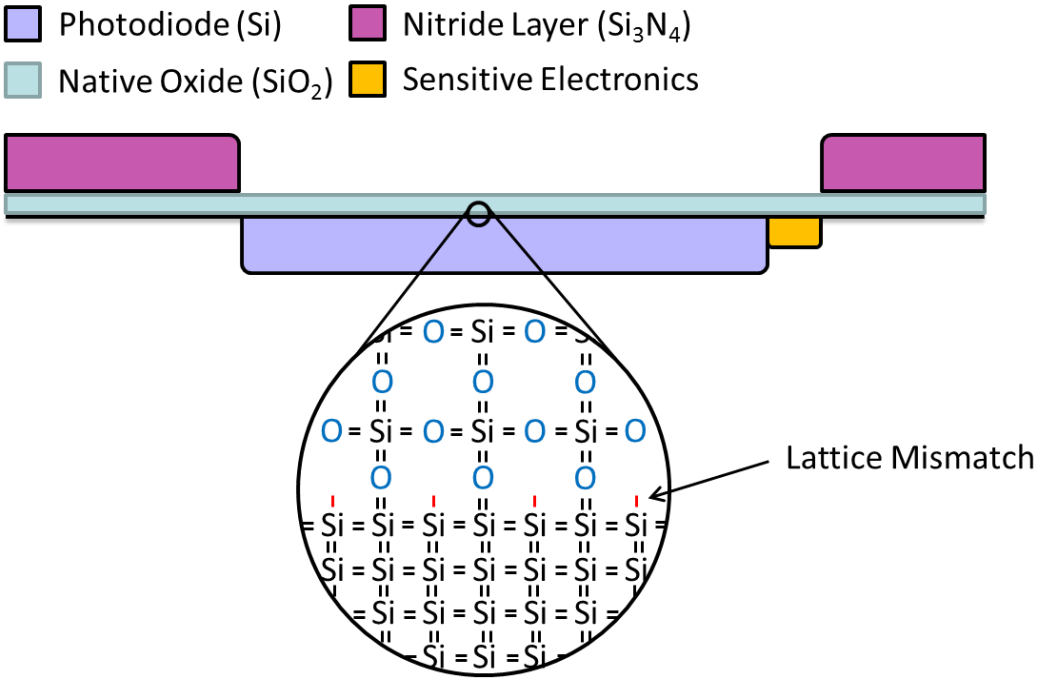

Figure 5.1. Schematic showing the interface bonding within a sensor pixel, showing lattice mismatch leading to intermediate energy levels within the bandgap resulting in a source of dark current.

During fabrication, devices are commonly subjected to a high temperature anneal in a hydrogen atmosphere, allowing monatomic hydrogen to diffuse into the surface of the detector where they will react with the dangling bonds, passivating them. In this passivated state, the bonds no longer provide a bandgap energy through which electrons can be more easily thermally excited into the conduction band. However, under irradiation, particularly from ionising sources such as gamma rays or electrons, these hydrogen atoms can be liberated and bond to form diatomic hydrogen, which will then leak out of the surface of the device, recreating the dangling bonds. Even before irradiation the process is not perfect

and interface states can still exist. To combat leakage current from the surface further, the photodiode can be pinned to store charge away from the surface as described in Chapter 2.

The issue is further complicated in APS with the introduction of Shallow Trench Isolation (STI), which are oxide regions that form trenches within the device to isolate CMOS components. These oxide regions are added by foundry design rules and can present further complications when interpreting results, as the location of such implants is often a foundry process commercial secret. Analysis of devices with a known STI design has shown that it can contribute to dark current and form interface states under irradiation (Goiffon *et al.* 2008). The states in the STI regions also often show different annealing characteristics to the surface oxide.

Depletion Dark Current

The depletion dark current is generated within the region of depleted silicon that surrounds the photodiode area. This region is depleted of carriers as shown in Chapter 3, and any generated carriers are quickly swept out of the region into the photodiode (or, in the case of holes, out of the photodiode) due to the electric field. This is what provides photon-sensing capability, but carriers can be excited into the conduction band thermally, especially if a trap exists within the bandgap, reducing the energy required (as shown in Chapter 4). These traps exist naturally within the silicon, and can also take the form of local crystal deformities.

Displacement radiation damage within the depletion region can increase the density of traps by generating vacancies which form stable bonds with dopant or impurity atoms, forming a stable defect that can enhance the thermal generation rate of carriers.

Bulk Dark Current

Bulk dark current is generated through similar mechanisms to depletion dark current, however the effect is reduced by the lack of electric field in the bulk of the device.

Thermally generated carriers must drift (via diffusion) to a region where a field is present in order to be collected on the photodiode. As this process takes a significantly longer time than collection from the depletion region, the probability of the generated carriers recombining is higher and this reduces the dark current from the bulk of the device.

5.1.1.2 Readout Noise

Beyond the noise on the photo-generated signal, there is readout noise associated with the chain of electronics through which the signal is read. CCDs benefit from a single readout node used for a large number of pixels, whereas APSs have some portion of the readout electronics on-pixel and other portions shared between rows or columns of pixels.

Reset Noise

Before discussing reset noise, it is important to understand a fundamental noise source in circuits, Johnson noise. Johnson noise describes the phenomenon that current flow against a resistance is not smooth, but instead erratic due to the thermal energy of the resistance's lattice and of the charge carriers causing collisions. The noise in the current flow is proportional to the temperature. Johnson noise does not vary with the frequency of the signal, hence it is referred to as a 'white noise' source.

Johnson noise is given by:

$$W = \sqrt{4kTBR} \tag{5.2}$$

Where W is the r.m.s. noise voltage (V) and R is the resistance of the conducting path (Ω). B is the equivalent noise power bandwidth (Hz) and is, in the case of an RC low-pass network (commonly used in CCD and APS):

$$B = \frac{1}{4RC} \tag{5.3}$$

Where R and C are the resistance (Ω) and capacitance (F) of the RC network, respectively. Substituting equation 5.2 into equation 5.1 yields the equation describing the noise on the reset node as a function of temperature and node capacitance

$$W = \sqrt{\frac{kT}{C}} \tag{5.4}$$

Johnson noise is present throughout the circuit, and is the fundamental source of the variability in reset noise.

Resetting refers to setting the charge on the sense node to a reference level by connecting it to a reference voltage. The noise associated with this action is due to Johnson noise on the reference voltage; thus the reference voltage, and therefore the reference signal level, is not accurately known. The noise N (e^- r.m.s.) is given by:

$$N = \sqrt{\frac{kTC}{q^2}} \tag{5.5}$$

This gives rise to the common name “kTC noise”.

Figure 5.2. shows typical voltage behaviour of the sense node during integration and readout of a 3T pixel, referencing Figure 3.6. When *ΦR* is turned ‘on’, the node is connected to RD, which suffers from Johnson noise generated by the ohmic resistance of the reset transistor. When *ΦR* is turned ‘off’, the node is ‘frozen’ at the instantaneous voltage level of the reset noise. At the end of the integration time, the integrated charge is read out, but this value has the reset noise associated with it, and so the level of signal cannot be accurately determined within the level of the reset noise.

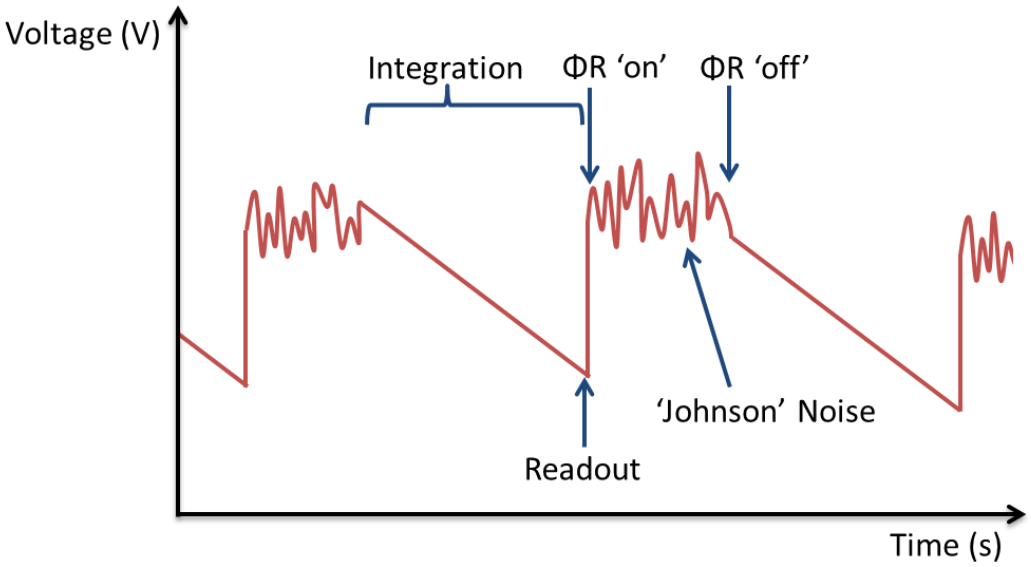

Figure 5.2. Plot of typical voltage measured at the sense node during several pixel integration times.

To combat this, CDS is used, as described in Section 3.3.2., enabled by separation of the photodiode from the readout node by introducing an extra transistor into the pixel. The voltage level at the output node can then be sampled at the end of integration and again directly after reset. The time between samples is short enough that the noise is correlated and can be measured and accounted for, normally in the readout circuitry.

It should be noted that there are two commonly used reset regimes, termed 'hard' and 'soft' reset. The treatment above refers to hard reset. During hard reset, the readout node is connected to a separate voltage line, $V_{RD} (\gg V_{DD} - V_T)$, which reduces charge deferred between images (image lag) and provides good linearity because V_{GD} remains positive. However to minimise electrical connections within the device, V_{RD} is often wired commonly with V_{DD}, resulting in a soft reset. In soft reset, the node approaches the reference voltage $V_{DD} - V_T$ asymptotically due to the reset transistor entering sub-threshold regime of operation. While the node is not entirely reset to a null level (depending on settle time), this technique does lessen the effects of kTC noise (Tian *et al.*, 1999).

1/f Noise

1/f noise or 'flicker' noise is generally considered to be a result of surface states, in a similar manner to surface generated dark current. However, it is a result of these surface states acting in the readout source follower MOSFET channel that generates a different noise characteristic to surface generated dark current noise.

As previously discussed, the Si-SiO_2 interface is populated with a large number of traps, a direct result of dangling bonds formed due to lattice mismatch. The surface traps have energy levels distributed in a 'U' shape across the silicon energy band. This leads to a distribution of 'deep' traps, which have a higher time constant and so generate low frequency noise, and 'shallow' traps, which contribute higher frequency noise. The noise power increases proportionally with the trap emission time constant, leading to the noise following the 1/f rule. At higher frequencies this is dominated by Johnson noise, as shown in Figure 5.3.

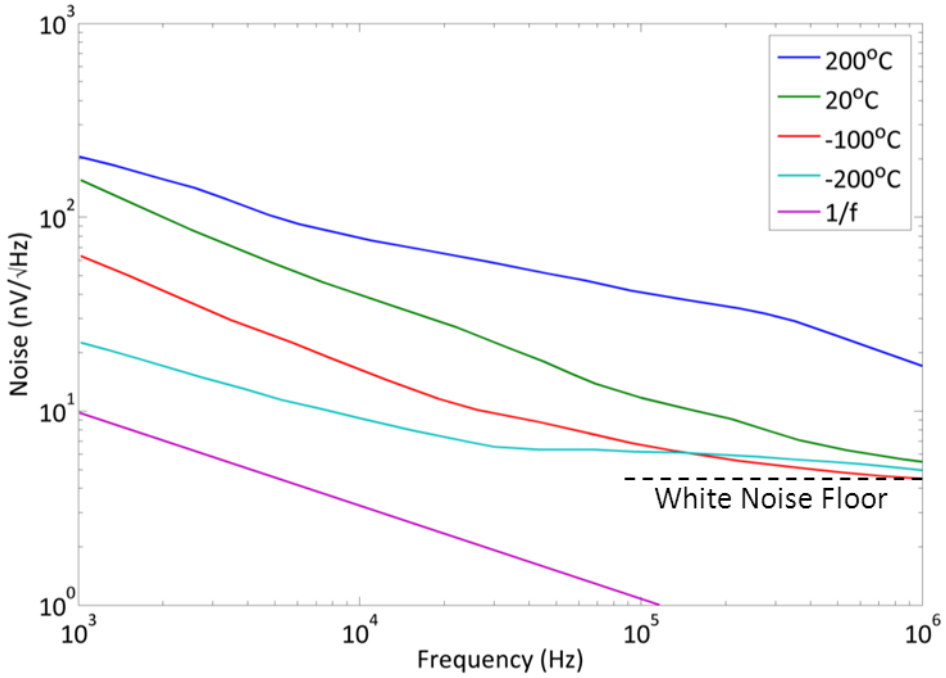

Figure 5.3. Graph showing the measured noise levels over the frequency spectrum for an example MOSFET after Janesick (2001). The gradient of 1/f noise is shown in purple.

As smaller MOSFETs are fabricated with smaller feature sizes, the number of traps located in the bandgap decreases until MOSFETs are manufactured with only a small number of

traps contributing to the 1/f noise. In this case the noise ceases to exhibit a 1/f spectrum and instead single mid-bandgap traps can cause discrete modulation of the current (Uren *et al.*, 1985). This discrete modulation is called 'Random Telegraph Signal' (RTS) and presents a significant problem to the miniaturisation of CMOS components. RTS is significantly harder to correct for due to the probabilistic nature of the modulation. Figure 5.4. shows a direct measurement of RTS in a 0.18 × 0.18 µm MOSFET made by the author.

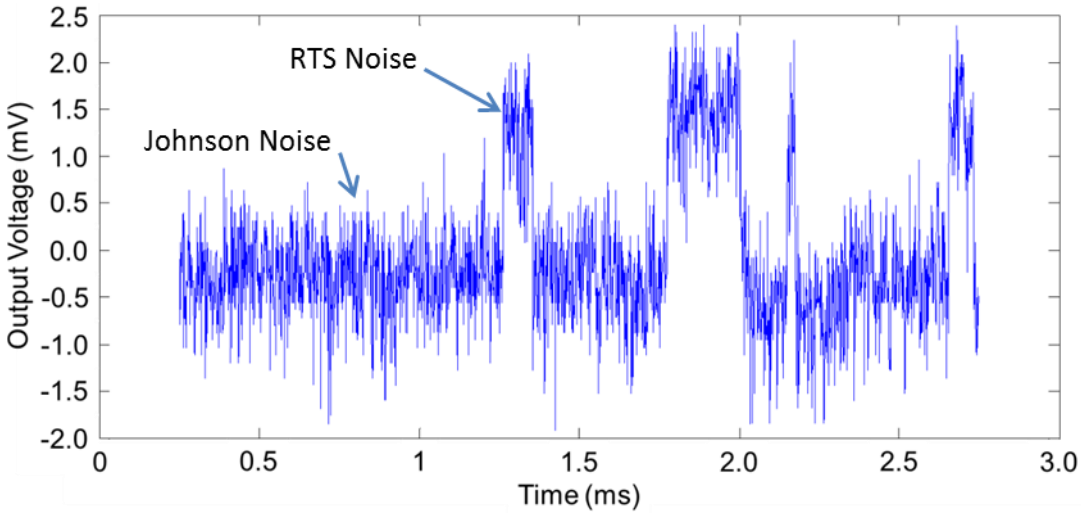

Figure 5.4. Graph of measured output voltage from an unirradiated 0.18 × 0.18 µm MOSFET under constant gate bias, exhibiting Johnson noise modulated by RTS noise.

RTS can also be caused by displacement damage in the depletion region of the photodiode, which is unrelated to 1/f noise. Both MOSFET and displacement damage induced RTS is discussed in further detail in Chapter 7.

5.1.1.3 Fixed Pattern Noise

Fixed Pattern Noise (FPN) is any variability of signal spatially over the device. In APSs, each pixel has individual readout circuitry so the variability between each pixel can be high. Most sources of FPN are introduced in the fabrication process. Differences in the manufacture of each MOSFET leads to each source follower having different DC offset and gain characteristics. The development of increased uniformity in MOSFET fabrication was a major factor in performance increase in early APS development. Besides the readout

circuitry, FPN can be introduced by the photodiode fabrication process, which can introduce Photo Response Non-Uniformity (PRNU) and Dark Signal Non-Uniformity (DSNU).

FPN can be introduced by radiation damage, either by non-uniform shielding of a uniform radiation such as gamma rays, or rare events of highly displacement damaging radiation such as heavy ions or protons, which create high dark current in random pixels over the imaging array. Additionally, presented in Chapter 6 is a case of FPN that is present in manufacturing, but worsens severely after irradiation by a uniform source, underlining the importance of reducing FPN for sensors designed for space applications.

5.1.2 Signal to Noise Ratio

There are many more noise sources in devices than what has been mentioned thus far, and details on any further noise sources are therefore introduced as needed.

The Signal to Noise Ratio (SNR or S/N) is an important figure of merit that determines the ability of a device to measure small variations in signal, and therefore the ability to image low contrast scenes. It provides an overall measure of the system, as it incorporates all noise sources and optical performance parameters. It is important to note that it varies with light intensity and operating conditions.

5.1.3 Fill Factor

For APSs (and similarly ILT CCDs), a further complication is low fill factor. Due to the pixels in APSs containing readout transistors, a large proportion of each pixel is not photosensitive. In the same way, ILT CCDs have alternating rows of shielded pixels used for readout. Both of these designs reduce the overall Quantum Efficiency (QE) of the system, as both incident photons and photogenerated charge can be lost to these dead areas. The fill factor of an APS can be increased by fabricating a sheet of ‘microlenses’ or ‘µlenses’ over the device, which focus incoming photons into the photosensitive regions of the pixel, shown in Figure 5.5, effectively pushing the fill factor back to near 100% and improving the

QE significantly, as seen in Figure 5.6. Scanning electron microscope (SEM) images of the microlenses as fabricated on the Jade APS are shown in Figure 5.7.

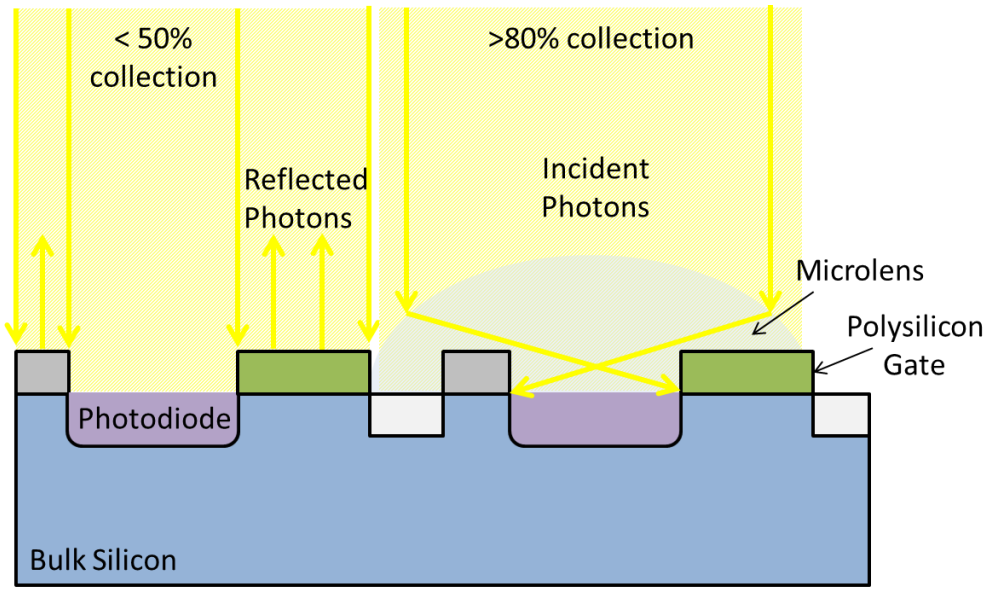

Figure 5.5. Illustration of captured incident light in the case of no microlens (left), and a present microlens being used to direct incident light onto active pixel regions (right).

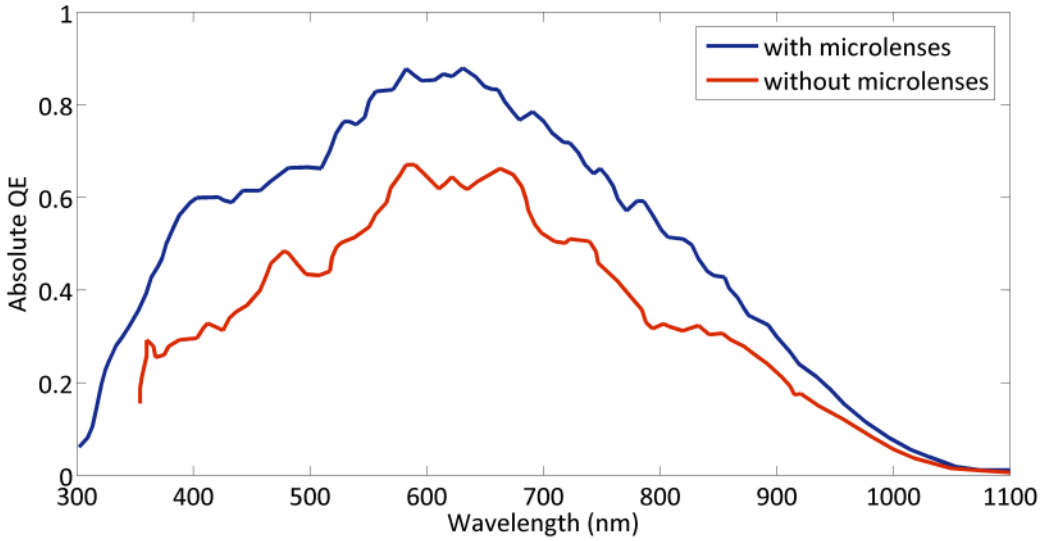

Figure 5.6. Graph showing measurements of QE for an ILT CCD with and without microlenses (after Ciccarelli, 2002).

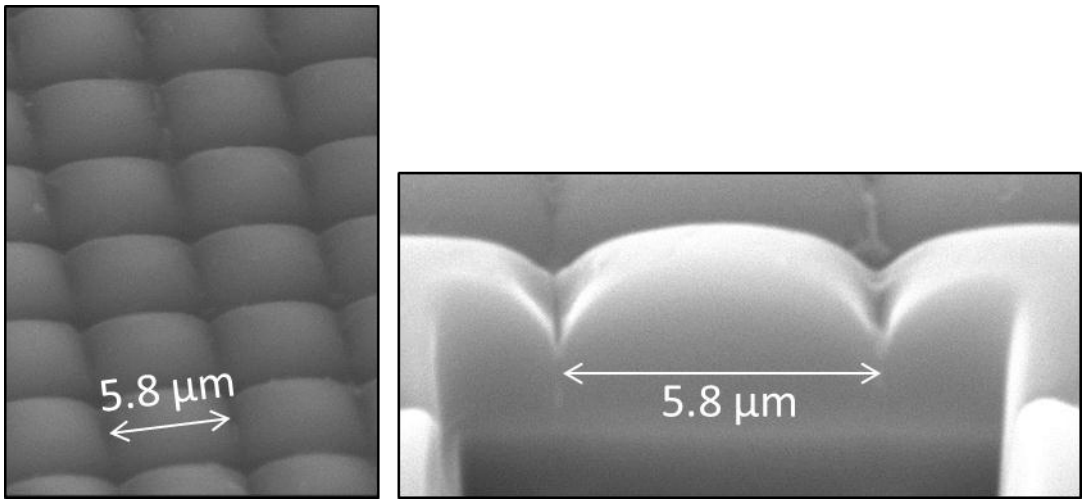

Figure 5.7. SEM image taken by the author of the microlens layer of the Jade APS seen from above (left). The right image shows a cross-section of one lens created using a focussed ion beam (FIB).

5.1.4 Responsivity

The responsivity of a sensor is a useful figure of merit related to the QE, commonly quoted in $V \cdot W^{-1}$ (*i.e.* volts measured from the pixel output per watt of light input). This can also be decoupled from the light input (and thus QE) by stating a figure in $\mu V \cdot electron^{-1}$. The responsivity varies from pixel to pixel, and varies with photodiode capacitance, so the responsivity can vary with illumination level (referred to as responsivity non-linearity). The responsivity stated as $V \cdot W^{-1}$ also varies with wavelength due to the difference in QE.

5.1.5 Linearity

Linearity of a sensor is very important for scientific applications. A perfectly linear sensor has a constant gain for any signal level. There are generally two main sources of non-linearity in sensors: the source follower amplifier which provides a gain proportional to the voltage across it, and the sense node diode. Modern source follower amplifiers can generally be manufactured to provide linearity to within 1%. In the case of CCDs, the sense node capacitance tends to be large meaning that collected charge does not affect the capacitance of the node significantly. However, in the case of APSs the sense node capacitance can be very small, meaning that collected charge can alter the node capacitance significantly (non-linearities of over 400% have been measured (Fossum,

1997)), altering the gain drastically. This is a major obstacle to overcome in APS development.

5.1.6 Modulation Transfer Function

The Modulation Transfer Function (MTF) is a measure of how accurately a device responds to a spatially changing input *i.e.* it is a compound measurement of the sharpness and contrast limit of the device, and it used as an encompassing quantification of imaging quality. There are several techniques used to measure and derive the MTF. e2v technologies use the vernier technique of MTF measurement detailed in the technical note by e2v technologies (2003).

5.2 Photon Transfer Curve

The variance Photon Transfer Curve (PTC), also sometimes termed the mean-variance curve is a versatile diagnostic of device performance, allowing measurement of many of the metrics detailed above. For more information see Janesick (2007).

5.2.1 Characteristics

A diagram of a typical PTC and its main characteristics is given in Figure 5.8.

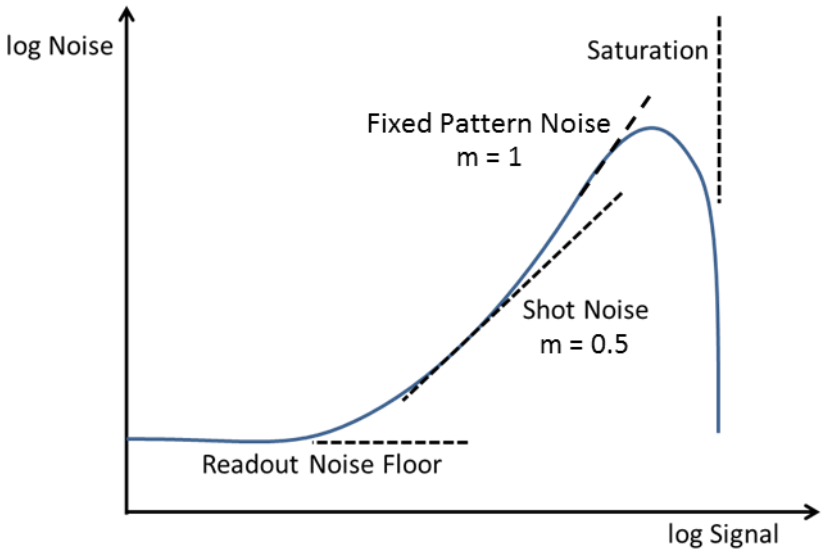

Figure 5.8. Diagram illustrating the main features of a photon transfer curve.

From the photon transfer curve the read noise floor of the device can be measured from the beginning of the curve, *i.e.* where the read noise dominates noise on the signal. The shot noise is present above this point, and should, if the device is operating properly, manifest as a gradient of 0.5 on log-log axes. This is clear from the Poissonian description, where the natural variation in a packet of N photons is $\sqrt{N}$.

As the signal approaches the well capacity, the noise no longer follows this Poissonian description, as a larger value of shot noise drives the number of photons over the well capacity, and so it not measured, giving the appearance of a lower noise. At saturation the noise decreases rapidly to zero (*i.e.* if the signal is far over saturation, the signal measured is simply the well capacity and the noise is zero).

5.2.2 Measurement

Figure 5.9. shows the measured photon transfer curve for the Jade APS measured at a setting of gain = 1. Each point on the graph represents the mean signal and variance for a given pixel at a given level of illumination (blue curve) measured over 100 frames. By subtracting the noise floor level of the blue points (the variance level at which the gradient becomes zero), we obtain the green curve, which shows a gradient of 1, typical of the shot noise. The noise floor is measured to be √0.3 or 0.56 DN.

By measuring the signal level at which the variance is 1 DN^2, we can determine the responsivity of the device in $e^-{\cdot}DN^{-1}$. For this device it is measured to be 50 $e^-{\cdot}DN^{-1}$, which gives the noise floor as 28 e^- r.m.s. Saturation of the device occurs at 256 DN, which corresponds to 12.8 ke^-. The feature at DN = 40 is caused by a subset of pixels with low full well capacity.

Interesting to note is the oscillating structure at low signal levels. This is caused by the quantisation of the signal, *e.g.* if the true signal is 1.49, the ADC reads it as 1 DN (if the threshold is 1.50 DN), and the noise only needs to be small to cause the true signal to

increase to 1.51 DN and therefore for the ADC to register it as 1 DN, causing a small amount of noise to seem larger due to quantisation. If the true signal is 1.0 DN instead, this effect is minimised as the noise must be ± 0.5 DN, which happens more rarely, and so the measured noise is lower.

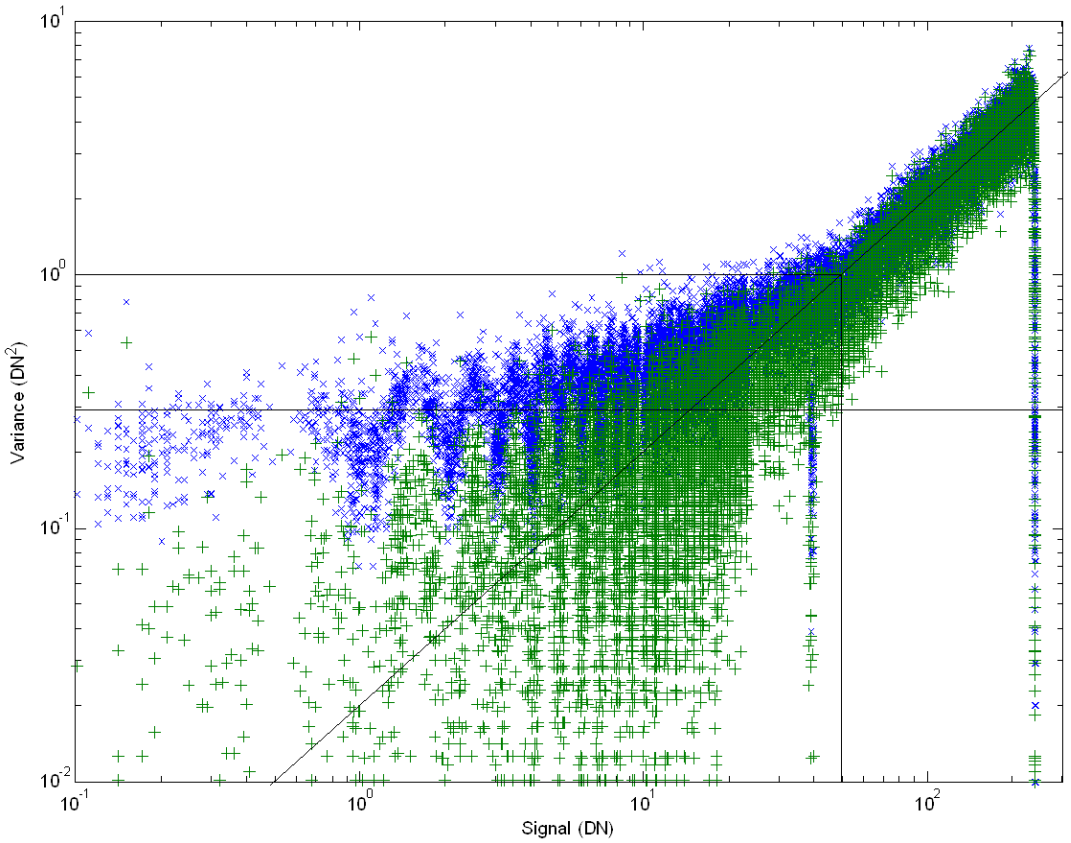

Figure 5.9. Measured photon transfer curve for the Jade FI device, measured data (blue) and noise floor subtracted data (green).

5.3 X-Ray Characterisation

5.3.1 X-Ray Detection Theory

There are two complicating factors when detecting hard X-ray photons (~0.1 to 100 keV) as opposed to optical photons (~1 to 3.65 eV) by virtue of their vastly higher energy: above 1 keV they exhibit a higher penetration through materials before interaction, and they liberate more than a single electron upon interaction. However, these complications can be exploited to enable characterisation techniques that are not possible using visible light.

5.3.1.1 Charge Cloud Generation

Due to their higher energy, X-rays generate more than a single electron when interacting with a device. The photo-generated electron has sufficient energy upon collision with a secondary valence-band electron to promote both to the conduction band of the device (termed Auger electrons). Depending on the X-ray energy, either or both of these electrons may have sufficient energy to cause further Auger transitions, resulting in a 'cloud' of electrons being promoted to the conduction band until the energy of each electron is insufficient to cause further transitions (Geist & Wang, 1983). The number of electrons in this cloud is simply determined by the energy of the interacting X-ray, as the energy to generate each electron is, on average, constant for a given material and temperature. The mean energy required to generate each electron in silicon at 293 K is 3.65 eV (Bertolini & Coche, 1968). This means that an ^{55}Mn k_α X-ray will generate, on average, a cloud of 1615 electrons.

Once this cloud is generated, it is drawn towards the photodiode by the potential field set up in the device. However the electron cloud will quickly diffuse by virtue of the high concentration of negative charge. If the timescale for the charge to be captured within a photodiode is longer than the timescale for the cloud to diffuse laterally by the order of a pixel dimension, then some of the signal from an X-ray arriving in one pixel will be captured as signal in a neighbouring pixel, resulting in a 'split event'. This is especially likely to happen if the X-ray interacts in un-depleted silicon, allowing a long timescale for the cloud to diffuse before coming into a high-field region of the device that captures the charge relatively quickly. This phenomenon can be used to estimate the true depletion depth of a device by modelling the size of the electron cloud for X-rays interacting at different depths and comparing to measurement (Murray, 2008). Figure 5.10. shows two X-rays interacting at different depths, and the effect this has on the dispersion of the charge before collection.

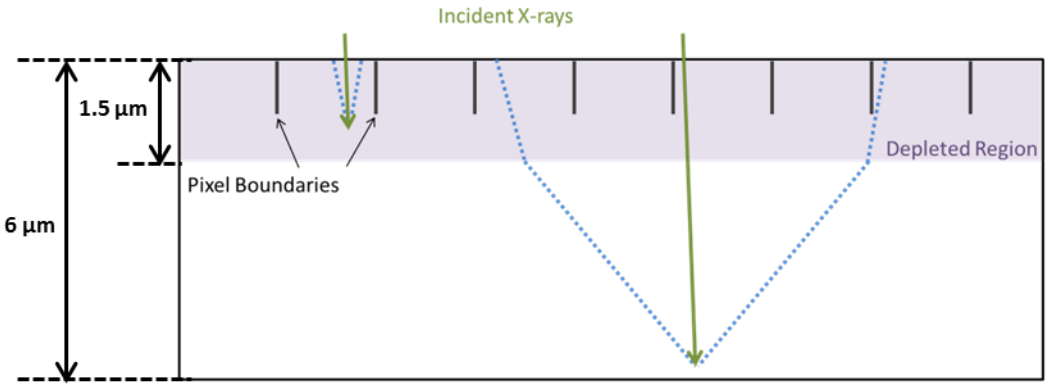

Figure 5.10. Schematic of electron cloud generation and capture for X-rays interacting within the depletion region (left) and in the undepleted bulk (right), indicative thicknesses for the Jade APS are given (not drawn to scale).

5.3.2 Experimental Setup

5.3.2.1 X-ray Generation

X-rays are generated in two ways: via the acceleration of a charged particle such as electrons (bremsstrahlung radiation), or via energy-level transitions within atoms. Described below are two common sources of X-rays used in the lab. Additionally X-rays may be generated at a facility such as a synchrotron, where a larger range of energies or more accurate measurements can be made. X-rays are also emitted in the black-body spectrum of objects hotter than ~10^6 K, making the detection and characterisation of X-rays an important technique for astronomical measurements of stellar objects (Helfand *et al*, 1980).

Hot Cathode X-ray Tube

A hot cathode tube is an X-ray tube that, initially, thermionically produces electrons from a tungsten filament which is also acting as the cathode. The electrons are accelerated towards an angled target anode, emitting a characteristic bremsstrahlung continuum of X-ray energies. The characteristic spectrum of photons extends in energy up to the accelerating voltage, beyond which there is no emission. Characteristic energies of the anode material k and l-lines are also often present due to secondary X-ray fluorescence. However, in the work presented in this thesis the tube used has a tungsten anode with a k_α

emission of ~59 keV which while operated at ~10 kV, only produces bremsstrahlung photons up to 10 keV, of too low an energy to produce fluorescence electrons from the X-ray tube target.

The hot cathode tube is then used in conjunction with a target material which fluoresces under illumination with X-rays, producing characteristic emission lines, *i.e.* the innermost electrons are liberated by the X-rays, and sometime later a higher energy electron emits a photon to occupy the more stable energy level. In this work a manganese target is used, as the industry standard is ^{55}Fe radioactive decay sources, described below, which emits the same Mn-k_α (5898 eV) and Mn-k_β (6490 eV) photons.

One drawback to the hot cathode source is the bremsstrahlung spectrum, which complicates analysis and does not give clean spectral lines to detect. However the source allows tuneable acceleration voltage and current, allowing fluorescence of different targets and modification of the source fluence, which is of particular use when avoiding event pileup.

Figure 5.11. shows the general experimental setup using the hot cathode source. The target wheel enables use of different fluorescing materials if different energies of X-rays are needed, and also introduces its own Al-k_α peak into the resulting X-ray spectrum.

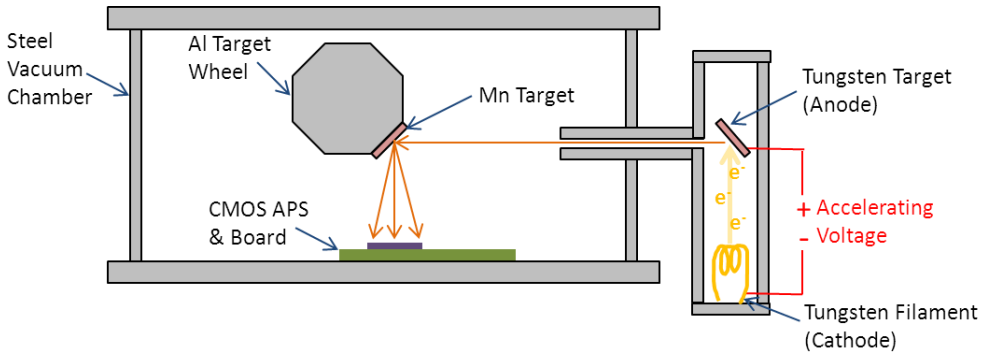

Figure 5.11. Diagram of experimental setup for illumination with hot cathode source after Gow (2009).

^{55}Fe source

^{55}Fe is an unstable isotope of iron that decays to ^{55}Mn through electron capture as shown in equation 5.6.

$$^{55}_{26}Fe + e^{-} \rightarrow ^{55}_{25}Mn + \nu_e \quad (5.6)$$

During this process, one of the ^{55}Fe atoms captures an electron from its own inner shell (typically k-shell or rarely l-shell) to convert a proton to a neutron, releasing a neutrino. Shortly afterwards an outer shell electron releases a photon to occupy the more stable energy level left behind. This preferentially emits Mn-k_α and Mn-k_β X-rays.

^{55}Fe produces monochromatic X-rays, making it more desirable for the measurement of spectroscopic performance than the hot cathode source. It has a half-life of 2.737 years, making it desirable for lab work as it is stable enough to provide uniform illumination over the course of an experiment, but unstable enough to be a relatively low threat to the environment. The source also requires no power source and is highly portable, making it ideal for integrating with existing equipment. The downside is that it is not inherently tuneable besides external attenuation, and if a higher flux is needed then a higher activity (and therefore more dangerous) source must be handled.

Figure 5.12. shows general experimental setup for use of the ^{55}Fe source. The target wheel in this instance is used as a safety measure, as the source can be turned away from the chamber opening when the sensor needs to be removed or adjusted, reducing the irradiation risk.

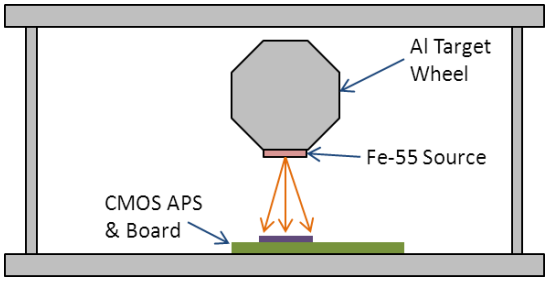

Figure 5.12. Experimental setup for ^{55}Fe source X-ray illumination.

5.3.2.2 X-ray Event Processing

Due to the nature of X-ray interaction described earlier, it is common for X-rays to interact throughout a device's depth. Taking the example of the Jade APS, only ~18% of incident Mn-k_α X-rays (5898 eV) will interact in the 6 µm of bulk silicon, with around 5% of the incident X-rays interacting in the ~1.5 µm of active silicon (Henke *et al.*, 1993). This results, on average, in a large amount of charge spreading before charge is collected, resulting in a large percentage of split events. If measurement of the incident X-ray energy is desired, these split events are undesirable as each pixel in the split event contains a fraction of the total event charge, degrading the measured energy resolution. It is possible to regain this performance to some degree by performing 'event processing' on the image dataset.

Figure 5.13. shows a general event processing scheme. The scheme examines pixels above a set threshold (normally above 2σ of the noise peak) and then categorises them into one of three classes; either isolated, '3 × 3' or '5 × 5' events. It begins with '5 × 5' events, looking around a locally maximum pixel at the 'considered' pixels as shown in Figure 5.13. If any of these pixels are above the threshold then the '5 × 5' area is summed and categorised as a '5 × 5' event. If none of these 'considered' pixels are above threshold, the algorithm then considers the 'considered' pixels in the '3 × 3' event. Likewise if any of these pixels are above the threshold then the '3 × 3' area is summed and the event is categorised as a '3 × 3' event. Finally, if there are no surrounding pixels higher than threshold then the event is categorised as an isolated event.

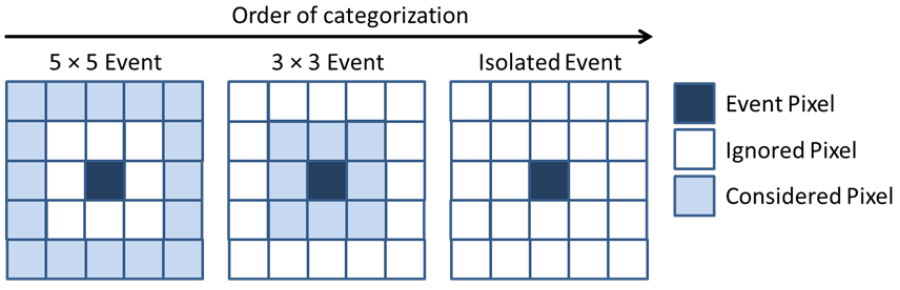

Figure 5.13. Diagram showing example event processing recognition scheme.

It is possible to carry out more detailed analysis of events by treating 1 × 2, 2 × 2, and other sizes and shapes of events separately (Murray, 2008). Determining the correct threshold for the best event reconstruction can be difficult, as too low a threshold may pick up noisy pixels as events, and too high a threshold will discard fainter pixels in split events; different devices may produce the best results with different thresholds.

The drawback to such a treatment is the additional noise introduced by summing larger numbers of pixels. Therefore with a relatively noisy sensor the best energy resolution is achieved by discarding split events and using isolated events to make measurements. However, in photon-starved applications this reduces the amount of statistics gathered.

5.3.3 Results

5.3.3.1 X-ray Spectroscopy

The X-ray performance of the Jade APS (FI) and two OCI test device variants (7 µm shallow depletion and 11 µm deep depletion, both BI) was measured and is presented here. Results from a BI variant of the Jade APS is presented for comparison, courtesy of Prof. Sakao Taro, based at JAXA.

Front Illuminated Jade APS

Images were taken at room temperature (22 °C) under illumination by X-rays fluoresced from a manganese target by a hot cathode source. 6600 images were captured at 10 frames per second.

It was not possible to measure the X-ray response of the entire device due to unsuccessful removal of the glass cover. Figure 5.14. shows the extent of the damage to the cover of the device due to attempts to remove it. However, the glass absorbs all but $\approx 10^{-6}$ % of incident Mn-k_{α} X-rays (Henke *et al.*, 1993), providing shielding and allowing comparison of the illuminated and non-illuminated areas. The device itself remained functional and un-damaged.

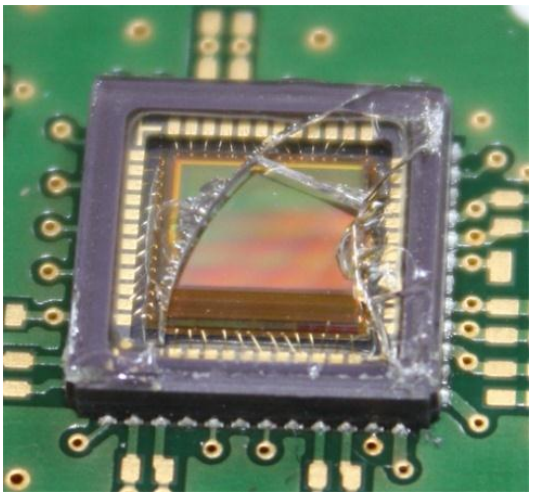

Figure 5.14. Photograph of the X-ray illuminated device, showing the resulting damage following attempted removal of the glass cover. This gives the same shape of X-ray illumination due to the glass being sufficiently thick to shield the device.

Figure 5.15. shows a portion of an image captured from the Jade APS under illumination by an ^{55}Fe source. Four incident X-rays are seen, each showing differing degrees of charge spreading.

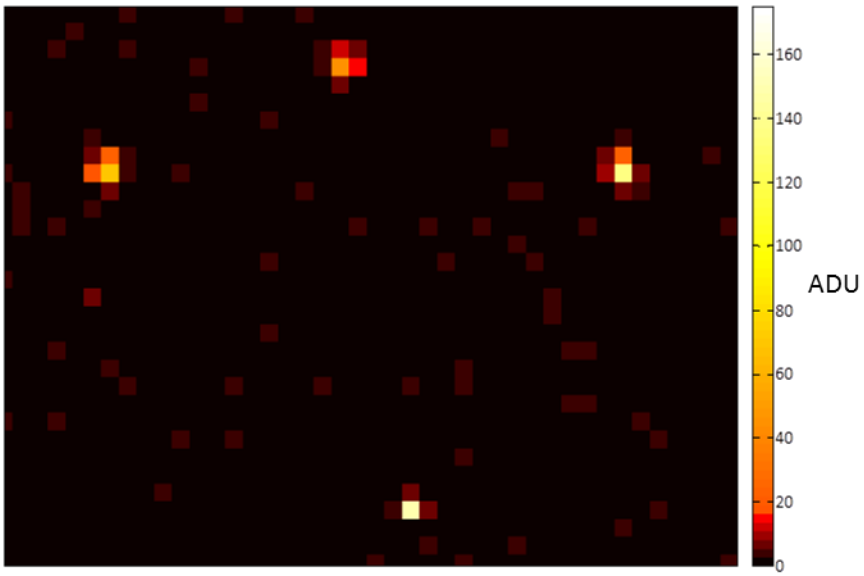

Figure 5.15. A portion of a contrast-stretched image showing four X-ray events in the Jade APS.

Figure 5.16. shows the whole-device spectrum for shielded and unshielded regions with the median value over all 6600 frames of each pixel subtracted to correct for non-X-ray dark signal and DC offset.

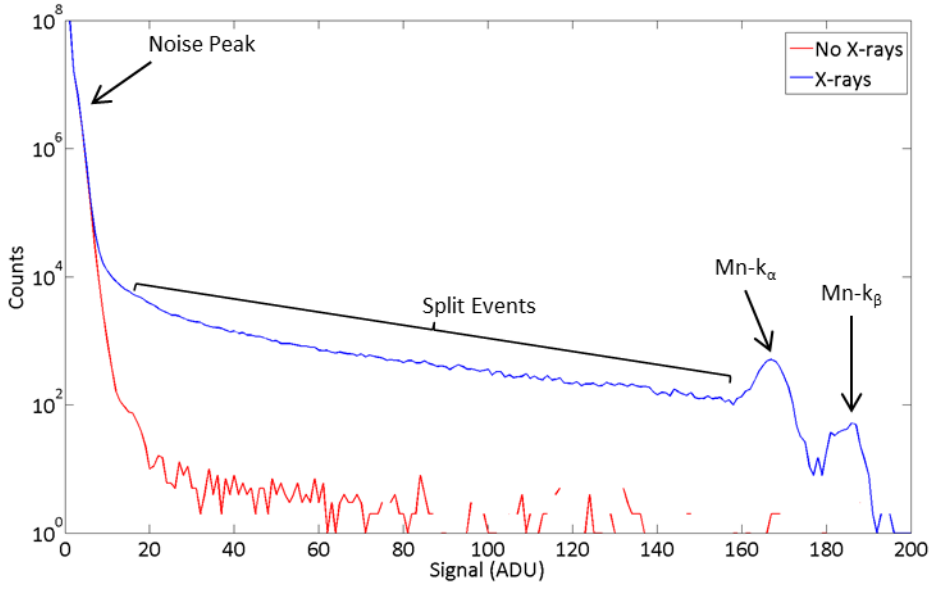

Figure 5.16. Graph showing logarithmic spectra for shielded region (red) and unshielded region (blue) in the Jade APS using ^{55}Fe X-rays.

It can be seen that very few X-rays are able to penetrate the glass cover. High signal pixels in the shielded region are likely to be due to noise rather than X-rays. The X-ray spectrum shows the characteristics of an unprocessed spectrum:

- Characteristic isolated event peaks relating to Mn-k_α and Mn-k_β X-rays at ~165 and ~185 ADU (measured with gain = 4);
- A long sloped section between the noise peak and these characteristic X-ray peaks composed of the various split event signal levels.

Figure 5.17. shows the resulting spectrum after event processing has been performed on each image. In this case the 'split event' spectrum only includes 3 × 3 events, as 5 × 5 events were either very rare, or too faint to be detected even at low (2σ) threshold.

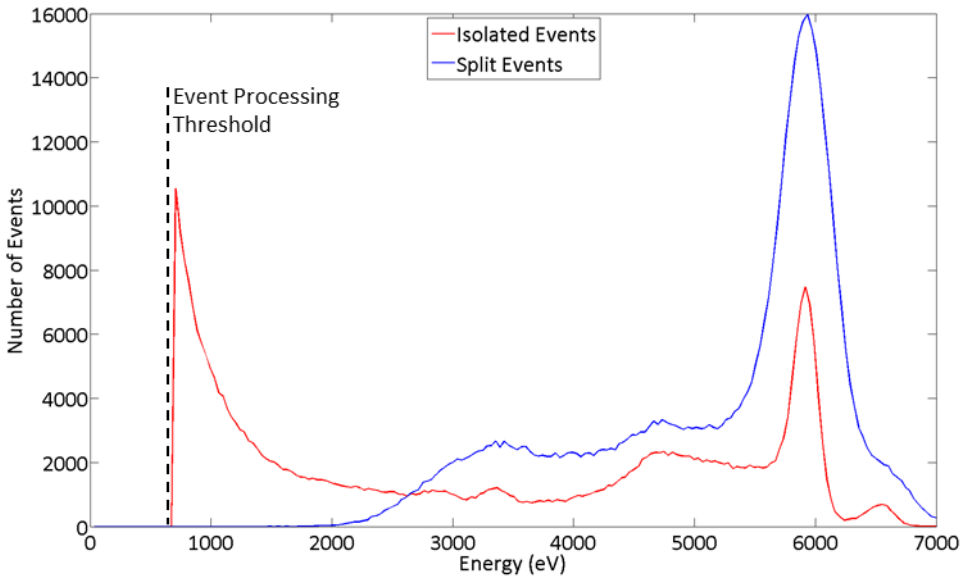

Figure 5.17. Graph showing linear event-processed spectra in the FI Jade APS, calibrated to the isolated Mn-k_α peak.

The Mn-k_α line is clear in both spectra, and the Mn-k_β line is clear in the isolated spectrum, but is distorted by the wide Mn-k_α peak in the split event spectrum. There are further features in the spectra below the peak, namely peaks at approximately 4700, 3300 and 2900 eV. These peaks do not coincide with any expected emission lines (for example Al-k lines or silicon escape peaks which are caused by silicon X-ray fluorescence within the detector). The peak at 4700 eV joined to the main response peak is in fact characteristic of sub-threshold charge loss and is an artefact of event processing algorithms and is commonly seen (Osborne *et al.*, 2005). By comparison with Figure 5.16. it is clear that the rise at low energies is not due to the noise peak; it has been seen to occur in CCDs and is

considered to originate from X-ray absorption in the gate insulator causing a partial loss of the detected signal charge (Katayama *et al.*, 2005).

Two important measures of the X-ray performance of the device can be determined from such a graph, namely the split event percentage, and the charge collection efficiency, which is of particular interest when using APSs due to the possibility of charge being lost to inactive areas of the pixel.

The split event percentage can be measured by the ratio of the volume of the Mn-k_α peak in both spectra, which is measured by fitting a Gaussian to the peaks. Using this technique around 22% of the events are determined to be isolated. This matches with the geometry of the device (~6 µm thick with a depleted layer of 1 to 2 µm).

Any charge collection inefficiency should manifest as a shift in energy of the peak of the split event spectrum compared to the isolated spectrum. Fitting Gaussian profiles to the peaks and determining the offset it is found that the shift is less than 1 ADU, making the charge loss (if any) less than 0.6 % at 5898 eV. This gives confidence that if an event is detected, the entire charge packet is likely to be collected and the energy of the event can be determined reliably with event processing.

Back Illuminated Jade APS

X-ray spectra measured with the BI Jade APS are provided courtesy of Prof. Sakao at JAXA. The event processing technique used was slightly different to that used for Jade FI and OCI measurements, with a high threshold used for detection of the bright central pixel, and a lower threshold used to characterise the presence of split events. This processing technique is not anticipated to alter the results drastically, apart from a higher detection percentage of larger split events due to looking for smaller charge fractions.

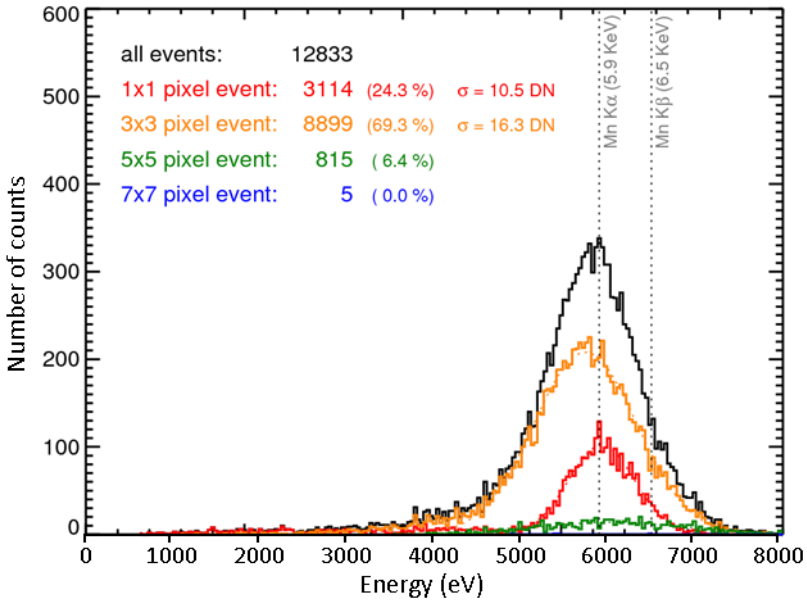

Figure 5.18. Graph showing event processed spectra in the BI Jade APS, calibrated to the isolated Mn-k_α peak.

Figure 5.18. shows the measured ^{55}Fe spectrum in terms of DN. The results are comparable to the FI Jade APS. This is due to the low absorption (~5% interaction probability in the entire device thickness) of X-rays at Mn-k_α wavelengths, meaning that X-ray events are distributed almost uniformly throughout the device thickness. BI devices show a more significant increase in performance at lower X-ray energies due to the X-ray photons not having to pass through the top-side which is covered with metal contacts, microlenses (which serve no purpose at X-ray wavelengths), and native oxide, which all absorb a significant fraction of lower energy photons.

Using the Mn-k_α peak for energy calibration, we can obtain measurements for the energy resolution (FWHM) of the isolated and 3 × 3 spectra of 384 and 597 eV respectively can be obtained. This can be compared directly to FWHMs measured on the FI device of 245 eV and 521 eV respectively, which are slightly worse, caused by more X-ray interactions occurring at the back side of the device.

Ocean Colour Imager

As introduced in Chapter 3, the OCI has a large number of on-device pixel variants. These are detailed in Figure 5.19., Table 5-1, and Table 5-2.

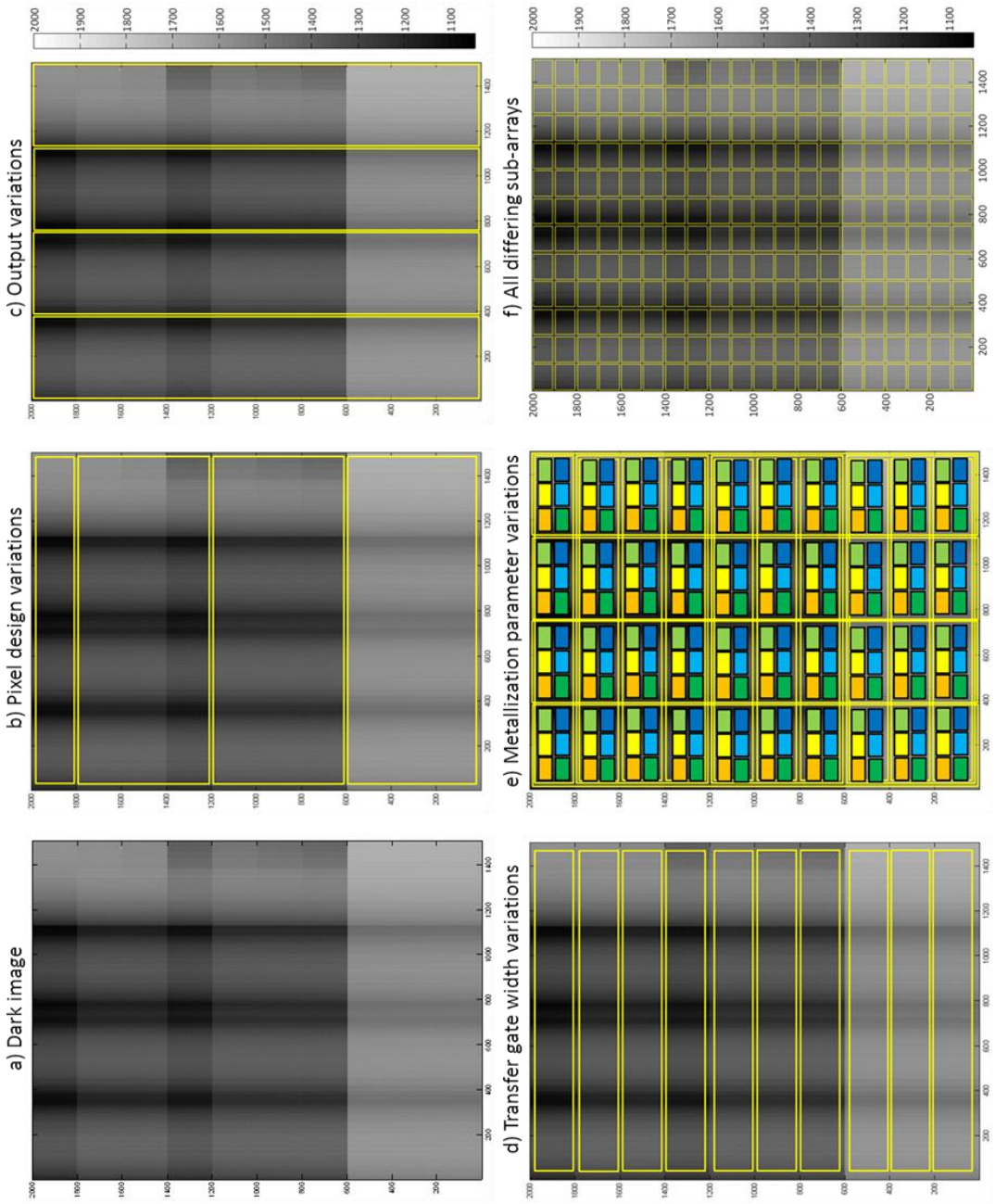

Figure 5.19: Figure showing differing pixel regions of the OCI, dark Image of the device is shown (a), then different design parameters are outlined in yellow: areas of different pixel design (b), areas of different output node (c), areas of different transfer gate width (d), areas of different metallisation parameter (e), and a map of each different pixel region (f).

Table 5-1 shows the parameters of the 4 output nodes present on the OCI test-devices outlined in Figure 5.19. c). Note that outputs 2 and 3 are identical.

Output No.	Type	Gain	Drive Characteristics
1	Transimpedence Amplifier	1	Up to 80 pF at 7.7 Mpix.s^{-1} over $V_{sat}/2$
2	Differential Op-Amp	1	Up to 8 pF at 7.7 Mpix.s^{-1} over $V_{sat}/2$
3	Differential Op-Amp	1	Up to 8 pF at 7.7 Mpix.s^{-1} over $V_{sat}/2$
4	N-channel Source Follower	0.75	Up to 8 pF at 7.7 Mpix.s^{-1} over $V_{sat}/2$

Table 5-1. Details of differences in output node as outlined in Figure 5.19. c) (outputs 1 to 4 are highlighted left to right).

Table 5-2 shows the pixel design for each sub-array row of different pixel type, summarising the differences in the regions shown in yellow in Figure 5.19. b) and d). Pix2-4, pix5-7 and pix8-10 have the same pixel design, but differ in transfer gate width.

Pixel Name	Cell Description	SF Size (µm)	Select Size (µm)	Transfer Gate Width (µm)	Extra Capacitance
pix1	Manufacturer Design	-	-	-	Yes
pix2	e2v U-shaped PD	0.70×0.60	0.70×0.43	1.9	No
pix3	e2v U-shaped PD	0.70×0.60	0.70×0.43	2.2	No
pix4	e2v U-shaped PD	0.70×0.60	0.70×0.43	2.5	No
pix5	e2v U-shaped PD	1.59×0.60	1.59×0.43	1.9	No
pix6	e2v U-shaped PD	1.59×0.60	1.59×0.43	2.2	No
pix7	e2v U-shaped PD	1.59×0.60	1.59×0.43	2.5	No
pix8	e2v Rectangular PD	1.59×0.60	1.59×0.43	1.9	Yes
pix9	e2v Rectangular PD	1.59×0.60	1.59×0.43	2.2	Yes
pix10	e2v Rectangular PD	1.59×0.60	1.59×0.43	2.5	Yes

Table 5-2. Table of the different rows of pixel designs, detailing the pixel design and transfer gate widths outlined in Figure 5.19. b) and d). Missing values in the pix1 row are withheld by the device manufacturer.

The OCI test-devices used in this work are of the 4T BI variant, with varying device thickness and resistivity.

The OCI presents a challenge for measuring X-ray spectroscopic performance due to its many pixel variants. Each of these variants must be treated separately, and this, combined with a relatively low activity ^{55}Fe source, the small window of time the device is available for experimental work, and the desire to characterise more than one device led to a reduction in the number of X-rays captured in each area. In order to increase the available statistics, the different metallisation options on the device were assumed to operate the same, an assumption backed up by e2v's own analysis of the optical performance of the

device (Pike & Kendall, 2011). This leaves 40 differing pixel design regions that were analysed separately over 2 devices.

The experimental setup was essentially the same as that in Figure 5.12. except that the device was mounted in a nitrogen purged dark chamber rather than a vacuum chamber. The nitrogen purge enables the device to be cooled without condensation forming on the device, however, during the experiments presented here, sufficient thermal coupling was not achieved and the device remained at room temperature.

The two devices analysed were both 4T BI OCI test devices as described in Chapter 3. Device '6-9' is a 'thin' 7 µm epitaxial layer (epi.) device fabricated with low resistivity (30 Ω.cm) substrate, resulting in a 1-2 µm depletion depth, very similar to the Jade. Device '12-51' is a 'thick' device with a 11 µm thick epi. fabricated with high resistivity (1-2 kΩ.cm) substrate, resulting in a deeper 9 µm depletion depth.

Three representative pixel designs were chosen to simplify analysis, as the differences in performance with differing source follower, select and transfer gate size were minimal. The outputs were seen to perform similarly except output 4 which had sufficiently higher readout noise. The pixels chosen were pix1, pix4 and pix8, as they gave the best performance of the different pixel designs. The design parameters of these pixel variants are shown in Table 5-3. Of these designs, pix1 was predicted to have best performance by virtue of its high MTF, as shown in Figure 5.20. From this we can also compare the measured MTF of each pixel design to the theoretical MTF possible in a sensor with a 8 µm or 9 µm depletion depth, this implies that the depletion depth is at least 8 µm.

Pixel Name	Cell Description	SF size (µm)	Select size (µm)	Transfer Gate width (µm)	Extra capacitance
pix1	Manufacturer Design	-	-	-	Yes
pix4	e2v U-shaped PD	0.70×0.60	0.70×0.43	2.5	No
pix8	e2v Rectangular PD	1.59×0.60	1.59×0.43	1.9	Yes

Table 5-3. Table of design parameters of the best performing OCI pixel regions. Missing values are withheld by the device manufacturer.

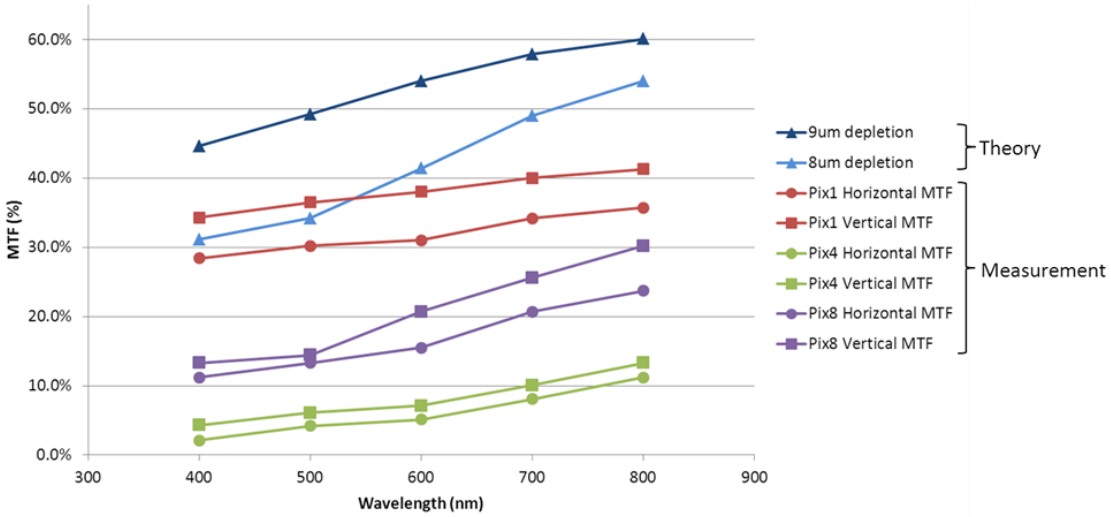

Figure 5.20. Graph showing MTF for device 12-31 (same fabrication as device 12-51, the 11 µm epi. device). Theoretical MTF measurements assume 8 µm and 9 µm depletion, and measured MTF is shown for pix1, pix4 and pix8.

Figure 5.21. shows the effect of changing the event processing threshold for three representative pixel designs. It is clear that some pixel designs present good results with a low event processing threshold (as seen in Pix8 with 2σ threshold), but some require a higher processing threshold to show a clear isolated spectrum (Pix1 with a 9σ threshold). Pix4 may need an even higher processing threshold to realise good isolated spectral performance, however as 9σ is already far outside of the dark signal distribution, it is not clear what physical significance moving the threshold further outside of the noise peak would have. The shift between the isolated and raw spectra is due to the altered event processing technique, described below.

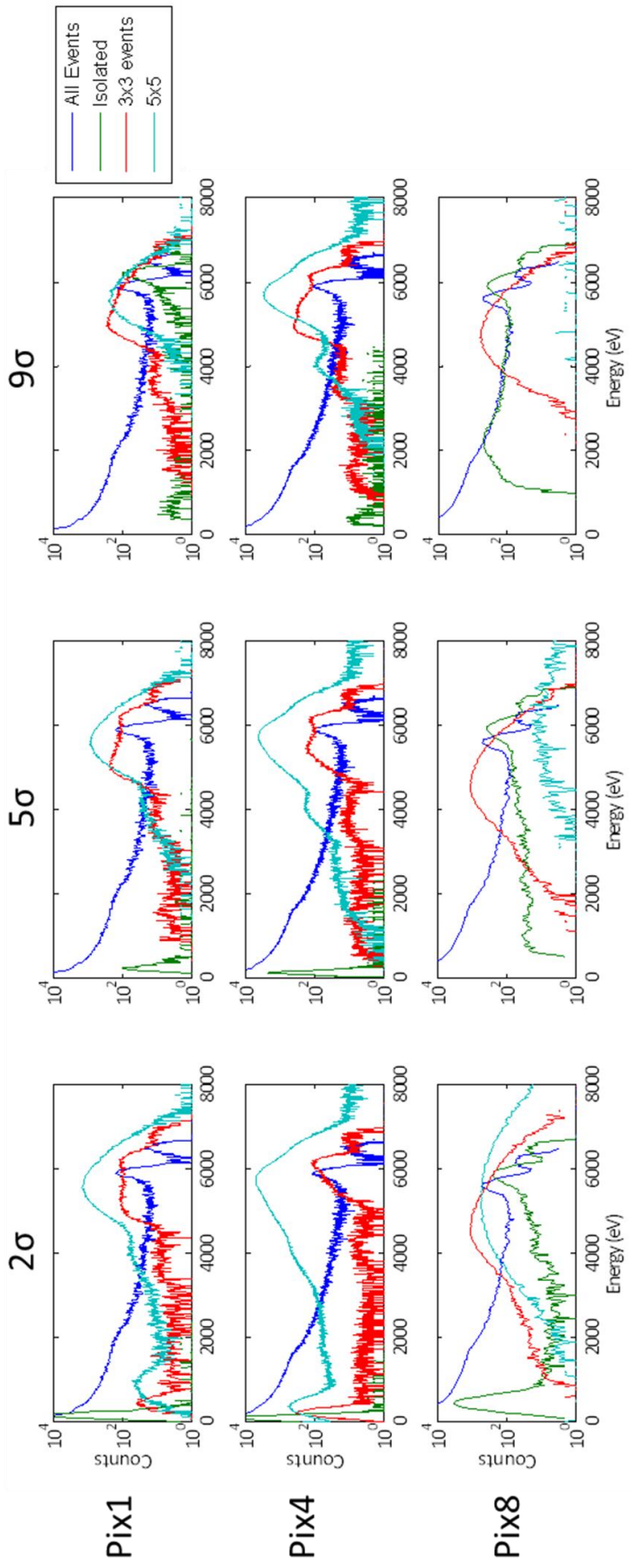

Figure 5.21.Graphs showing part of a threshold study for event processing on the 7 µm epi. device.

Figure 5.22. shows the altered event processing technique used during OCI analysis. This was required due to an observation that most isolated events were accompanied by a small amount of charge in an adjacent pixel in the readout direction, as shown in Figure 5.23.

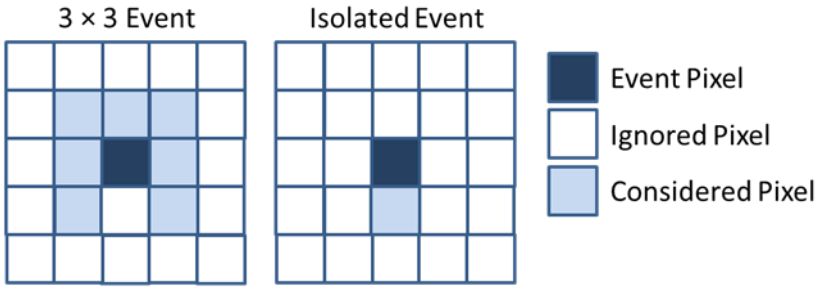

Figure 5.22. Diagram of 'altered' event processing characterisation.

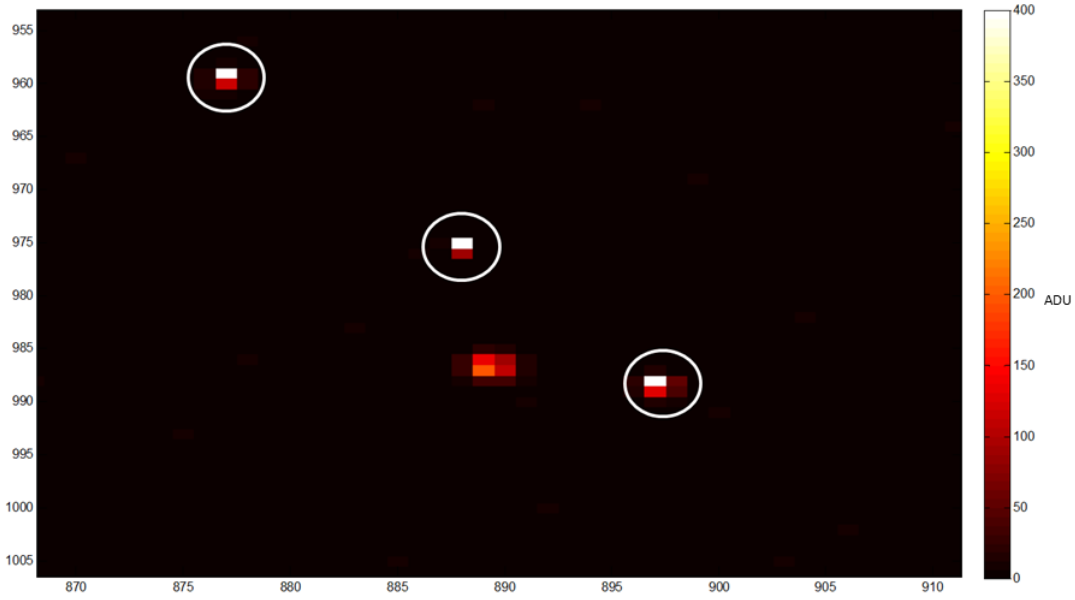

Figure 5.23. Image of X-rays incident on the OCI, showing preferential charge spreading in the vertical direction.

This is suspected to be either charge leakage, deferred charge or electrical crosstalk. It was proposed to use the altered processing technique to present a 'worst possible' performance, which can then be re-analysed if further experiments show the cause of the additional charge. The altered processing technique assumes the additional charge is useful signal from the X-ray event. It results in a lower and wider isolated peak due to the associated extra noise with summing the extra pixel. Conversely the 3 × 3 peak is higher and narrower.

Figure 5.24. and Figure 5.25. highlight the differences between the 11 µm and 7 µm epi. device variants. Figure 5.24. shows spectra for pixel design 1 in both devices. It is clear that the 7 µm epi. device demonstrates a far more recognisable isolated spectrum with a FWHM of 217 eV. Both spectra show some peak-shift from the isolated spectra to the 3 × 3 and 5 × 5 spectra, indicating some degree of charge loss, however the peaks are not well enough defined for the amount to be quantified, and in some cases the 5 × 5 peak is higher in energy than the 3 × 3 peak. It should be noted that Pix1 is an anomaly in the sense that the 11 µm epi. device shows very poor X-ray performance compared to the 7 µm epi. device. In other pixel designs the performance is far more comparable. This may be a device-specific defect and testing of further devices would identify the cause.

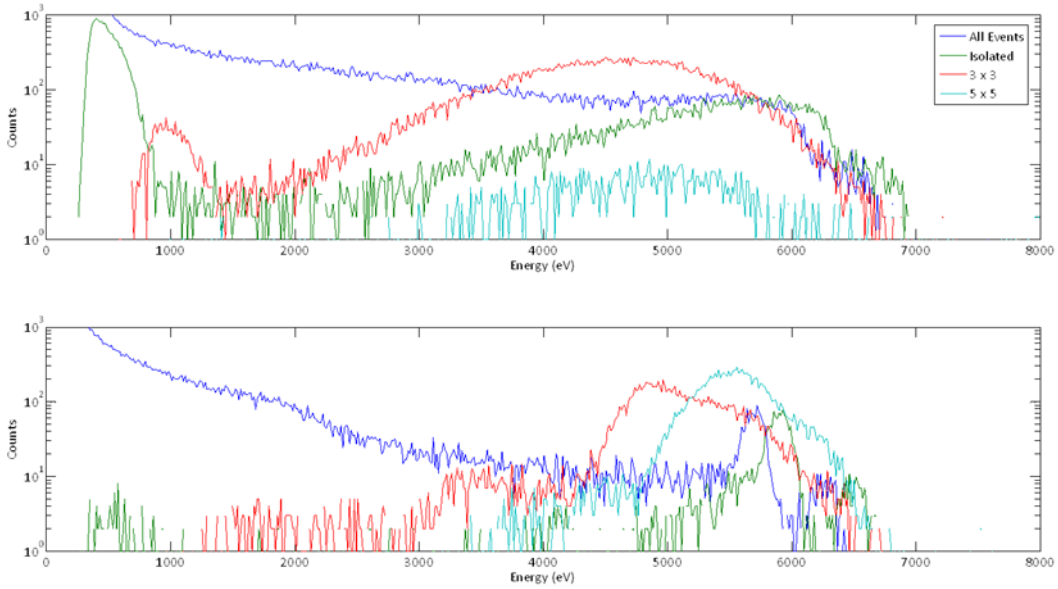

Figure 5.24. Comparison of Pix1 11 µm (top) and 7 µm (bottom) spectra processed with 9σ threshold.

Figure 5.25. shows 7 µm and 11 µm epi. device spectra (5σ) for pixel designs 4 and 8. In the case of pixel design 4, there are no detected isolated X-ray events. The 3 × 3 event spectra are better resolved in the 7 µm epi. device. Likewise, for pixel design 8, the tightest isolated peak is on the 7 µm epi. device with a FWHM of 206 eV, compared to a FWHM of 218 eV measured on the 11 µm epi. device. However, secondary features such as the escape peak are resolved in the 11 µm epi. device but are not present in the 7 µm epi. device. Again, the

3 × 3 and 5 × 5 spectra suggest a certain degree of charge loss, but the peak positions vary making the loss difficult to quantify.

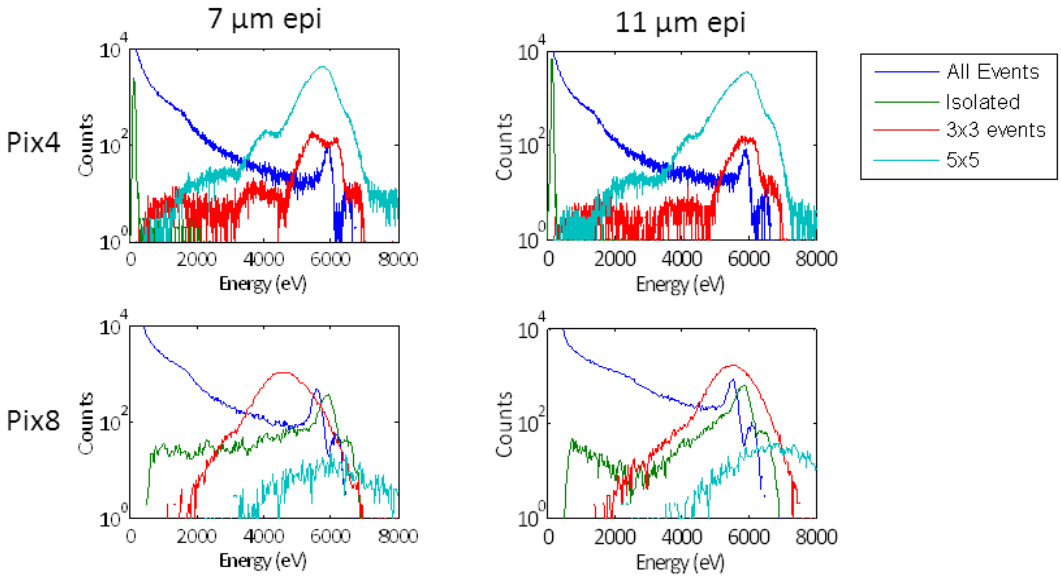

Figure 5.25. Comparison of spectra obtained from 7 µm and 11 µm epi. devices processed with 5σ threshold.

Figure 5.26. shows a logarithmic plot of Jade FI and OCI 11 µm epi. Pix8 detected X-ray spectra, with isolated peak height normalised. It can be seen that in terms of the principal Mn-k_α and Mn-k_β peaks, the devices operate virtually identically in terms of peak height and width. Where the devices differ in performance is in split events and the isolated spectrum below the principal peaks.

Comparing the isolated and split event peaks for each device, it is clear that the Jade has a lower split event fraction (~81% compared to 94% for the OCI). Unlike the Jade split event peak, the OCI split event peaks are significantly shifted from the location of the isolated peak. While this would normally be associated with charge loss to dead areas of the pixels, the 5 × 5 peak is in fact shifted higher than the isolated peak which is inconsistent with this explanation. The increase in number of split events is likely due to the increased thickness of the device.

The quality of the isolated spectrum obtained is significantly better in the OCI device. Looking at the isolated spectrum below the Mn-K_α peak shows a much lower background level (commonly measured at 1 keV), making the peak to background ratio approximately 50 times better in the OCI. Part of this effect may be due to an ^{55}Fe source being used as opposed to a tungsten source with a manganese target that was used for the Jade tests, including the bremsstrahlung spectrum. However, the OCI is expected to show a positive effect in the suppression of this tail due to the increased resistivity. Many less prominent spectral features are present in the OCI, for example the silicon fluorescence peak at 1740 eV and the silicon escape peak at 4158 eV. The Jade isolated spectrum, in contrast shows an oddly shaped peak at ~4500 eV, which is commonly associated with sub-threshold charge-loss. Table 5-4 details the measured peak heights, widths, and event fractions for the FI and BI Jade and OCI.

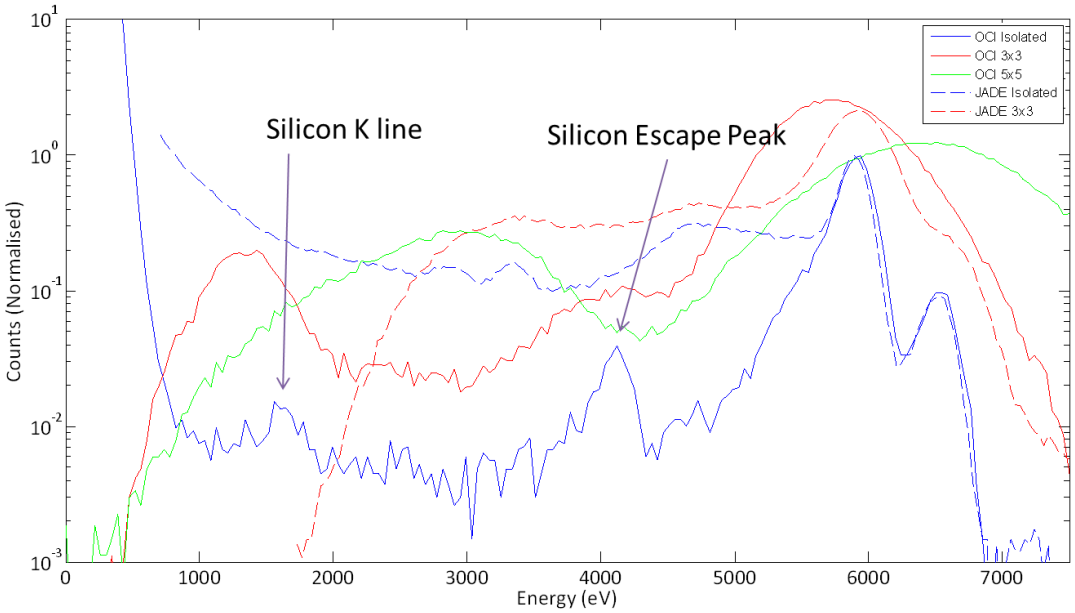

Figure 5.26. Graph of event processed X-ray spectra for Jade and OCI, normalised to Jade isolated peak.

Device	Event	Peak Location (eV)	FWHM (eV)	Normalised Split Event Ratio	Split Event Percentage
Jade FI	Isolated	5898	245	1.0	19 %
	3 × 3	5932	521	4.4	81 %
	5 × 5	-	-	-	
Jade BI	Isolated	5898	384	-	24 %
	3 × 3	5788	597	-	69 %
	5 × 5	-	-	-	7 %
OCI BI 11 µm epi.	Isolated	5898	274	1.1	6 %
	3 × 3	5746	961	9.4	54 %
	5 × 5	6394	1555	7.0	40 %

Table 5-4: Measurements of peak position and width from Figure 5.26.

5.3.4 Responsivity Map

The responsivity of a device is the conversion ratio of integrated electron charge into an output, such as voltage or digital units. In the case of a single photodiode, one can measure the responsivity of the device by measuring the output when the diode is illuminated with photons of a known energy, and spacing measurements frequently enough such that only a single photon is sampled at a time, *i.e*. photon-counting is achieved.

It is possible to extend this technique to an array of photodiodes such as an APS, which allows measurement of a 'map' of responsivity variation across the array, given sufficient time to build up enough photons hitting each pixel. This technique can be used to categorise CCDs also, but the output is less useful as CCD pixels share readout circuitry, leading to little inter-pixel variation. The large variation in responsivity over the pixel array in APSs makes the measurement of individual pixel responsivity a useful calibration tool.

When extending the technique to an APS, especially a device with small pixels and a small depletion depth, the majority of events are split over several pixels. As event processing introduces further error into measurement of the energy of events, the best results are obtained by ignoring split events and obtaining a histogram of isolated events. This requires a large number of X-ray photons to capture enough isolated events in each pixel.

Furthermore the X-ray flux must be low to avoid pileup, which is when more than one photon hits the same pixel within one integration period.

Figure 5.27. shows a spectrum for each pixel in a line segment of the device, showing the background peak, isolated Mn-k_α peak and the split X-ray events in between. For each pixel a Gaussian curve is fitted to the isolated X-ray peak and the number of isolated events and their mean value in ADU is acquired.

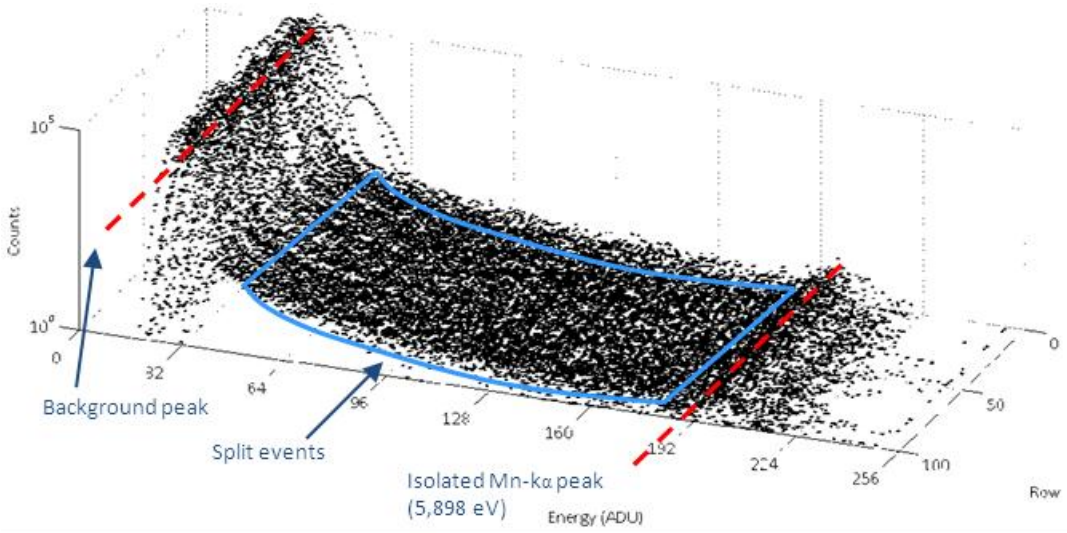

Figure 5.27. Sample spectra for a line section of pixels on the device. The dashed red lines indicate the noise and isolated X-ray peaks for each pixel, while the blue area is indicative of split events.

Figure 5.28. shows the resulting measurement of the responsivity map for a FI Jade APS. A threshold of 20 isolated events per pixel was applied to ensure that statistics were robust enough to determine a reliable measurement of the peak position. Figure 5.28. highlights the cross-device variation in responsivity. Figure 5.29. is a subsampled version of the same data shown in Figure 5.28. and shows the trends in the data more clearly. The shape of the data is due to the incomplete removal of the glass cover, as seen in Figure 5.14.

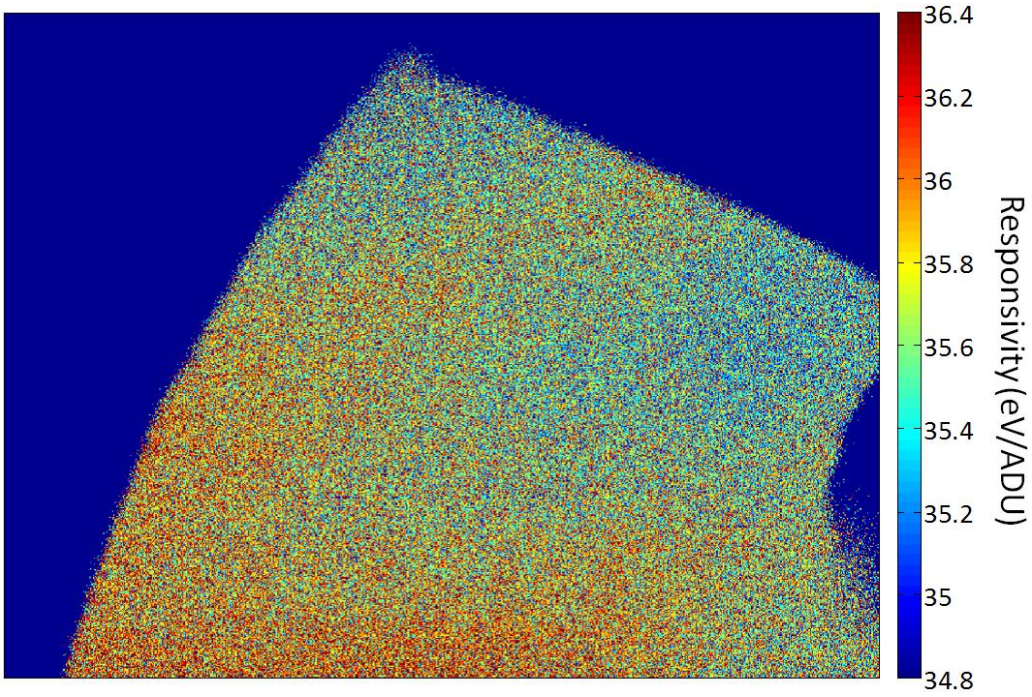

Figure 5.28. Measured responsivity map for front illuminated Jade APS.

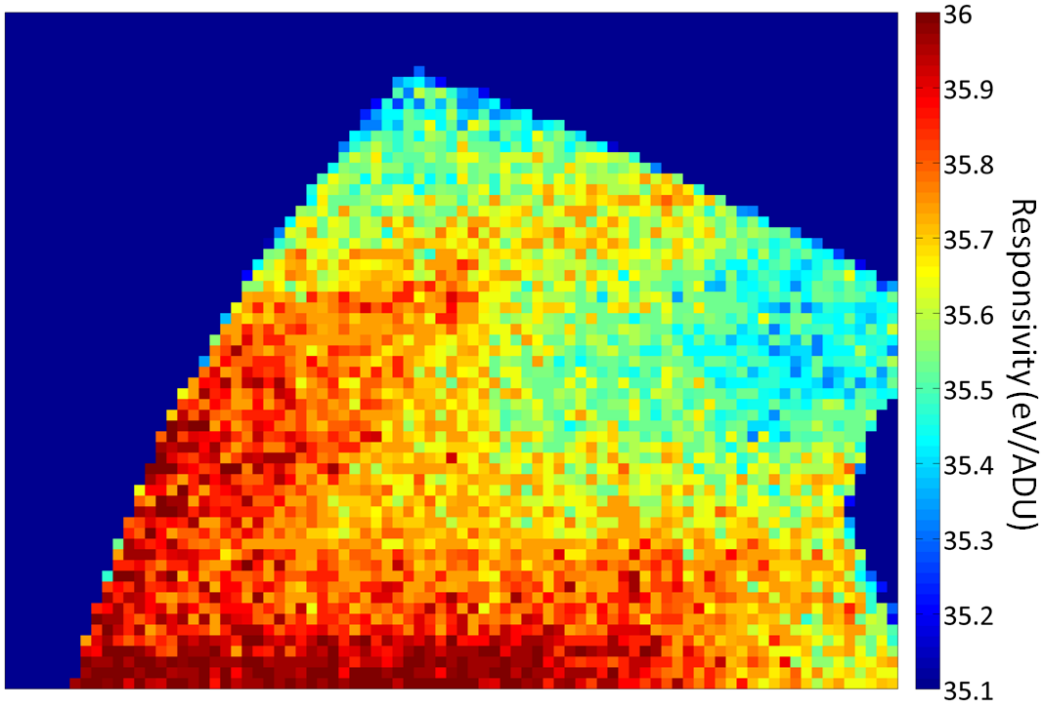

Figure 5.29. Subsampled responsivity map of front illuminated Jade APS.

It can be seen that the responsivity varies between 34.8 eV·ADU^{-1} and 36.4 eV·ADU^{-1}, equivalent to nearly 4.5% at Mn-k_{α}. Having characterised the responsivity variation across the device, it is now possible to use the measurements as additional corrections (on top of the background noise correction) to enhance spectroscopic performance. Figure 5.30. and

Figure 5.31. show the corrections to spectra that are possible using this characterisation technique. It can be seen in comparing the raw spectrum (blue) and event processed spectrum (black) to the responsivity non-uniformity corrected spectrum (red) that there is a 33% improvement in X-ray energy resolution over the event processed data.

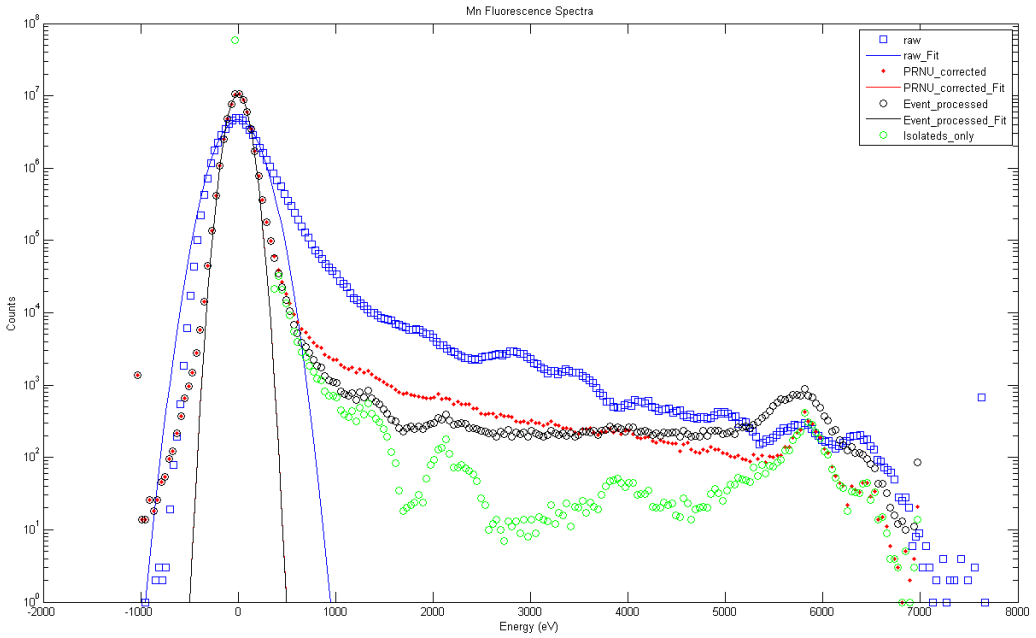

Figure 5.30. X-ray spectra obtained with a responsivity-characterised Jade APS. Different levels of applied corrections are shown: raw spectrum (blue), pixel responsivity non-uniformity corrected (red), event processed spectrum (black) and isolated only spectrum (green).

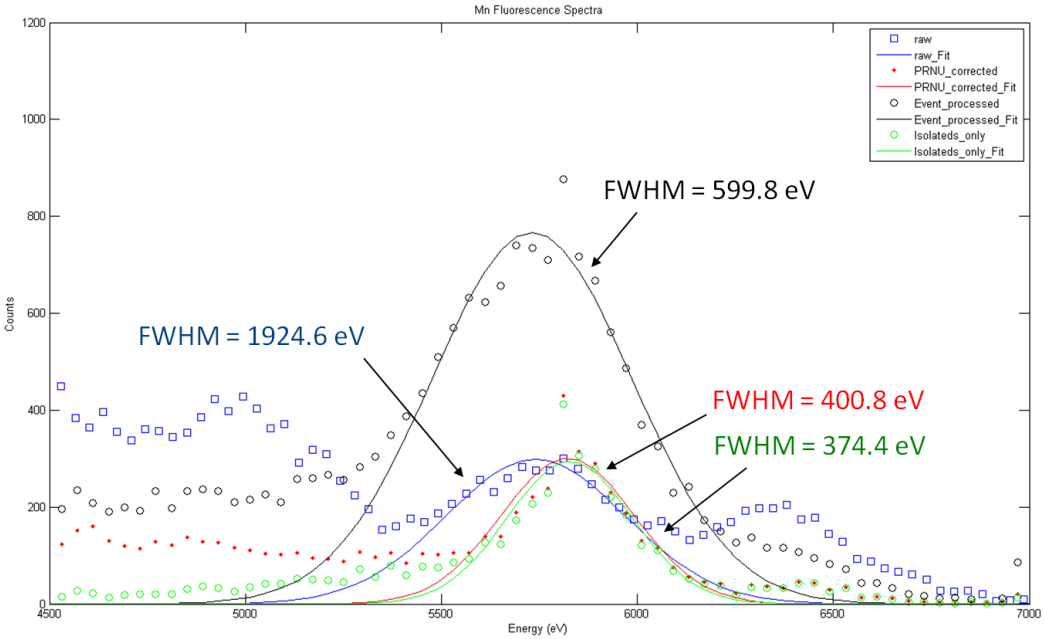

Figure 5.31. Scaled X-ray peaks from Figure 5.30.

5.4 Conclusions

In this chapter the techniques for measuring the baseline characteristics of a device such as noise, full well capacity and responsivity are discussed and performed on the Jade APS. Of particular interest is the X-ray detection performance in CMOS, especially for future missions such as Solar-C which requires a high speed sensor that can measure soft X-ray energies to a high resolution. With this in mind the X-ray spectroscopic performance of the Jade and OCI APSs have been measured and presented. While photon counting spectroscopy was achieved, it is clear that there are a number of areas for improvement. The most marked increase in performance observed when moving from the Jade to the OCI was a vastly improved peak:background ratio, allowing fainter components of the X-ray spectrum to be seen, such as the silicon escape peak. This trend could be extended further by increasing the depletion depth and thickness of future devices.

There are areas of further investigation and work that could be performed with regard to sensor evaluation for Solar-C. Specifically the OCI showed several unexplained phenomena in the results that require further investigation to understand fully:

- Pixel design 1 is measured to have the best MTF of all pixel variants in the 11 µm epi. devices (Figure 5.20), and the 7 µm epi. device showed good X-ray performance in pix1. Both of these results suggest that pix1 should give very good X-ray performance in the 11 µm epi. device. However, the 11 µm epi. device used for X-ray measurements showed very poor X-ray performance, leaving the question of whether the result is specific to the device measured, or if there is a further effect to be analysed.
- The preferential pixel cross-talk has now been shown to be due to leaving insufficient time to discharge the sense node, and so the results can be improved in future by slowing down the pixel readout rate to allow time for full discharge

during pixel reset. Currently the effect is hard to correct for as it increases the uncertainty of signal detected in affected pixels.

- In many cases the 5 × 5 spectra show a peak shifted to a higher energy than in the isolated or 3 × 3 spectra. This is unexpected as, if anything, the peak may shift to lower energies as charge could be lost to inactive areas of the pixel when the charge spreads to neighbouring pixels.

The OCI design specification shows promise for movement towards a bespoke APS for an X-ray spectroscopy imager.

Measurement of individual pixel responsivity was achieved using Mn-k_α X-rays and the resulting map used to improve spectroscopic performance of the device. While this technique had limitations due to the specifications of the device, particularly the 8 bit ADC resolution, the technique was shown to have potential for characterisation and performance improvement of devices designed for X-ray spectroscopy (*i.e.* deep depleted, thick devices with large pixels).

There is future opportunity to test Ruby, a larger, low noise variant of Jade which could suppress some of the background noise observed in the spectra obtained with Jade. Furthermore, work towards producing a high soft X-ray energy-resolution APS is ongoing and testing of future test-devices and designs will contribute significantly to understanding X-ray detection in APSs and how they differ from CCDs.

Chapter 6: Gamma Radiation Damage Characterisation

As described in Chapter 4, a major source of radiation induced traps is located at the Si-SiO_2 interface and caused by depassivation of the hydrogen-annealed surface. Normally, a buried channel is used in conjunction with the hydrogen passivation, which in CCDs is enough to isolate the collected charge from the surface, meaning that even if radiation induced surface states are liberated, charge promoted to the conduction band through these states is not collected as signal charge.

There is a further complication in APS fabrication that is somewhat of an unknown. Before fabrication of transistors, shallow trench isolation (STI) is laid down to electrically isolate the areas in which these transistors will be fabricated. This STI consists of small 'plugs' or channels of oxide material that are deep enough to isolate transistors from one another. The issue with regards to dark current is that these STI areas without careful radiation hard design, often extend down to the buried channel depth, and can present a surface-state filled 'surface' to the collected charge (Goiffon *et al.*, 2008, 2012). Due to this, passivation is required to achieve a low dark current, but as previously discussed, depassivation under gamma irradiation can cause this dark current to return (Johnston *et al.*, 2010*)*.

The other major damage phenomenon caused by gamma ray irradiation is flat-band voltage shift. Unfortunately, due to the nature of the integrated circuitry and pre-made demonstration readout board, investigation of these voltage shifts was not possible with the Jade device.

This chapter describes a series of experimental campaigns to measure the Jade APSs response to ionising radiation up to 0.25 Mrad(Si), specifically the increase in dark current with increasing dose. During these campaigns a relatively new phenomenon dubbed 'central brightening' was discovered, and investigation into the cause and appearance of this phenomenon was performed.

6.1 Experimental Procedure

All irradiations were carried out at either Harwell or ESA gamma cells. Both facilities use a ^{60}Co source to produce gamma rays through radioactive decay, the relevant reaction being:

$$^{60}_{27}Co \rightarrow ^{60}_{28}Ni + e^{-} + 2\gamma$$

Each decay produces two photons of energy 1.17 MeV and 1.33 MeV and the ejected electron is easily shielded. Due to the highly penetrating nature of gamma rays, the source is withdrawn into lead casing when not in use, and the 'cell' is generally made with lead-impregnated concrete. Masking the device to provide un-irradiated control regions is complicated by requiring a large thickness of lead to attenuate the signal (*e.g.* 5 cm of lead will attenuate 1.33 MeV gamma rays to about 10% of incident flux), and this can introduce shadowing effects due to misalignment of the shield and source. Furthermore, if shielding is used, secondaries, most commonly Compton electrons, are ejected from nearby surfaces, further complicating the received dose.

Dosimetry for gamma ray irradiations is difficult due to the high penetration and high rate of secondaries, so the inaccuracy of such dosimetry can be as high as 20%. Dosimetry accuracy can also vary based on the energy of the gamma ray being detected.

During the course of the irradiation campaigns, it was decided that an X-ray sensitive film could be used to determine the across-device variation in irradiation which could then be calibrated using the official dosimetry from the facility. The film used was GAFchromic® HD-810 dosimetry film, which changes colour (changes from transparent to blue) in response to radiation dose. For ^{60}Co gamma rays the blue-filtered change is linear with dose up to (and possibly beyond) 25 krad and independent of dose rate (International Speciality Products, 2008).

Figure 6.1. shows the resulting scan of the film after irradiation, showing non-uniform change of colour of the film. Annotated on the image are the device and imaging areas of the device.

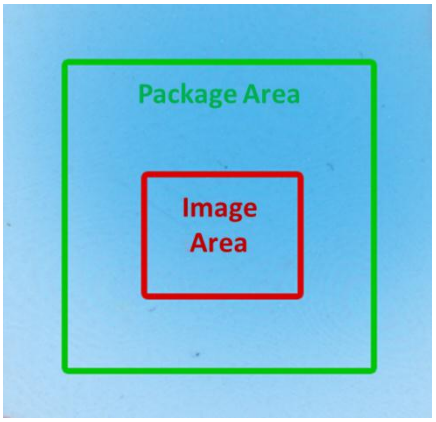

Figure 6.1. Image showing scanned area of the photometric film behind the device.

Figure 6.2. shows the irradiation dose map derived from the X-ray film after irradiation utilising a 5 cm thick lead brick to shield the readout electronics as shown in Figure 6.3. The image has been rotated to match images from the device shown in this work. The film was used during a short irradiation window, as it has only been calibrated for linear response up to 25 krad (International Speciality Products, 2008).

The dose received by the device was not uniform, but the variation across the device was within the errors of the dosimetry given by the facility. There is a clear trend for decreasing dose towards the top of the device, which is likely to be due to mis-alignment of the lead shielding with respect to the source. The result has been smoothed to reduce the appearance of Moiré effects that are due to thin-film interference during the digitisation of the film.

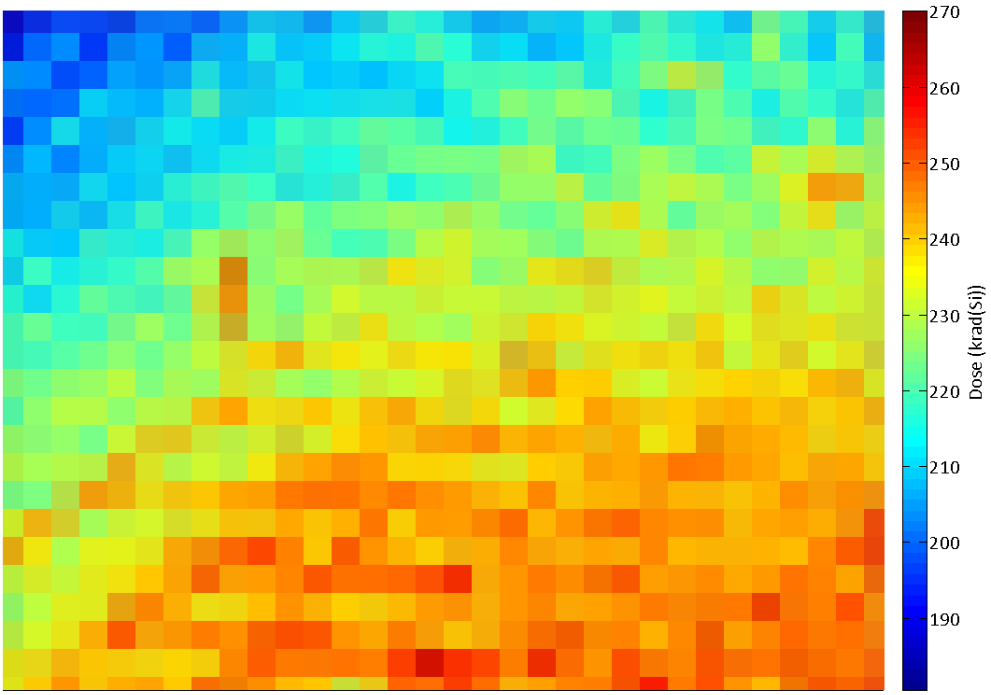

Figure 6.2. Oversampled device map of received gamma dose to the image area of the Jade device (i.e. red area in Figure 6.1., measured using X-ray sensitive film. Image has been rotated to match the readout of the device shown in images taken from the device in other figures.

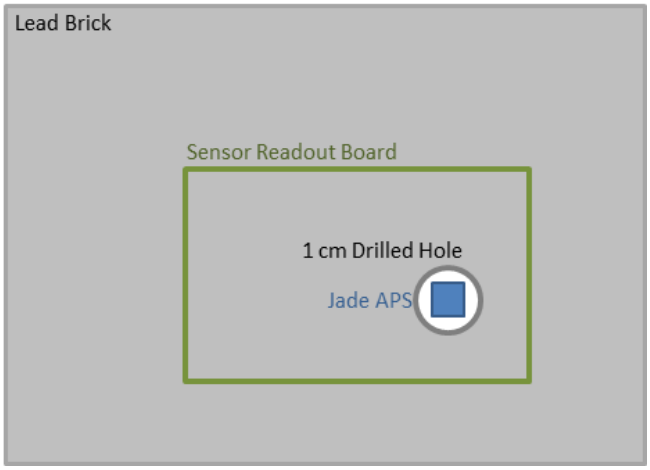

Figure 6.3. Positioning of Jade APS behind lead brick to shield readout electronics from irradiation.

6.2 Irradiation Results

For clarity this section is separated into four sub-sections, each containing experimental details and results from each of four gamma irradiations performed on Jade APSs.

6.2.1 Irradiation 1: FI Jade - Total Dose 450 krad(Si)

The first irradiation took place at the Harwell gamma cell based at Rutherford Appleton Laboratory (RAL). A single FI Jade device (S/N BW 206) was irradiated whilst on the readout board. The main half of the readout board was shielded with 10 mm of lead, reducing the received dose of these components by 40%, but leaving some components on the readout board close to the device unshielded. The device was irradiated to a total dose of 450 krad(Si) at a rate of 6 krad·hr^{-1}. The device was running throughout the irradiation. Figure 6.4. shows still frames obtained during device irradiation up to 80 krad(Si), at which time communication with the device was lost.

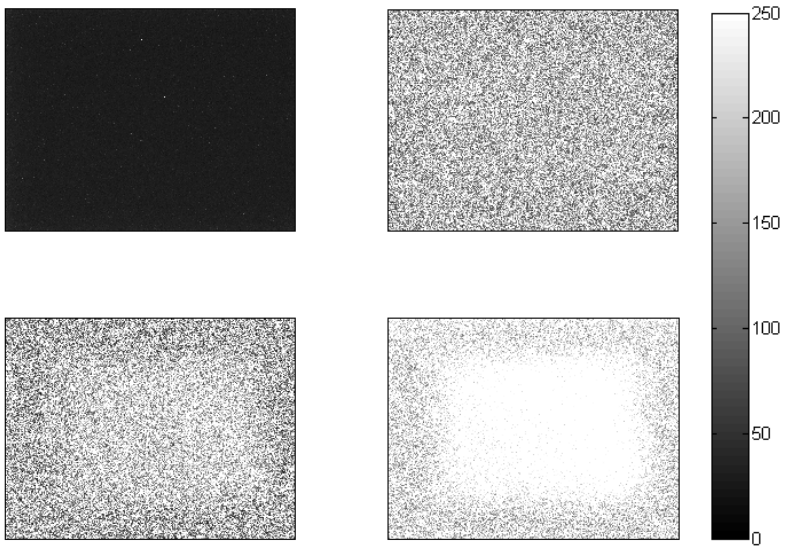

Figure 6.4. Still frames obtained during ^{60}Co irradiation of device BW 206 at 0 krad(Si) (no gamma flux), 0 krad(Si) (gamma flux incident), 30 krad(Si) (gamma flux incident), and 80 krad(Si) (gamma flux incident). (Top left, top right, bottom left, bottom right, respectively).

The gamma flux is apparent as a uniform noise across the whole sensor. As the irradiation progresses, it becomes apparent that the signal in the centre of the imaging area is increasing at a greater rate than that in the border of the imaging area. As the dose approaches 120 krad(Si), the device becomes completely saturated over the whole device. At 120 krad(Si), communication with the device was lost, either due to a failure of the device, or due to failure in the un-shielded area of the readout board. Further irradiation of the device was performed, but re-establishment of communications with the device were

unsuccessful after replacing the readout board, either because the device had been damaged sufficiently to be non-operational, or because efforts to replace the readout board were unsuccessful.

Figure 6.5. shows signal current increase measurements with gamma flux incident taken at intervals of 0.1 krad(Si) during the irradiation, and plotted as an average over the inner and outer areas of the device.

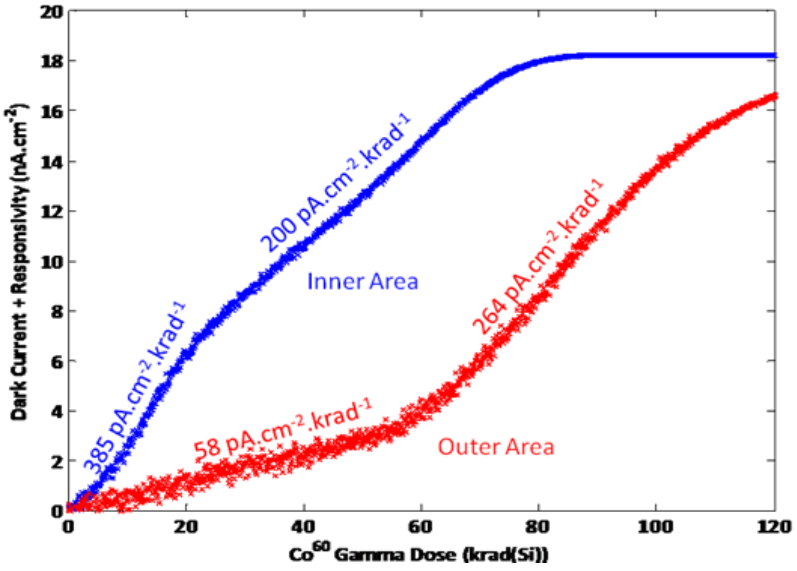

Figure 6.5. Measurements of the dark current for inner bright area, and outer area, during irradiation.

The inner area of the device shows a much higher increase in non-uniformity of the signal than the outer area, especially for the first 25 krad(Si). The outer area, in contrast, shows a high degree of radiation hardness up to 60 krad(Si), then begins to become damaged more quickly until device saturation. The device becomes fully saturated at around 80 krad(Si) in the inner area, hence the slope returning to 0 $A \cdot cm^{-2} \cdot krad(Si)^{-1}$ at that point. The growing non-uniformity in the signal observed in these images could be a result of three separate effects: a non-uniform increase in dark current, a non-uniform increase in responsivity, or a non-uniform increase in signal due to the irradiation of the unshielded area of the readout board. As the device is no longer responsive, it is difficult to decouple these separate effects, to determine which may be the more significant cause.

6.2.2 Irradiation 2: FI Jade - Total Dose 20 krad(Si)

A second irradiation was performed at Harwell on a second FI Jade device (S/N BW 204). This device had already received a proton dose of 5×10^9 10 MeV eq. p·cm^{-2} to the right hand side of the imaging array (described in Chapter 7). The readout board was shielded with ~10 mm of lead, reducing the received dose by 40%. The device was irradiated to a dose of 20 krad(Si) at a rate of 10 krad(Si)·hr^{-1}. The lower total dose was chosen to ensure that the device would be fully operational after irradiation so that the source of the dark current and dark current non-uniformity could be explored.

Figure 6.6. shows dark images obtained at room temperature from the device after 20 krad(Si) of gamma irradiation immediately after the irradiation was performed (left) and after a 6 month anneal at room temperature (right).

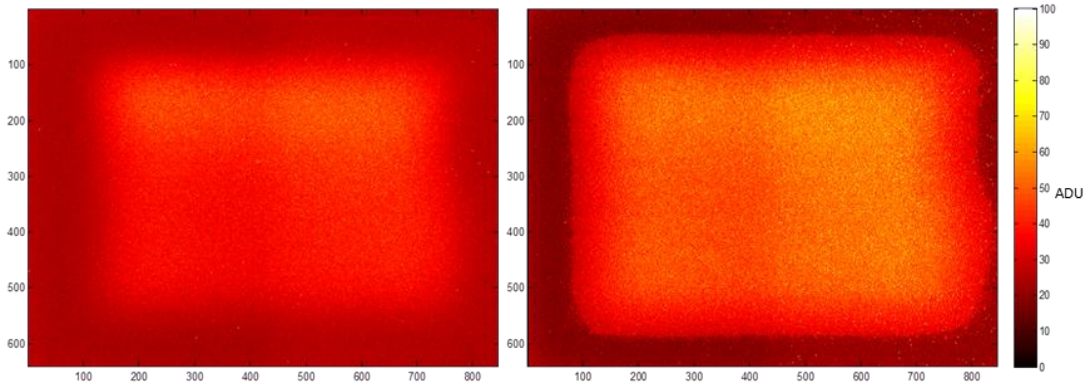

Figure 6.6. Dark image of device BW 204 showing dark current non-uniformity immediately after 20 krad(Si) of irradiation (left), and after a further 6 months of annealing at room temperature (right).

Figure 6.7. shows a comparison of the mean dark signal in each column before and after the 6 month anneal.

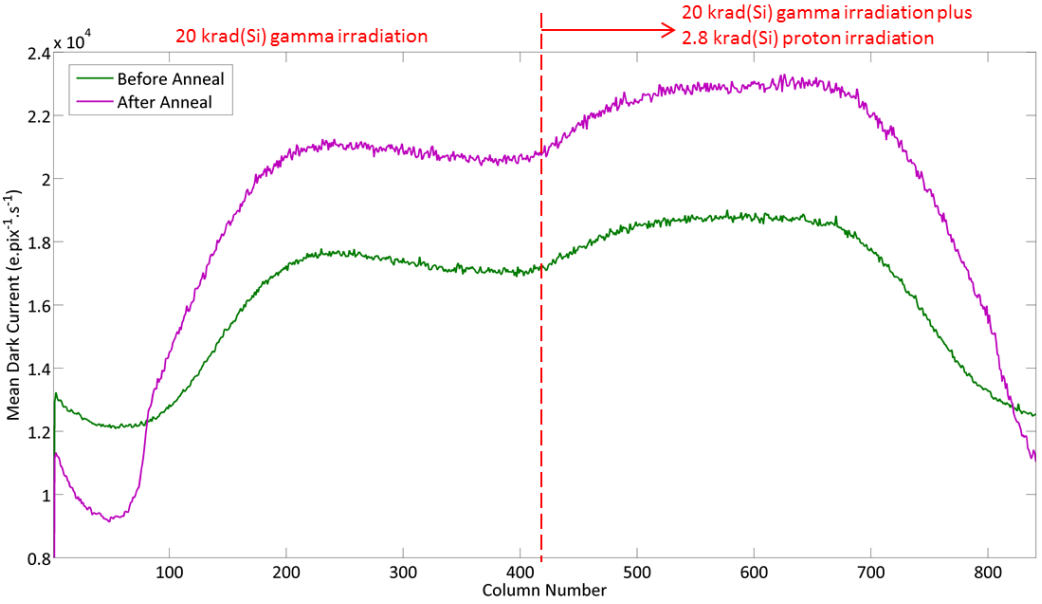

Figure 6.7. Mean dark current at room temperature down each column showing the change in profile immediately after irradiation, and after a 6 month anneal. The 'after anneal' image shows clearly sharper edge effects.

The dark images clearly show the same dark-current non-uniformity pattern to that shown in the previous irradiation to 120 krad(Si). Additionally, the right hand side of the image shows a slightly higher average dark current as well, as these pixels also show significantly higher dark current due to proton irradiation.

It can be seen that after anneal, the dark current pattern becomes much less diffuse. The outer areas of the imaging area show a higher reduction in dark current after anneal than the central region. Figure 6.8. shows the measured dark current against total received dose at pauses in the irradiation of device BW 204.

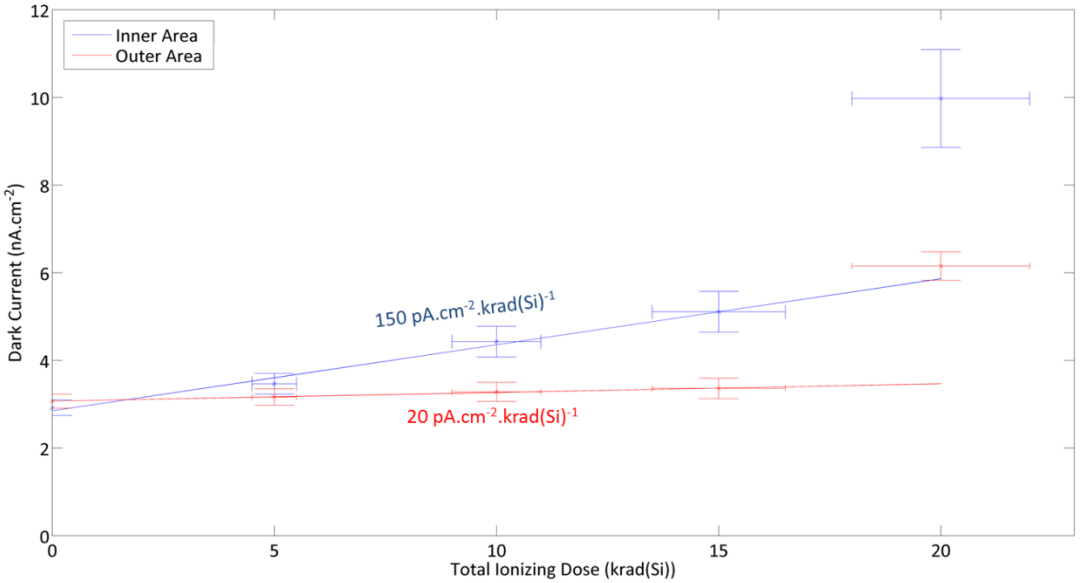

Figure 6.8. Plot showing average dark current with increasing radiation dose over the inner area (blue), and outer area (red).The lines are fitted to the linear portions of points to give a measure of low dose dark current increase per krad(Si).

It can be seen that much lower dark current figures are measured than were seen in Figure 6.5, which suggests that much of the increase in non-uniformity is due to an increase in either responsivity to the gamma radiation, or damage to the readout board. However it is also clear that the non-uniform increase in dark current is still a factor, as the inner area of the image area increases in dark current more quickly than the outer area (and shows a large jump of about 1 nA·cm^{-2}·krad(Si)$^{-1}$ between 15 and 20 krad(Si)). This plot also shows the radiation hardness of the Jade APS, with even the inner area showing only an increase in dark current of 150 pA·cm^{-2}·krad(Si)$^{-1}$. The outer area shows an even lower measurement of 20 pA·cm^{-2}·krad(Si)$^{-1}$. Both areas show an anomalously high increase in rate of dark current generation per krad(Si) after 15 krad(Si). This is likely to be the beginnings of the steady increase at low doses seen in Figure 6.5. These figures compare to similar measurements made in the literature on CCDs (2 nA·cm^{-2}·krad(Si)$^{-1}$ (Holmes-Seidle & Adams, 2002)), standard APSs (0.5-1.7 nA·cm^{-2}·krad(Si)$^{-1}$ (Bogearts *et al.*, 2003)), and radiation hardened APSs (2.4 pA·cm^{-2}·krad(Si)$^{-1}$ (Innocent, 2009), 1-2 pA·cm^{-2}·krad(Si)$^{-1}$ (Eid *et al.*, 2001), 1-2 pA·cm^{-2}·krad(Si)$^{-1}$ (Bogearts *et al.*, 2003)).

Figure 6.9. shows the behaviour of the device dark current with temperature.

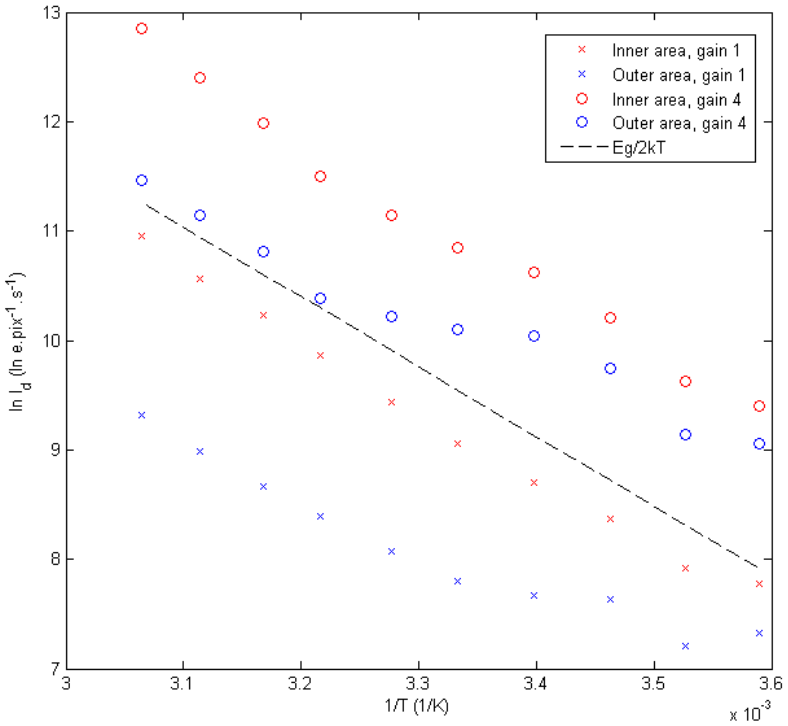

Figure 6.9. Behaviour of dark current, plotted as ln(I_{dark}) against 1/T for inner and outer areas (circle and cross markers) at gains of 1 and 4 (black and grey).

Figure 6.9. shows that, in both regions of the imaging area, the dark current follows the expected relationship for mid bandgap traps of:

$$I_{dark} \propto exp^{(\frac{E_g}{2kT})} \tag{6.1}$$

The data follows this line more closely at high temperatures where there is more signal. The outer area shows less adherence to the trend at lower temperatures – but this could be attributed to the very low signals at low temperatures in the more radiation hard area, thus increasing the fractional error. It does suggest that there may be a systematic effect; however it is not currently understood.

6.2.3 Irradiation 3: FI Jade - Total Dose 242 krad(Si)

A third irradiation of a FI Jade APS was performed at ESTEC to achieve a higher total dose with proper shielding of the device to ensure that if the device were to fail it would be due to device failure (*e.g.* due to flat-band voltage shift) rather than failure of the readout board. Furthermore, the irradiation was halted periodically to acquire dark images for later

analysis. The device was irradiated to 242 krad(Si) at a rate of 5.4 krad·hr^{-1}. The readout board was shielded from the device using a 50 mm lead brick with a hole drilled in the position of the sensor. Dosimetry film was used to calibrate received dose of the sensor and uniformity of dose across the sensor, as shown in Figure 6.2. While the device was still operational immediately after irradiation, the device became unresponsive under testing ~24 hours later, possibly due to settling of the damage effects.

Figure 6.10. shows dark current histogram measurements from dark images at different stages of the irradiation.

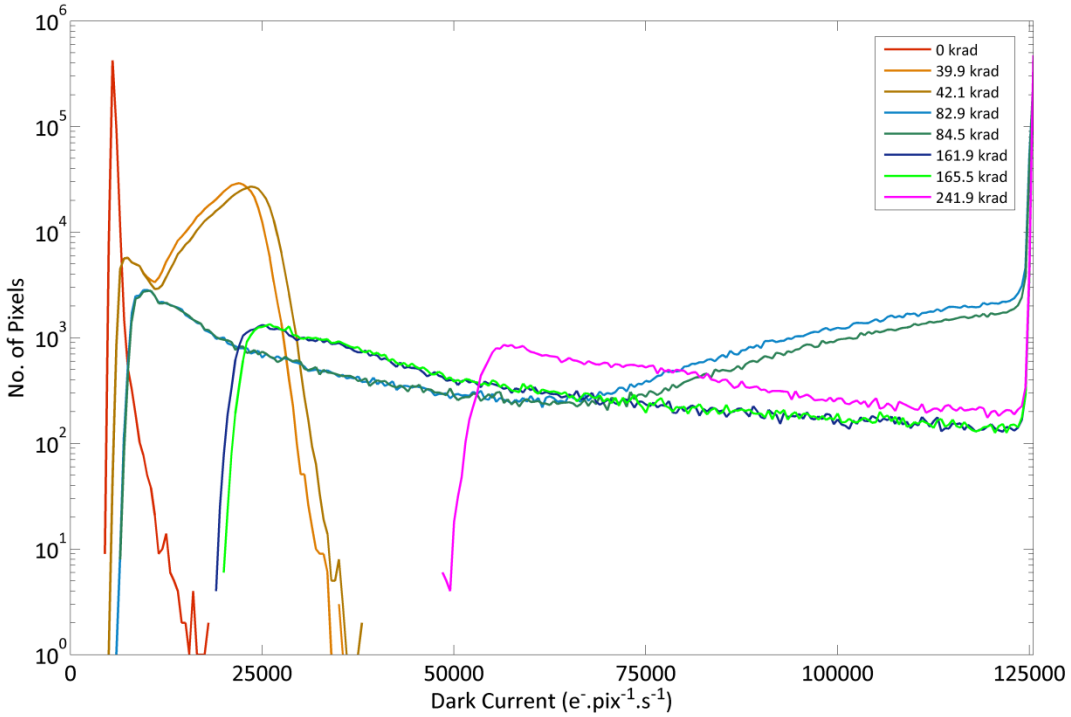

Figure 6.10. Dark current histograms at each of the irradiation levels analysed.

The unirradiated histogram is normal, showing a Gaussian noise peak followed by a short tail made up of higher dark current pixels. Looking at the next step in the irradiation, 40 krad(Si), and there is already obvious distortion in the histogram caused by the different response of the inner and outer areas. This trend continues as the dose increases, and some pixels within the central region begin to saturate (with the integration times used) at

83 krad(Si). As the irradiation progresses, more and more of the image area becomes saturated.

Figure 6.11. shows progression of the dark current in the inner and outer regions of the device as total received dose increases.

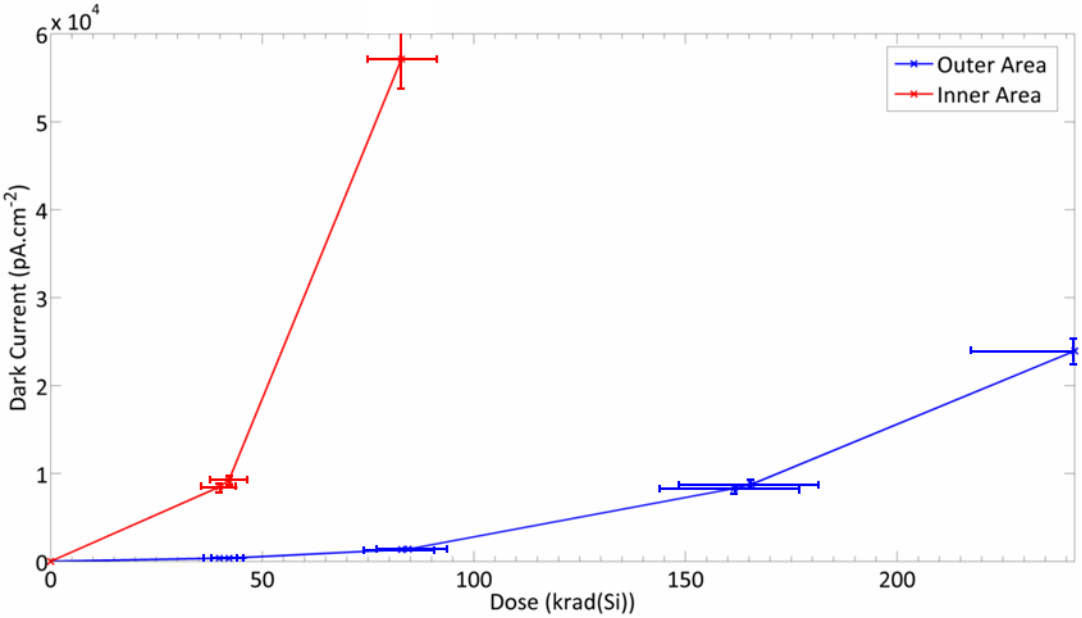

Figure 6.11. Graph showing dark current increase with total received gamma dose for inner (red) and outer (blue) areas of the image area. Measurements are joined by a line.

This shows a very similar result to the first irradiation shown in Figure 6.8., with a sharply increasing dark current in the inner area which quickly saturates, and a more slowly increasing dark current in the outer area. The outer area shows an increase in dark current of 92 $pA{\cdot}cm^{-2}{\cdot}krad(Si)^{-1}$ over the whole irradiation period, but for the first 80 krad(Si) it is lower at around 10 $pA{\cdot}cm^{-2}{\cdot}krad(Si)^{-1}$. The inner region shows a much higher increase of 828 $pA{\cdot}cm^{-2}{\cdot}krad(Si)^{-1}$ over the first 80 krad(Si), although the true figure is likely to be higher due to saturation of a proportion of the pixels.

6.2.4 Irradiation 4: BI Jade - Total Dose 32 krad(Si)

A further irradiation was performed by Eric Mueller, a Master's student at ESA, under guidance of the author. A BI variant was irradiated to reproduce the results obtained by Elliott (2010) showing no central brightening effect after irradiating a BI Jade to

200 krad(Si). Due to time constraints, the device was only irradiated to 32 krad(Si), as the central brightening effect is visible on FI Jade devices after only 20 krad(Si) (Figure 6.7).

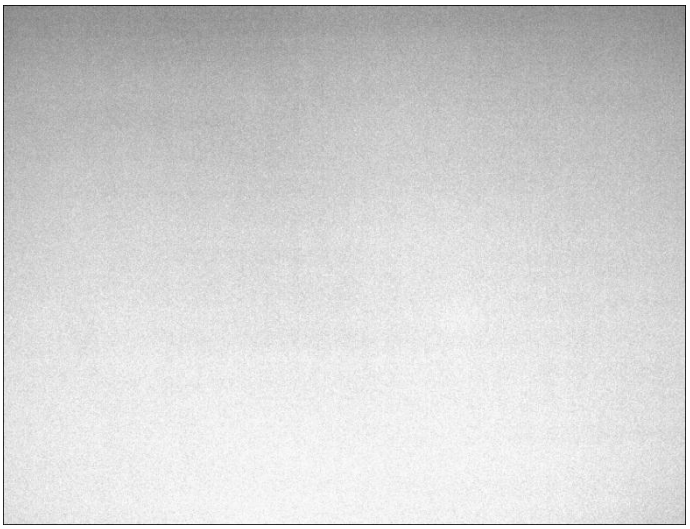

Figure 6.12. Dark image taken by BI Jade after 32 krad(Si) at 31°C.

This image shows no central brightening effect. The gradient from top to bottom is similar to that shown by Elliott (2010), where it is explained as a manifestation due to the rolling shutter operation of the device. However, in this case it is more likely to be due to non-uniformities in irradiation, as the device was operating in global shutter mode. The exact calibration of the device has not yet been performed, but it is clear that the central brightening phenomenon is not occurring in these BI Jade devices at these levels of irradiation.

6.2.5 Unirradiated Dark Current Pattern

An experiment was performed to investigate presence of the 'central brightening' pattern in an unirradiated device. Figure 6.13. shows a dark current image obtained from a FI Jade device at 80°C.

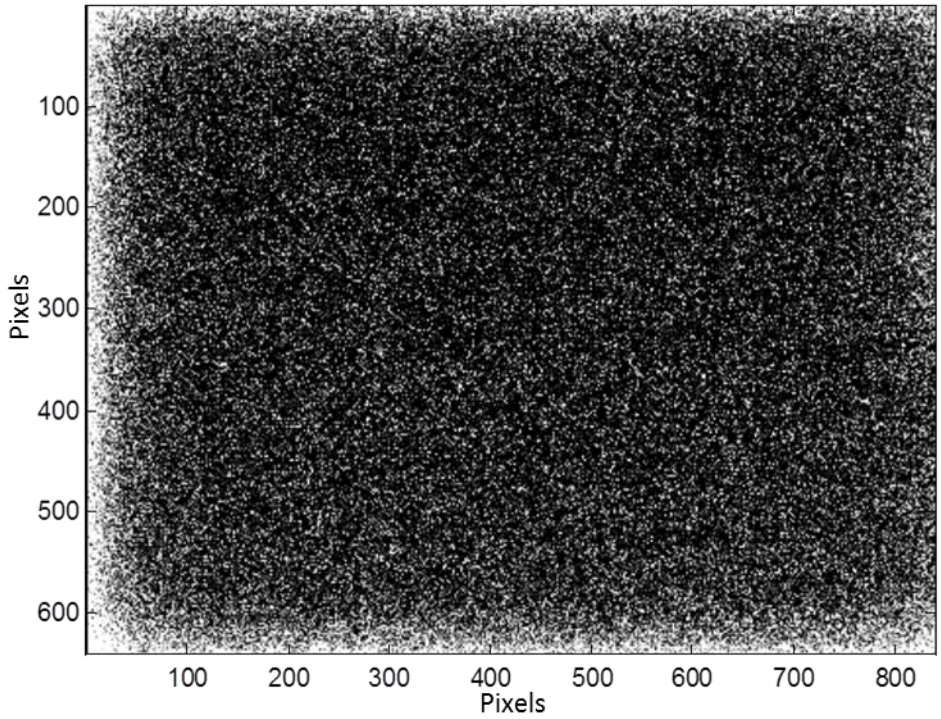

Figure 6.13. Dark image obtained from an un-irradiated Jade device at 80°C (Contrast adjusted).

The image clearly shows the same dark current pattern that is observed under gamma irradiation, but in this case the edges show a higher dark current while the centre shows reduced dark current. In particular, the effect shows more proximity to the right edge of the image area, also seen in the irradiated images (Figure 6.7). This suggests that the central brightening effect is due to an effect on-device, possibly caused by a fabrication technique. The effect proximity to the right hand edge corresponds to an area of extended metallisation seen on the device as seen in Figure 6.14. This metallisation may provide some alteration of the edge effect leading it to extend beyond the imaging area.

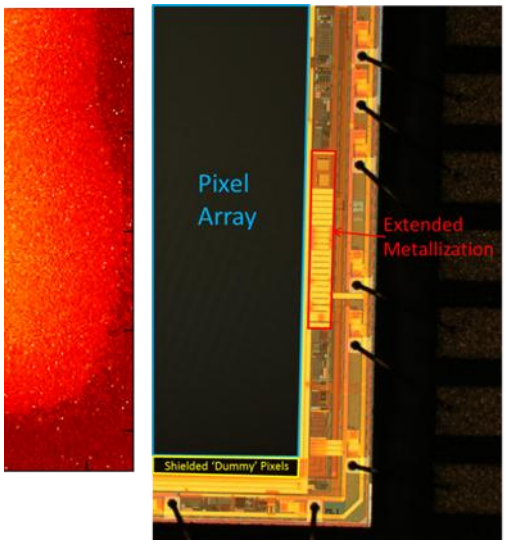

Figure 6.14. Device image showing corresponding part of the dark current central brightening after anneal (left). Microscope photograph of the right hand edge of the imaging area (right), showing extended metallisation that corresponds to artefacts seen in the central brightening pattern.

6.3 Microlens Browning

An interesting side-note is the damage that microlenses sustain under gamma irradiation, described in Chapter 2. To investigate the change, four devices without readout boards were irradiated with differing doses: 84, 165 and 329 krad respectively and one unirradiaed. This was achieved by sequentially shielding each device behind lead after the target dose was received.

The device colour was then analysed using a digital scanner to provide uniform illumination and consistent images of each device. As the devices are highly reflective and display thin-film interference, the colour is difficult to capture, introducing large errors into the measurement. Figure 6.15. shows the resulting colours of each sensor, with the average value of each image colour channel plotted vs. dose.

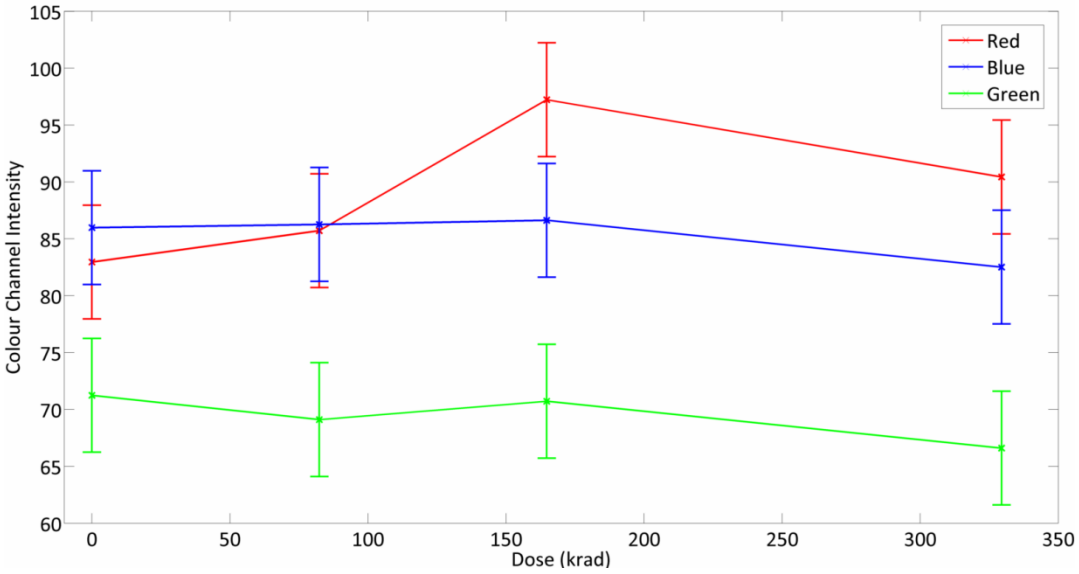

Figure 6.15. Measured alteration of device colour after irradiation of Jade APS.

The plot shows a clear increase in the average 'redness' of the device, while the 'blueness' and 'greenness' stay relatively stable, indicating a 'browning' of the device. This results in a lower red QE of the device, which could impact measurement of the light intensity of an object of interest if the change in QE is not calibrated and corrected. The increase in 'redness' of the device between unirradiated and 200+ krad(Si) is observed to be around 20%, indicating that some degree of the red response of the device will be lost.

6.4 Discussion

6.4.1 Dark Current Increase

The dark current increase observed following gamma irradiation of a Jade APS is measured to be between 20 and 800 $pA \cdot cm^{-2} \cdot krad^{-1}$ (depending on the image region being analysed and the total dose received). The lower end of this range is comparable to similar non radiation-hardened CCD technology, for example an e2v CCD57-10 operated in partially inverted mode showed an increase in dark current of 30 $pA \cdot cm^{-2} \cdot krad(Si)^{-1}$ (Hopkinson & Mohammadzadeh, 2003). However it is clear that the central brightening issue is a large obstacle to creating a APS of this design that is suitable for use in high gamma ray dose environments.

The dark current in both inner and outer areas follow an $e^{\frac{E_g}{2kT}}$ relationship, suggesting mid-bandgap traps, which are associated with the Si-SiO_2 interface states. Due to the pinned nature of the device, the surface should not affect the dark current of the device significantly, even when de-passivated. This points to STI implants that are added as part of foundry processing as a source of the dark current. Surface-states created in these regions may well be close enough to the photodiode to provide additional dark current when de-passivated. Exact details of the fabrication of STI areas in the device are unavailable due to the commercial sensitivity of foundry processes.

6.4.2 Central Brightening

The central brightening effect described in this chapter, clearly visible in Figure 6.4. and Figure 6.5., has rarely been observed and discussed in the literature. The only occurrences that this author is aware of were observed by Hopkinson *et al.* (2004) in the STAR-250 FI APS (Figure 6.16.) with no explanation given. A number of irradiations were performed under differing conditions to identify the cause of the central brightening. Table 6-1. summarises the irradiations performed on Jade APSs and the occurrence of central brightening in these tests. Also included are test conditions of an irradiation of the STAR-250 FI APS performed by Hopkinson *et al.* (2004).

This section outlines probable causes for the dark-current non-uniformity and the evidence for each. Table 6-1. shows that central brightening occurs in FI devices and was not seen in BI devices, suggesting that hydrogen depassivation or µlens degradation are the most likely causes. It should be noted that in some cases assumptions have to be made about the exact techniques used to fabricate the devices, as the foundry incorporates a number of protected techniques of which the details are generally unavailable, making investigation into the cause of the central brightening pattern more difficult. Further work is needed,

with less integrated hardware, to better isolate the cause of the central brightening phenomenon.

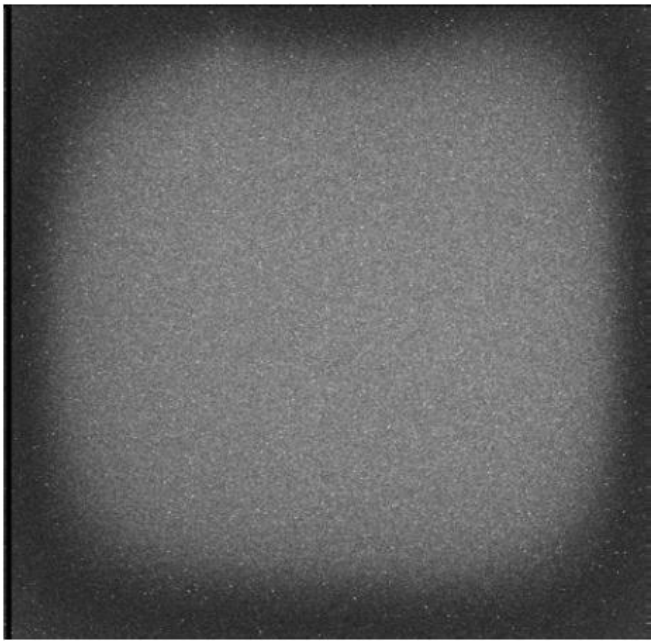

Figure 6.16. Central brightening observed by Hopkinson et al. (2004) on a STAR-250 APS after gamma irradiation.

Device	Performed By	Bias	Experimental Setup	Total Dose	Central Brightening Present
Jade FI	Author	Yes	Minimal shielding	200 krad	**Yes**
Jade FI	Author	Yes	Shielding of electronics	20 krad	**Yes**
Jade FI	Author	Yes	Total shielding except device	242 krad	**Yes**
Jade BI	Elliott	No		200 krad	**No**
Jade BI	Mueller	Yes	Total shielding except device	32 krad	**No**
STAR-250 FI	Hopkinson *et al.*	No		80 krad	**Yes**

Table 6-1. Table summarising irradiations performed on Jade APSs by the author and others, and other occurrences of central brightening in the literature.

6.4.2.1 Dose Non-Uniformity

The most immediate explanation for the central brightening would be dose non-uniformity across the device, causing the centre of the device to receive a higher dose than the outer region. The source of this non-uniformity would be most likely due to two sources:

- Shadowing of the outside edges of the device due to either the device package or the shielding used to prevent damage to the readout electronics board.
- Dose enhancement due to Compton electrons scattered from the package, underlying silicon or surrounding shielding.

Care was taken in each case to ensure that shadowing was minimised, and furthermore the dose non-uniformity was measured with dosimetric film. Figure 6.2. shows the measured dose uniformity using gamma-sensitive film placed between the back of the device connected to the readout board, and a rear shielding lead brick. This result reassures that the dose was not non-uniform in the way that dark-current non-uniformity was observed on the device. The dosimetry film used also has measured sensitivity to electron doses – suggesting that the Compton-electron population was also uniform.

Furthermore the non-uniformity was not observed after irradiation of BI devices at the same ESA gamma cell with similar shielding setup as the FI study, suggesting a difference in device manufacture rather than experimental setup.

6.4.2.2 Electronics Damage

Due to the highly integrated nature of CMOS, coupled with the Jade device being mounted directly to a readout board, there is additional risk of damage to the readout electronics that could affect the amount of dark current that is measured. Damage to the transistors in-pixel are unlikely to be the cause of non-uniformity, as they should show uniform effects due to uniform dose, unless there is some complication in fabrication that is unknowable without better understanding of foundry processing. Similarly, addressing and amplifying transistors off-pixel should, if anything, show a non-uniformity trend across the device due to dose received, rather than a central feature. Unfortunately attempts to mount an irradiated sensor onto an unirradiated readout board were unsuccessful.

6.4.2.3 Hydrogen Depassivation

Hydrogen passivation is used by device manufacturers to supress surface dark current of the device as described at the beginning of this chapter. In the normal case, the surface is depassiviated by the radiation creating protons which then react with hydrogen bonded at the surface which then quickly diffuses out of the device, leaving behind noisy 'dangling' bonds. In the case of APS, there are also STI channels in the device, which can cause large degrees of dark current even in a pinned photodiode device designed to eliminate surface dark current.

In the case of FI APS, microlenses are used to improve the QE of the device by focussing light onto active areas of the pixel. These microlenses are fabricated, commonly, from polyimide or polyamide, a highly un-permeable plastic (so un-permeable, that polyimides are choice materials for gas-separation (Hayes, 1987)). This impermeable layer on top of the device limits the diffusion route for liberated hydrogen, causing it to diffuse laterally from the centre to the edges of the device. As the hydrogen diffuses, it may be able to repassivate dangling bonds as it passes to the edges, resulting in a lower dark current around the edge. In the case of the BI APS, the microlenses are not fabricated, enabling the process of back-thinning, and so no dark current shift is observed.

6.4.2.4 Microlens Decomposition

It has been observed that microlenses degrade under irradiation, the theory of which is presented in Chapter 4. The colour change noted by the author is caused by bonds breaking in the microlens material and rebonding within the material to form unwanted, opaque compounds. It is known that these fragments are able, instead of rebonding within the microlenses, to diffuse into the device itself, where they are free to react with passivation at the surface, passivation in STI channels, and to a lesser extent dopants in the silicon,

causing excess dark current. Again, as microlenses are removed to fabricate BI devices, the non-uniformity is not seen.

The formation of the well-defined pattern is still difficult to explain with this mechanism and so is the observation of the opposite brightening effect under high temperature measurement.

6.5 Conclusions

The Jade APS was shown to be still operational after gamma ray irradiation to 200 krads. The dark current increase of the device was measured to be anywhere between 10 and 800 $pA \cdot cm^{-2} \cdot krad^{-1}$, depending on the previous dose received by the device and the area of the device being characterised, comparable to CCD technologies that are not optimised for radiation-hard performance. The source of the dark current is linked to surface-state traps, which have been known to depassivate under gamma irradiation. However it is suggested that the majority of the dark current does not come from the surface interface, but rather STI channels within the device, investigation of which is difficult due to the sensitivity of foundry fabrication techniques.

There is more than an order of magnitude difference in the dark current increase shown in the inner part of the image area when compared to the outer area, which is rarely seen in the literature, and is specific to a small number of APSs. It is proposed that this 'central brightening' is linked to the decomposition of the layer of microlenses on the device and the microlens interaction with the passivation process during manufacture.

The microlenses are seen to change colour in response to irradiation, turning ~20% more red after 200+ krad(Si) which indicates a change in the transmission of the microlenses at long optical wavelengths. This is due to the breakdown of the polyimide compound by the energetic gamma photons. These fragments then re-bond, forming new, non-transparent

compounds in the microlens layer. This negatively impacts the red QE of the device, as more red light is reflected back towards the source.

The damage caused by gamma irradiation of the FI Jade device is clearly undesirable for space applications, and could severely impact the performance of an instrument. However the increase in dark current is stable over time, and could be calibrated out of measurements by subtracting a relevant dark image. Furthermore, the work highlights the importance for research into the effects of adding fairly benign features such as microlenses, as they can complicate sensor performance and increase degradation under irradiation, and it is possible that their interaction with certain sensor designs may produce unexpected and undesirable results. The BI Jade shows less of these complications due to the additional processing removing the microlens layers, and may be a better candidate for radiation studies in future.

6.6 Further Work

This work has direct application to the radiation damage experiment to be launched on board UKube-1, using the larger e2v technologies Sapphire imager. It will be interesting to compare the damage obtained in the real space environment to that seen in lab-based experiments designed to mimic components of that environment.

Chapter 7: Proton Radiation Damage Characterisation

As discussed in Chapter 4, protons form a large component of the damaging radiation in the space environment, and compared to ionising radiation which causes a uniform and slow increase in the dark current of the device, the displacement damage caused by protons forms discrete traps which cause single pixels to have vastly increased dark current, or dark current which changes over time.

In this chapter, a proton radiation campaign is detailed, and the appearance of increased dark current, bright pixels, and bright pixels with varying dark current is measured and discussed. Specifically the bright pixel and varying dark current measurements are compared to dark current generation theory suggested by other authors to add to the scientific understanding of these phenomena.

7.1 Random Telegraph Signal Theory

In a CCD or APS, especially those that have undergone displacement damage, it is common to see pixels switching between two (see Figure 7.1) or more distinct brightness levels or dark current generation states. These pixels are said to exhibit 'Random Telegraph Signal' (RTS) behaviour. These signals are also commonly seen in submicron MOSFETs. While MOSFET RTS is well modelled, the physical mechanisms behind dark current RTS (such as in CCDs) are not well understood, although recently progress is being made in characterising and modelling its behaviour as it becomes a dominant noise source in irradiated devices that is difficult to mitigate.

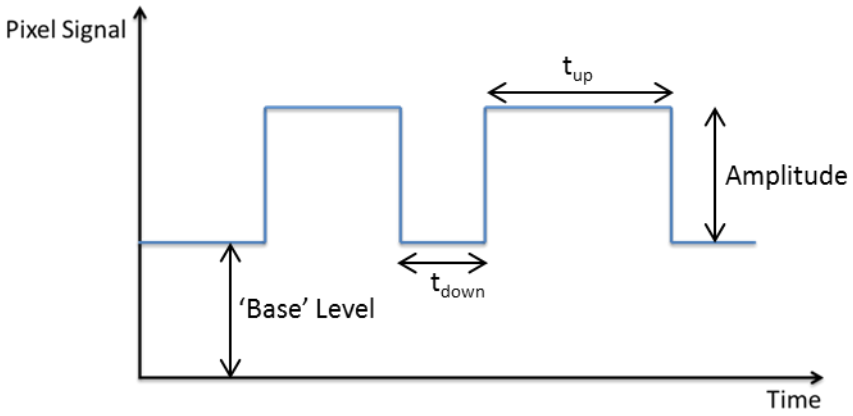

Figure 7.1. Schematic of the signal of a simple two-state RTS pixel over time.

Although this work focusses on the appearance of RTS in the Jade APS, it is of merit to review previous studies of RTS appearance in CCDs and MOSFETs, as APSs contain elements of both.

7.1.1 MOSFET Random Telegraph Signal

RTS in MOSFETS has been seen in micron sized MOSFETs under certain biasing conditions, however, as CMOS technology has evolved with smaller feature sizes, RTS has become more frequently seen in sub-micron and nanometre sized MOSFETs. It has been shown that RTS in MOSFETs can be linked to the same source as 1/f noise (Uren *et al.*, 1985), *i.e.* that 1/f noise is the product of many surface state traps all exhibiting RTS characteristics, and that as feature sizes reduce, the spectrum of noise frequencies becomes RTS-like because the number of contributing traps is fewer.

The source of the most common occurrence of MOSFET RTS can be modelled as a single trap in a MOSFET channel (Kandiah *et al.*, 1989). If the trap is unoccupied then current freely flows through the channel, however when the trap is occupied with a majority carrier, the trap acts as a resistance in the area of the trap, causing a lower current to flow. It follows that the species and position of the trap within the channel will cause differences in the amplitude and frequency of the RTS. It has also been shown that changing gate bias voltages can alter the appearance of RTS, and that switching the MOSFET operation mode

between inversion and accumulation can also reduce the appearance of RTS (Dierickx & Simoen, 1992). Simulation of such a model shows results close to those measured (Asenov *et al.*, 2003). It is predicted that as MOSFETs become even smaller, the RTS caused by the trapping of a single electron will have an even greater effect on performance, as the field of the single electron occupies a larger fraction of the conduction channel.

It is important to note that this is a model for the most common cause of RTS in MOSFETS, and it is possible to observe RTSs that are not adequately explained by this model such as anomalously large RTS amplitudes (Uren *et al.*, 1988), that may be better explained by the model given below for RTS observed in CCDs.

MOSFET RTS can be supressed significantly by implementation of CDS for noise reduction of the sensor, as is used in the Jade APS. CDS can still sample the RTS but only if the signal switches between the double sampling period, and results in 3 amplitude levels in the signal: from no transition during sampling, a transition from low to high during sampling, and a transition from high to low during sampling. If the time between sampling is significantly lower than the RTS switching time, MOSFET RTS is not expected to be seen at all. Wang *et al.*, 2006 show the manifestation of CDS sampled MOSFET RTS.

7.1.2 Bulk Dark Current RTS

As CCD pixels and therefore CCD transfer widths are generally on the order of micron-sized as opposed to the sub-micron sized CMOS MOSFET fabrication, RTS pixels in CCDs cannot be accurately modelled as a single trap inhibiting charge flow. RTS pixels are rarely seen in newly manufactured CCDs unlike in MOSFETs, and are commonly seen after displacement damage has occurred via irradiation. The RTS comes from a source within the pixel, and the mechanism is not well understood. Several hypotheses have been put forward to explain the generation of RTS in the pixel but generally do not explain all features of the

phenomenon. These hypotheses are detailed and contrasted with the data presented in this chapter in the discussion section.

7.2 Experimental Procedure

Two devices were irradiated over half of the imaging area (shielded with a steel plate) with protons at the Kernfysisch Versneller Instituut (KVI). The beam energy was measured to be 44 MeV, and the beam flux of 1.95×10^{7} protons·cm^{-2}·s^{-1} was delivered for 256 and 512 s respectively. This resulted in total 10 MeV equivalent proton fluences of 5.0×10^{9} protons·cm^{-2} and 10.0×10^{9} protons·cm^{-2} (equivalent to 2.8 and 5.6 krad(Si)) respectively. Dosimetry measurements taken at the time using a LANEX scintillation film gave beam uniformity measurements of ±10 % over the entire beam diameter of 70-80 mm, and ±3 % over 10.5 mm (van de Graaf, 2008).

7.3 Results

7.3.1 Dark Current Increase

Figure 7.2. is a graph showing the pixel dark current distribution for irradiated and unirradiated portions of the two proton-irradiated devices.

There are two main components in the change between unirradiated and irradiated histograms. Firstly the noise peak is shifted to the right, suggesting that a large fraction of the pixels show increased dark current generation rates. This is linked to ionisation damage causing depassivation of surface states as discussed in Chapter 6. In this case the increase is measured to be 275 pA·cm^{-2} and 600 pA·cm^{-2} for 5×10^{9} and 1×10^{10} 10 MeV protons·cm^{-2} respectively. Figure 7.3. shows the increase of ionising dark current increase as a function of dose, resulting in a measurement of 105 pA·cm^{-2}·krad^{-1}.

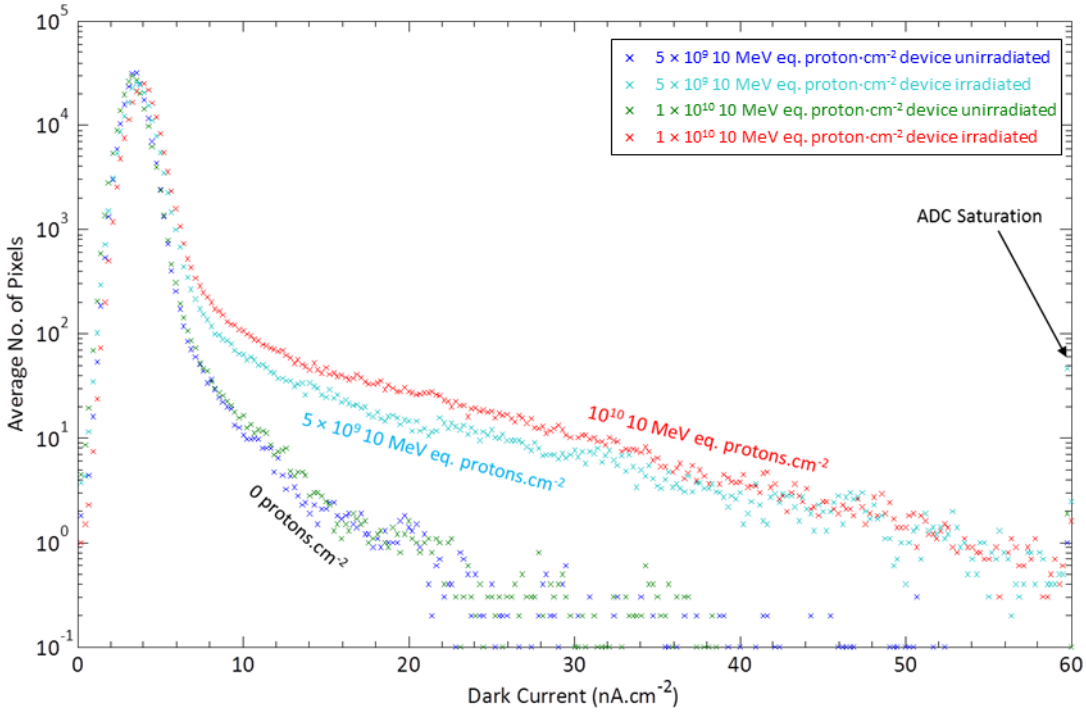

Figure 7.2. Graph showing a histogram of pixel dark current measurements averaged over 100 frames for two proton irradiated Jade APSs taken at 20°C, gain = 1.

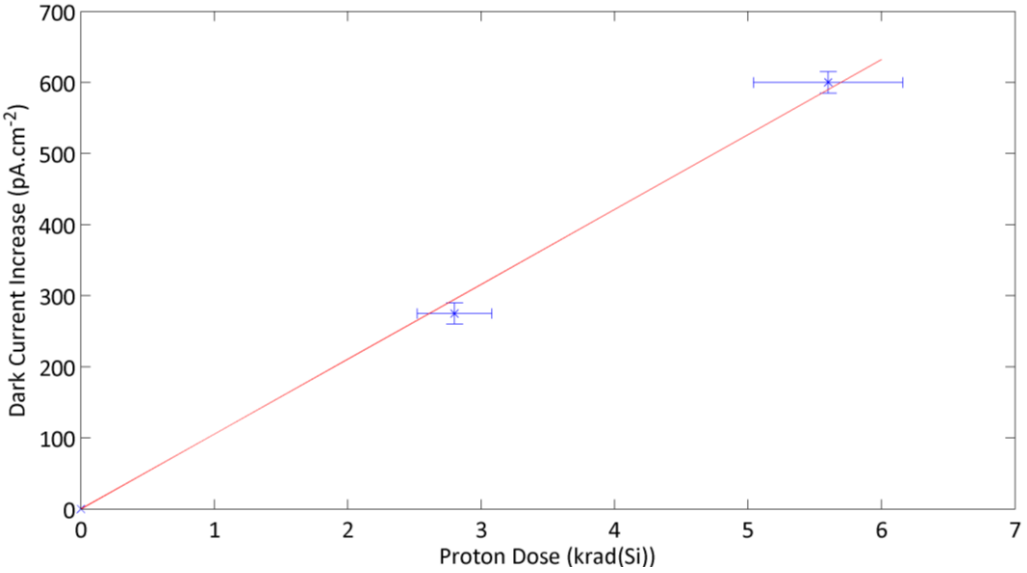

Figure 7.3. Graph of ionising dark current increase against proton dose with best linear fit (forced through origin).

In addition to the ionisation damage, the tail of the histogram rises significantly, indicating a vast increase in the number of bright pixels, linked to displacement damage events that cause a larger increase in dark current. Taking a definition of bright pixels as pixels with a dark current 5σ above the mean noise, anomalously above the noise distribution, we

measure 119 bright pixels in the unirradiated case, and 1350 and 2750 bright pixels after irradiation of 5×10^{9} and 1×10^{10} 10 MeV protons·cm^{-2} respectively.

7.3.2 Random Telegraph Signal Analysis

A study was carried out to investigate the features of proton-induced RTS pixels in the Jade device.

7.3.2.1 Data Acquisition

For this study the device irradiated to 1×10^{10} 10 MeV eq. protons·cm^{-2} was used. The device was operated in an oven and the temperature was monitored with a PT1000 mounted on the device package. Data were acquired for 2 hours at 20, 40 and 60 ^{o}C.

7.3.2.2 Detection

As RTS behaviour becomes more of a concern for the radiation response of detectors, significant effort has been put towards the automatic detection of RTS pixels. Several different methods have emerged, each of which has advantages and drawbacks. Three relevant techniques are detailed in this section.

7.3.2.2.1 Standard Deviation Threshold

The most fundamental way to characterise RTS pixels is to analyse the standard deviation of the pixel's signal over time. Pixels with a large RTS amplitude and a fast enough time constant will have a significantly higher standard deviation than a pixel with no RTS behaviour. Figure 7.4. shows a histogram of pixel standard deviations for a Jade device irradiated to 1×10^{10} 10 MeV eq. protons·cm^{-2}. There is a significant skewing of the distribution, and the pixels with higher standard deviations are found to exhibit RTS behaviour.

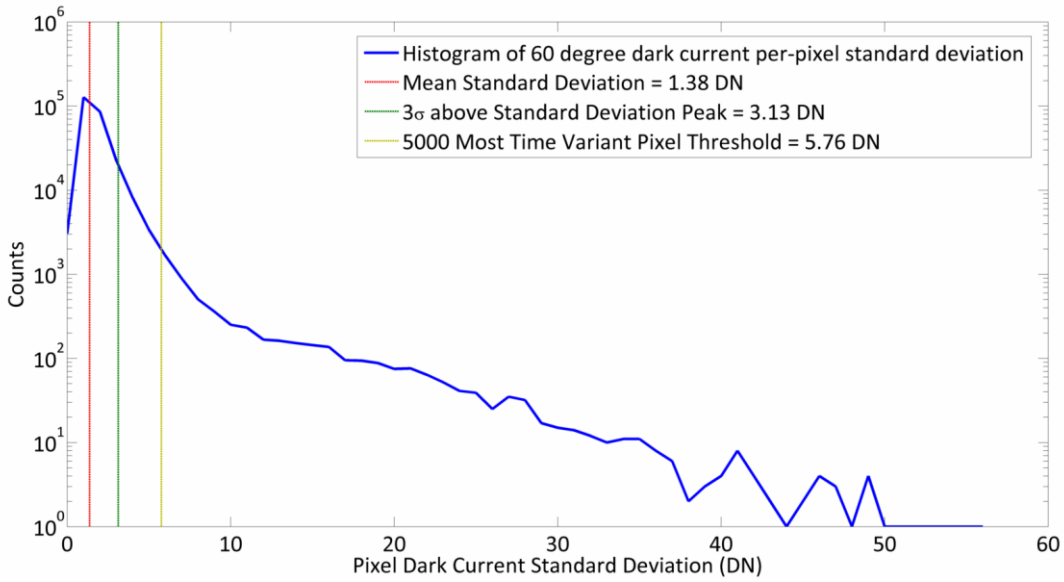

Figure 7.4. Graph showing standard deviation histogram at 60 °C for all pixels in the irradiated area of the 1 × 10^{10} 10 MeV eq. protons·cm^{-2} device.

However, a threshold must be used to classify pixels as exhibiting RTS or not. In general, there are going to be non-RTS exhibiting pixels above the threshold (just with a higher noise than usual, for example) or pixels with low amplitude RTS that exist below the threshold. Determining a suitable threshold is difficult, and false-positives and false-negatives will occur frequently with this technique. It is useful when considering RTS susceptibility for an application, to come at the detection threshold from a mission-oriented point of view, which is generally given in terms of an RTS amplitude or time constant above which the RTS is unacceptable. It is therefore more useful to classify possible RTS first and filter them according to the mission specifications as a secondary step. Using the standard deviation threshold technique can result in needing a very low threshold to ensure capturing all possible RTS and therefore resulting in a large number of false-positives. As the standard deviation threshold decreases, the probability of capturing pixels with high noise increases, but Figure 7.5., for example, shows a pixel detected as above the standard deviation threshold, but not exhibiting RTS behaviour.

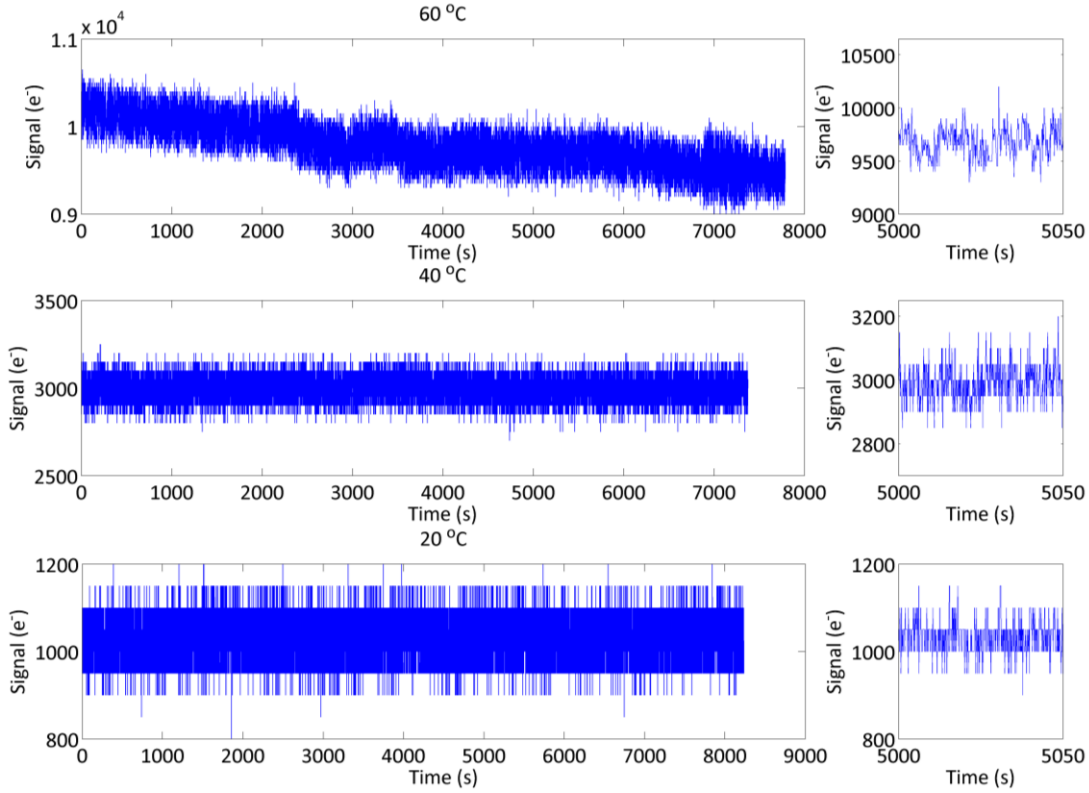

Figure 7.5. A pixel with a high standard deviation, but no visible RTS behaviour.

Standard deviation thresholding is very fast to perform. The technique can therefore be useful for a preliminary characterisation and rough quantification of pixel variability, but presents significant difficulties for performing more sophisticated analysis.

7.3.2.2.2 Histogram Peak Detection

A more robust method for RTS detection is performing peak detection on a histogram of each pixel's signal over time. This results in a single peak in the case of a pixel that does not exhibit RTS, and several peaks in the case of a pixel exhibiting RTS. The histogram is then differentiated and peaks are detected by filtering the differentiated histogram for the points at which it passes 0 (Smith *et al.*, 2004).

The number of peaks detected in this way provides a quick and effective method for filtering pixels with no RTS characteristic (*i.e.* a single peak with a Gaussian envelope), and leaves a much smaller data set to analyse in more detail. The remaining pixels all show

some degree of abnormal behaviour outside of the Gaussian envelope, and so should the set of pixels remaining should be considered for further analysis.

A mixed Gaussian least squares fit is then applied, using the peak height, peak position, and typical noise standard deviation (1.38 DN) as initial guesses. The number of iterations of the fitting algorithm is increased until the error in the regression of the sum of Gaussians is less than 10%. The procedure is shown in Figure 7.6.

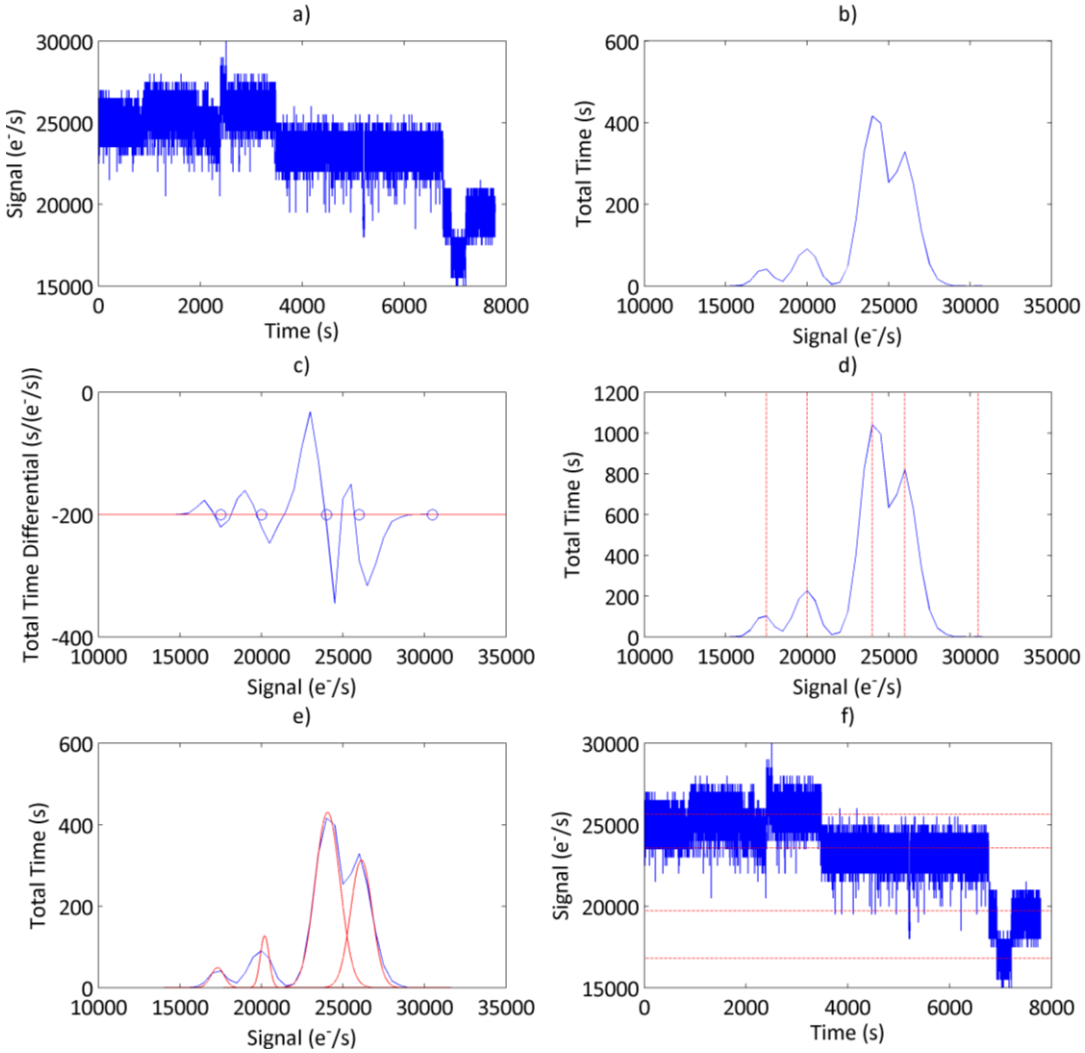

Figure 7.6. Method of histogram peak detection of RTS pixels. The pixel signal (a) is plotted as a histogram (b) which is then differentiated (c) to detect the histogram peaks (d). These peak positions can then feed into a mixed Gaussian fitting algorithm to determine more detailed characteristics (e). The peak positions plotted over the raw data are shown in f).

7.3.2.2.3 Edge Detection Filter

Although not used in this work, recent work (Goiffon *et al.*, 2009) has shown success in using an edge detection filter for detection of RTS. The detection method assumes the RTS signal is step-like with a Gaussian noise background. A step filter is swept across a pixel's signal with a filter width that is tweaked to obtain the best performance between detecting RTS of a small enough amplitude or fast enough switching time (*i.e.* a narrower filter produces higher time resolution steps), and filtering the Gaussian noise (*i.e.* a wider filter reduces the noise in the output). If the filter width is correctly balanced, the output is a series of positive and negative spikes that represent the location and height of steps in the signal as shown in Figure 7.7.

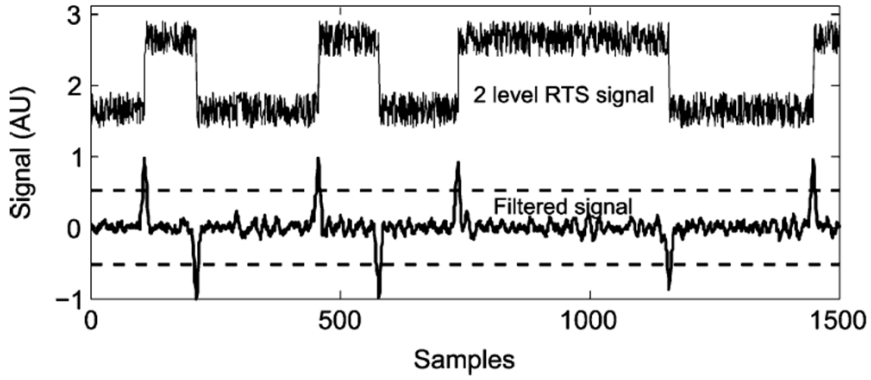

Figure 7.7. Graph showing typical bi-stable pixel output (top) and output of the edge-detection filter (bottom) with suitable detection threshold (dashed lines) (Goiffon et al., 2009).

By thresholding this filtered signal, a noiseless representation of the signal can be constructed, allowing much better capability to measure RTS parameters. The threshold is determined either by trying to find the threshold just above the noise, or more simply, if a certain RTS specification is required for an application, the threshold can identify steps above a certain magnitude.

This method, therefore, facilitates the accurate determination of all RTS parameters for even very complex signals (as shown in Figure 7.8). Furthermore signal filtering is fairly computationally fast, especially in Matlab which is optimised for array operations, allowing

for better exploration of threshold levels and deeper analysis of the data. This technique is being implemented and tested at the CEI for future RTS analysis campaigns.

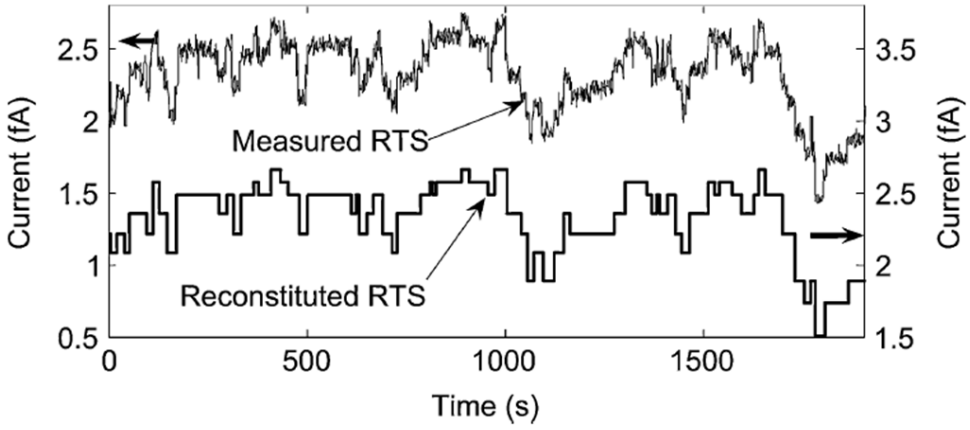

Figure 7.8. Graph showing highly complex RTS signal (top, axis left), and the reconstructed representation after applying edge detection filter (bottom, axis right) (Goiffon et al., 2009).

7.3.2.2.4 Manual Characterisation

While the standard deviation and histogram peak detection techniques described above provide good detection for idealised bi-stable data, it is found that real device data are significantly more complex in a number of ways:

- RTS transition amplitudes that are too small to give two clearly defined peaks. (Figure 7.9. a)
- RTSs exhibiting two levels with a continuum of signal levels in between. (Figure 7.9. b)
- RTS or non-RTS exhibiting a lower or higher level that is visited for only a few frames at a time, leading to uncertainty of whether it is RTS or some other phenomenon. (Figure 7.9. c)
- A large number of RTS levels resulting in a hard to minimise (and thus time consuming) least squares fit. (Figure 7.9. d)
- Change in the 'mode' of an RTS pixel in the middle of integration time, resulting in poor measurement of time constants. (Figure 7.9. e)
- A combination of the above effects. (Figure 7.9. f)

These complications mean that a further manual characterisation of the data is required. As such the results measuring time constants are based on a subset of 500 pixels that were deemed to be bi-stable over the sampled time, and the signal values for each level was set by eye. For future studies, the edge detection filter technique could significantly increase the accuracy of characterisation of RTS pixels.

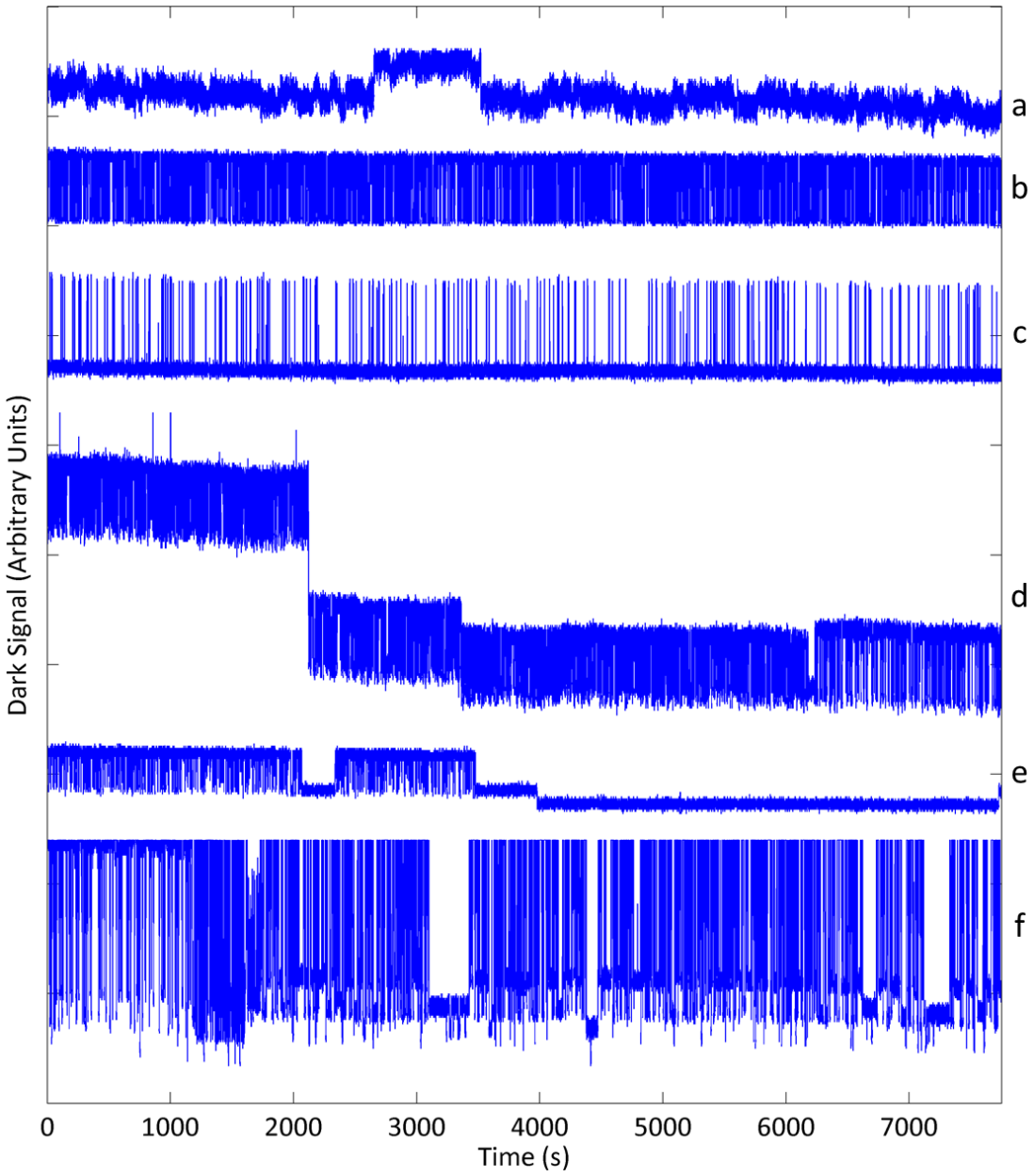

Figure 7.9. Dark signal generation rates for 6 selected pixels over time showing a wide variety of RTS pixel behaviours which presents difficulty in automated RTS characterisation. a) exhibits very small changes in amplitude, b) exhibits 2 well differentiated levels, but with a continuum of dark current levels in between, c) exhibits a generally stable level, but with very short periods of higher generation, d) exhibits large changes in dark current generation behaviour over the measurement period, e) exhibits smaller changes in dark current generation behaviour over the measurement period, and f) exhibits a very complex RTS that has some combination of the other effects, as well as reaching saturation at the highest generation level.

7.3.2.3 Measured Bulk RTS Properties

The majority of the presented analysis is performed on 60 ^{o}C data, as this enhances the difference in dark current generation between the two or more pixel states, and lowers the amount of time spent in each state, enabling analysis of RTS with slower switching times.

Figure 7.10. shows the distribution of all irradiated pixels for a Jade APS, comparing the pedestal (the minimum signal over all frames) to the switching amplitude (the range of the signal over all frames). There are four major areas of interest. The large cluster with low amplitude and pedestal values represent non-RTS, non-bright pixels.

The black line represents a clustering of pixels representing bright pixels that show no RTS behaviour in the measured time period. The switching amplitude of these pixels increases at a rate of 0.131 e^-_{amp}/e^-_{ped}.

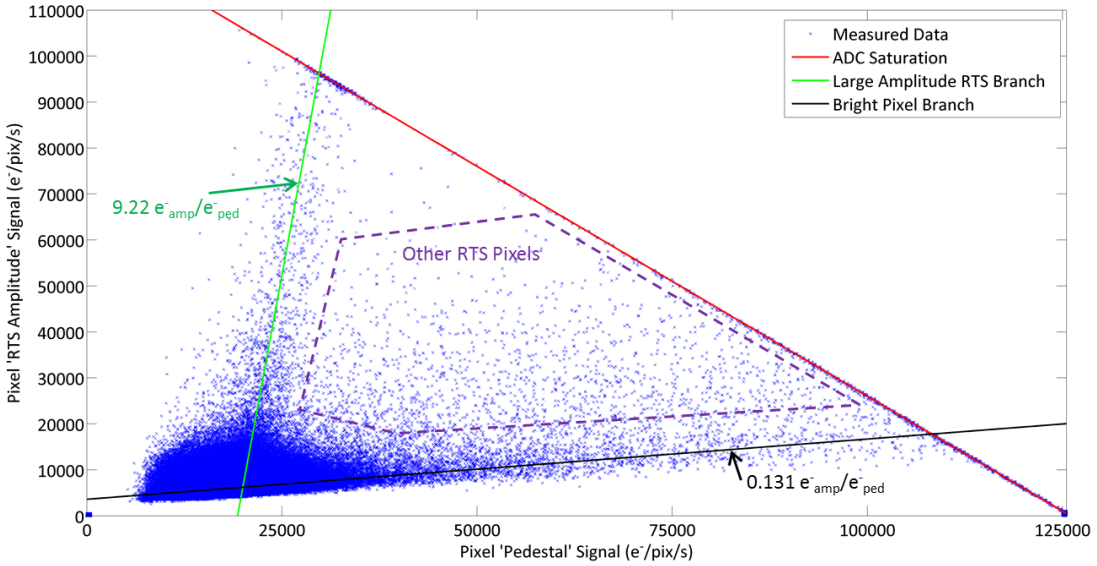

Figure 7.10. Scatterplot of all irradiated pixel RTS amplitude (range of pixel values over time) against the pixel pedestal.

We can characterise pixels significantly above this line (*i.e.* within the purple dashed boundary) as RTS pixels, as they show a larger range of values than the expected noise. An interesting trend is indicated by the green trend line. These pixels show clear RTS behaviour, and the RTS switching amplitude shows a clear relationship to the pedestal amplitude of roughly 9.2 e^-_{amp}/e^-_{ped}. Figure 7.11. shows the behaviour of a typical pixel from this branch.

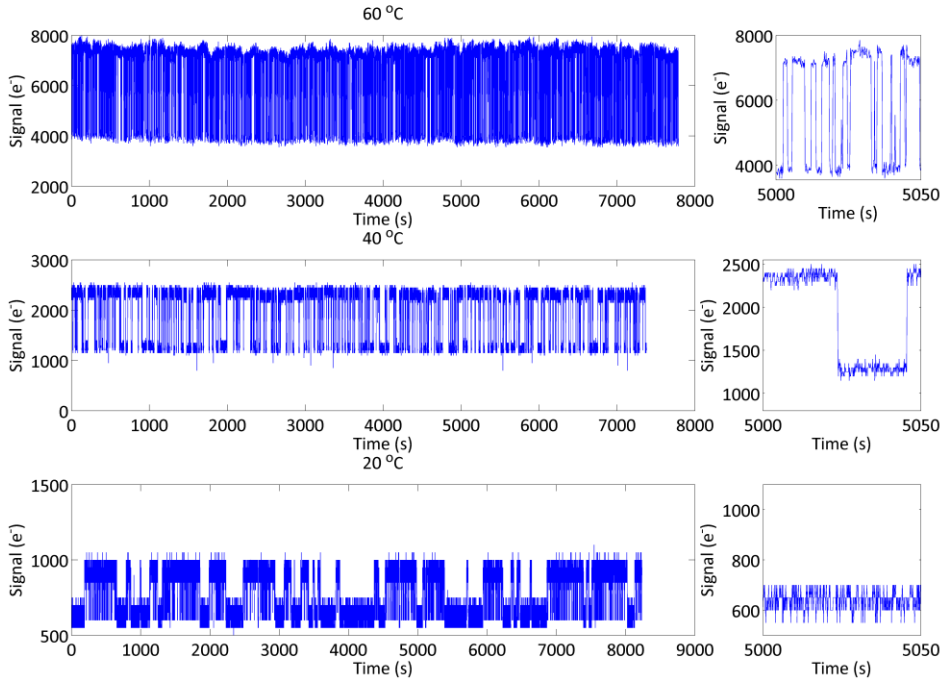

Figure 7.11. Typical characteristic of a pixel in the 'Large Amplitude RTS branch' indicated in Figure 7.10. Signal over time is shown for 60 °C, 40 °C and 20 °C, with a small portion of higher time resolution shown on the right.

Previous work (*e.g.* Goiffon *et al.*, 2009, Hopkins & Hopkinson, 1995) shows that a large fraction of pixels exhibiting a high mean dark current also exhibit RTS behaviour. Figure 7.12. shows a comparison of the coincidence of pixels with extreme dark current generation, and extreme variance over time (5000 pixels represents a standard deviation above 5.76 DN, and is a high enough threshold to avoid false detection of noisy but non-RTS pixels). Between these two groups of pixels, 1974 pixels are shared representing a nearly 40% coincidence, which strongly links bright and RTS pixels. Some authors have posited that all bright pixels may exhibit RTS behaviour if sampled quickly enough, or if monitored for a long enough time (Smith *et al.*, 2004). The pixels are evenly distributed across the irradiated area with no sign of effects such as central brightening.

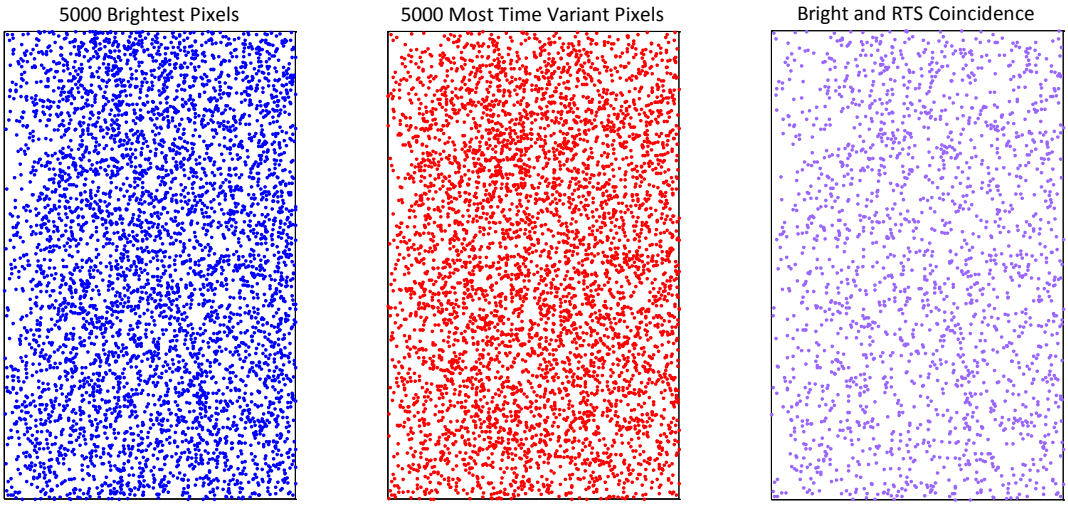

Figure 7.12. Comparison of the position of 5000 brightest and 5000 highest standard deviation pixels, and the 1974 pixels that are coincident between the two groups.

7.3.2.4 RTS Time constant analysis

Due to RTS detection issues outlined above, manual RTS detection was performed after suitable standard deviation and histogram fitting was performed to limit the pool of candidate pixels. The dataset contains all pixels that do not show complications outlined in Section 0., *i.e.* pixels that show behaviour close to the ideal bi-stable RTS pixel shown in Figure 7.1. at 60 ^{o}C, to ensure that measurements most accurately reflect single bi-stable RTS behaviour without artefacts from other effects. This dataset contains 500 RTS pixels. The ability to resolve the levels at lower temperatures varies between pixels, with some showing no RTS behaviour over the time period at 40 ^{o}C or 20 ^{o}C at all, due to either reduction of the switching amplitude, or increase in the switching time constant.

Figure 7.13 shows measured time constants (mean time spent in a state before switching) for the 500 RTS pixels in this dataset.

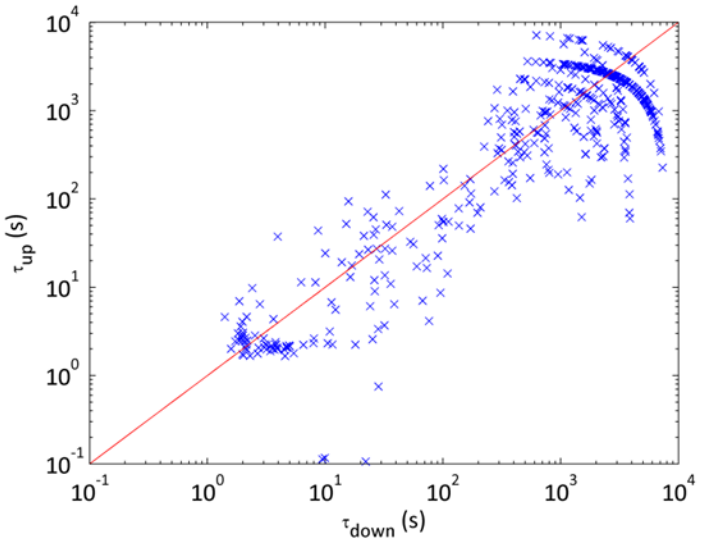

Figure 7.13. Comparison of mean time spent in a high dark current state (τ_{up}) to mean time spend in a low dark current state (τ_{down}) for manually selected bi-stable RTS pixels at 60 °C. Red line represents equal time spent in each state.

The arcs present in the data at high time constant values represent pixels with long time constants that flip only a few times within the measured time period. The measured mean time constants for these pixels are artificially reduced by this effect. The most discernible clustering is at time constant values of 4 ± 2 s. In general, the dataset lies below the red line representing equal time in the high and low dark current states. Figure 7.14. shows a histogram of the ratio of the time spent in these two states.

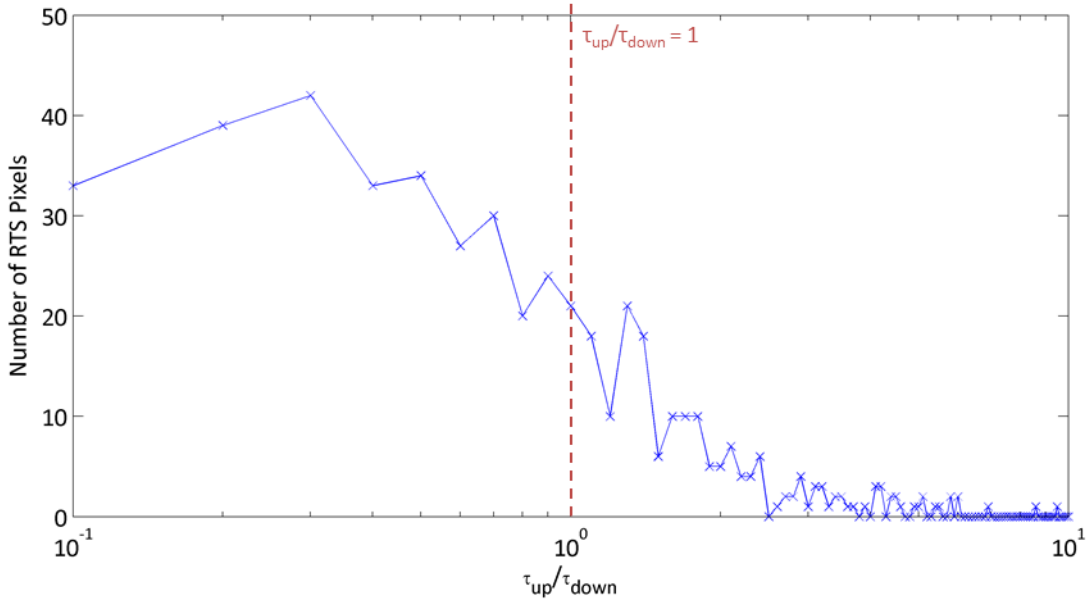

Figure 7.14. Histogram of measured ratio of mean times spent in high and low dark current states at 60 °C.

As can be seen from Figure 7.14, the majority (294 of 500) of RTS time constant ratios exists below 1. The higher time constant ratios have a significantly high error, as these points are due to pixels with long time constants compared to the measurement time, and so the switch from high to low dark current state can happen at any point in the measurement window.

Figure 7.15. shows the time constant scatterplots for the 40 °C and 20 °C datasets.

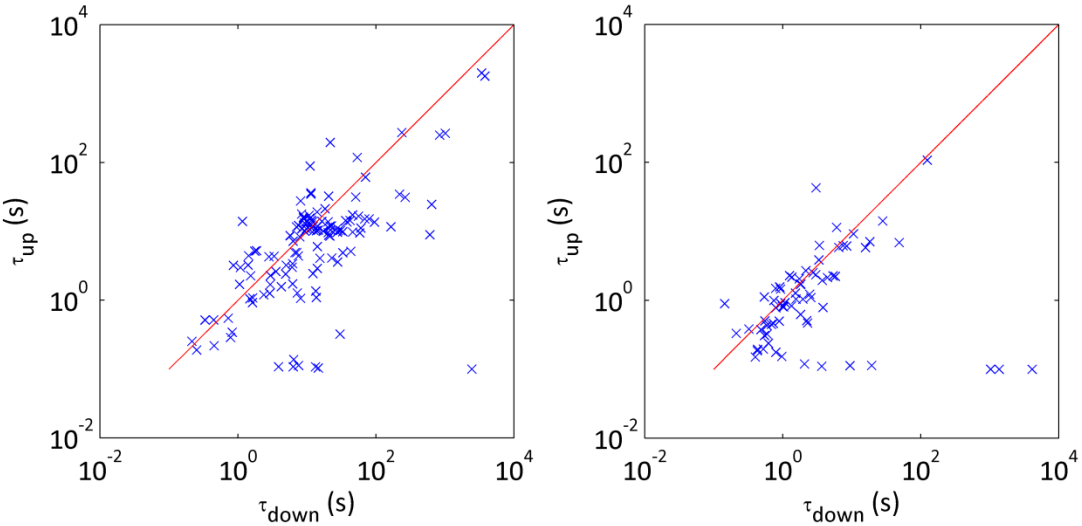

Figure 7.15. Comparison of mean time spent in a high dark current state (τ_{up}) to mean time spend in a low dark current state (τ_{down}) for manually selected bi-stable RTS pixels at 40 °C (left) and 20 °C (right). Red line represents equal time spent in each state.

The 40 °C plot shows a cluster at around 45 ± 30 s, linked to the pixels showing time constants of 4 ± 2 s at 60 °C. At 20 °C the amplitude is generally too low to give accurate results, so this cluster no longer appears. These temperatures show faster time constants despite the lower temperature, but this is due to inaccuracy in defining the states due to the low amplitude of the switching.

7.4 Discussion

7.4.1 Theories of RTS generation

Several phenomena have been proposed to explain the behaviour seen in RTS pixels. One main difficulty is identifying something in the current understanding of defect generation

that can generate currents changes of, in some cases, over 200,000 $e^{-}{\cdot}s^{-1}$. This also applies to the generation of dark current in bright pixels, which again is not well understood. Additionally, RTS seems linked strongly to temperature, with emission amplitude and the switching time constants linked strongly to operating temperature, suggesting that the bi-stable nature is thermally activated. The high dark current and meta-stable behaviour are discussed separately below.

7.4.1.1 High Dark Current Generation

7.4.1.1.1 Field Enhanced Emission

It is observed that some RTS show switching from the readout noise level to above ADC saturation (over 200,000 $e^{-}{\cdot}s^{-1}$). As a mechanism for the switching of large defect clusters is unknown, this suggests that the dark current source must exist in a region of high field in order to cause a high enough dark current emission from a single defect via Poole-Frenkel enhanced emission (see Chapter 4). The emission of a defect can be modelled using the Shockley-Read-Hall equation (Sze, 1981):

$$J = \frac{C_n C_p v_{th} n_i}{C_n e^{-E/kT} + C_p e^{E/kT}} \tag{7.1}$$

Where v_{th} is the carrier thermal velocity:

$$v_{th} = \left(\frac{3kT}{m^*}\right)^{\frac{1}{2}} \tag{7.2}$$

Therefore, since the negative exponential is negligible:

$$J = \frac{C_n n_i}{e^{E/kT}}\left(\frac{3kT}{m^*}\right)^{\frac{1}{2}} \tag{7.3}$$

Where J (A) is the junction leakage current, C_n (cm^2) is the electron capture cross section, n_i (cm^{-3}) is the intrinsic carrier concentration of silicon, E (eV) is the energy difference between the intrinsic Fermi level and the defect energy level, and

m^* ($0.25 \times 9.11 \times 10^{-31}$ kg) is the effective mass of the majority carrier (e^-). C_n is taken as 10^{-14} cm², and from standard theory n_i = 1.2 x 10^{10} cm^{-3}. For Si-A and Si-E centre defects, E = 0.39 eV and 0.12 eV respectively. This results in dark current generation rates at room temperature of J = 0.008 $e^-{\cdot}s^{-1}$ and 26.4 $e^-{\cdot}s^{-1}$ respectively. These dark current generation rates are clearly orders of magnitude lower than those measured and so the dark current cannot be generated by a single trap in a field free region. However, in high field regions, the dark current generation can be substantially increased via Poole-Frenkel enhancement.

The effect of Poole-Frenkel enhancement is modelled by Umeda *et al.* (2006). At the highest fields experienced in an APS (~0.4 $MV{\cdot}cm^{-1}$ (Wang, 2008)), the emission is enhanced by a factor of 200 (Umeda *et al.*, 2006), resulting in a dark current generation rate of 5300 $e^-.s^{-1}$, still more than an order of magnitude lower than those measured. This makes it unlikely that these large dark current RTS amplitude pixels are caused by a single lattice defect.

7.4.1.1.2 Defect Clusters

It has been suggested that high amplitude bright pixels can be caused by a cluster of defects created by a high energy PKA (Gill *et al.*, 1997). These events make up a large fraction of the NIEL at even low energy proton irradiation (Beck *et al.*, 2006). If these clusters were created in the high field region discussed above, clusters totalling to more than 40 defects with similar dark current generation rates would be needed to saturate the Jade sensor.

The mechanism by which these clusters would create meta-stable dark current generation levels is however uncertain. The possibility of cluster meta-stability is discussed further in Hopkinson & Mohammadzadeh (2008).

7.4.1.2 Meta-stable behaviour

7.4.1.2.1 Bulk Defect Reorientation

Measurement of the P-V centre defect by Watkins & Corbett (1964) included observation that the defect can re-orient through thermal excitation, as shown in Figure 7.16. The orientation of the P-V centre changes its energy level by virtue of the dipole vector in an external electric field. As shown above, the dark current generation from a trap can vary significantly with small changes in the trap energy level.

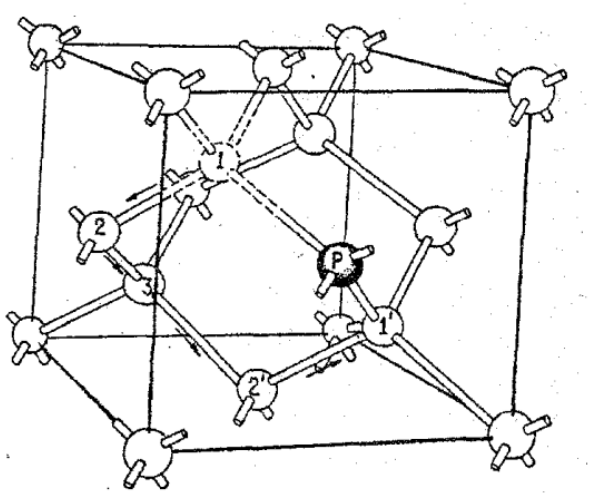

Figure 7.16. Figure from Watkins & Corbett (1964) showing the dynamics of P-V re-orientation. If the vacancy is initially in position 1, it is stable, but can be thermally excited through position 2 to position 3. From this point there are two probable routes to re-establish the stable bond with the phosphor impurity, back through 2 to 1, or through 2' to 1'.

Watkins & Corbett (1964) measure the kinetics of the re-orientation of the defect to be

$$\tau^{-1} = 1.6 \times 10^{13} e^{(\frac{-E_{act}}{kT})} \quad (7.4)$$

Where E_{act} = 0.93 ± 0.05 eV. This results in time constants of 1 s to 45 s at 60°C, 10 s to 400 s at 40°C and 100 s to 5000 s at 20°C. This correlates with the measured time constants of 4 ± 2 s at 60°C and 45 ± 30 s at 40°C for a large number of the measured RTS, suggesting that this defect may be the cause of the RTS signal in a fraction of the measured pixels.

Hopkins & Hopkinson (1995) and Smith *et al.* (2004) also measure RTS behaviour in CCDs as having time constants correlating with P-V centre re-orientation. However, very large amplitude RTS was measured in this work, unlikely to be caused by re-orientation of a single defect.

7.5 Conclusions

Two sensors were irradiated with 44 MeV protons to 5×10^{9} and 1×10^{10} 10 MeV eq. protons·cm^{-2}, equivalent to the dose received at L2 over a mission lifetime of ~5 years, and therefore showing equivalent effects to those that may be seen on such a mission at end of life. The dark current increase was measured to be 275 pA·cm^{-2} and 600 pA·cm^{-2} respectively, indicating a linear increase in dark current, with no appearance of the 'central brightening' effects seen in Chapter 6.

With increasing irradiation dose, an increase in the occurrence of bright and RTS pixels was observed. In rare cases the bright pixels produced enough dark current to saturate the ADC at room temperature, corresponding to a dark current of over 200,000 e^{-}·s^{-1}. This dark current was shown to be far higher than is expected from a single defect even with field enhanced emission, suggesting that the emission from multiple defects within a pixel, or a defect cluster may be the cause.

Despite a large percentage of RTS pixels having highly complex behaviour, RTS signal bi-stable time constants were measured for a filtered subset of RTS pixels, and some portion of the RTS pixels were shown to have time constants not contradicting those measured for the reorientation of the P-V centre. However, other 'populations' of RTS pixels were identified with largely varying time constants, amplitudes and behaviours that are not consistent with the P-V reorientation model. Complex RTS pixel behaviours are assumed to be caused by several traps exhibiting different, and possibly yet to be identified bi-stable mechanisms within a single pixel.

However, RTS amplitude and switching frequency was shown to decrease dramatically with reduced temperature, suggesting that moderate cooling to sub-zero temperatures may be an effective way to mitigate RTS in space based instruments, depending on the imager's operational parameters for the instrument (*e.g.* framerate).

Chapter 8: Heavy Ion Damage Characterisation

The determination of the extent to which heavy ions damage a CMOS device is of great importance to space instrumentation, as heavy ions can cause Single Event Effects (SEEs) which can lead to permanent loss of function of a sensor.

This chapter details an experimental campaign to determine the SEE, SEFI and SEU threshold of the Jade APS. Alongside this, measurements of the radiation damage effects of heavy ions to the Jade APS were made, and due to the simple USB readout of the device, it was possible to image heavy ion impacts, leading to investigations into the possibilities of heavy ion spectroscopy, beam uniformity measurement, and monitoring of bright pixel formation and mobility immediately after creation.

8.1 Heavy Ion Interactions

Heavy ions cause both ionising (by virtue of their charge) and displacement (by virtue of their high mass and energy) damage in silicon detectors. Furthermore, heavy ions are able to cause SEE damage, generally not seen to be caused by other forms of radiation. While ionisation and displacement damage can cause a device to cease to function after some time, due to the alteration of the operating parameters such as changing the threshold voltage beyond the operational specification, or an increase in dark current to the point that the sensor is not able to perform useful measurement, SEEs can cause the temporary or permanent failure of a device from the effects of a single particle. As described in Chapter 4, the particle LET determines the device susceptibility to SEEs, and it is important to establish the threshold LET at which a device begins experiencing SEEs when characterising devices for space use.

The threshold LET is of most importance in the case of APS characterisation, where the devices suffer more readily from SEEs due to the higher amount of sensitive MOS circuitry,

and the large amount of this circuitry that is in-pixel, making it very difficult to shield effectively.

8.2 Experimental Procedure

8.2.1 CYCLONE Heavy Ion Facility

Two heavy ion irradiation experiments were performed at the CYClotron of LOuvain-la-NEuve (CYCLONE) in Belgium. The CYCLONE Heavy Ion Irradiation Facility (HIF) generates a 'cocktail' of heavy ions through Electron Cyclotron Resonance (ECR) which are then magnetically selected into the main beam line (Berger *et al.*, 1997). The beam is focussed into an isolatable vacuum chamber as shown in Figure 8.1., within which is an X, Y, Z, theta translation stage to which the device under test can be mounted.

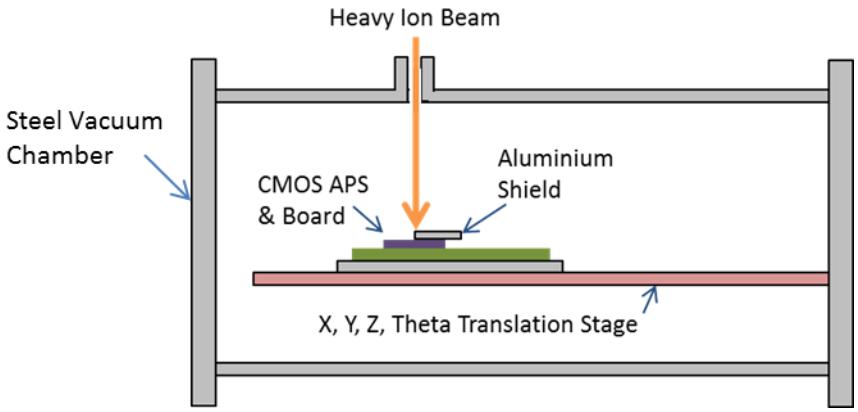

Figure 8.1. Schematic of the experimental setup for heavy ion irradiation of the Jade APS at the CYCLONE HIF. The shield covers half of the sensor to provide a control region.

The translation stage allows not only for the positioning of the device in the beam, but more importantly for tilting the device to the beam, allowing for an artificial incremental enhancement of the beam LET for SEU testing, as it increases the number of charges generated in the sensitive volume due to increasing the particle track length. This is true in approximation due to the geometry of the sensitive volume, which is thin in the Z direction, but wider in other dimensions, making the ion unlikely to exit the sensitive volume through the side, leading to a reduction in number of charges generated. Of course, in a real space

mission application, there may or may not be control over the direction which heavy ions impact from, depending on the mission operational parameters.

The facility allows selection between two 'cocktails', each containing ions with similar mass:charge ratio. These particles are selected from the 'cocktail' by fine-tuning of the magnetic fields. In this case 'cocktail 1' (mass/charge = 5) was chosen for containing a suitable range of LET and enough particle range in silicon to easily penetrate the sensor's sensitive region. The particles used from 'cocktail' 1 and their relevant characteristics are shown in Table 8-1. Particles of higher LET are also available in the 'cocktail' but the particles listed were found to be sufficient to induce SEEs.

Ion Species	Particle Energy (MeV)	LET (MeV.cm^2.mg^{-1})	Range in Silicon (µm)
$^{15}N^{3+}$	60	3.3	59
$^{20}Ne^{4+}$	78	6.4	45
$^{40}Ar^{8+}$	151	15.9	40

Table 8-1. Relevant ions and their energies from 'Cocktail 1' at the HIF beam line.

SEEs were monitored by reading the imaging output of the readout board, and also by measuring the voltage across the power rails of the USB connection. The voltage supplied to the readout board is not constant and decreases with increased signal in the device due to the ADCs drawing more current. During SEUs, the voltage is expected to increase, as the device ceases to image.

In addition to determining the SEE susceptibility of the Jade APS, imaging was performed under heavy ion irradiation to determine if heavy ion spectroscopy could be performed, using techniques similar to those used for X-ray spectroscopy as described in Chapter 5.

8.3 Results

8.3.1 Radiation Damage

Although the main focus of heavy ion irradiation is to determine susceptibility to SEEs, because heavy ions are not a large radiation damage component in the space environment,

some measurement of the extent of damage caused by heavy ions was able to be measured by comparing pre-irradiation and post-irradiation device performance. Due to the high mass and charge of heavy ions, they are expected to cause much more damage per ion than a proton or gamma ray causes per impact.

8.3.1.1 Dark Current

While heavy ions do cause ionisation damage, like protons the most notable effects are due to displacement, but even more so due to the increased mass of heavy ions over protons.

Figure 8.2. shows the shift in the dark signal histogram for increasing dose of heavy ions. The dose is estimated from the available dosimetry provided by the facility, and involved a mixture of the three ions used in cocktail 1.

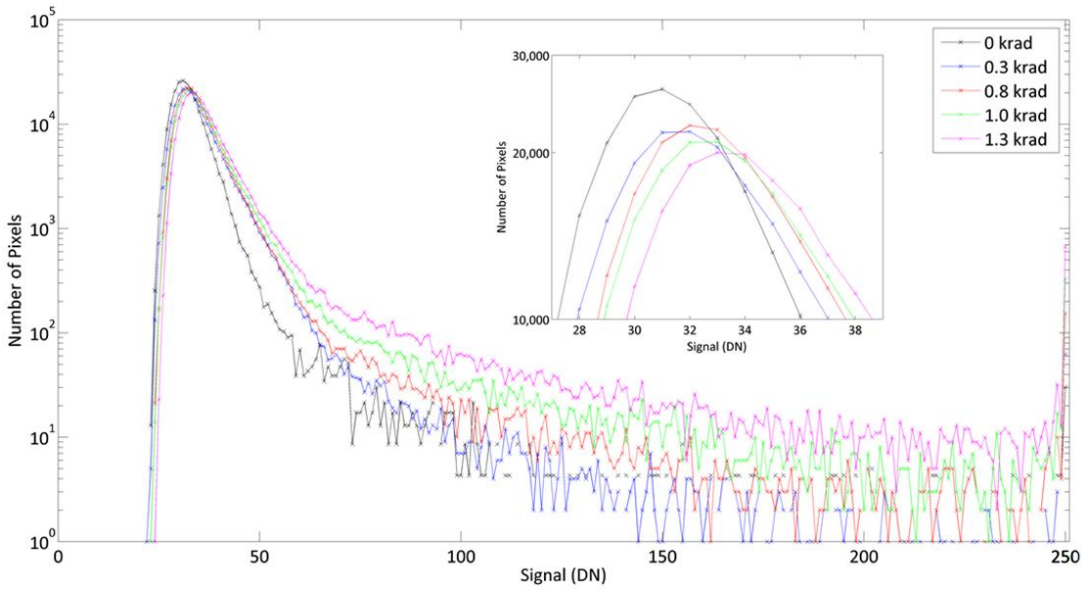

Figure 8.2. Graph showing room temperature dark signal increase with increasing heavy ion dose at room temperature, gain = 4 (50 e^-·DN^{-1}), at 10 fps. Inset graph shows a zoom of the histogram peaks.

The shift in the dark level of the images is minor, corresponding to a shift of 3 DN after 1.3 krad, corresponding to less than 300 pA·cm^{-2}. However the bright pixel tail is seen to increase significantly with dose. This can be directly compared to proton damage after 5.6 krad, which had been caused to the shielded side of the device. This device had been left to anneal for around 2 years at room temperature after the proton irradiation. In

general the traps caused by displacement damage that cause bright pixels should not anneal at room temperature, but in the ionisation damage case shown in Chapter 6 there is clear shifting of the appearance of damage after annealing at room temperature. Therefore, while the damage is not directly comparable, some qualitative analysis can be made, especially in terms of displacement damage effects such as bright pixels. Figure 8.3. is an image obtained from the device post-irradiation, showing the effects of 1.3 krad of heavy ions to the left hand side of the device, and 5.6 krad of 44 MeV protons to the right side. A small strip in the middle of the device was left unirradiated. The contrast of the image has been modified to show more clearly the bright defects.

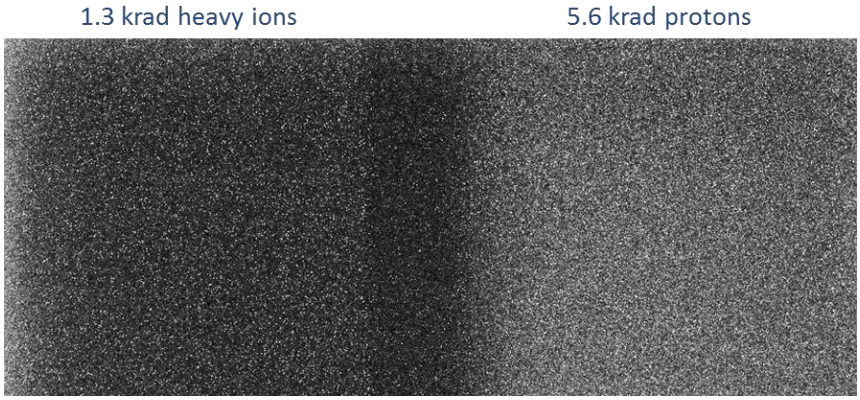

Figure 8.3. Section of the dark image taken from the Jade APS irradiated over one half with 1.3 krad of heavy ions (left) and the other half with 5.6 krad of protons (right).

Figure 8.4. shows more clearly a comparison of the effects of these irradiations. The signal has been normalised to the number of pixels in each area, so the y-axis shows the percentage of pixels exhibiting the signal level.

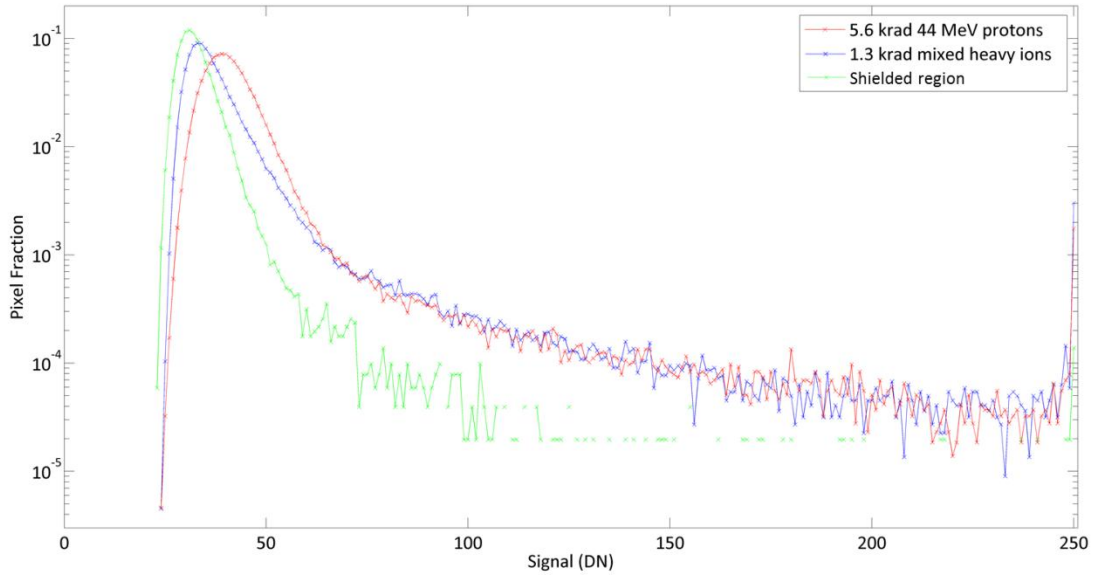

Figure 8.4. Normalised graph showing dark signal increase after irradiation with 1.3 krad of mixed heavy ions compared to that after 5.6 krad of 44 MeV protons.

This normalised histogram shows, serendipitously, that the effects of 1.3 krad of mixed heavy ions and 5.6 krad of 44 MeV protons (after anneal) exhibit the same number and distribution of bright pixel levels, meaning that per krad, heavy ions produce more displacement damage effects. In contrast, the overall dark current increase, mostly due to ionisation damage, shows little difference between the heavy ion and proton dose (19 and 15 $DN \cdot pix^{-1} \cdot s^{-1} \cdot krad^{-1}$ respectively). It is interesting to note that the number of particles to reach a krad is around 3.6 $Mions \cdot krad^{-1}$ whereas the equivalent number for 44 MeV protons is 1800 $Mprotons \cdot krad^{-1}$. When considering this with the above measurement it becomes clear that the damage caused per ion is far greater than the damage per proton.

An interesting technique allowed by the real-time imaging of the incident ions and the relatively high amount of radiation damage per incident ion is the tracing of a bright pixel back to the imaged event that caused it. Figure 8.5. shows one such event.

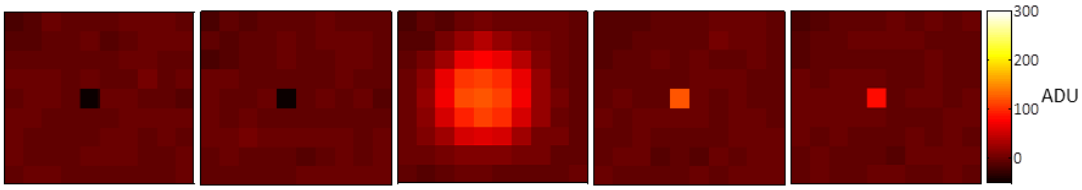

Figure 8.5. Five background subtracted 10 × 9 images taken from the device at different moments in time (leftmost first, rightmost last). The central image shows the ion impact.

The figure presents five sequentially captured frames (not necessarily sequential moments in time) showing background subtracted images (the background was determined by a mean over all frames, so the pixel appears to have less signal than the background before the damage occurs). In the central frame, a portion of the charge cloud created by an ion passing through the brightest pixel is imaged, indicating an ion incident on that pixel. After this impact, the pixel shows significantly higher dark current than before, *i.e.* it has become a bright pixel. Furthermore, since we can image for long periods of time, we can trace the behaviour of these pixels immediately after creation, which may give insight into the creation of traps and damaged pixels. Figure 8.6. shows the signal over time for a pixel showing no radiation damage after a heavy ion event is detected. Figure 8.7. shows some interesting examples of damaged pixels that are traceable back to an impact event.

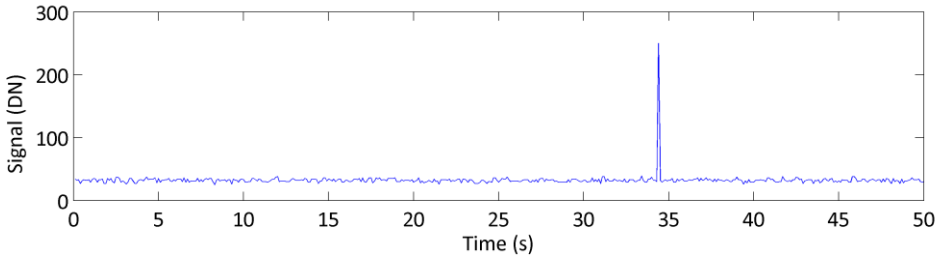

Figure 8.6. Signal over time for a signal showing no radiation damage effects after being hit by a heavy ion at t = 34.7 s.

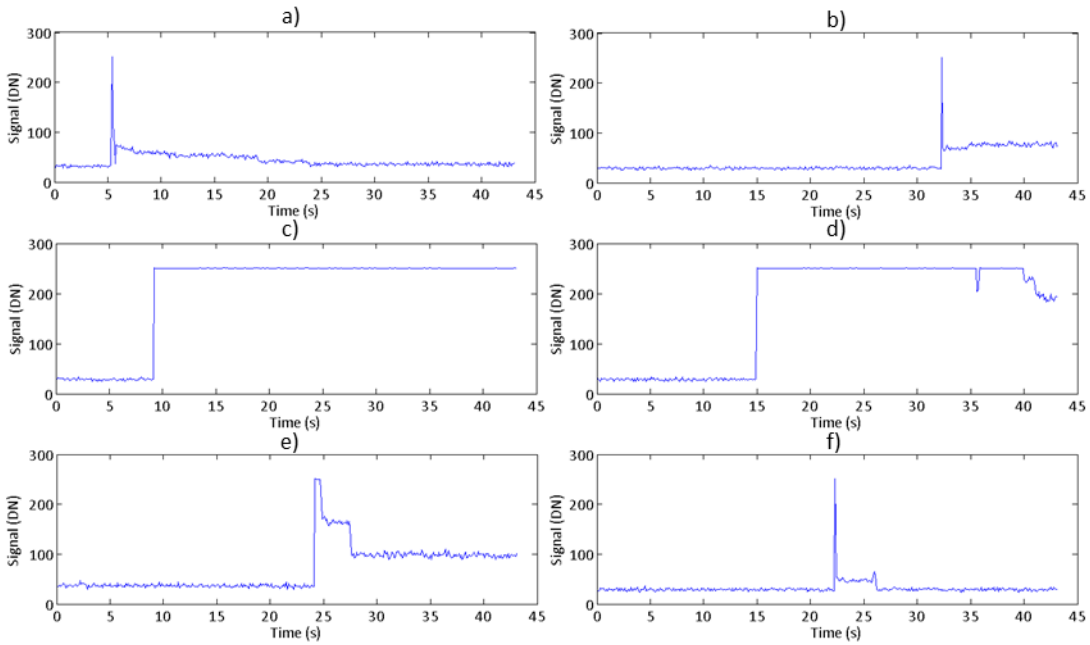

Figure 8.7. Time series of signal from single pixels under heavy ion irradiation showing live radiation damage and, in some cases, annealing.

These graphs show the signal from single pixels around a heavy ion impact that causes lasting damage to the sensor. The ion impact occurs at the highest signal level, before which only base sensor noise is exhibited. The defect dynamics after the initial damage can be characterised as three key types:

- Permanent (b, c)
- Permanent with anneal (e, f)
- Transient (a, d)

While permanent and annealing traps are expected from the literature, transient effects show unexpected behaviour, in that the dark current slowly decreases over time. While detection of such live radiation damage was rare, design of an experiment with longer imaging times under irradiation could significantly increase the detection rate. Measurement of this trap dynamism shortly after the damaging effect is rarely mentioned in the literature, and could provide a novel technique for the measurement of aspects of trap mobility shortly after creation.

8.3.1.2 Single Event Effects

Detection of SEEs was achieved by monitoring the voltage between the power rails of the USB cable supplying power (and data) to the device. Figure 8.8. shows one example of how SEEs manifest in the voltage stream of the APS readout board.

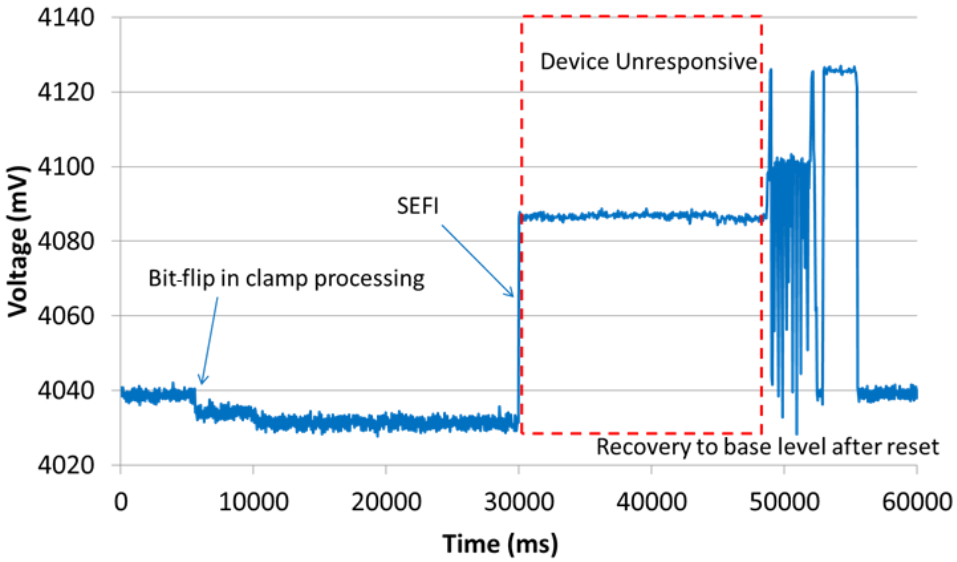

Figure 8.8. Graph showing the manifestation of SEEs in the sensor voltage stream.

This voltage stream was monitored for discrete steps which indicate a change in the device operation, which could then be correlated with the effects seen on the device. In this case, the smaller step labelled 'bit-flip in clamp processing' (occurring again at 10,000 ms) corresponded with an alteration of the background level of the device, shown in Figure 8.9. It can be seen that the mean and variance of the sensor noise increases after the SEE. Heavy ions are known to flip bits in memory, so it is likely that some part of the on-chip processing was altered, most likely part of the clamp and sample chain.

The larger step labelled as a Single Event Functional Interrupt (SEFI) corresponded to the device ceasing to output any data, and instabilities in the interface software. The turbulent signal at 48,000 ms corresponds to manual power cycling of the device in order to correct the SEFI. When the device is reconnected, the voltage signal returns to the level at the beginning of the monitoring period, indicating that the SEEs observed are temporary.

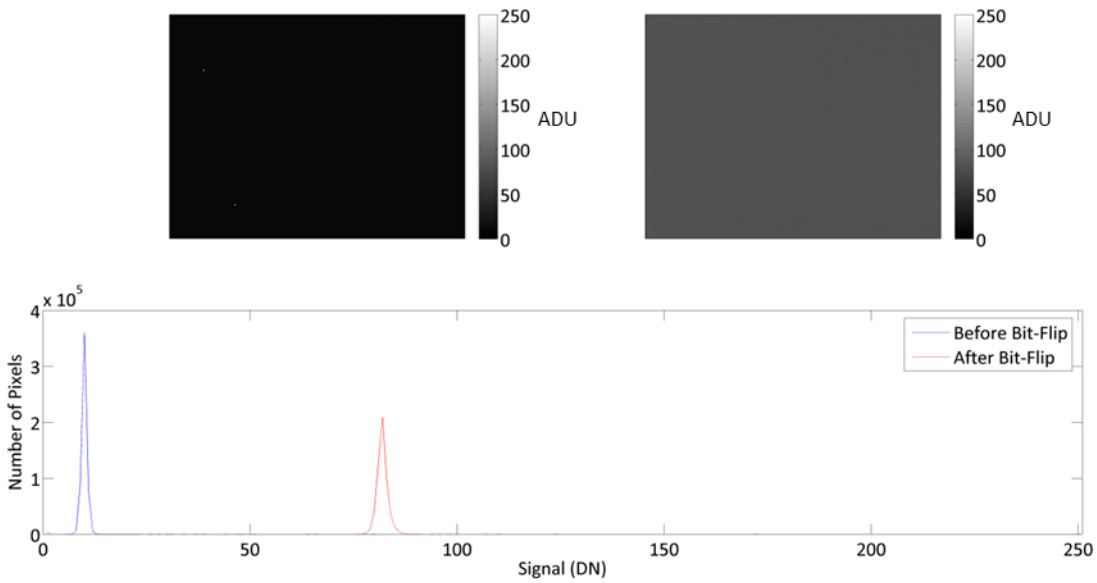

Figure 8.9. Image taken from the device before (top-left) and after (top-right) a heavy ion has caused a SEE. At bottom is shown a histogram of both images.

Table 8-2 shows measurements of SEE occurrence under heavy ion irradiation. Due to the limited time available for the experiment and the care taken not to destroy the device, the determination of the LET threshold was somewhat inaccurate, but it can be seen that the threshold occurs at some point below 15.90 $MeV \cdot cm^2 \cdot mg^{-1}$. Above this threshold, SEFI occurs about once in every 300,000 particles that hit the detector package. There may be some evidence to suggest that particles with higher LET can cause a higher incidence of SEFI per particle due to the angle of the device reducing the perpendicular surface area, but the available data are scarce. There is little evidence of single event latch-up occurring, as the functioning of the device ceased so frequently. A remote readout board may be of use in future experiments to measure latch-up occurrence on the device as distinct from latch-up on the readout board.

Ion Species	Angle (°)	Effective LET (MeV·cm^2·mg^{-1})	Total Fluence (ions·cm^{-2})	Bit-Flips	SEFIs
$^{20}Ne^{4+}$	0	6.20	3007	0	0
	0	6.20	150594	0	0
	0	6.20	301900	0	0
	40	8.09	301432	0	0
	52	10.07	301162	0	0
	60	12.40	301493	0	0
$^{40}Ar^{8+}$	0	15.90	301357	1	0
	0	15.90	905638	1	3
	37	23.31	904990	1	2
	60	31.80	905454	1	3

Table 8-2. Table of results and enumerated instance of SEFI and bit-flip incidence at each LET and particle fluence.

8.3.2 Heavy Ion Detection

Very little work has been done to assess the suitability of APS for detection and characterisation of heavy charged ions, one example being Lomheim *et al.* (1990), as most efforts have been concentrated on lighter particles such as alpha and beta particles and protons (Hancock & Soli, 1997). Passivated Implanted Planar Silicon (PIPS) detectors are generally used by heavy ion facilities to perform spectroscopic and uniformity measurements (Berger *et al.*, 1997). PIPS detectors do not image, but simply output a signal proportional to the number of electron-hole pairs generated within a fast sampling time. The PIPS is scanned over the beam area to produce uniformity measurements. One possible application for using an imaging detector would be to improve measurements of uniformity by allowing sub-pixel spatial dosimetry. Some work has been performed to assess CCD performance for measuring heavy ion and proton beam uniformity, *e.g.* Beavis *et al.* (1987).

8.3.2.1 Direct Detection

While an X-ray interacts by generating an electron cloud at a single point, a heavy ion will interact by generating electrons along the length of the ion path. From each of these points along the particle track, the generated electron clouds then diffuse towards the depletion region and are collected as signal charge, as shown in Figure 8.10. A similar schematic for a heavy ion incident at an angle is shown in Figure 8.11.

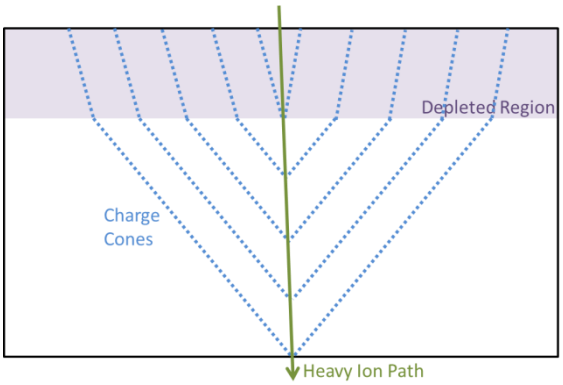

Figure 8.10. Schematic of charge collection area from electron-hole pairs generated along a heavy ion event track.

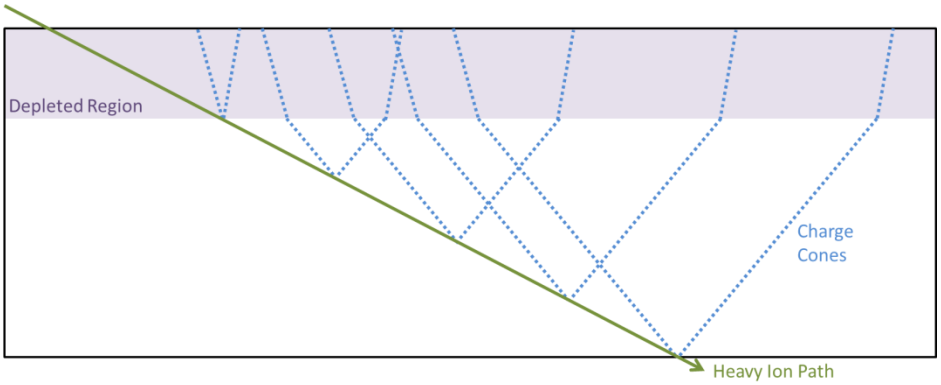

Figure 8.11. Schematic of charge collection area from electron-hole pairs generated along a heavy ion event track, incident at some angle to the device. The path is elongated resulting in an extruded distribution of a larger number of electrons.

In the case that a negligible fraction of the ion's total energy is deposited during transit, the number of electron-hole pairs generated along the path in silicon at 293 K can be shown to be:

$$n_{eh} \cong 64000\ LET\ l \tag{8.1}$$

where n_{eh} is the number of electron-hole pairs generated, LET is the LET of the incident particle in MeV·cm^2·mg^{-1} and l is the length of the particle track in µm. As the device is often tilted to increase the effective LET of the event, this can be written as:

$$n_{eh} \cong 64000\ LET\ x\ \sec(\theta) \tag{8.2}$$

where x is the thickness of the device in µm, and θ is the angle of the device to the heavy ion beam. For example, taking the lowest LET example of $^{15}N^{3+}$ ions with an LET of 3.3 MeV·cm^2·mg^{-1} perpendicularly incident on the Jade APS ($l \cong 6\ \mu m$), around 1.25 million

electron-hole pairs are generated along the track. When compared to the full well capacity of the Jade APS of ~23 ke^- it is clear that a large fraction of the generated charge will not be collected in a single pixel, leading to it being either lost to dead areas, or blooming to adjacent pixels. Analysis of images taken under heavy ion irradiation can therefore reveal details of the pixel design, such as shielded drain structures.

Blooming is caused by the number of captured electrons diminishing and even reversing the photodiode bias to a point where further electrons are no longer attracted to the photodiode and the field from adjacent pixels is larger than that from the target pixel. With a large enough number of electrons this can occur many times until all electrons are collected, resulting in a large 'blob' of saturated pixels.

Figure 8.12. shows an illustration of the characterisation performed by software. The software detects adjacent pixels above a threshold (1σ above the noise) and groups them into single 'events'. Some filtering is performed to eliminate bright pixels through further thresholding. The software then performs measurements of metrics such as weighted centroid, ellipticity, semi-major and minor axes, total event signal, semi-major axis angle, and others.

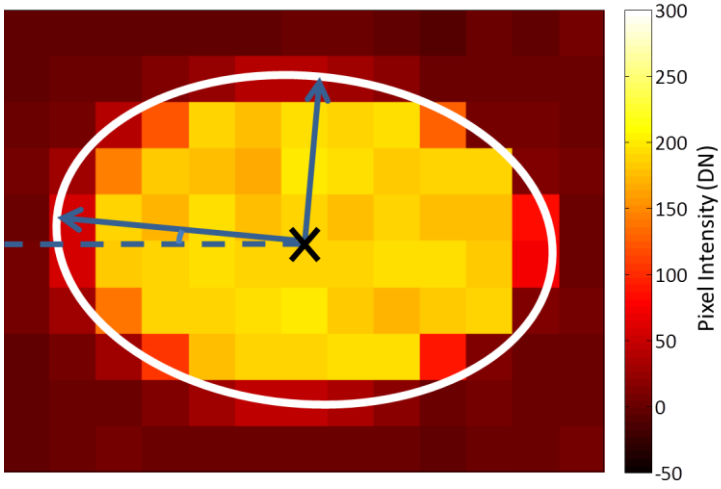

Figure 8.12. Example of an image of a heavy ion incident at a 60° angle to the sensor. Annotations show automated measurements of orientation and ellipticity.

8.3.2.2 Beam Uniformity

Figure 8.13. shows the weighted centroid position on the sensor for all heavy ions imaged during the $^{40}Ar^{8+}$ irradiations with x and y histograms along the bottom and sides. Note that the centre of the sensor and thus the centre of the beam is located at (420,320) on the position graph. An aluminium shield was covering the top half of the device.

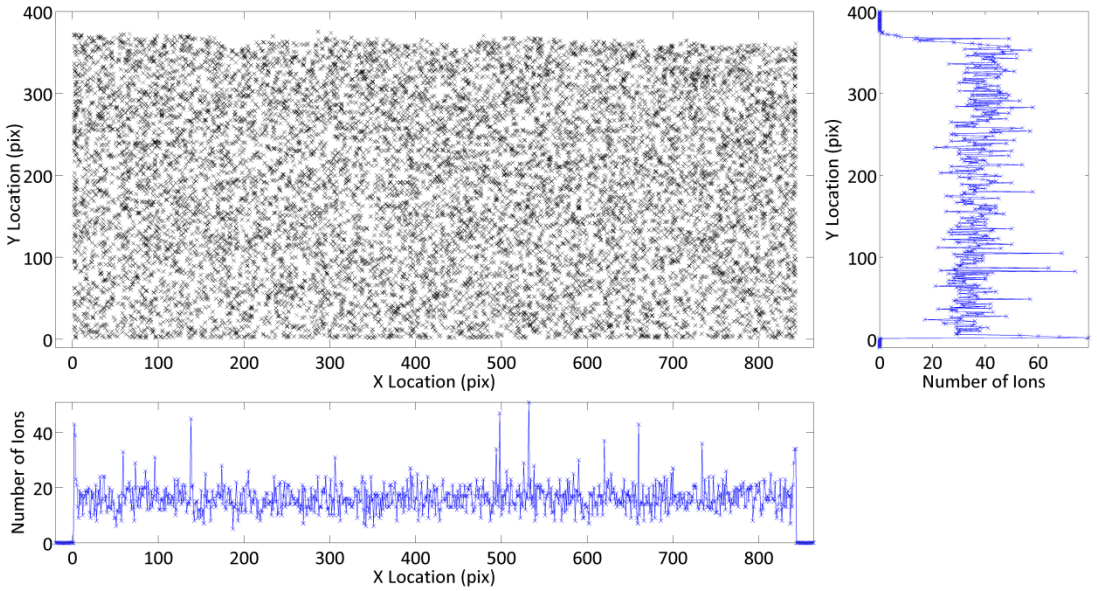

Figure 8.13. Graph showing measured image sensor ion impact position and x and y position histograms.

This shows beam uniformity at the CYCLONE facility as measured with the Jade APS. The x direction shows good uniformity while the y direction shows a slight decrease in flux away from the centre of the beam. The x direction corresponds to the cyclotron and magnetic selection axis, and so the beam uniformity is expected to be better in this axis. Figure 8.14. shows measurements of the beam uniformity using the heavy ions imaged during both $^{40}Ar^{8+}$ and $^{20}Ne^{4+}$ irradiations to improve measurement accuracy.

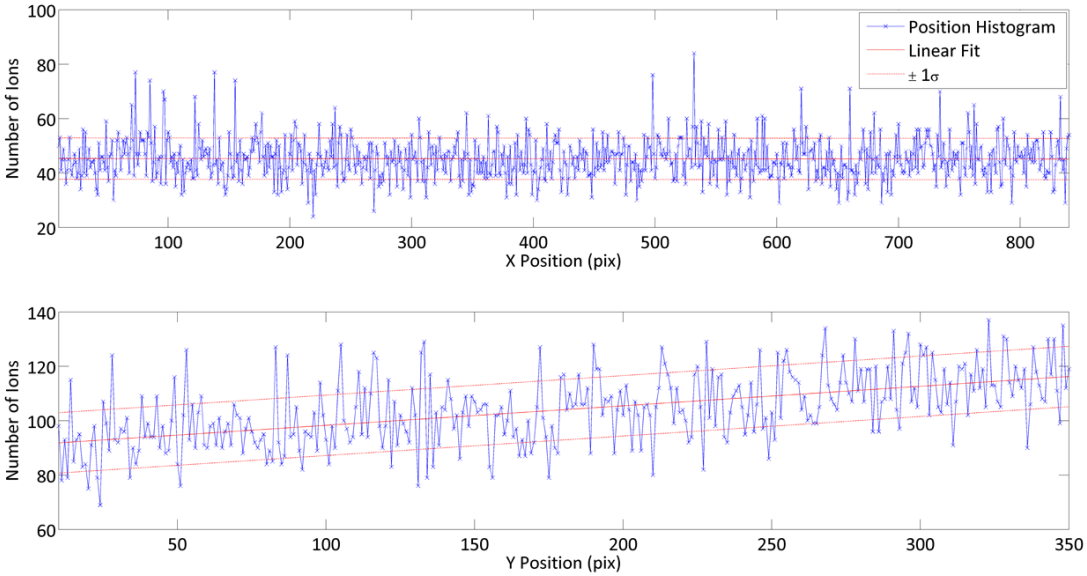

Figure 8.14. Graphs showing x and y position histograms after analysis of a larger dataset, with best linear fits.

Figure 8.14. confirms that the x axis is uniform to within experimental errors. However the y axis shows a noticeable slope. The slope equates to a decrease in flux of 0.07 ions per pixel away from the centre of the beam (assuming that the decrease is linear, which is not likely to be the case). This corresponds to a decrease of 10% after only 1 mm, which is far larger than the facility's stated non-uniformity of 10% across 25 mm.

Due to the extended and symmetrical nature of the events, it is possible to calculate a weighted centroid to calculate a sub-pixel position of the ion interaction. To calibrate the technique and highlight any problems in the measurement, the sub-pixel components of the weighted centroid position were plotted as an image, shown in Figure 8.15.

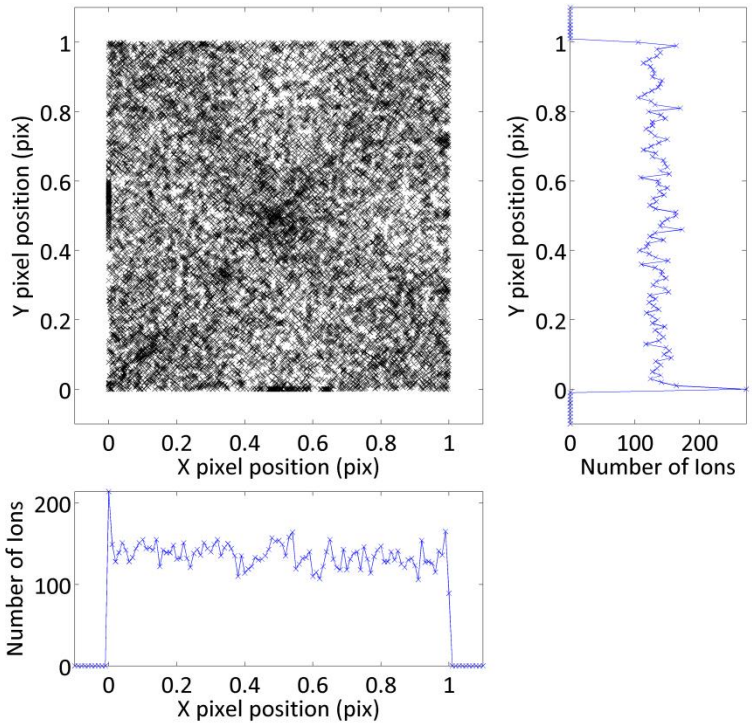

Figure 8.15. Graph showing calculated sub-pixel ion impact position and x and y position histograms.

One might expect, because of the complex pixel structure in an APS, to see some preferential positioning of the sub-pixel position that might indicate a preferential direction of charge blooming. However such an effect is not seen. The 'structure' seen in Figure 8.15. is algorithmic in nature *i.e.* due to the pixelated nature of the device, the calculated centroid position is likely to be along a pixel boundary or at a pixel centre, and does not reflect any true physical effect. The histograms at the bottom and side show that the sub-pixel distribution is, for the most part, uniform.

8.3.2.3 Imaging Heavy Ion Species Interactions

It is useful to look at images of heavy ion events to confirm that the images reflect the theory of interaction and stated above. Figure 8.16. shows a typical event imaged with 100 ms integration time at a gain of 4 for each of the particle species used.

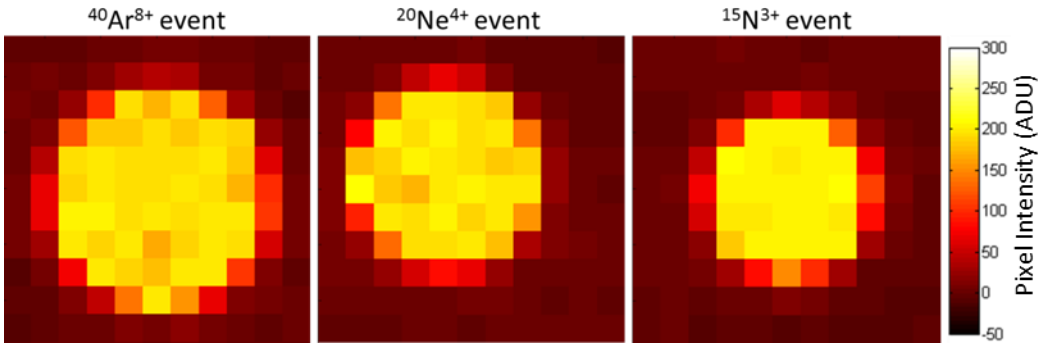

Figure 8.16. Images of a typical large event from each particle species impacting at normal incidence showing increase in event size for heavier elements.

It can be seen that the imaged event is smaller for ions with a lower LET, due to the reduced number of electron-hole pairs generated. This can be explained by both a higher electrostatic repulsion due to a higher number of electron-hole pairs (*i.e.* drifting happens in the field free region), or by wells filling and charge blooming into adjacent pixels (*i.e.* drifting happening in the depletion region). It is interesting to note that only a single pixel width border around the saturated section of the events shows charge above the background level, suggesting that blooming is the dominant factor in determining the event size. Figure 8.17. shows imaged heavy ion events at different incident angles.

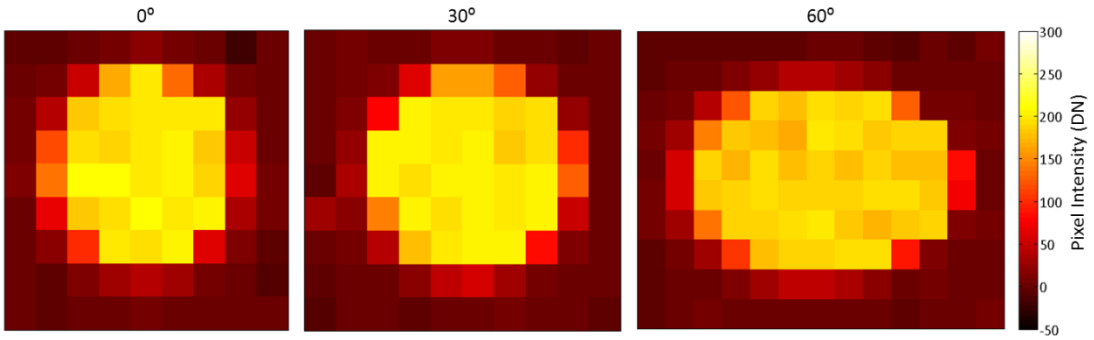

Figure 8.17. Images of a typical 'large' $^{15}N^{3+}$ event imaged at 0°, 30° and 60° incident angle. For these events ellipticities are measured to be 0.32, 0.40 and 0.65 respectively.

The imaged event at large angles such as 60° is elongated enough to be visible by eye. The elongation is of the order of the horizontal travel length in the field free region (6 µm of silicon at an angle of 60° results in a horizontal travel of 12 µm *i.e.* just over 2 pixels). It can also be seen that the non-saturated signal at the right hand side of the elongated event is sharper than seen on the left side. This indicates that the particle was travelling from right

to left, as the charge collection is significantly faster in the depletion region, resulting in less charge spreading (refer to Figure 8.11.). This suggests that while blooming is the dominant effect for charge spreading, the effects of charge cloud diffusion are still relevant and visible in events. The above results are as expected but there are a few results that are harder to explain due to the integrated nature of the device. Figure 8.18. shows typical $^{40}Ar^{8+}$ events imaged using the sensor at a gain of 1 and a gain of 4.

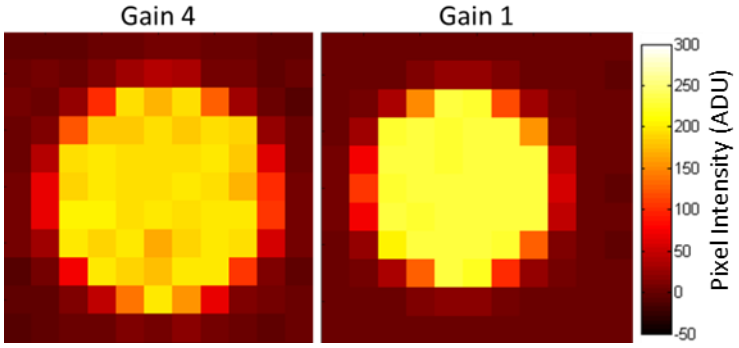

Figure 8.18. Images of a typical 'large' event with the sensor at a gain of 1 and of 4 impacting at normal incidence.

The gain setting alters the amount of charge needed to increment the ADC during readout, and does not affect the well capacity of the device. The central saturated region in both cases indicates that the full well capacity is beyond the maximum signal in the ADC. Furthermore, the smaller event size shows that saturated pixels in the gain of 4 case are not at full well capacity but instead are saturating the ADCs. This makes it difficult to calculate the total charge represented by these events, as there is charge beyond the capacity of the ADC. The brighter centre in the gain of 1 image is due to a lower background signal being subtracted. This saturation results in the integrated signal not being 4 times smaller in the gain of 4 case when compared to the gain of 1 case.

Figure 8.19. shows a series of frames being read from the device, that highlight two differing instances of charge from a single event being split between multiple frames. It should be noted that the frames may not be sequential in time, due to intermittent freezing of the device during readout, most likely due to the USB readout cable being close to the

limit for consistent USB performance. However, the charge in sequential frames gives reassurance that those images were sequential in time.

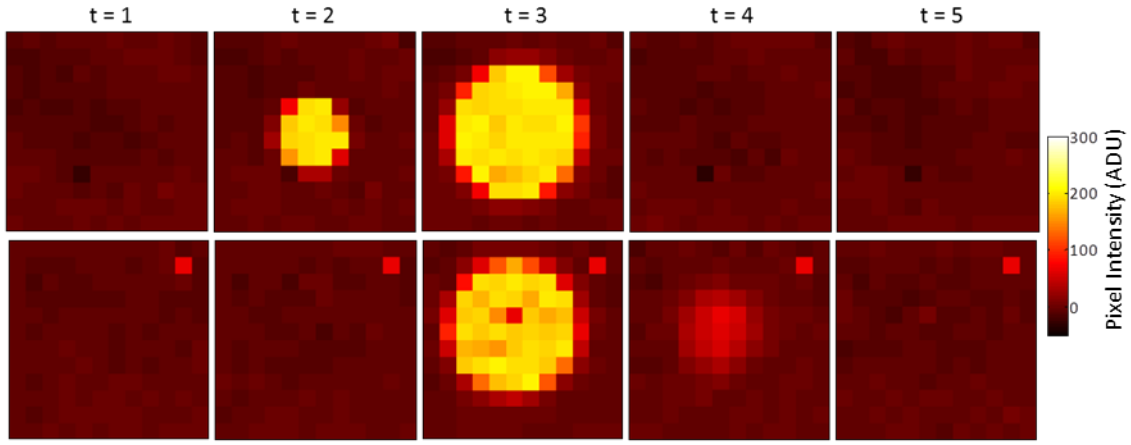

Figure 8.19. Two series of frames taken around impact events, seen in the central frame, showing incomplete charge capture. The bright pixel at the top-right of the bottom set of frames is due to previous damage by an earlier heavy ion interaction.

This figure shows in the top case a small amount of charge being captured before the rest of the event, and in the bottom case a small amount of charge being captured after the rest of the event. This can be explained by the ion arriving close to the point in time at which the array is being read out, meaning that an amount of charge is deferred from one frame to the next. This also explains the sharp nature of the event occurring in the frame before (charge does not spread due to being in the depletion region) compared to the diffuse nature of charge being captured in the frame after (charge spreading due to drift through the field free region).

However, if one considers the time taken for drift to occur in a typical sensor which is statistically represented by a time constant equation:

$$\tau = \frac{L^2}{2D} \tag{8.3}$$

where τ (s) is the time taken for $1 - 1/e = 63.2\ \%$ of the charge to be collected, L (m) is the length over which the diffusion is occurring, and D ($m^2 \cdot s^{-1}$) is the diffusion constant (≈36 $cm^2 \cdot s^{-1}$ at room temperature in silicon (Canali *et al.,* 1985)). In the case of charge

generated in the field free region of the Jade APS furthest from the photodiode, $\tau \approx 4$ ns, which is 7 orders of magnitude faster than the integration time. We should not expect to see this effect even once with an experiment that images only a few thousand events if this were the source of the deferred charge. Furthermore, there are cases when only the deferred charge is captured and not the main event. This may be caused by the problems in capturing sequential frames as described above.

Figure 8.20. shows the total integrated signal measured for all $^{40}Ar^{8+}$ ion events recorded at normal incidence.

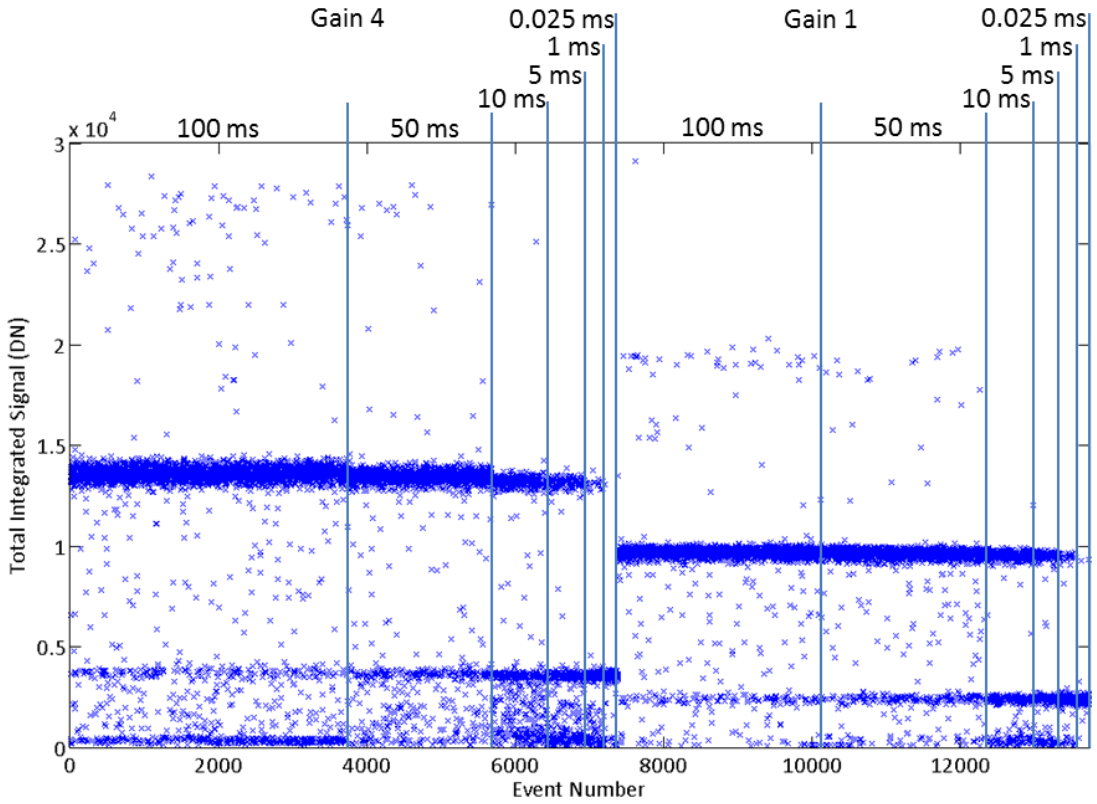

Figure 8.20. Graph of detected integrated signal of each normal incidence $^{40}Ar^{8+}$ event for a number of integration times from 0.025 to 100 ms, and with two different gain levels.

The graph, referring to the gain of 4 side, shows that the signal output is constant for each event (≈ 14,000 DN), and that for longer integration times, double events (pileup) are commonly seen (≈ 27,000 DN). Interestingly, the small events that are characterised as 'deferred charge' above generally appear at a two levels (≈ 4,000 DN, and ≈ 500 DN). The gain of 1 portion of the graph shows scaling of these levels, but the scaling relation is not

linear due to ADC saturation. If the deferred charge explanation above were accurate, one would expect to see a continuum of integrated charge amounts for the deferred charge, but Figure 8.20. shows that there is little if any such continuum. Additionally, as the integration time decreases, the fraction of 'large' to 'small' events decreases until at 0.025 ms integration all events are measured to be in the 'small' category. Note that this integration time is still far longer than the calculated drift time, and so this result, along with the small events having a fixed size, is not expected at all. So far a satisfying explanation for these effects has not been proposed.

It can also be seen that the sensor operating at a gain of 1 and a gain of 4 does not show a 4 times increase in the detected signal as would be expected. This is due to saturation of the ADC with such high signal levels, and in both cases the full well and ADC are saturated in the central region of the events. The small shift between gain settings is due to the change in the output signal in the ring of pixels around the saturated central pixels in a given heavy ion event.

8.3.2.4 Performing Heavy Ion Spectroscopy

Since the event size is constant and changes with exposure conditions and particle energy and angle, we can use equation 8.2 to calculate the 'effective' LET of non-perpendicularly incident ions, and plot the integrated signal against the effective LET. Figure 8.21. shows the collected signal for particles of different LETs under different exposure conditions using the large event size.

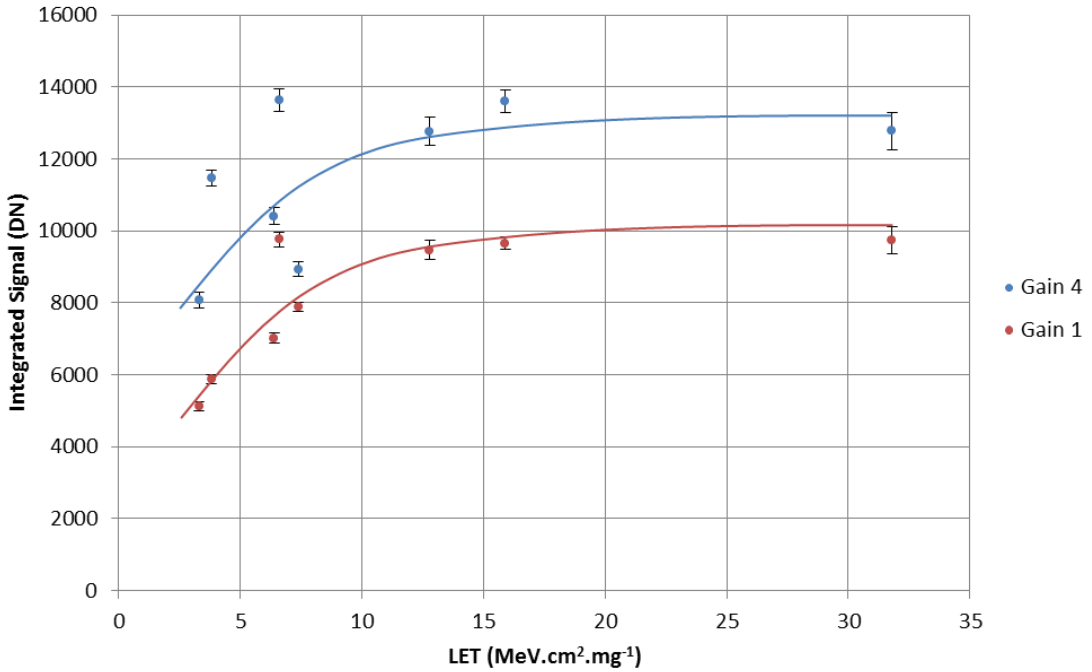

Figure 8.21. Graph of integrated signal against particle LET. The lines show a spline fit.

As LET increases, a large fraction of the event pixels are saturated, leading to the integrated signal levelling off at high LET values. However, the integrated charge clearly has a dependence on the particle LET. A spline fit is added to each data set in the figure to guide the eye. Figure 8.22. shows a similar plot to that in Figure 8.21. but with the integrated charge in the deferred charge peak.

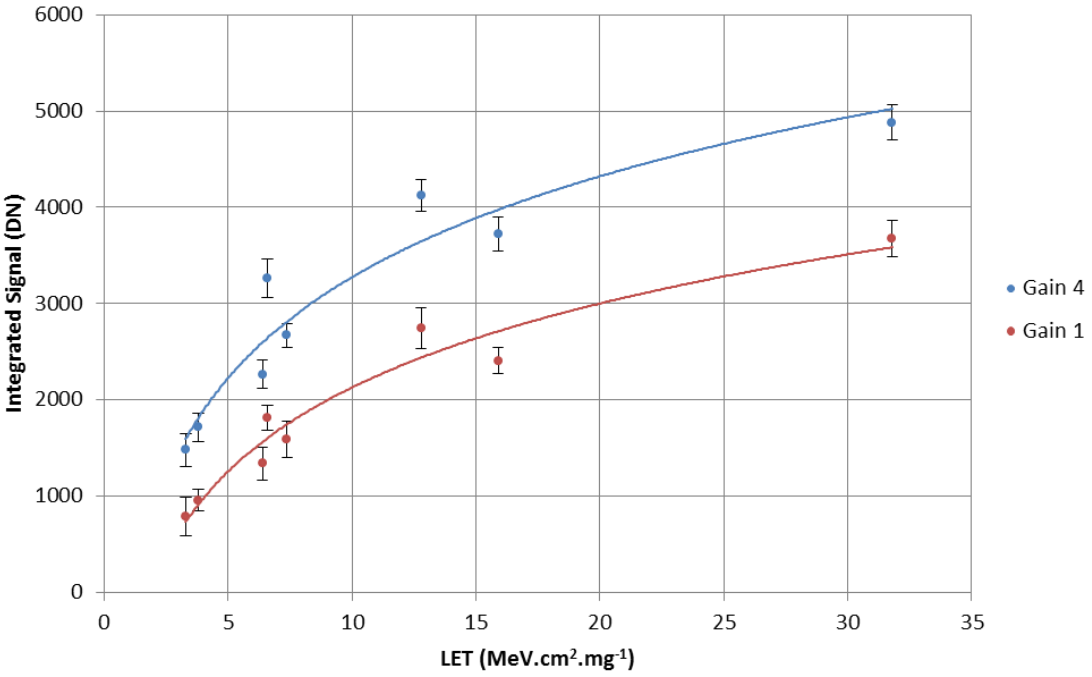

Figure 8.22. Graph of integrated signal against particle LET. The lines show a logarithmic fit.

This graph shows that the deferred integrated charge level does not level off to the same extent as the main signal charge. This is due to the lower number of saturated pixels, *i.e.* a larger fraction of the event charge is being measured without loss. A future experiment with lower LET ions or a device with a larger full well capacity would be expected to show a linear relationship between LET and integrated signal charge.

It was also considered whether the angle of the incident particles could be measured to some degree of accuracy. To accomplish this, the eccentricity and the angle of the imaged events were measured. Figure 8.23. shows the mean eccentricity for each ion species, gain and incident angle.

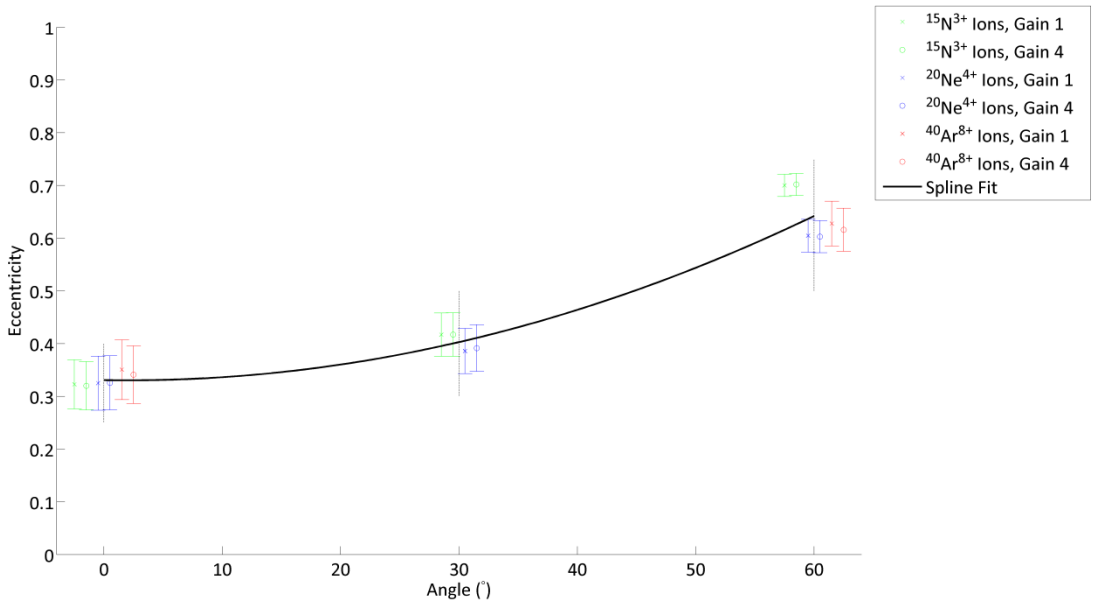

Figure 8.23 Graph showing measured event eccentricity against incident angle. Points are displaced from their true x value for legibility, the true x value is represented by the vertical black lines.

The plot shows that the eccentricity increases with particle incidence angle, and suggests that the angle can be inferred from the eccentricity, with the accuracy of the inferred value increasing as the angle becomes more oblique. The biases in the algorithm are clear from the fact that at 0^o incident angle the eccentricity should be 0, and is caused by the discrete nature of each event being pixelated, so the charge is always spreading preferentially to

pixels closer to the sub-pixel impact position. Figure 8.24. shows polar histograms showing the measured semi-major axis direction of the imaged events.

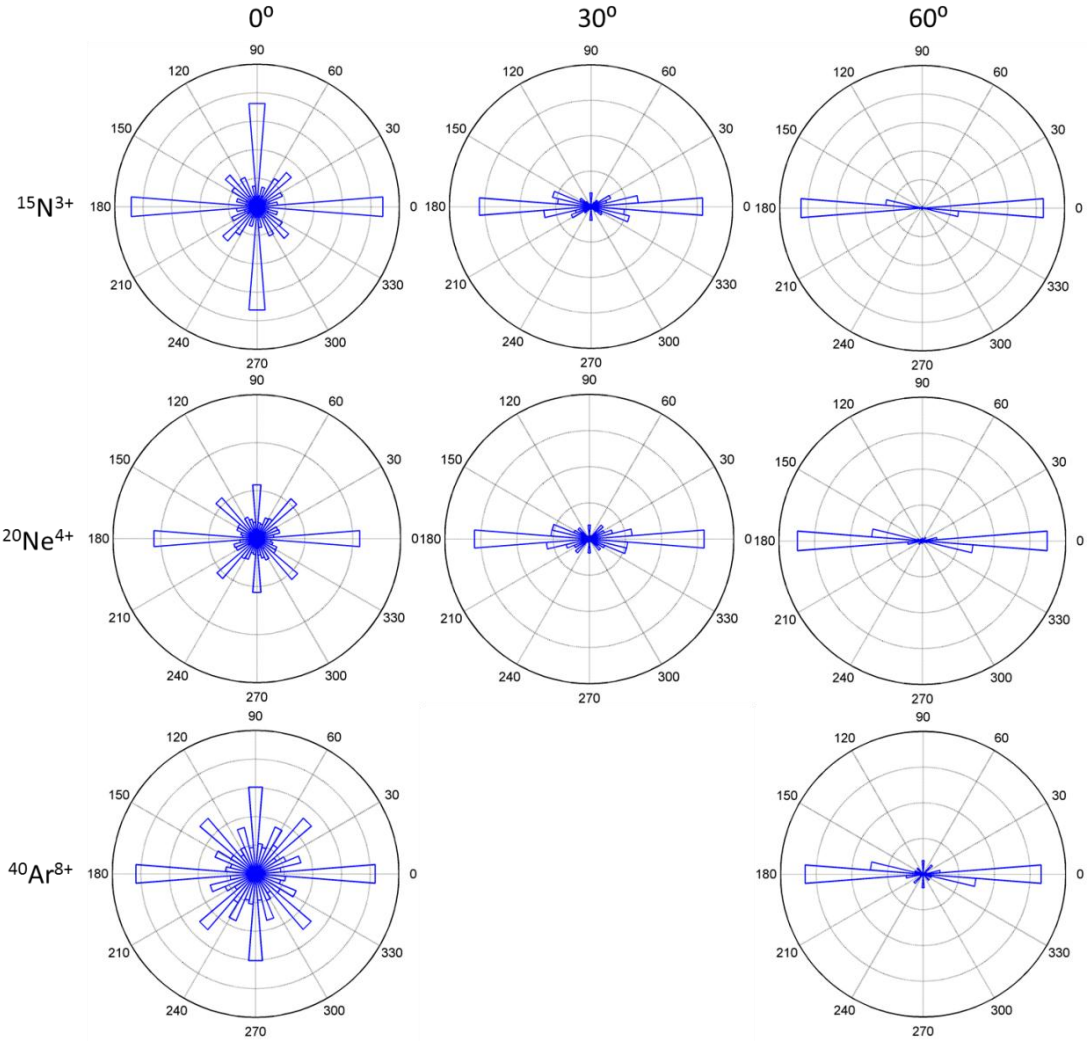

Figure 8.24. Radial histograms showing measured orientation of heavy ion images vs. incidence angle. Each graph is mirrored over the 90/270 plane.

This figure shows that as the incidence angle increases the algorithm can more accurately determine the axis that the particle is travelling in. The 0° polar histograms are interesting from an algorithmic point of view. If the pixel size was very small, one would expect a uniform measurement of the semi-major axis orientation, but due to the finite pixel size, the algorithm preferentially measures orientation in the cardinal directions. This is due to charge blooming from saturated pixels being more likely to happen in orthogonal directions, as that is where the closest potential well is likely to be.

8.4 Conclusions

This chapter has discussed the effects of heavy ions on the Jade APS. The SEE threshold was determined to be below 15.90 MeV·cm^2·mg^{-1}. The effects of SEEs in the clamp processing were shown, and could adversely impact mission performance if not filtered properly. Device performance was shown to return to base level after power cycling the device, demonstrating the temporary nature of these SEEs. It is known that a SEE may cause permanent damage to the ability of a device to operate, even after cycling the power, and further work should concentrate on determining whether such effects are possible in APS devices with a design similar to Jade.

The ability to perform spectroscopic and directional measurements of incident heavy ions was demonstrated. Results with the Jade APS were hindered by the small well capacity, and the high gain of the ADCs. An APS with improvements in these regards, as well as a thicker and more deeply depleted substrate, would perform more accurate measurements (by virtue of collecting more charge to measure more accurately the LET of the particle) and enable accurate spectroscopy. When paired with other instruments, an imaging spectrometer (much like the X-ray analogue discussed in Chapter 5) could produce new science data for solar spectrometry.

Real-time imaging of generation and subsequent evolution of new bright defects caused by displacement damage was achieved. By monitoring a defect immediately after creation, it is shown that a defect is not always created as a stable dark current source, but that some degree of annealing or total annealing can happen over a time period of seconds following defect generation. With further development this technique could allow insight into trap stability shortly after creation.

A potential use of APSs in the calibration of heavy ion beams was shown. The CYCLONE HIF beam intensity was measured to be uniform to within uncertainties in the x direction, but

exhibited a 10% reduction in heavy ion flux over 1 mm of the beam in the y direction. The limiting factors for this application will be the damage caused by the ions and the prominence of SEEs at even low incident particle LET. Improvement of the device's radiation hardness could merit further investigation of this application.

Chapter 9: Conclusions and Further Work

The work presented in this thesis focussed around a number of APS irradiations with varying particle species to measure radiation damage effects as well as the resulting imaging and spectroscopic performance. The primary particle species and facilities used are listed in Table 9-1. The following sections summarise the key findings from the studies performed.

Species	Primary Energy	Facility	Method
Gamma	1.17, 1.33 MeV	ESA, Harwell	^{60}Co Source
Proton	44 MeV	KVI AGOR	Cyclotron
Heavy Ion	Assorted	CYCLONE	Cyclotron

Table 9-1. Summary of particle irradiation species and facilities used in this work.

9.1 Radiation Induced Dark Current in Jade APS

During the course of this work the author has characterised the effect of radiation on the dark current generation rate of the Jade APS. The Jade APS has been shown to remain operational up to 0.25 Mrad(Si) of total ionising dose. The results are summarised in Table 9-2.

Irradiation Type	Dose (krad(Si))	Dark Current Increase (300K) ($pA \cdot cm^{-2} \cdot krad(Si)^{-1}$)
Gamma (Centre of device)	242	828
Gamma (Edge of device)	242	92
44 MeV Proton	5.6	107
Mixed Heavy Ions	1.3	135

Table 9-2. Dark current measurements for irradiations carried out in this work.

These measurements have contributed to the understanding of the radiation hardness of a 'baseline' APS technology, and will lead to the development of more radiation hard pixel designs for dedicated use in space applications.

9.2 APS Radiation Phenomena

Several phenomena that are not well understood in the current scientific literature have been described and characterised, namely central brightening and RTS behaviour.

9.2.1 Central Brightening

Central brightening is an effect that has only been seen in a few APSs, and not at all in CCDs. The work in this thesis shows that the extent of central brightening on the Jade APS is severe after being subjected to ionising radiation. For some dose levels and irradiation conditions the difference in mean dark current generation for differing areas of the APS can reach as high as 10 $nA.cm^{-2}$ at room temperature.

The effect was confirmed to be a physical effect occurring on the device as opposed to non-uniform irradiation or some other systematic effect. The effect was not seen in BI devices, which do not have a microlens layer to improve device QE, hence the effect is believed to be due to the processing required for adding this layer, and interactions between the device and this layer during and after irradiation.

9.2.2 Random Telegraph Signal Noise

While FET RTS is well understood, bulk RTS has several differing explanations, and could very well be caused by a number of different phenomena. The work in this thesis shows the manifestation of bulk RTS in the Jade APS, and compares experimentally observed RTS parameters to those predicted by theory and seen by other authors, suggesting that a number of RTS phenomena detected in the Jade APS are linked to the P-V defect.

Understanding RTS is very important for space applications, as the effect cannot be effectively calibrated out like other radiation effects can.

9.3 X-ray Spectroscopy Performance

The performance of the Jade APS for spectroscopy of X-ray events is of importance for several instruments wishing to perform X-ray spectroscopy in radiation hard environments, such as those planned for future Jupiter and solar missions. The X-ray performance of the Jade APS and OCI test array were measured, and is summarised in Table 9-3.

It is clear that these performance characteristics (in particular the isolated FWHM) are much worse than those measured in CCD technologies such as EMCCDs and swept charge devices, which are approaching the limit of Fano noise (~120 eV for ^{55}Fe Mn-k_α events). Further development of APS technology is needed to provide the X-ray spectroscopic performance needed for a future imaging spectroscopy mission.

Device	Event	Peak Location (eV)	FWHM (eV)	Normalised Split Event Ratio	Split Event Percentage
Jade FI	Isolated	5898	245	1.0	19 %
	3 × 3	5932	521	4.4	81 %
	5 × 5	-	-	-	
Jade BI	Isolated	5898	384	-	24%
	3 × 3	5788	597	-	69%
	5 × 5	-	-	-	7%
OCI BI 11 µm epi.	Isolated	5898	274	1.1	6 %
	3 × 3	5746	961	9.4	54 %
	5 × 5	6394	1555	7.0	40 %

Table 9-3. Summary of measurements of APS X-ray spectroscopic performance.

While event recognition techniques can re-gain some spectroscopic performance, larger split events show much lower energy resolution, partially due to loss of signal charge during event processing thresholding. The results suggest that a deep depleted sensor with large pixels would significantly increase the fraction of isolated events resulting in higher X-ray energy resolution.

9.4 Characterisation Technique Development

During the course of the work conducted for this thesis, several novel detector characterisation techniques have been developed.

9.4.1 X-ray Responsivity Map

While similar measurements are often made using optical characterisation to generate individual pixel mean-variance curves which can characterise a sensor's responsivity non-uniformity at optical wavelengths, the development of a technique to do so at X-ray wavelengths is considerably more difficult, owing to the splitting of charge between multiple pixels, leading to charge loss to pixel dead areas. By using a large number of incident X-rays, an isolated event spectrum was generated for every pixel, and using this the array can be characterised for responsivity non-uniformity, allowing corrections to collected image data to be made that lead to improvements in X-ray spectroscopy measurements.

While the calibration amounted to an increase in energy resolution of around 1% over event processed data, this technique could be performed before launch for APS arrays to allow calibration of responsivity non-uniformity to increase the accuracy of on-orbit results.

9.4.2 Heavy Ion Spectroscopy

It has been shown through characterisation of heavy ion events imaged with the Jade APS that spectroscopy can be performed with an imaging sensor of this type. The device could be used for calibration of heavy ion facilities in terms of beam uniformity as an alternative to the commonly used PIPS detector, and it also has some advantages by virtue of being an imaging sensor, allowing more accurate spatial sampling.

However, the current Jade APS device is significantly damaged by heavy ions, leading to quick degradation of the device. Further improvement in the radiation hardness of the design could allow the device to be used for such applications.

9.4.3 Heavy Ion Transient Dark Current Effects

Due to the highly damaging nature of heavy ions (*i.e.* the chance that an ion will generate increased dark current after collision is high), it has been shown that images from an APS device obtained during irradiation allow the identification of an event leading to damage. This allows observation of a defect directly after generation, and it has been shown that the nature of the dark current changes dramatically in the seconds or minutes after defect creation.

Further investigation of this phenomenon with a dedicated experimental campaign could contribute significantly to the understanding of trap generation and mobility in the time after defect creation.

References

Abalakin, V K, M Bursa, M E Davies, C de Bergh, J H Lieske, J Oberst, J L Simon, E M Standish, P Stooke, and P C Thomas. 2002. “Report of the IAU/IAG Working Group on Cartographic Coordinates and Rotational Elements of the Planets and Satellites: 2000.” *Celestial Mechanics and Dynamical Astronomy* 82 (1): 83–111.

Ait-Aider, O, N Andreff, J Lavest, and P Martinet. 2006. “Simultaneous Object Pose and Velocity Computation Using a Single View from a Rolling Shutter Camera.” *Computer Vision–ECCV 2006*: 56–68.

De Angelis, G, M S Clowdsley, J E Nealy, R K Tripathi, and J W Wilson. 2004. “Radiation Analysis for Manned Missions to the Jupiter System.” *Advances in Space Research* 34 (6): 1395–1403.

Asenov, A, A R Brown, J H Davies, S Kaya, and G Slavcheva. 2003. “Simulation of Intrinsic Parameter Fluctuations in Decananometer and Nanometer-scale MOSFETs.” *Electron Devices, IEEE Transactions On* 50 (9): 1837–1852.

Ausman, G A, and F B McLean. 1975. “Electron-hole Pair Creation Energy in SiO_2.” *Applied Physics Letters* 26 (4): 173–175.

Badhwar, G D. 1997. “Drift Rate of the South Atlantic Anomaly.” *Journal of Geophysical Research* 102 (A2): 2343–2350.

Bagenal, F, T E Dowling, and W B McKinnon. 2007. “*Jupiter: The Planet, Satellites and Magnetosphere*.” Vol. 1. Cambridge University Press.

Barth, J L, C S Dyer, and E G Stassinopoulos. 2003. “Space, Atmospheric, and Terrestrial Radiation Environments.” *Nuclear Science, IEEE Transactions On* 50 (3): 466–482.

Bayer, B E. 1976. “Color Imaging Array”. Google Patents.

Beavis, D, R Debbe, M J LeVine, J H Van Dijk, H E Wegner, Y Ikeda, and T Sugitate. 1987. “A CCD (charge Coupled Device) Beam Profile Monitor for 14.6 GeV Oxygen-16 Ions.” Brookhaven National Lab., Upton, NY (USA); Kyushu Univ., Fukuoka (Japan); Hiroshima Univ.(Japan).

Bell, J, D Lail, C Martin, and P Nguyen. 2011. “*Radiation Shielding for a Lunar Base*”. NASA report.

Bemski, G. 1958. “Recombination in Semiconductors.” *Proceedings of the IRE* 46 (6): 990–1004.

Berger, G, G Ryckewaert, R Harboe-Sorensen, and L Adams. 1997. “Cyclone – A Multipurpose Heavy Ion, Proton and Neutron See Test Site.” In *1997 RADECS Conference Data Workshop*, 51.

Bertolini, G, and A Coche. 1968. “Semiconductor Detectors.” Elsevier Science.

Bethe, H A. 1930. “Theory of Passage of Swift Corpuscular Rays Through Matter.”

Boesch, H E, F B McLean, J M McGarrity, and G A Ausman. 1975. “Role Transport and Charge Relaxation in Irradiated SiO2 MOS Capacitors.” *Nuclear Science, IEEE Transactions On* 22 (6): 2163–2167.

Bogaerts, J, B Dierickx, G Meynants, and D Uwaerts, 2003, “Total Dose and Displacement Damage Effects in a Radiation-Hardened CMOS APS”, IEEE Transactions on Electron Devices, Vol. 50, No. 1

Boyle, W S, and G E Smith. 1970. “*Charge Coupled Semiconductor Devices*.” B.S.T.J. Briefs.

Brown, W L, J D Gabbe, and W Rosenzweig. 1963. “Results of the Telstar Radiation Experiments.” In *Telstar I*, 32: 1505.

Canali, C, F Nava, and L Reggiani. 1985. “Hot Electron Transport in Semiconductors.” *Topics in Applied Physics* 58: 107–110.

Ciccarelli, A S, W V Davis, W Des Jardin, H Doan, E J Meisenzahl, L J Pace, G G Putnam, J E Shepherd, E G Stevens, and J R Summa. 2002. “Front-illuminated Full-frame Charge-coupled-device Image Sensor Achieves 85% Peak Quantum Efficiency.” In *Electronic Imaging 2002*, 153–160. International Society for Optics and Photonics.

Corbett, J W. 1966. “*Electron Radiation Damage in Semiconductors and Metals*.” Academic Press New York.

Corbett, J W, and G D Watkins. 1965. “Production of Divacancies and Vacancies by Electron Irradiation of Silicon.” *Physical Review* 138 (2A): A555.

Dale, C J, P W Marshall, E A Burke, G P Summers, and E A Wolicki. 1988. “High Energy Electron Induced Displacement Damage in Silicon.” *Nuclear Science, IEEE Transactions On* 35 (6): 1208–1214.

Dierickx, B, and E Simoen. 1992. “The Decrease of ‘Random Telegraph Signal’ Noise in Metal-oxide-semiconductor Field-effect Transistors When Cycled from Inversion to Accumulation.” *Journal of Applied Physics* 71 (4): 2028–2029.

Divine, N, and H B Garrett. 1983. “Charged Particle Distributions in Jupiter’s Magnetosphere.” *Journal of Geophysical Research* 88 (A9): 6889–6903.

Dyck, R H, and G P Weckler. 1968. “Integrated Arrays of Silicon Photodetectors for Image Sensing.” *Electron Devices, IEEE Transactions On* 15 (4): 196–201.

Dyer, C. 1998. “Space Radiation Environment Dosimetry.” In *Notes from 1997 IEEE Nuclear and Space Radiation Effects Conference Short Course*.

e2v technologies, 2003, “Technical Note on the MTF of CCD Sensors”, Technical Report, available from http://www.e2v.com

Eid, S L, R H Tsai, E R Fossum, R Spagnuolo, J J Deily and H Anthony, 2000, “Radiation-induced dark signal in 0.5-µm CMOS APS image sensors.” Proc. SPIE 4134

Einstein, A. 1905. “On a Heuristic Viewpoint Concerning the Production and Transformation of Light.” *Annalen Der Physik* 322 (6): 132–148.

Elliott, Tom. 2010. “*Gamma Radiation Study of e2v EV76C454”*. Technical Report

Emery, F E, and T A Rabson. 1965. “Average Energy Expended Per Ionized Electron-hole Pair in Silicon and Germanium as a Function of Temperature.” *Physical Review* 140 (6A): A2089.

Evans, R D, and A Noyau. 1955. *The Atomic Nucleus*. Vol. 892. McGraw-Hill New York.

Feigl, F J, W B Fowler, and K L Yip. 1974. “Oxygen Vacancy Model for the E1’ Center in SiO_2.” *Solid State Communications* 14 (3): 225–229.

Fieseler, P D, S M Ardalan, and A R Frederickson. 2002. “The Radiation Effects on Galileo Spacecraft Systems at Jupiter.” *Nuclear Science, IEEE Transactions On* 49 (6): 2739–2758.

Fimmel, R O, J Van Allen, and E Burgess. 1980. “Pioneer: First to Jupiter, Saturn, and Beyond.” *NASA Special Publication* 446.

Finlay, C C, S Maus, C D Beggan, T N Bondar, A Chambodut, T A Chernova, A Chulliat, V P Golovkov, B Hamilton, and M Hamoudi. 2010. “International Geomagnetic Reference Field: The Eleventh Generation.” *Geophysical Journal International* 183 (3): 1216–1230.

Fossum, E R. 1997a. “CMOS Image Sensors: Electronic Camera-on-a-chip.” *Electron Devices, IEEE Transactions On* 44 (10): 1689–1698.

Fossum, E R. 1997. “CMOS Active Pixel Image Sensors.” *Nuclear Instruments and Methods in Physics Research Section A: Accelerators, Spectrometers, Detectors and Associated Equipment* 395 (3): 291–297.

Frenkel, J. 1938. “On Pre-breakdown Phenomena in Insulators and Electronic Semi-conductors.” *Physical Review* 54 (8): 647.

Geist, J, and C S Wang. 1983. “New Calculations of the Quantum Yield of Silicon in the Near Ultraviolet.” *Physical Review B* 27 (8): 4841.

Goiffon, V, G R Hopkinson, P Magnan, F Bernard, G Rolland, and O Saint-Pé. 2009. “Multilevel RTS in Proton Irradiated CMOS Image Sensors Manufactured in a Deep Submicron Technology.” *Nuclear Science, IEEE Transactions On* 56 (4): 2132–2141.

Goiffon, V, P Magnan, F Bernard, G Rolland, O Saint-Pé, N Huger, and F Corbière. 2008. “Ionizing Radiation Effects on CMOS Imagers Manufactured in Deep Submicron Process.” Proc. SPIE 6816.

Goiffon, V, P Magnan, O Saint-Pé, F Bernard, and G Rolland. 2008. “Total Dose Evaluation of Deep Submicron CMOS Imaging Technology Through Elementary Device and Pixel Array Behavior Analysis.” *Nuclear Science, IEEE Transactions On* 55 (6): 3494–3501.

Goiffon, V, C Virmontois, P Magnan, P Cervantes, S Place, M Gaillardin, S Girard, P Paillet, M Estribeau, and P Martin-Gonthier. 2012. “Identification of Radiation Induced Dark Current Sources in Pinned Photodiode CMOS Image Sensors.” *Nuclear Science, IEEE Transactions On* 59 (4): 918–926.

Gorbunov, D, P Tinyakov, I Tkachev, and S Troitsky. 2008. “On the Correlation of the Highest-energy Cosmic Rays with Nearby Extragalactic Objects Reported by the Pierre Auger Collaboration.” *JETP Letters* 87 (9): 461–463.

Gosney, W M. 1972. “Subthreshold Drain Leakage Currents in MOS Field-effect Transistors.” *Electron Devices, IEEE Transactions On* 19 (2): 213–219.

Gow, J. 2010. “*Radiation Damage Analysis of the Swept Charge Device for the C1XS Instrument.*”, Brunel University School of Engineering and Design PhD Theses.

van de Graaf, E. 2008. "*Flux Calibration Irradiation for October 28, 2008.", Facility Irradiation Report.*

Greig, T A. 2008. "*Development of CMOS Active Pixel Sensors.*" Brunel University School of Engineering and Design PhD Theses.

Grove, A S. 1967. "*Physics and Technology of Semiconductor Devices."* Vol. 143. Wiley New York.

Gurney, R W, and N F Mott. 1940. "*Electronic Processes in Ionic Crystals.*" Oxford: Clarendon Press.

Hancock, B R, and G A Soli. 1997. "Total Dose Testing of a CMOS Charged Particle Spectrometer." *Nuclear Science, IEEE Transactions On* 44 (6): 1957–1964.

Harland, D M, and R Lorenz. 2005. "*Space Systems Failures: Disasters and Rescues of Satellites, Rocket and Space Probes*." Praxis.

Harriss, R D, A D Holland, S J Barber, S Karout, R Burgon, B J Dryer, N J Murray, D J Hall, P H Smith, and T Grieg. 2011. "Compact CMOS Camera Demonstrator (C3D) for UKube-1", Proc. *SPIE* 8146: 286.

Hayes, R A. 1987. "Polyimide Gas Separation Membranes". Google Patents.

Heirtzler, J R. 2002. "The Future of the South Atlantic Anomaly and Implications for Radiation Damage in Space." *Journal of Atmospheric and Solar-terrestrial Physics* 64 (16): 1701–1708.

Helfand, D J, G A Chanan, and R Novick. 1980. "Thermal X-ray Emission from Neutron Stars." *Nature* 283: 337–343.

Helms, C R, and E H Poindexter. 1999. "The Silicon-silicon Dioxide System: Its Microstructure and Imperfections." *Reports on Progress in Physics* 57 (8): 791.

Henke, B L, E M Gullikson, and J C Davis. 1993. "X-Ray Interactions: Photoabsorption, Scattering, Transmission, and Reflection at E = 50-30,000 eV, Z = 1-92." *Atomic Data and Nuclear Data Tables* 54 (2): 181–342.

Hess, W N. 1968. "*The Radiation Belt and Magnetosphere*.", Blaisdell Pub. Co.

Holmes-Seidle, A, and L Adams, 2002, "*Handbook of* Radiation Effects.", Oxford University Press, USA; 2nd edition.

Hopkins, I H, and G R Hopkinson. 1993. “Random Telegraph Signals from Proton-irradiated CCDs.” *Nuclear Science, IEEE Transactions On* 40 (6): 1567–1574.

Hopkins, I H, and G R Hopkinson. 1995. “Further Measurements of Random Telegraph Signals in Proton Irradiated CCDs.” *Nuclear Science, IEEE Transactions On* 42 (6): 2074–2081.

Hopkinson, G R, and A Mohammadzadeh. 2003. “Comparison of CCD Damage Due to 10- and 60-MeV Protons.” *Nuclear Science, IEEE Transactions On* 50 (6): 1960–1967.

Hopkinson, G R, and A Mohammadzadeh. 2008. “Low Temperature Alpha Particle Irradiation of a STAR1000 CMOS APS.” *Nuclear Science, IEEE Transactions On* 55 (4): 2229–2234.

Hopkinson, G R, A Mohammadzadeh, and R Harboe-Sorensen. 2004. “Radiation Effects on a Radiation-tolerant CMOS Active Pixel Sensor.” *Nuclear Science, IEEE Transactions On* 51 (5): 2753–2762.

Horne, R B, R M Thorne, Y Y Shprits, N P Meredith, S A Glauert, A J Smith, S G Kanekal, D N Baker, M J Engebretson, and J L Posch. 2005. “Wave Acceleration of Electrons in the Van Allen Radiation Belts.” *Nature* 437: 227–230.

Hubbell, J H, H A Gimm, and I Øverbø. 1980. “Pair, Triplet, and Total Atomic Cross Sections (and Mass Attenuation Coefficients) for 1 MeV to 100 GeV Photons in Elements Z= 1 to 100.” *Journal of Physical and Chemical Reference Data* 9: 1023.

Inguimbert, C, P Arnolda, T Nuns, and G Rolland. 2010. “‘Effective NIEL’ in Silicon: Calculation Using Molecular Dynamics Simulation Results.” *Nuclear Science, IEEE Transactions On* 57 (4): 1915–1923.

Innocent, M, 2009, “A Radiation Tolerant 4T Pixel for Space Applications.“ presented at the Proc. Int. Image Sensor Workshop (IISW), Bergen,.

Janesick, J, J Pinter, R Potter, T Elliott, J Andrews, J Tower, M Grygon, and D Keller. 2010. “Fundamental Performance Differences Between CMOS and CCD Imagers, Part IV” *Proc. SPIE* 7742.

Janesick, J R. 2001. “*Scientific Charge-coupled Devices*.” SPIE Press.

Janesick, J R. 2007. “*Photon Transfer*.” SPIE Press.

Jun, I, H B Garrett, R Swimm, R W Evans, and G Clough. 2005. “Statistics of the Variations of the High-energy Electron Population Between 7 and 28 Jovian Radii as Measured by the Galileo Spacecraft.” *Icarus* 178 (2): 386–394.

Kandiah, K, M O Deighton, and F B Whiting. 1989. “A Physical Model for Random Telegraph Signal Currents in Semiconductor Devices.” *Journal of Applied Physics* 66 (2): 937–948.

Katayama, H, H Tomida, M Matsuoka, H Tsunemi, E Miyata, D Kamiyama, and N Nemes. 2005. “Development of the X-ray CCD Camera for the MAXI Mission.” *Nuclear Instruments and Methods in Physics Research Section A: Accelerators, Spectrometers, Detectors and Associated Equipment* 541 (1): 350–356.

Kirton, M J, and M J Uren. 1989. “Noise in Solid-state Microstructures: A New Perspective on Individual Defects, Interface States and Low-frequency (1/ƒ) Noise.” *Advances in Physics* 38 (4): 367–468.

Kittel, C, 1996, “*Introduction to Solid State Physics.”* Wiley.

Knoll, GF. 1979. “*Radiation Detection and Measurement*.” Lohn Wiley & Sons, New York.

Koyama, K, V Gotthelfii, and U I-lwangi. 1995. “Evidence for Shock Acceleration of High-energy Electrons in the supernova remnant SN1006.” *Nature* 378: 255-258.

Lee, P P, R M Guidash, T H Lee, and E G Stevens. 1997. “Active Pixel Sensor Integrated with a Pinned Photodiode”. Google Patents.

Lesser, M P, 1994, “Improving CCD Quantum Efficiency”, Proc. SPIE 2198.

Linnenbom, V J. 1962. “Range-energy Relationships for Protons and Electrons Penetrating Aluminum, Silicon and Silicon Dioxide.” *NRL Report 5828.*

Lomheim, T S, R M Shima, J R Angione, W F Woodward, D J Asman, R A Keller, and L W Schumann. 1990. “Imaging Charge-coupled Device (CCD) Transient Response to 17 and 50 MeV Proton and Heavy-ion Irradiation.” *Nuclear Science, IEEE Transactions On* 37 (6): 1876–1885.

Luchkov, B I. 1981. “On the Origin of Jupiter’s Great Red SPOT.” *Pis Ma Astronomicheskii Zhurnal* 7: 566–569.

Madan, S K, B Bhaumik, and J M Vasi. 1983. “Experimental Observation of Avalanche Multiplication in Charge-coupled Devices.” *Electron Devices, IEEE Transactions On* 30 (6): 694–699.

Martin, P A. 1981. “Electric Field Enhanced Emission from non-Coulombic Traps in Semiconductors.” *Journal of Applied Physics* 52 (12): 7409–7415.

McLean, F B. 1980. “A Framework for Understanding Radiation-induced Interface States in SiO2 MOS Structures.” *Nuclear Science, IEEE Transactions On* 27 (6): 1651–1657.

Mendis, S K, S E Kemeny, and E R Fossum. 1993. “A 128× 128 CMOS Active Pixel Image Sensor for Highly Integrated Imaging Systems.” In *Electron Devices Meeting, 1993. IEDM’93. Technical Digest., International*, 583–586. IEEE.

Moore, G E. 2005. “Cramming More Components onto Integrated Circuits, 1965.” *Intel Corporation.*

Mott, N F. 1930. “The Collision Between Two Electrons.” *Proceedings of the Royal Society of London. Series A* 126 (801): 259–267.

Mukashev, B N, K A Abdullin, and Y V Gorelkinskii. 2000. “Metastable and Bistable Defects in Silicon.” *Physics-Uspekhi* 43 (2): 139–150.

Murray, N J. 2008. “*Improvements to MOS CCD Technology for Future X-ray Astronomy Missions.*”, Brunel University School of Engineering and Design PhD Theses.

Nakamura (Particle Data Group), K. 2010. “Review of Particle Physics.” *J. Phys. G: Nucl. Part. Phys* 37: 75021.

National Aeronautics and Space Administration (NASA). 1970. “*Space Radiation Protection*.” NASA-SP5094.

Oldham, T R, and J M McGarrity. 1983. “Comparison of ^{60}Co Response and 10 KeV X-ray Response in MOS Capacitors.” *Nuclear Science, IEEE Transactions On* 30 (6): 4377–4381.

Oldham, T R, and F B McLean. 2003. “Total Ionizing Dose Effects in MOS Oxides and Devices.” *Nuclear Science, IEEE Transactions On* 50 (3): 483–499.

Osborne, J P, A P Beardmore, O Godet, A F Abbey, M R Goad, K L Page, A A Wells, L Angelini, D N Burrows, and S Campana. 2005. “The In-flight Spectroscopic Performance of the Swift XRT CCD Camera.” *arXiv Preprint Astro-ph/0510489*.

Paranicas, C, B H Mauk, K Khurana, I Jun, H Garrett, N Krupp, and E Roussos. 2007. "Europa's Near-surface Radiation Environment." *Geophysical Research Letters* 34 (15): L15103.

Pike, A, and J Kendall. 2011. "*Ocean Colour CMOS Image Sensor Test Report*." Internal Technical Report, e2v technologies.

Pinto, O, W D Gonzalez, I Pinto, A L C Gonzalez, and O Mendes. 1992. "The South Atlantic Magnetic Anomaly: Three Decades of Research." *Journal of Atmospheric and Terrestrial Physics* 54 (9): 1129–1134.

Products, International Speciality. 2009. "*GAFCHROMIC(R) EBT2: Self-Developing Film for Radiotherapy Dosimetry*."

Reames, D V. 1999. "Particle Acceleration at the Sun and in the Heliosphere." *Space Science Reviews* 90 (3): 413–491.

Reichmanis, E, and J H O'donnell. 1989. "*Effects of Radiation on High-technology Polymers*.", American Chemical Society.

Reiff, P H. 1999. "Plasma Entry, Transport, and Loss in the Magnetosphere and Ionosphere." *Geophysical Monograph Series* 109: 149–159.

Rogalski, A. 2002. "Infrared Detectors: An Overview." *Infrared Physics & Technology* 43 (3): 187–210.

Rogalski, A. 2012. "History of Infrared Detectors." *Opto-Electronics Rev., 20, no. 3*

Russell, C T, and J G Luhmann. 1997. "Jupiter: Magnetic Field and Magnetosphere." *Encyclopedia of Planetary Sciences*. Chapman and Hall, New York.

Rutherford, Professor E. 1911. "The Scattering of α and β Particles by Matter and the Structure of the Atom." *The London, Edinburgh, and Dublin Philosophical Magazine and Journal of Science* 21 (125): 669–688.

Seitz, F. 1949. "On the Disordering of Solids by Action of Fast Massive Particles." *Discussions of the Faraday Society* 5: 271–282.

Seltzer, S M. 1994. "Updated Calculations for Routine Space-shielding Radiation Dose Estimates: SHIELDOSE-2." *NIST Publication NISTIR* 5477.

Sexton, F W. 2003. “Destructive Single-event Effects in Semiconductor Devices and ICs.” *Nuclear Science, IEEE Transactions On* 50 (3): 603–621.

Sexton, F W, D M Fleetwood, M R Shaneyfelt, P E Dodd, and G L Hash. 1997. “Single Event Gate Rupture in Thin Gate Oxides.” *Nuclear Science, IEEE Transactions On* 44 (6): 2345–2352.

Shemansky, D E. 1988. “Energy Branching in the Io Plasma Torus- The Failure of Neutral Cloud Theory.” *Journal of Geophysical Research* 93: 1773–1784.

Short, A, G Hopkinson, A Laborie, P Pouny, C Vetel, T Eaton, R Steward, A Holland, I Hutchinson, and D Smith. 2005. “Gaia Astrometric CCDs and Focal Plane.” *Proc. SPIE 5902.*

Sloanaker, R M. 1959. “Apparent Temperature of Jupiter at a Wave Length of 10 Cm.” *The Astronomical Journal* 64: 346.

Smith, D R, A D Holland, and I B Hutchinson, 2004, “Random Telegraph Signals in Charge Coupled Devices.”, *Nuclear Instruments and Methods in Physics Research A: Volume 530, Issue 3, p. 521-535.*

Solar-C Working Group. 2011. “*Solar-C Plan-B*.” http://solar-b.nao.ac.jp/SOLAR-C/Documents/Interim_report2011.html.

Soliman, K, and D K Nichols. 1983. “Latchup in CMOS Devices from Heavy Ions.” *Nuclear Science, IEEE Transactions On* 30 (6): 4514–4519.

Stassinopoulos, E G, and K A LaBel. 2004. “The Near-Earth Space Radiation for Electronics Environment.” NASA Technical Document.

Stassinopoulos, E G, and J P Raymond. 1988. “The Space Radiation Environment for Electronics.” *Proceedings of the IEEE* 76 (11): 1423–1442.

Swordy, S P. 2001. “The Energy Spectra and Anisotropies of Cosmic Rays.” *Space Science Reviews* 99 (1): 85–94.

Sze, S M. 1981. “*Physics of Semiconductor Devices*”. New York: Wiley.

Taubes, G. 1993. “Pattern Emerges in Cosmic Ray Mystery.” *Science* 262 (5140): 1649.

Thomson, N R, C J Rodger, and M A Clilverd. 2005. “Large Solar Flares and Their Ionospheric D Region Enhancements.” *J. Geophys. Res* 110 (A6).

Tian, H, B Fowler, and A El Gamal. 1999. “Analysis of Temporal Noise in CMOS APS.” *Proc. SPIE*, 3649: 177–185.

Umeda, T, K Okonogi, K Ohyu, S Tsukada, K Hamada, S Fujieda, and Y Mochizuki. 2006. “Single Silicon Vacancy-oxygen Complex Defect and Variable Retention Time Phenomenon in Dynamic Random Access Memories.” *Applied Physics Letters* 88 (25).

Uren, M J, D J Day, and M J Kirton. 1985. “1/f and Random Telegraph Noise in Silicon Metal-oxide-semiconductor Field-effect Transistors.” *Applied Physics Letters* 47 (11): 1195–1197.

Uren, M J, M J Kirton, and S Collins. 1988. “Anomalous Telegraph Noise in Small-area Silicon Metal-oxide-semiconductor Field-effect Transistors.” *Physical Review B* 37 (14): 8346.

Van Allen, J A, and L A Frank, 1959. “Radiation around the Earth to a radial distance of 107,400 km.” Nature, 183.

Van de Voorde, M. 1973. “Results of Physical Tests on Polymer Materials at Cryogenic Temperatures.” *Nuclear Science, IEEE Transactions On* 20 (3): 693–697.

Vasilescu, A, and G Lindström. 2000. “Notes on the Fluence Normalisation Based on the NIEL Scaling Hypothesis.” *ROSE Collaboration Note: ROSE/TN/2000-02*.

Vette, J I. 1991. “The AE-8 Trapped Electron Model Environment.” *NASA STI/Recon Technical Report N* 92.

Wang, R V, Y H Lee, Y L R Lu, W McMahon, S Hu, and A Ghetti. 2009. “Shallow Trench Isolation Edge Effect on Random Telegraph Signal Noise and Implications for Flash Memory.” *Electron Devices, IEEE Transactions On* 56 (9): 2107–2113.

Wang, X, P R Rao, A Mierop, and A J P Theuwissen. 2006. “Random Telegraph Signal in CMOS Image Sensor Pixels.” In *Electron Devices Meeting, 2006. IEDM’06. International*, 1–4. IEEE.

Watkins, G D. 2000. “Intrinsic Defects in Silicon.” *Materials Science in Semiconductor Processing* 3 (4): 227–235.

Watkins, G D, and J W Corbett. 1961. “Defects in Irradiated Silicon. I. Electron Spin Resonance of the Si-A Center.” *Physical Review* 121 (4): 1001.

Watkins, G D, and J W Corbett. 1964. “Defects in Irradiated Silicon: Electron Paramagnetic Resonance and Electron-nuclear Double Resonance of the Si-E Center.” *Physical Review* 134 (5A): A1359.

Watkins, G D, and J W Corbett. 1965. “Defects in Irradiated Silicon: Electron Paramagnetic Resonance of the Divacancy.” *Physical Review* 138 (2A): A543.

Weckler, G P. 1967. “Operation of Pn Junction Photodetectors in a Photon Flux Integrating Mode.” *Solid-State Circuits, IEEE Journal Of* 2 (3): 65–73.

Williams, D J, B Mauk, and R W McEntire. 1998. “Properties of Ganymede’s Magnetosphere as Revealed by Energetic Particle Observations.” *Journal of Geophysical Research* 103 (A8): 17517–17523.

Winokur, P S, J R Schwank, P J McWhorter, P V Dressendorfer, and D C Turpin. 1984. “Correlating the Radiation Response of MOS Capacitors and Transistors.” *Nuclear Science, IEEE Transactions On* 31 (6): 1453–1460.

Winokur, P S, F W Sexton, G L Hash, and D C Turpin. 1987. “Total-dose Failure Mechanisms of Integrated Circuits in Laboratory and Space Environments.” *Nuclear Science, IEEE Transactions On* 34 (6): 1448–1454.

Zhang, J, X Song, Y Li, P G Richards, X Sun, and F Waldhauser. 2005. “Inner Core Differential Motion Confirmed by Earthquake Waveform Doublets.” *Science* 309 (5739): 1357–1360.

Ziegler, J F, and J P Biersack. 2008. “SRIM-2008, Stopping Power and Range of Ions in Matter.”, http://www.srim.org